Contents

Preface

This book is devoted to the problems connected with detailed analysis of coherent fields and images and their application in remote sensing. Our consideration is based on several coherent phenomena, such as the Doppler effect, which is related to the phase variation of radiation reflected by a moving object, and the effect of speckle pattern formation on the radiation scattered by rough objects. Since the beginning of the twentieth century, coherent phenomena, including interference, have been actively used in radio and acoustic communication and in location techniques. At first, applications were concerned with rather simple effects such as interference of two mutually coherent plane waves leading to a sinusoidal pattern. However, in the second half of the century, rapid development of laser technology brought more complicated problems related to interference effects. Those who observed images of rough objects by means of laser radiation noticed their strongly inhomogeneous structure. This structure is called the speckle pattern. The speckle pattern also appears in laser radiation scattered by a rough object or by a large number of randomly distributed particles. A multicolor speckle pattern can be observed for white light scattered by rough objects, randomly distributed particles, and diffraction gratings with a random period. For instance, if one looks at the sun with blinking eyes, light is scattered by one's eyelashes, which is a similar effect as a diffraction grating with a random period, and a speckle pattern consisting of colored spots can be seen.

Although effects of this kind are well known to everyone, it was M. Von Laue[1] who first described this phenomenon and studied it for the case of scattering by multiple particles. A bibliography of his fundamental papers on the theory of coherence , including speckle optics, can be found in the books by Mandel and Wolf [2] and Goodman.[10] In the beginning of the twentieth century, he pointed out for the first time that a speckle pattern is built by many interfering waves diffracted by the elements of the scattering medium. However, up until the mid-1960s, effects related to speckle pattern formation did not attract much attention. This is evident, for instance, from the fact that such phenomena were not considered in the monumental book of Born and Wolf.[3] One of the first works that used speckle pattern formation analysis for light scattered by rough surfaces was by Rigden and Gordon.[4] One of the first works to analyze the dynamic speckle pattern was by Anisimov et al.[5]

In the 1970s and beginning of the 1980s, many authors suggested using speckle pattern formation to determine the shape, velocity parameters, and dynamic para-

meters of deformations for various objects. These proposals are summarized in Refs. 6–9. In the 1980s, a consistent statistical description of coherent phenomena was developed,[10] and the statistical characteristics of coherent fields scattered by rough objects as well as coherent images of those objects were studied in detail.[11,12] Due to further development of this subject, the terms "coherent field" and "coherent image" (meaning, respectively, a field scattered by a rough object and by its image[11,12]) became widely used. In this book, a scattered field is *coherent* if its value at each point is given by a sum of amplitudes (interference) of all waves scattered by the object surface and reaching this point. A *coherent image* of a rough object is defined as an image that satisfies the following condition: at each point, there is interference of all waves coming from the smallest area of the object surface that is resolvable by the imaging system. In particular, coherent fields and images are formed when an object is illuminated by monochromatic light. Conditions under which coherent fields and images are formed will be considered in detail in Appendix 4 and in Sec. 2.5.

Finally, beginning in the 1990s there appeared a number of works analyzing phenomena connected with coherent light scattering by moving rough objects. In such phenomena, both the Doppler effect and the speckle effects are manifested, and they can be used for determining the parameters of an object's motion. Among these works, one of the most important is that by Asakura and Okomato.[13]

At present, the use of coherent fields and images in remote sensing is increasingly drawing more attention from the scientific community. This is due to a growing understanding of the fact that coherent fields and images can provide significant information about remote objects in a variety of practical situations.[12] For example, coherent remote sensing can be very helpful when either the scattered radiation is seriously distorted because of propagation through an inhomogeneous (turbulent) medium or remote objects with low reflection, or when the resolution of the imaging system is too low. Development of fast computers, sensitive detectors, and high-power sources of coherent radiation increased the feasibility of coherent remote sensing.

A bright example of the progress in coherent remote sensing is *Fourier telescopy*.[14–18] This technique, which enables exact imaging of remote objects in a turbulent atmosphere, is proposed for the ambitious project GLINT,[15] which aims to image objects that are 40,000 km away from Earth. Most alternative methods for achieving this goal use adaptive elements to compensate for the phase distortions accumulated while the scattered radiation propagates to the observer. This approach requires a large number of highly sensitive detectors and a lot of computations. Fourier telescopy uses a matrix of coherent sources controlled in such a way that sinusoidal interference patterns formed by radiation from particular source pairs on the object's surface have different periods and directions. Selecting portions of the scattered radiation corresponding to a given interference pattern, one can compensate for the phase distortions using a special (*phase-closure*) algorithm and build the Fourier components of the object's true image. The image itself is formed by applying the inverse Fourier transform to these components. This imaging technique does not require powerful computers or sensitive detectors.

Another example of a successful application of coherent fields and images is a radically new kind of holography that was developed by the author, i.e., *time background holography* of moving objects. This technique enables remote sensing of transparent or weakly reflecting objects that are moving against a relatively bright, inhomogeneous background. Although there had been several earlier attempts to solve this problem,[19,20] only time background holography provides a practical solution.[21–23] The approach involves obtaining information about the moving object from the time spectrum of the coherent fields scattered by an object and its background. Two papers report the results of experiments performed in the microwave and ultrasonic ranges.[21,23]

A special part of time background holography is the time averaging method. The method implies that the time-averaged amplitude of the scattered field, i.e., the point of the spectrum corresponding to the frequency of the illuminating radiation, contains information about the object. The time averaging method enables one to detect moving objects and to determine their shapes even when they are either transparent, weakly reflecting, or indistinguishable from the background. One of the most important advantages of the method is that it allows a completely absorbing object to be detected with the same probability as an object whose reflection does not differ from that of the background. Akapov and Mandrosov proposed a conceptual schematic of a device that uses the time averaging method in environmental monitoring, specifically for detecting clusters of pollution particles—including completely absorbing particles—and determining their concentration, average size, and average velocity.[22]

Naturally, applications of coherent remote sensing are not limited to the above two examples. However, since they are both illustrative and promising, they will be given detailed consideration in this book.

The above considerations were taken into account when the framework for this book was formulated. Therefore, in the first and second chapters, statistical characteristics of speckle patterns in coherent fields scattered by rough objects and in the coherent images of such objects are studied. These chapters will help the reader to understand the relationship between speckle patterns and a surface's geometric and roughness parameters. The third chapter describes methods that use coherent images to determine the dynamic parameters of an object, such as linear velocity, rotation rate, and the angle of rotation. A distinguishing feature of these coherent remote sensing methods is that they require no reference beam and therefore do not need highly coherent sources. In particular, one can use laser sources with a coherence length not exceeding 1 m.

The fourth and the fifth chapters are devoted to issues closely connected with the above two examples. The fourth chapter presents the basics of Fourier-telescopic imaging. Theoretical consideration shows that the images obtained by means of Fourier telescopy are similar to conventional coherent images; in particular, they are *speckle patterns*. For this reason, the images can be successfully used in the methods to determine the geometric and dynamic parameters of various objects, which are considered in the third chapter. In the fourth chapter, we analyze

how the dimensions of the receiving and transmitting apertures affect the resolving power of Fourier telescopy systems, and how noise factors and surface roughness influence image quality. In the same chapter, it is shown that Fourier telescopy can be used to construct a panoramic laser microscope, an instrument that provides broad-angle, high-resolution imaging in medicine and biology.[18] Such a microscope can be applied for imaging extended ($\sim$10 cm) objects with a resolution of about 1 μm.

In the fifth chapter, it is shown how one can use time background holography for the detection and determination of parameters of moving objects that are indistinguishable against the background, transparent, or weakly reflecting. A fast algorithm is proposed for the detection of objects with reflectance considerably lower than that of the surrounding background.

This book is addressed to a broad community of researchers interested in coherent phenomena and their applications. For one's first reading, I recommend that the reader pay attention to the numbered equations and ignore the algebra. The reader should concentrate on the physical essence of coherent phenomena, the description of the arrangements based on those phenomena, the figures—which play an important role in this book—and on the enumerated conclusions to each chapter. The introductions to each chapter and several other sections will expose the reader to the history of the problems posed in a variety of applicable fields. In subsequent readings, one may give special attention to the study of particular devices or to the derivation of particular formulas. The relatively large number of formulas is not surprising: while deriving rather simple engineering equations for the devices based on coherent fields and images in remote sensing, one cannot bypass the mathematical analysis of the statistical structure of fields scattered by objects and their images.

At the same time, the mathematics used here is within the framework of courses taught in technical institutes. Therefore, this book can be helpful not only for researchers and engineers working in the field where coherent fields and images in remote sensing can be used, but also for senior university and graduate students specializing in this field. The most complicated consideration of the statistical structure of coherent fields and images, which is presented in Appendixes 1–3, would be interesting for the reader who wishes to understand the particular details of the mathematical analysis of this structure.

In Appendix 4, problems connected with the coherence of fields scattered by rough objects and with contrast of the scattered field intensity distribution are considered. In particular, a detailed answer is given to the question, what is a coherent field? Appendix 5 contains a semi-qualitative explanation of the physics of speckle pattern formation in the images of rough objects.

The basic results included in this text were published previously in proceedings and journals. However, some of the results were obtained during the preparation of this manuscript. For this reason, not all ideas presented in the book can be considered as equally conventional; some of them need further discussion and development. The author is grateful to anyone who wishes to discuss them or suggests any comments.

I would like to express special gratitude to Prof. P. Bakut, an outstanding scientist in the field of the statistical methods of obtaining and processing information about remote objects from the scattered radiation in the radio and visible frequency ranges. It is our long and fruitful collaboration that stimulated the idea of this book. I am also indebted to Prof. I. Troitsky for valuable and fruitful discussions on the statistics of coherent fields and images, especially about the mathematical methods of their processing.

I am grateful to V. Barinov and R. Poliakov, who carried out high-quality experiments on the registration and processing of radiation scattered by both stable and moving rough objects as well as on the registration of their images. The results of their experiments are presented in the book.

I would like to thank Dr. V. Gamiz for his support of this work and valuable discussions of the results, and Dr. M. Chekhova for help with the manuscript preparation and valuable remarks on the statistics of coherent fields. I feel special gratitude to Dr. E. Akopov, whose help provided the crucial condition for the launch of the book project.

I also express my sincere gratitude to Dr. Boris Ginzburg, whose invaluable support was a great help for overcoming obstacles in my scientific career in the field of coherent remote sensing.

Finally, I feel especially grateful to my wife Maria, whose constant support made this work possible.

Valery Mandrosov
January 2004

Notation

$\mathbf{r}_\Sigma$	radius vector of the random surface of the object under study
$\mathbf{r}$	radius vector of the mean surface of the object under study
u, v	surface coordinates on the mean surface of the object under study
$\xi(\mathbf{r})$	distribution of surface roughness height
$\mathbf{n}, \mathbf{N}$	external normal to the surface at point (u, v)
$\mathbf{N}$	external normal to the mean surface at point (u, v)
x, y, z	Cartesian coordinates of point (u, v)
X, Y, Z	Cartesian coordinate axes
w_n	n-dimensional probability density
$B_{12}(\mathbf{r}_1, \mathbf{r}_2)$	correlation function of the surface roughness height distribution
σ	standard deviation of the surface roughness height distribution
ℓ	correlation radius of the surface roughness height distribution
$k(\mathbf{r})$	field reflection coefficient distribution on the surface of the object under study
$\boldsymbol{\rho}$	radius vector of the scattered field observation plane (of the imaging system aperture)
S_ρ	imaging system aperture area
d_ρ	imaging system aperture size
$\boldsymbol{\rho}_s$	radius vector of the illuminating source
S_s	aperture area of the illuminating source

E_s	complex amplitude of the illuminating source
λ	wavelength of the illuminating source
ω	circular frequency of the wave
ω_0	mean circular frequency of the wave
$S_r(\omega)$	spectrum of the illuminating source
$f = \omega/2\pi$	frequency of the wave
$\boldsymbol{\nu}_i = (\mathbf{r}_\Sigma - \boldsymbol{\rho}_s)/\lvert\mathbf{r}_\Sigma - \boldsymbol{\rho}_s\rvert \approx (\mathbf{r} - \boldsymbol{\rho}_s)/\lvert\mathbf{r} - \boldsymbol{\rho}_s\rvert$	unit propagation vector of the incident field
$\boldsymbol{\nu}_o = -(\mathbf{r}_\Sigma - \boldsymbol{\rho})/\lvert\mathbf{r}_\Sigma - \boldsymbol{\rho}\rvert \approx -(\mathbf{r} - \boldsymbol{\rho})/\lvert\mathbf{r} - \boldsymbol{\rho}\rvert$	unit vector directed from the point $\mathbf{r}_\Sigma$ to the observation point $\boldsymbol{\rho}$
$\mathbf{q} = \boldsymbol{\nu}_o - \boldsymbol{\nu}_i \approx (\boldsymbol{\rho} - \mathbf{r}_c)/\lvert\boldsymbol{\rho} - \mathbf{r}_c\rvert + (\boldsymbol{\rho}_s - \mathbf{r}_c)/\lvert\boldsymbol{\rho}_s - \mathbf{r}_c\rvert$	scattering vector
$q_t = (q^2 - q_N^2)^{0.5}$	projection of vector $\mathbf{q}$ on the mean surface tangent plane
$q_N = \mathbf{q} \cdot \mathbf{N}$	projection of vector $\mathbf{q}$ on vector $\mathbf{N}$
t	time of the field processing
t_0	the start time of the field processing
T	the duration of the field processing
$E(\boldsymbol{\rho}, t)$	distribution of the complex amplitude of the field scattered by the object under study in the observation plane (the imaging system aperture)
$B(\boldsymbol{\rho}_1, t_1, \boldsymbol{\rho}_2, t_2)$	correlation function of the complex amplitude of the field scattered by the object under study in the observation plane
$E_i(\mathbf{r}_\Sigma, \omega)$	the spectral amplitude of the incident field on the object surface
$E_0(\boldsymbol{\rho}, \omega)$	the spectral amplitude of the field scattered by the object
$I(\boldsymbol{\rho}, t)$	intensity distribution of the field scattered by the object under study on the imaging system aperture
S_o	area of the illuminated surface of the object under study
d_o	diameter of the illuminated surface of the object under study

S_e	effective area of the backscattering surface of the rough object. For a flat object, $S_e = S_o$
$\mathbf{r}_c$	vector of the object's center of mass
$r_c = \lvert\mathbf{r}_c\rvert$	the distance to the object under study
$\mathbf{v}, v$	velocity vector and its length for a point (u, v) on the object surface
$\mathbf{a}, a$	acceleration vector and its length for a point (u, v) on the object surface
$\mathbf{v}_c, v_c$	velocity vector and its length for the center of mass (center of gravity) of the object
$\mathbf{a}_c, a_c$	acceleration vector and its length, respectively, for the center of mass (center of gravity) of the object
$\boldsymbol{\Omega}, \Omega$	angular velocity vector of the object rotation and its length, respectively
ρ_{cx}, ρ_{cy}	correlation radii along the X and Y axes of the field scattered by the object under study
t_c	correlation time of the complex amplitude of the field scattered by the object
$k_i(\mathbf{r})$	a function proportional to the averaged distribution in the object image
C	contrast of the speckle pattern in a coherent scattered field and a coherent image
ν_d	the Doppler frequency in the plane where the scattered field is observed
f_D	the Doppler frequency in the image plane
f_c	correlation frequency
f_s	the relative Doppler shift in the image plane
z_i	distance from the imaging system aperture plane to the image plane
$\mu = r_c/z_i$	scaling factor
$h(\mathbf{r}, \boldsymbol{\delta})$	pulse response (the point spread function) of the imaging system
S_ρ	the area of the imaging system aperture
d_ρ	the diameter of the imaging system aperture
$\boldsymbol{\delta}$	radius vector in the image plane

δ_c	radius vector of a point in the image plane optically conjugated to the object's center of mass
$E(\delta)$	complex amplitude of the field in the coherent image
$B_f(\delta_1, \delta_2)$	field correlation function in the object image
$I(\delta) = \lvert E(\delta)\rvert^2$	intensity distribution in the object image
$B_i(\delta_1, \delta_2)$	intensity correlation function in the object image
ρ_{ix}, ρ_{iy}	correlation radii of the intensity distribution in a coherent image along the X and Y axes, for equal correlation radii, $\rho_{ix} = \rho_{iy} = \rho_i$
P_{rx}, P_{ry}	sizes of the object surface domain resolved according to Rayleigh's criterion along the X and Y axes, for equal domain sizes $P_{rx} = P_{ry} = P_r$
M	the number of speckles in the scattered coherent field and coherent image of the object under study
$\delta_{mn} = \begin{cases} 1 \text{ for } m = n \\ 0 \text{ for } m \neq n \end{cases}$	the Kronecker function
L_c	coherence length of the illuminating source
(ω, β)	the frequency and deviation in the Fourier–Fresnel time transform
M_b	the number of speckles in the coherent image of the background surface
δ_x, δ_y	Cartesian coordinates in the image plane
$k_b(x, y)$	field reflection coefficient distribution on the background surface of the object under study

Explanation of Terms

Random surface is the rough surface of an object under study.

Roughness of an object's surfaces, $\xi(u, v, t) = \xi(\mathbf{r})$, is the distribution of the deviations of the random surface from the mean surface at time t at each point (u, v) of the mean surface along its normal $\mathbf{N}$. Here, $\mathbf{r}(u, v, t)$ is the radius vector of a point (u, v) on the surface.

The **mean surface** is an imaginary smooth surface that lies between the maximums and minimums of $\xi(u, v)$, so that the mean value of the surface roughness ξ is equal to zero. This means that $\langle\xi\rangle = 0$, where the brackets $\langle\rangle$ denote averaging over various realizations of ξ [Sec. 1.2, relation (1.2)].

The **correlation function** of surface roughness $\xi(r)$ is a function given by the relation $\mathbf{B}_{12}(\mathbf{r}_1, \mathbf{r}_2) = \langle\xi(\mathbf{r}_1)\xi(\mathbf{r}_2)\rangle$. The standard deviation of surface roughness σ is given by the relation $\sigma(r) = \sqrt{\langle\xi^2(\mathbf{r})\rangle}$ [see Eq. (1.6)].

Correlation radii of surface roughness in given directions u and v, ℓ_u and ℓ_v, are defined as $\ell_u(\mathbf{r}) \approx \int[B_{12}(\mathbf{r}, u, 0)/\sigma^2]du$ and $\ell_v(\mathbf{r}) \approx \int[B_{12}(\mathbf{r}, 0, v)/\sigma^2]dv$, where $B_{12}(\mathbf{r}, u, v) = B_{12}(\mathbf{r}, \mathbf{r} - \mathbf{s})$, $\mathbf{r} = \mathbf{r}_1$, and $\mathbf{s} = \mathbf{r}_1 - \mathbf{r}_2$ is a vector close to the object surface, with the components $u = u_1 - u_2$ and $v = v_1 - v_2$. For the case of isotropic roughness, $\ell_u = \ell_v = \ell$. In this case, the **correlation radius** ℓ of surface roughness is the mean size of the area where $\xi(\mathbf{r})$ is practically constant.

A **separate element of the rough surface** is a part of the rough surface with the area $\sim \ell^2$.

The **coherence length** L_c of the radiation source probing the object under study is determined by its **spectrum** $S_r(\omega)$. It can be estimated from the relation $L_c \approx c/\Delta\omega \approx \lambda^2/\Delta\lambda$, where c is the velocity of light, λ is the mean wavelength of the probing radiation, $\Delta\omega$ is the radiation spectrum width at half maximum, and $\Delta\lambda$ is the width of the wavelength spectrum at half maximum. As a rule, in this book we will deal with narrow-band probing radiation, for which $L_c > 10\lambda$ ($\Delta\omega < 0.1\omega_0$, where $\omega_0 = c/\lambda$ is the mean frequency of the source spectrum). For the probing radiation source, one can define the achromaticity, which determines L_c and possible geometric parameters of the object under study; one distinguishes three grades of achromaticity (see Appendix 4).

The probing radiation is called **monochromatic** if its coherence length $L_c > 100L_s$, where L_s is the depth of the object's backscattering surface. As a rule, we will assume here this kind of probing radiation.

The probing radiation is called **quasi-monochromatic** if its coherence length satisfies the condition $10L_s \geq L_c \geq 10\lambda$.

The probing radiation is called **polychromatic** if its coherence length $L_c \leq 10\lambda$.

A scattered field is called **coherent** if at each point of its observation, it is formed by amplitude superposition (interference) of all waves scattered by the object's surface and coming to that point.

An image of a rough object will be called **coherent** if at each point, it is formed by interference of all waves coming from the area of the object's surface resolvable by the imaging system. The conditions under which coherent fields and images are formed depend mostly on the coherence length of the probing radiation. These are considered at the end of Sec. 1.2 and analyzed in detail in Appendix 4 and Sec. 2.5. In particular, coherent fields and images are formed if the probing radiation is monochromatic.

The scattered field **intensity** is $I = |E|^2$, where E is the scattered field **complex amplitude** [Sec. 1.2, relation (1.28)].

The field **intensity** in the image is $I = |E|^2$, where E is the field **complex amplitude** in the image of the object under study.

The **mean value** of a value V, which is related to the roughness height distribution ξ, is $\langle V \rangle$, where brackets denote averaging over various realizations of ξ. In this book, we consider mean values for determined object parameters and for the amplitude and intensity distributions of the coherent field scattered by the object as well as the field and intensity distributions in coherent images of this object.

The **correlation function** of a distribution (random process) $D(\boldsymbol{\rho}, t)$ is defined as

$$\langle D(\boldsymbol{\rho}_1, t_1) D^*(\boldsymbol{\rho}_2, t_2) \rangle - \langle D(\boldsymbol{\rho}_1, t_1) \rangle \langle D^*(\boldsymbol{\rho}_2, t_2) \rangle,$$

where $\boldsymbol{\rho}$ is the radius vector of a point in the plane where the distribution is observed, and t is the moment of observation. In this book, we consider correlation functions for the distributions of a coherent field scattered by an object and for the field in the coherent image of an object. We also consider correlation functions for the intensity distributions in the coherent field scattered by an object and in the coherent image of an object. Similarly to the case of surface roughness, one can introduce the **correlation time** τ_c of a distribution and the **correlation radii** ρ_c in various directions as the ranges in time and space where the distribution $D(\boldsymbol{\rho}, t)$ does not change (Secs. 1.3 and 1.4). In the case of isotropic distributions, one can introduce a single correlation radius ρ_c, which is equal to the mean size of the domain where the distribution $D(\boldsymbol{\rho}, t)$ is practically constant.

A **functional** of some function is a value depending, via an integral relation, on this function.[29] Below, there are some examples of functionals for which the function under study is the observed field scattered by a rough object $E(\boldsymbol{\rho}, t, \boldsymbol{\alpha})$, where $\boldsymbol{\rho}$ is the radius vector of the observation domain, t is the observation time, and $\boldsymbol{\alpha}$ is the vector of the measured parameters of the object.

The **Gaussian probability density functional** (PDF) of E is

$$P[E(\boldsymbol{\rho}, t, \boldsymbol{\alpha})] \sim \exp L[E(\boldsymbol{\rho}, t, \boldsymbol{\alpha})],$$

where

$$L[E(\boldsymbol{\rho}, t, \boldsymbol{\alpha})] = -\frac{1}{2} \iiiint W(\boldsymbol{\rho}_1, t_1, \boldsymbol{\rho}_2, t_2)[E(\boldsymbol{\rho}_2, t_2, \boldsymbol{\alpha}) - \langle E(\boldsymbol{\rho}_2, t_2, \boldsymbol{\alpha})\rangle]$$
$$\times [E_t(\boldsymbol{\rho}_2, t_2, \boldsymbol{\alpha}) - \langle E_t(\boldsymbol{\rho}_2, t_2, \boldsymbol{\alpha})\rangle]^* d\boldsymbol{\rho}_1 dt_1 d\boldsymbol{\rho}_2 dt_2$$

is also a **functional** [see relation (1.30)], $\boldsymbol{\alpha} = (\alpha_1, \ldots, \alpha_n)$ is the set of the determined object parameters, and $W(\boldsymbol{\rho}_1, t_1, \boldsymbol{\rho}_2, t_2)$ is the inverse correlation function of the scattered field E.

A **speckle pattern** is a spotty, strongly inhomogeneous intensity distribution in the scattered coherent field and in the coherent image of a rough object or a strongly inhomogeneous distribution in the **frequency-time coherent image**, which is the time spectrum of a coherent field scattered by a moving rough object (Sec. 2.7).

The **contrast** of a random distribution D is the measure of its fluctuations determined by the relative dispersion, $C = (\langle D^2\rangle - \langle D\rangle^2)/\langle D\rangle^2$. For example, the contrast of an intensity distribution I in a coherent image is $C = (\langle I^2\rangle - \langle I\rangle^2)/\langle I\rangle^2$. In this text, we consider the contrast of intensity distribution in the scattered coherent field (also called the **blinking index**, Sec. 1.3) and in the coherent image of an object (Sec. 2.2), as well as the contrast in the power (energy density) distribution in the coherent image of an object obtained by means of partially coherent radiation (Sec. 2.5).

The **quasi-static principle** is a means of calculating the instantaneous coherent field scattered by a moving object by assuming the object to be stationary. This assumption is valid at $(v^2 T)/(\lambda c) \ll 1$, where T is the observation time for the radiation scattered by the object, c is the velocity of light, and v is the object's velocity (Sec. 1.4).

The **Doppler effect** is the frequency variation (**Doppler shift**) that occurs when coherent radiation is scattered by a moving surface.

Resolution of an imaging system is the maximum size P_r of the minimally resolved domain of the object's surface according to the Rayleigh criterion. This size is approximately equal to $(\lambda r_c)/d_\rho$, where λ is the wavelength of the radiation illuminating the object, r_c is the distance between the imaging system's aperture center and the object's center of mass, and d_ρ is the aperture size.

The **speckle number** M is the average number of **speckles** in the field scattered by a rough object on the imaging system's aperture, in the coherent image of a rough object, and in its frequency-time coherent image (Sec. 2.7). It is approximately equal to the number of domains of the rough object's surface that are resolvable by the imaging system (Sec. 2.2.3).

The **estimate** $\hat{V}$ for the measured parameter V of an object is determined by the measurement algorithm, which, in its turn, depends on both the measurement geometry and the statistical properties of V (see Chapter 3). The estimate is called **unbiased** if $\langle \hat{V} \rangle = V$. Here, the brackets $\langle\rangle$ also denote averaging over various realizations of ξ.

The **estimation accuracy** for the parameter V is given by the estimate dispersion. This dispersion is caused by either the randomness of V, which is related to the randomness of the object surface, or by the peculiarities of the measurement scheme. In the first case, the accuracy is given by the standard deviation $\sigma_v = \sqrt{\langle \widehat{V}^2 \rangle - \langle \widehat{V} \rangle^2}$. The second case is considered in Sec. 3.3. In this text, the standard deviations for the estimates of the following parameters are given: linear velocity (Sec. 3.2), the angular velocity of rotation (Sec. 3.3), the local angular deformations of the object surface (Sec. 3.4), and the size of the surface details (Sec. 4.4).

Fourier telescopy is a method of building a coherent image of an object. In this method, a set of sinusoidal interference patterns (fringes) with various orientations and various periods is formed on the object's surface, the energy of the coherent field scattered by the object is registered, and finally, the image is reconstructed by performing the Fourier transform of the registered set of energies. The interference patterns are formed by illuminating the surface of the object under study by two mutually coherent sources, which change their positions so that the distance between them is varied and the orientation of the line connecting them with respect to the object's surface is changed.

Chapter 1

Basic Concepts of the Statistical Theory of Light Scattering

1.1 Introduction

In practice, one deals mostly with objects having a continuous and, as a rule, rough surface. The surface of an object is formed under the influence of numerous random factors, such as nonideal mechanical processing, effects of temperature, and so on. As a result, the surface of an object is almost always of random shape and can generally be described by a random function of space coordinates and time. Recall that a random function of one parameter—say, time—is called a single-parameter random process.[24] Further consideration shows that random functions depend on four (three coordinates plus time) or more parameters. Such functions are called multiparameter random processes or *random fields*. This term should be used particularly for functions describing wave fields scattered by objects with random surfaces. Evidently, such fields have random structure.

It is clear that the study of wave scattering by objects with rough surfaces should be considered a statistical problem that involves finding probability characteristics of the scattered field, including distribution functions, field moments, and correlation properties, from given probability characteristics of the surface. In this chapter, we consider the basic concepts relating to the probability characteristics of random surfaces and the random fields scattered by them. The main results of the theory of diffraction by random surfaces in the Kirchhoff approximation are reviewed. Field correlation characteristics and moments scattered by moving or standing objects are considered.

1.2 Random surfaces and fields scattered by them; the Kirchhoff method

Consider the surface of an arbitrarily rough object in motion. During the course of its motion, the surface can be deformed by various forces. It is usually difficult to describe the space–time characteristics of such a surface. However, for a random surface in practice, its deviation from the mean smooth surface is small compared with the curvature radius of this surface. Such random deviations appear due to uncontrollable effects of the formation and processing of surfaces. As an example of

random deviations, one can consider the wavy surface of the sea that is formed by the influence of wind and other factors. A surface that changes its shape or position in time can be described by a radius vector that depends on the two parameters u and v, and time: $\mathbf{r} = \mathbf{r}(u, v, t)$. Random surfaces can be represented in the following form (see Fig. 1.1):

$$\mathbf{r}_\Sigma(u, v, t) = \mathbf{r}(u, v, t) + \mathbf{N}(u, v, t)\xi(u, v, t), \tag{1.1}$$

where $\mathbf{r}(u, v, t)$ is the radius vector of the mean surface, $\mathbf{N}(u, v, t)$ is the external normal to this surface at point (u, v), and $\xi(u, v, t)$ is the deviation of the random surface from the unperturbed mean surface at point (u, v) along the normal; it satisfies the condition $\langle \xi(u, v, t) \rangle = 0$. Furthermore, $\xi(u, v, t)$ will be called the surface roughness height distribution, and the mean surface is the shape of the object surface.

It is convenient to consider the parameters u and v as surface coordinates on the mean surface. We assume the corresponding coordinate frame to be orthogonal, which implies that the mean surface has certain necessary properties. In the case when the mean surface is parallel to the plane $z = 0$, we have $u = x$, $v = y$, and

$$\mathbf{r}_\Sigma(x, y, t) = \mathbf{i}x + \mathbf{j}y + \mathbf{k}[z(t) + \xi(x, y, t)],$$

where $z(t)$ describes the motion of the mean surface and $\mathbf{i}$, $\mathbf{j}$, and $\mathbf{k}$ are unit vectors in the direction of the coordinate axes.

The wave field (acoustic, electromagnetic field, etc.) scattered by a random surface is functionally related to the shape of the object, its motion, and the random function $\xi(u, v, t)$.[12] This relation can be used for studying the characteristics of

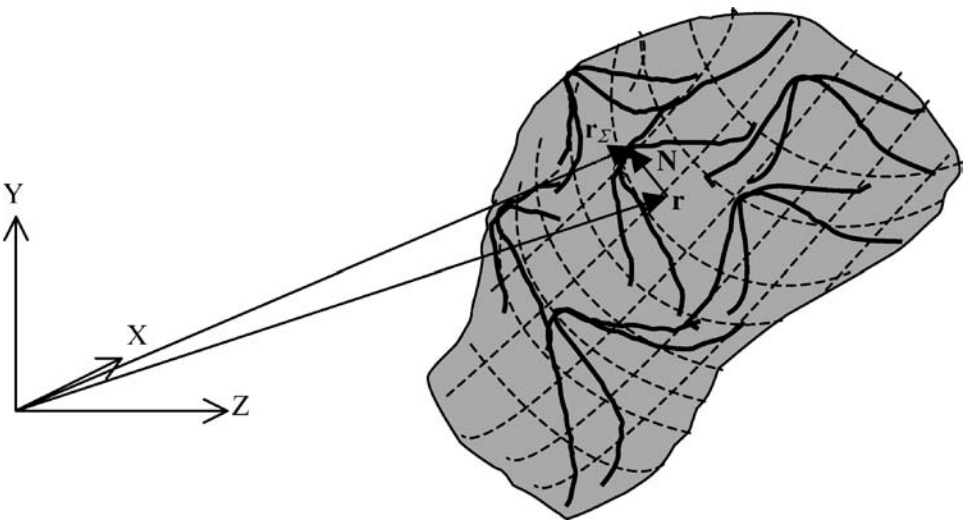

Figure 1.1 Geometry of a small part of a rough object surface. Dashed lines show the coordinates u, v on the mean surface.

the object surface and for identifying and distinguishing different objects and determining their parameters.

The advantage of such wave influence is that it does not damage the object under study and hence is a nondestructive method of control. There is a problem of determining the results of influence as a functional of the random function $\xi(u, v, t)$.[25] The result of a wave field influence is a complex process, and it is a complicated problem to describe this process for each specific realization of the surface $\xi(u, v, t)$. Usually, relatively simple analytic dependencies can be found for a field diffracted by simple structures such as a plane, smooth cylinder, smooth ball, etc., and also by periodic structures containing these simple ones. However, even diffraction of a field by gratings formed by regular flat stripes leads to a complicated field structure that has a large number of maxima and minima with different amplitudes.

In the microwave antenna technique, the field distribution in the vicinity of the main maximum is called the *main lobe*. Other maxima are called *side lobes*. Random deviations of the antenna shape from the ideal one are caused by various reasons, such as deviations of the antenna mirror surface from the ideal one (for the case of antennas with continuous opening) or irregular positions of the transmitters (for antenna arrays). Even the smallest deviation of the scattering object's position from the ideal leads to a considerable change of both amplitude and position of maxima and minima. Naturally, a field scattered by a surface with random roughness $\xi(u, v, t)$ has a complicated distribution. A complete description of field realizations is, in this case, useless in practice.

This fact has been taken into account in the antenna technique[26] and in radiolocation,[27] and a probability description of the scattered field has been developed. For instance, the values of side lobes appearing due to the deviation $\xi(u, v, t)$ of the mirror surface from the ideal one is characterized by the probability of not exceeding a given value. This statistical approach to estimating the scattered field has turned out to be quite fruitful. For instance, it allows estimation of the mean square deviation of the mirror surface from the ideal one at which the side lobes do not exceed a given value.

In the antenna technique, it is often necessary to distribute radiated energy in such a way that it is uniformly spread in space. For this purpose, the ideal mirror surface should be randomly perturbed by significant values of $\xi(\mathbf{r})$. Naturally, this problem also requires a statistical approach. Further development of this approach leads to finding such a random distribution $\xi(\mathbf{r})$ that forms a given mean distribution of the scattered field.

Hence, whenever it is necessary to study a field scattered by a random surface, of major practical interest are the statistical characteristics (mainly, mean values) of the scattered field for a group of scattering surfaces that have the same mean surface and random deviations $\xi(\mathbf{r})$ determined by identical surface processing conditions, such as grinding the surface with a fixed-size abrasive. Another example of a statistical group is a water surface. In this case, given statistical characteristics of random deviations from the mean surface are determined by the depth of the water

basin, direction and duration of the wind, and other parameters that are the same for all groups. Thus, each surface from a given group is one of the realizations described by random deviations, with fixed statistical characteristics and fixed mean surface.

The value of $\xi(u, v, t)$ at each fixed point in space–time is a random function, which can be conveniently described by the probability density $w_1(\xi, u, v, t)$. Although the function $w_1(\xi, u, v, t)$ gives the probability density distribution $\xi(u, v, t)$ at each point (u, v, t), it does not provide information about the values of the random process at neighboring points. A more detailed description of the process $\xi(u, v, t)$ is contained in the two-dimensional probability density $w_2(\xi_1, u_1, v_1, t_1, \xi_2, u_2, v_2, t_2)$ of random variables $\xi_1(u_1, v_1, t_1)$ and $\xi_2(u_2, v_2, t_2)$. Here, w_2 describes the ensemble of all functions ξ_1 and ξ_2. The most complete description of random deviations $\xi(u, v, t)$ from the mean surface is given by n-dimensional probability densities of random variables $\xi(u_1, v_1, t_1), \xi(u_2, v_2, t_2), \ldots, \xi(u_n, v_n, t_n)$:

$$w_n = w_n(\xi_1, u_1, v_1, t_1, \xi_2, u_2, v_2, t_2, \ldots, \xi_n, u_n, v_n, t_n),$$

which are connected by means of recurrent relations (matching conditions)

$$w_{n-1}(\xi_2, \ldots, \xi_n) = \int_{-\infty}^{\infty} w_n(\xi_1, \xi_2, \ldots, \xi_n) d\xi_1$$

and satisfy the normalization conditions $\int \ldots \int w_n d\xi_1 d\xi_2 \ldots d\xi_n = 1$.

Knowing the probability density w_n, one can calculate the probability densities for an arbitrary function $f(\xi_1, \xi_2, \ldots, \xi_n)$ by means of the relation

$$P(x) = \int \ldots \int \delta[x - f(\xi_1, \xi_2, \ldots, \xi_n)] w(\xi_1, \xi_2, \ldots, \xi_n) d\xi_1 d\xi_2 \ldots d\xi_n,$$

where $\delta(x - f)$ is a delta function. In particular, this leads to the equation for the mean value of a function,

$$\langle f(\xi_1, \ldots, \xi_n) \rangle = \int \ldots \int f(\xi_1, \ldots, \xi_n) \times w_n(\xi_1, u_1, v_1, t_1, \ldots, \xi_n, u_n, v_n, t_n) d\xi_1 \ldots d\xi_n. \quad (1.2)$$

Here, angle brackets $\langle\rangle$ denote averaging of the function f over the ensemble of all functions ξ.

A convenient way to describe random processes is by means of the functional of the process $\xi(u, v, t)$ probability density. This functional is defined as the limit

$$P[\xi(u, v, t)] = \lim_{n \to \infty} w_n(\xi_1, u_1, v_1, t_1, \ldots, \xi_n, u_n, v_n, t_n),$$

and, in fact, it fully determines the probability of any realization of the process $\xi(u, v, t)$. In most cases, it is not necessary to give a complete probability description of a random process. Therefore, one usually needs only simplified characteristics of the process $\xi(u, v, t)$:

the mean value of the process $\xi(u, v, t)$ (the first-order moment),

$$\langle \xi(u, v, t) \rangle = \int_{-\infty}^{\infty} \xi w_1(\xi, u, v, t) d\xi, \tag{1.3}$$

$$\psi_{12}(u_1, v_1, t_1, u_2, v_2, t_2) = \langle \xi(u_1, v_1, t_1) \xi(u_2, v_2, t_2) \rangle, \\ \int_{-\infty}^{\infty} \int_{-\infty}^{\infty} \xi_1 \xi_2 w_2(\xi_1, u_1, v_1, t_1, \xi_2, u_2, v_2, t_2) d\xi_1 d\xi_2; \tag{1.4}$$

the correlation function

$$B_{12}(u_1, v_1, t_1, u_2, v_2, t_2) = \psi_{12}(u_1, v_1, t_1, u_2, v_2, t_2) \\ - \langle \xi(u_1, v_1, t_1) \rangle \langle \xi(u_2, v_2, t_2) \rangle; \tag{1.5}$$

and variance of the random process

$$\sigma^2(\mathbf{r}) = \sigma^2(u, v, t) = B_{12}(u, v, t, u, v, t), \tag{1.6}$$

where σ is the standard deviation of the random process.

In practice, for any surface,

$$B_{12}(u_1, v_1, t_1, u_2, v_2, t_2) \to 0 \quad \text{at } |u_1 - u_2|, |v_1 - v_2|, t_2 - t_1 \to \infty.$$

If a random process is not statistically isotropic, it is reasonable to introduce a correlation radius in each direction, for instance, along the coordinate lines u and v on the object surface:

$$\ell_u(\mathbf{r}) = \frac{1}{\sigma^2(\mathbf{r})} \int_{-\infty}^{\infty} B_{12}(\mathbf{r}, t, \mathbf{r} + \mathbf{s}, t) r_u du$$

and

$$\ell_v(\mathbf{r}) = \frac{1}{\sigma^2(\mathbf{r})} \int_{-\infty}^{\infty} B_{12}(\mathbf{r}, t, \mathbf{r} + \mathbf{s}, t) r_v dv, \tag{1.7}$$

where $\mathbf{r} = \mathbf{r}_1$ and the vector $\mathbf{s} = \mathbf{r}_2 - \mathbf{r}_1$ has the components $s_u \approx \mathbf{r}_u(u_2 - u_1)$ and $s_v \approx \mathbf{r}_v(v_2 - v_1)$, and where $\mathbf{r}_u = (\partial x/\partial u, \partial y/\partial u, \partial z/\partial u)$ and $\mathbf{r}_v = (\partial x/\partial v, \partial y/\partial v, \partial z/\partial v)$ are two orthogonal vectors tangent to the object's mean surface at point

u_1, v_1. It is useful also to introduce the correlation time of the process $\xi(u, v, t)$:

$$\tau_c = \frac{1}{\sigma^2(\mathbf{r}, t)} \int_{-\infty}^{\infty} B_{12}(\mathbf{r}, t, \mathbf{r}, t + \tau) d\tau. \tag{1.8}$$

For statistically isotropic processes, where $\ell_u(\mathbf{r}) = \ell_v(\mathbf{r})$, one can define the correlation radius as

$$\ell(\mathbf{r}) = \ell_u(\mathbf{r}) = \ell_v(\mathbf{r}).$$

In the simplest cases, the correlation radius is an explicit parameter of the function B_{12}. For instance, in the case of an anisotropic Gaussian correlation function[12] and for such a mean surface that $\langle \xi(\mathbf{r}, t) \rangle = 0$,

$$B_{12}(u_1, v_1, t_1, u_2, v_2, t_2) = \sigma^2 \exp\left[-\frac{r_u^2 (u_1 - u_2)^2}{\ell_u^2} - \frac{r_v^2 (v_1 - v_2)^2}{\ell_v^2} - \frac{(t_1 - t_2)^2}{\tau_c^2} \right]. \tag{1.9}$$

Here, partial derivatives are taken at point u_1, v_1.

Furthermore, we assume, as a rule, that surface roughness is isotropic and the surface roughness height distribution is practically constant in time during the determination of the object parameters. In this case, $\ell(\mathbf{r}) = \ell_u(\mathbf{r}) = \ell_v(\mathbf{r})$; $\tau_c = \infty$; $\xi(u, v, t) = \xi(u, v, t_0) = \xi(\mathbf{r})$, where $\mathbf{r} = \mathbf{r}(u, v)$, and

$$\begin{aligned} B_{12}(u_1, v_1, t_1, u_2, v_2, t_2) &= B_{12}(u_1, v_1, t_0, u_2, v_2, t_0) = B_{12}(\mathbf{r}_1, \mathbf{r}_2, t_0) \\ &= \langle \xi(\mathbf{r}_1) \xi(\mathbf{r}_2) \rangle \\ &= \sigma^2 \exp\left[-\frac{r_u^2 (u_1 - u_2)^2 + r_v^2 (v_1 - v_2)^2}{\ell^2} \right], \end{aligned} \tag{1.10}$$

where t_0 is the initial moment of determining parameters of the object. Also, we will often use the notion of a *separate element of the rough surface.* This means that a part of the surface of the object under study has the area of $\sim \ell^2$. One can show that, on average, such a part contains not more than two maxima of the function $\xi(u, v)$. For instance, Fig. 1.1 shows a part of a surface that contains six separate elements of the rough surface. To avoid the account of multiple scattering, we will also assume that the surface is smooth ($\ell > 3\sigma$); and to distinguish between small changes of the object surface and the surface roughness, we will assume that $\ell < 10^3 \lambda$ and $\sigma < 10^2 \lambda$, where λ is the mean wavelength of radiation scattered by the object.

In addition to the first- and second-order moments, one can introduce higher-order moments of a random process. The mth moment is given by the relation

$$\begin{aligned} &\psi_{12\ldots m}(u_1, v_1, t_1, \ldots, u_m, v_m, t_m) \\ &\quad = \int \ldots \int \xi_1 \ldots, \xi_m w_m(\xi_1, u_1, v_1, t_1, \ldots, \xi_m, u_m, v_m, t_m) d\xi_1 \ldots d\xi_m. \end{aligned} \tag{1.11}$$

The first- and the second-order moments give a rather approximate description of a random process $\xi(\mathbf{r}, t)$. However, there exists an important class of random functions (processes) for a complete description of which it is sufficient to know these two characteristics. These are Gaussian processes. Most often, random processes describe phenomena caused by numerous independent factors. For instance, for the surface of a metal detail, deviations from the mean surface appear due to many types of mechanical processing (turning, milling, grinding, etc.). Accumulation of a large number of factors lead—according to the central limit theorem of the probability theory—to a Gaussian distribution of a random process $\xi(\mathbf{r}, t)$. For a Gaussian distribution,

$$w_1(\xi) = \frac{1}{\sqrt{2\pi}\sigma} \exp\left(-\frac{\xi^2}{2\sigma^2}\right),$$

$$w_2(\xi_1, \xi_2) = \frac{1}{2\pi\sqrt{\sigma^4 - B_{12}^2}} \times \exp\left[-\frac{\sigma^2(\xi_1 - \langle\xi_1\rangle)^2 - 2B_{12}(\xi_1 - \langle\xi_1\rangle)(\xi_2 - \langle\xi_2\rangle) + \sigma^2(\xi_2 - \langle\xi_2\rangle)^2}{2(\sigma^4 - B_{12}^2)}\right],$$

and

$$w_n(\xi_1, \ldots, \xi_n) = \frac{1}{(2\pi)^{n/2}\sqrt{\det[B_{jk}]}} \exp\left[-\frac{1}{2}\sum_{j,k=1}^{n} W_{jk}(\xi_j - \langle\xi_j\rangle)(\xi_k - \langle\xi_k\rangle)\right], \tag{1.12}$$

where $[W_{jk}] = [B_{jk}]^{-1}$ is the matrix inverse to the correlation matrix:

$$\sum_{k=1}^{n} W_{jk}B_{km} = \delta_{jm}, \quad B_{jk} = \langle\xi_j\xi_k\rangle - \langle\xi_j\rangle\langle\xi_k\rangle. \tag{1.13}$$

Evidently, the following relation holds for the second joint moment of a random process and its derivative:

$$\left\langle [\xi(u_2, v_2, t_2)]\left[\frac{\partial\xi(u_1, v_1, t_1)}{\partial u_1}\right]\right\rangle = \frac{\partial B_{12}(u_1, v_1, t_1, u_2, v_2, t_2)}{\partial u_1}.$$

This relation follows from the linearity of averaging and differentiating.

Similarly, the following relation holds:

$$\left\langle \left[\frac{\partial\xi(u_1, v_1, t_1)}{\partial u_1}\right]\left[\frac{\partial\xi(u_2, v_2, t_2)}{\partial u_2}\right]\right\rangle = \frac{\partial^2 B_{12}(u_1, v_1, t_1, u_2, v_2, t_2)}{\partial u_1 \partial u_2}.$$

For statistically uniform processes,

$$\left\langle \frac{\partial \xi(u,v,t)}{\partial u} \right\rangle = 0,$$
$$\left\langle \frac{\partial \xi(u,v,t)}{\partial u \xi(u+\Delta u,v,t)} \right\rangle = 0.$$

It follows from these relations that the variance of a random process derivative is $B''_{xx12}(0)$. In the case of a Gaussian correlation function, the following useful relation holds:

$$\left\langle \left[\frac{\partial \xi(u,v,t)}{\partial u} \right]^2 \right\rangle = \left(\frac{\sigma}{\ell_u} \right)^2, \left\langle \left[\frac{\partial \xi(u,v,t)}{\partial v} \right]^2 \right\rangle = \left(\frac{\sigma}{\ell_v} \right)^2. \tag{1.14}$$

From the equality

$$\left\langle \frac{\partial \xi(u,v,t)}{\partial u \xi(u,v,t)} \right\rangle = \frac{\partial B_{12}(0)}{\partial u} = 0, \tag{1.15}$$

it follows that in the case of a Gaussian correlation function, the value of the random process at some point and its derivative at the same point are statistically independent. This leads to an important relation,

$$\left\langle f_1\left(\frac{\partial \xi}{\partial u} \right) f_2(\xi) \right\rangle = \left\langle f_1\left(\frac{\partial \xi}{\partial u} \right) \right\rangle \langle f_2(\xi) \rangle.$$

Let us return to the n-dimensional probability density of a Gaussian process and take the limit at n tending toward infinity. Evidently, summation in relations (1.12) and (1.13) will turn into integration according to Riemann's definition of an integral. As a result, we obtain the Gaussian probability density function (PDF), which corresponds each realization of a random process $\xi(u,v,t)$ to a certain number $P[\xi(u,v,t)]$. Equation (1.13) for the inverse correlation matrix is transformed in this case into the equation for the inverse correlation function $W(u_1, v_1, t_1, u_2, v_2, t_2)$:

$$\begin{aligned} P[\xi] &= \lim_{n\to\infty} w_n(\xi_1, \xi_2, \ldots, \xi_n) \\ &= C_f \exp\left\{ -\frac{1}{2} \iint W(u_1, v_1, t_1, u_2, v_2, t_2) \right. \\ &\qquad \times [\xi(u_1, v_1, t_1) - \langle \xi(u_1, v_1, t_1) \rangle][\xi(u_2, v_2, t_2) - \langle \xi(u_2, v_2, t_2) \rangle] \\ &\qquad \left. \times du_1 dv_1 dt_1 du_2 dv_2 dt_2 \right\}, \end{aligned} \tag{1.16}$$

where C_f is a constant and the function W satisfies the integral equation

$$\int W(u_1, v_1, t_1, u_2, v_2, t_2)B(u_2, v_2, t_2, u_3, v_3, t_3)du_2dv_2dt_2 = \delta(u_1 - u_3)\delta(v_1 - v_3)\delta(t_1 - t_3), \quad (1.17)$$

where $\delta(s)$ is a δ-function.

1.2.1 Random field scattered by an object with a random surface

Let us now consider a random field scattered by an object with a random surface. This field is formed by the summation of fields scattered by different parts of the surface. The rougher a surface and the faster its fluctuations, the larger the number of independent terms contributing to the field and, hence, the closer the field distribution function is to the Gaussian one. If the scattering surface deviates from the mean surface according to the Gaussian distribution, then its roughness and its time fluctuations are determined by four parameters: σ, ℓ_u, ℓ_v, and τ_0. In addition to the random factors mentioned above, there are certain deterministic factors that influence the scattered field, such as the shape of the mean surface, polarization of the incident wave, reflecting characteristics of the scattering surface, and the time spectrum of the radiation. A mathematical description of the scattered field that accounts for all of these factors is an extremely complicated problem. Its approximate solution can be obtained with the help of the Kirchhoff approach. Let us review its basic ideas.[3,12]

A wave source (Fig. 1.2) illuminates the surface of the object under study. The electric vector of the field $\mathbf{E}(\boldsymbol{\rho}, t)$ scattered by the object satisfies the relation

$$\mathbf{E}(\boldsymbol{\rho}, t) = \int_{-\infty}^{\infty} \mathbf{E}_0(\boldsymbol{\rho}, \omega) \exp(i\omega t)dt, \quad (1.18)$$

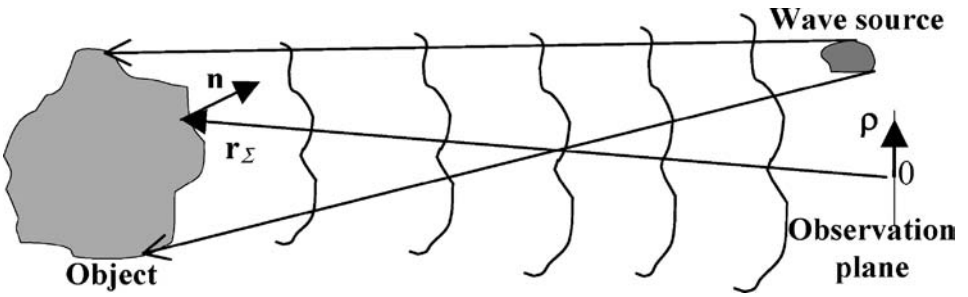

Figure 1.2 Geometry of radiation scattering by a rough object. Here, **n** is a unit vector normal to the object surface.

where

$$\mathbf{E}_0(\boldsymbol{\rho},\omega)=\frac{1}{4\pi}\int \mathbf{E}_0(\mathbf{r}_\Sigma,\omega)\frac{\partial}{\partial \mathbf{n}}\frac{\exp\left(-i\frac{\omega}{c}|\boldsymbol{\rho}-\mathbf{r}_\Sigma|\right)}{|\boldsymbol{\rho}-\mathbf{r}_\Sigma|}d\mathbf{r}_\Sigma$$
$$+\frac{1}{4\pi}\int \frac{\partial}{\partial \mathbf{n}}[\mathbf{E}_0(\mathbf{r}_\Sigma,\omega)]\frac{\exp\left(-i\frac{\omega}{c}|\boldsymbol{\rho}-\mathbf{r}_\Sigma|\right)}{|\boldsymbol{\rho}-\mathbf{r}_\Sigma|}d\mathbf{r}_\Sigma; \qquad (1.19)$$

$\boldsymbol{\rho}$ is the radius vector of the point of observation; $\mathbf{E}_0(\boldsymbol{\rho},\omega)$ is the vector of the scattered field spectral amplitude at the point of observation; $\mathbf{E}_0(\mathbf{r}_\Sigma,\omega)$ is the vector of the spectral amplitude on the object surface, which is given by the radius vector $\mathbf{r}_\Sigma$; $\partial/\partial\mathbf{n}$ is the normal derivative on the object surface; ω is the angular frequency of spectral amplitudes; and c is the velocity of light. The integration in Eq. (1.19) runs over the object surface. Derivation of Eq. (1.19) can be found, for instance, in Ref. 3. It what follows, we will denote the field spectral amplitudes $\mathbf{E}_0(\boldsymbol{\rho},\omega)$ and $\mathbf{E}_0(\mathbf{r}_\Sigma,\omega)$ as field amplitudes.

From Eqs. (1.18) and (1.19) we see that for an accurate calculation of the electric vector of the field $\mathbf{E}(\boldsymbol{\rho},t)$, it is sufficient to know the field amplitude and its normal derivative on the object's surface. Yet, accurate calculation of the surface field and its normal derivative is very complicated. However, assuming that the curvature radii of the incident field phase front and of a separate element of the rough scattering surface are much larger than the wavelength $\lambda=2\pi c/\omega$ of the incident radiation, one can find a rather simple relationship between the incident and scattered fields near the surface. For this purpose, let us fix a point $\mathbf{r}_\Sigma$ on the surface (Fig. 1.3). Using the above assumptions, one can consider the local part of

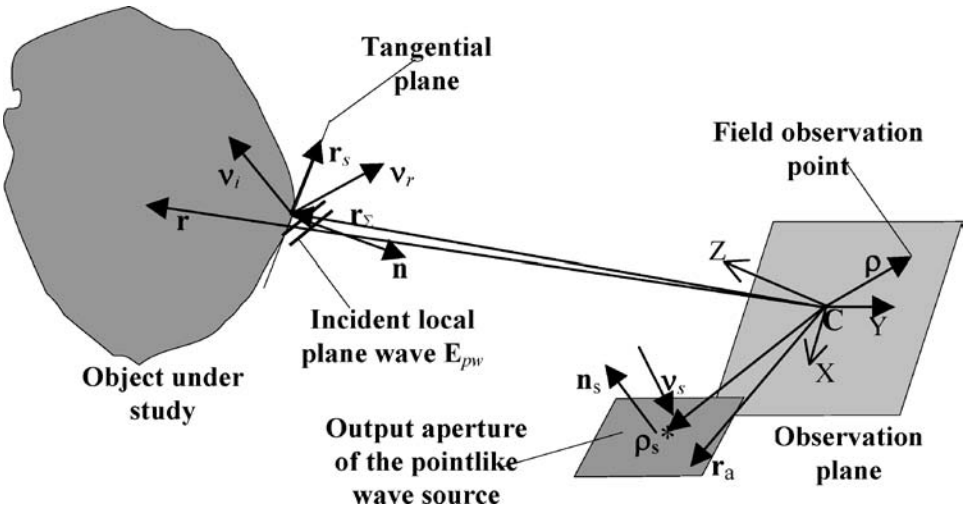

Figure 1.3 Illustration of the derivation of Eq. (1.27), which gives the observed spectral amplitude $E_0(\boldsymbol{\rho},\omega)$ of the field scattered by a rough object illuminated by a pointlike wave source as the integral over the object's mean surface.

the incident field as a plane wave $\mathbf{E}_{pw} = \mathbf{E}_i(\mathbf{r}_\Sigma, \omega)\exp[-i(\omega/\mathrm{c})\boldsymbol{\nu}_i \cdot \mathbf{r}_s]$, where $\boldsymbol{\nu}_i$ is the unit vector giving the propagation direction of the incident field: $\mathbf{E}_i(\mathbf{r}_\Sigma, \omega)$ is the incident field spectral amplitude, which varies in this direction much more slowly than does the exponent $\exp[-i(\omega/\mathrm{c})\boldsymbol{\nu}_i \cdot \mathbf{r}_s]$; and $\mathbf{r}_s$ is the radius vector of the tangential plane point. The reflected wave in the vicinity of the surface area under consideration can also be assumed to be on a local plane and in the form $\mathbf{E}_0(\mathbf{r}_\Sigma, \omega) \approx \mathbf{E}_r(\mathbf{r}_\Sigma, \omega)\exp[-i(\omega/\mathrm{c})\boldsymbol{\nu}_r \cdot \mathbf{r}_s]$, where $\boldsymbol{\nu}_r$ is the unit propagation vector of the reflected wave, and $\mathbf{E}_r(\mathbf{r}_\Sigma, \omega)$ is the reflected field amplitude. It follows directly that

$$\frac{\partial}{\partial \mathbf{n}}\mathbf{E}_0 \cong -i\frac{\omega \boldsymbol{\nu}_r \cdot \mathbf{n}}{\mathrm{c}}\mathbf{E}_0, \tag{1.20}$$

where $\mathbf{n}$ is the unit vector normal to the object surface at the fixed point $\mathbf{r}_\Sigma$. The relationship between $\boldsymbol{\nu}_i$ and $\boldsymbol{\nu}_r$ can be found from the equality between the incidence and reflection angles:

$$\boldsymbol{\nu}_r \cdot \mathbf{n} = -\boldsymbol{\nu}_i \cdot \mathbf{n}. \tag{1.21}$$

Substituting relation (1.20) into Eq. (1.19) and taking into account that, as a rule, $|\boldsymbol{\rho} - \mathbf{r}_\Sigma| \gg \mathrm{c}/\omega$ and that the surface is smooth ($\ell > 3\sigma$), we obtain

$$\frac{\partial}{\partial \mathbf{n}}\frac{\exp\left(-i\dfrac{\omega}{\mathrm{c}}|\boldsymbol{\rho} - \mathbf{r}_\Sigma|\right)}{|\boldsymbol{\rho} - \mathbf{r}_\Sigma|} \cong i\boldsymbol{\nu}_o \cdot \mathbf{n}\frac{\omega \exp\left(-i\dfrac{\omega}{\mathrm{c}}|\boldsymbol{\rho} - \mathbf{r}_\Sigma|\right)}{|\boldsymbol{\rho} - \mathbf{r}_\Sigma|\mathrm{c}},$$

where $\boldsymbol{\nu}_o = (\boldsymbol{\rho} - \mathbf{r}_\Sigma)/|\boldsymbol{\rho} - \mathbf{r}_\Sigma|$ is the unit vector along the direction from the point $\mathbf{r}_\Sigma$ to the observation point $\boldsymbol{\rho}$. As $\mathbf{r}_s$ tends toward zero and hence, $\mathbf{E}_0(\mathbf{r}_\Sigma, \omega) \to \mathbf{E}_r(\mathbf{r}_\Sigma, \omega)$, we obtain, taking into account Eq. (1.20) and the foregoing relation, that

$$\mathbf{E}_0(\boldsymbol{\rho}, \omega) = \frac{i\omega}{2\mathrm{c}}\int (\boldsymbol{\nu}_o + \boldsymbol{\nu}_r) \cdot \mathbf{n}\mathbf{E}_r(\mathbf{r}_\Sigma, \omega)\frac{\exp\left(-i\dfrac{\omega}{\mathrm{c}}|\boldsymbol{\rho} - \mathbf{r}_\Sigma|\right)}{|\boldsymbol{\rho} - \mathbf{r}_\Sigma|}d\mathbf{r}_\Sigma. \tag{1.22}$$

For further consideration, it is important to find the relation between the incident field amplitude $\mathbf{E}_i(\mathbf{r}_\Sigma, \omega)$ and the reflected ("locally scattered") field amplitude $\mathbf{E}_r(\mathbf{r}_\Sigma, \omega)$. This can be done by using the well-known relations[3]

$$B_p = \frac{tg(\theta_i - \theta_r)}{tg(\theta_i + \theta_r)}A_p, \quad B_t = \frac{\sin(\theta_i - \theta_r)}{\sin(\theta_i + \theta_r)}A_t,$$
$$\frac{\sin\theta_i}{\sin\theta_r} = \sqrt{\frac{\varepsilon_2\mu_2}{\varepsilon_1\mu_1}}, \quad \theta_i = \arccos(\boldsymbol{\nu}_i \cdot \mathbf{n}), \tag{1.23}$$

where A_t is the component of the vector $\mathbf{E}_i$ lying in the local plane of incidence and orthogonal to the vector $\boldsymbol{\nu}_i$; B_t is the corresponding component of the reflected field

vector $\mathbf{E}_r$ orthogonal to the vector $\boldsymbol{\nu}_r$; A_p and B_p are components of the vectors $\mathbf{E}_i$ and $\mathbf{E}_r$ orthogonal to the local plane of incidence; ε_1 and μ_1 are dielectric and magnetic functions of the propagation medium; and ε_2 and μ_2 are the corresponding values for the object under study. It is worth noting that in the optical range, ε_1, ε_2, μ_1, and μ_2 essentially depend on the frequency of the incident radiation.[3]

Now assume that the incident field is linearly polarized: $\mathbf{E}_i(\mathbf{r}_\Sigma, \omega) = \mathbf{i}E_i(\mathbf{r}_\Sigma, \omega)$, where $\mathbf{i}$ is a unit vector. Suppose that in the reflected and scattered fields, the same polarization is observed, i.e., in Eq. (1.22), $\mathbf{E}_r(\mathbf{r}_\Sigma, \omega) = \mathbf{i}E_r(\mathbf{r}_\Sigma, \omega)$ and $\mathbf{E}_0(\boldsymbol{\rho}, \omega) = \mathbf{i}E_0(\boldsymbol{\rho}, \omega)$, where E_0 is the spectral amplitude of the scattered field. In this case, it follows from Eq. (1.23) that $E_r(\mathbf{r}_\Sigma, \omega)$ is proportional to the incident field amplitude, with the proportionality coefficient depending on $\boldsymbol{\nu}_i$, $\mathbf{n}$, ε_1, μ_1, ε_2, and μ_2, which in turn depend on $\mathbf{r}_\Sigma$, so that

$$E_r(\mathbf{r}_\Sigma, \omega) = k(\omega, \boldsymbol{\nu}_i, \mathbf{n}, \varepsilon_1, \mu_1, \varepsilon_2, \mu_2)E_i(\mathbf{r}_\Sigma, \omega) = k(\mathbf{r}_\Sigma, \omega)E_i(\mathbf{r}_\Sigma, \omega). \quad (1.23a)$$

Here, $k(\mathbf{r}_\Sigma, \omega)$ is the reflection coefficient at frequency ω and at point $\mathbf{r}_\Sigma$.

One can suppose that due to the linearity of scattering, similar relations hold in other practically important cases, for instance, for an object being a nonhomogeneous absorbing dielectric. So the radius vector $\mathbf{r}_\Sigma$ of the real object surface is definitely related to the radius vector $\mathbf{r}$ of the mean object surface [see relation (1.1) and Fig. 1.1], and we can replace $k(\mathbf{r}_\Sigma, \omega)$ in Eq. (1.23a) with $k(\mathbf{r}, \omega)$. Furthermore, the set of local coefficients $k(\mathbf{r}, \omega)$ will be called the reflection coefficient distribution for the surface of the object under study.

Substituting Eqs. (1.21) and (1.23) into Eq. (1.22), we obtain

$$E_0(\boldsymbol{\rho}, \omega) = \frac{i\omega}{2\mathrm{c}} \int (\boldsymbol{\nu}_o - \boldsymbol{\nu}_i) \cdot \mathbf{n} k(\mathbf{r}_\Sigma, \omega) E_i(\mathbf{r}_\Sigma, \omega) \frac{\exp\left(-i\dfrac{\omega}{\mathrm{c}}|\boldsymbol{\rho} - \mathbf{r}_\Sigma|\right)}{|\boldsymbol{\rho} - \mathbf{r}_\Sigma|} d\mathbf{r}_\Sigma. \quad (1.24)$$

This equation, which is usually referred to as the Kirchhoff-Fresnel formula, gives the relation between the observed spectral amplitude $E_0(\boldsymbol{\rho}, \omega)$ of the field scattered by the rough surface and the incident field $E_i(\mathbf{r}_\Sigma, \omega)$ on the object's surface.[30] Next, we have to express the incident field $E_i(\mathbf{r}_\Sigma, \omega)$ in terms of the parameters of the illuminating source. The incident field will be calculated according to Eq. (1.24) as the spectral amplitude $E_i(\mathbf{r}_\Sigma, \omega)$ of the source field taken on the object surface,[30] the integration domain being given by the output aperture of the illuminating source (see Fig. 1.3). Let the source be pointlike. In practice, such a source can be represented by a very small, flat mirror reflecting the plane wave $E_{pi}(\mathbf{r}_a, \omega) = E_s S_r(\omega)$ incident in the direction $\boldsymbol{\nu}_s$, close to the normal $\mathbf{n}_s$ to the mirror surface, $\boldsymbol{\nu}_s \cdot \mathbf{n}_s \approx -1$, where E_s and $S_r(\omega)$ are the wave amplitude and spectrum, respectively. Then,

$$E_i(r_\Sigma, \omega) = \frac{i\omega}{2c} \int (\boldsymbol{\nu} - \boldsymbol{\nu}_s) \cdot \mathbf{n} k(r_a, \omega) E_{pi}(r_a, \omega) \frac{\exp\left(-i\dfrac{\omega}{c}|\mathbf{r}_a - \mathbf{r}_\Sigma|\right)}{|\mathbf{r}_a - \mathbf{r}_\Sigma|} d\mathbf{r}_a, \quad (1.24a)$$

where r_a is the radius vector of the output aperture point, r_Σ is the radius vector of the random rough surface of the object under study [see relation (1.1)], which is substituted in Eq. (1.24) for $\rho, \nu = (r_\Sigma - r_a)/|r_\Sigma - r_a|$.

The very small, flat mirror plays the role of the source output aperture, with $k(r_a, \omega) = 1$ inside the aperture and $k(r_a, \omega) = 0$ outside the aperture. Usually, the object under study is close to the line orthogonal to this aperture and passing through its center (an asterisk in Fig. 1.3); here, $\boldsymbol{\nu} \cdot n_s \approx 1$. Taking into account the relations $\boldsymbol{\nu}_s \cdot n_s \approx -1$, $\boldsymbol{\nu} \cdot n_s \approx 1$, and the fact that the function $k(r_a, \omega)$ is much narrower in r_a than other functions in the integral (1.24a), we obtain

$$E_i(\mathbf{r}_\Sigma, \omega) \approx \frac{iS_s\omega}{c} E_s S_r(\omega) \frac{\exp\left(-i\frac{\omega}{c}|\boldsymbol{\rho}_s - \mathbf{r}_\Sigma|\right)}{|\boldsymbol{\rho}_s - \mathbf{r}_\Sigma|}, \tag{1.25}$$

where S_s is the area of the source output aperture, and $\boldsymbol{\rho}_s$ is the radius vector of the source aperture center (see Fig. 1.3). Here, E_s is the amplitude of the source field and $S_r(\omega)$ is the source radiation spectrum.

In the case where the object is illuminated by a pointlike source, from relations (1.24) and (1.25) we find for the spectral amplitude of the scattered field

$$E_0(\boldsymbol{\rho}, \omega) = -\frac{\omega^2 E_s S_r(\omega) S_s}{2c^2} \int \mathbf{n} \cdot \mathbf{q} k(\mathbf{r}_\Sigma, \omega) \times \frac{\exp\left(-i\frac{\omega}{c}|\boldsymbol{\rho}_s - \mathbf{r}_\Sigma|\right)}{|\boldsymbol{\rho}_s - \mathbf{r}_\Sigma|} \frac{\exp\left(-i\frac{\omega}{c}|\boldsymbol{\rho} - \mathbf{r}_\Sigma|\right)}{|\boldsymbol{\rho} - \mathbf{r}_\Sigma|} d\mathbf{r}_\Sigma, \tag{1.26}$$

where $\mathbf{q} = \boldsymbol{\nu}_o - \boldsymbol{\nu}_i$ is the scattering vector.[12]

Now we make the following assumptions, which usually hold in practice with high accuracy. Assume that the illuminating source and the observation point of the scattered field E_0 are far from the object and the center of coordinate C is close to the observation point (see Fig. 1.3). Then,

$$|\boldsymbol{\rho}_s - \mathbf{r}_\Sigma| \approx |\boldsymbol{\rho}_s - \mathbf{r}_c|, \ \mathbf{q} \approx \frac{\boldsymbol{\rho}_s - \mathbf{r}_c}{|\boldsymbol{\rho}_s - \mathbf{r}_c|} + \frac{\boldsymbol{\rho} - \mathbf{r}_c}{|\boldsymbol{\rho} - \mathbf{r}_c|},$$

where $\mathbf{r}_c$ is the radius vector of some average point of the object, for instance, the object's center of mass. Then, after passing in Eq. (1.26) from integration over the rough object surface to integration over the mean object surface, by substituting $\mathbf{r}$ for $\mathbf{r}_\Sigma$ we obtain for the spectral amplitude of the scattered field

$$E_0(\boldsymbol{\rho}, \omega) = -\frac{\omega^2 E_s S_r(\omega) S_s}{2c^2 r_c |\mathbf{r}_c - \boldsymbol{\rho}_s|} \times \int \frac{\mathbf{n} \cdot \mathbf{q}}{\mathbf{n} \cdot \mathbf{N}} k(\mathbf{r}, \omega) \exp\left[-i\frac{\omega}{c}(|\mathbf{r}_\Sigma - \boldsymbol{\rho}_s| + |\mathbf{r}_\Sigma - \boldsymbol{\rho}|)\right] d\mathbf{r}, \tag{1.27}$$

where $\mathbf{N}$ is the normal to the mean surface and $1/(\mathbf{n}\cdot\mathbf{N})$ is the Jacobian of the coordinate transform of $\mathbf{r}_\Sigma$ into $\mathbf{r}$. The final expression for the instantaneous vector of the scattered field $E(\boldsymbol{\rho}, t)$ is obtained by substituting $\mathbf{E}_\omega = \mathbf{i}E_0(\boldsymbol{\rho}, \omega)$, where $\mathbf{i}$ is a unit vector, into Eq. (1.18). If the object is illuminated by a pointlike cw monochromatic source with a very narrow spectrum, for which $\Delta\omega \lll \omega_0$, $\Delta\omega$ and ω_0 being the width and the mean frequency of the spectrum $S_r(\omega)$, and if the source radiation spectrum is normalized, $\int S_r(\omega)d\omega = 1$, then

$$E(\boldsymbol{\rho}, t) = -\frac{E_s S_s \exp(i\omega_0 t)}{2\lambda^2 r_c |\mathbf{r}_c - \boldsymbol{\rho}_s|} \times \int \frac{\mathbf{n}\cdot\mathbf{q}}{\mathbf{n}\cdot\mathbf{N}} k(\mathbf{r}) \exp\left[-i\frac{2\pi}{\lambda}(|\mathbf{r}_\Sigma - \boldsymbol{\rho}_s| + |\mathbf{r}_\Sigma - \boldsymbol{\rho}|)\right] d\mathbf{r}, \quad (1.28)$$

where $k(\mathbf{r}) = k(\mathbf{r}, \omega_0)$. Furthermore, $E(\boldsymbol{\rho}, t)$ will be called the complex amplitude of the field scattered by the object under study (or simply the field amplitude). Usually, if a source has a narrow spectrum, $\Delta\omega \ll \omega_0$, it is called a *monochromatic source*.[3] This notion is discussed in more detail in Appendix 4.

Thus, one can see from Eqs. (1.24) and (1.26)–(1.28) that the field scattered by an object with random surface roughness is related to the roughness height distribution—namely, to deviations $\xi(\mathbf{r},t)$ from the mean surface—via integral relations. This fact confirms the necessity of using a statistical approach for studying wave diffraction by such surfaces.[28–30]

Consider now an important class of problems that is becoming increasingly popular at present, i.e., determining the properties of objects and identifying these objects by means of the scattered field. Such problems require a statistical approach since, as a rule, the field in the observation plane, which we have to process (see Figs. 1.2 and 1.3), is a sum of the field scattered by the object under study and a random additive noise field. The noise field, for instance, can originate from scattering by atmospheric aerosols. The main problems are to find the probability density function (PDF) of the observed random field, including the scattered field and the noise field, which fully determine the field statistical properties, and to use this function to obtain the most complete information about the scattering object. In particular, such a function is used in the statistical theory of decisions.[27] Furthermore, we consider the general case of this theory, where decisions about the object parameters are taken in the presence of a noise field.[12] In this case, the total observed field is

$$E_t(\boldsymbol{\rho}, t) = E(\boldsymbol{\rho}, t, \boldsymbol{\alpha}) + E_n(\boldsymbol{\rho}, t). \quad (1.29)$$

Here, $\boldsymbol{\alpha} = (\alpha_1, \ldots, \alpha_n)$ is the set of the key object parameters that can be determined; for example, the object's dimensions and velocities, the distance from the object, the statistical parameters σ, ℓ_u, ℓ_v, and τ_0 of the object surface roughness $\xi(\mathbf{r}, t)$ [see relations (1.6–1.8)], and so on. $E(\boldsymbol{\rho}, t, \boldsymbol{\alpha})$ is the complex amplitude of

the field scattered by the object; $E_n(\boldsymbol{\rho}, t)$ is the complex amplitude of the noise field.

If such a function were constructed using a deterministic description of the field scattered by a deterministically described surface, this field would depend, in addition to the measurable parameters $\alpha_1, \ldots, \alpha_n$, on a large number of parameters $\theta_1, \ldots, \theta_m$ used for a detailed analytical description of the rough surface of the object under study. For instance, a rough surface is often described by means of quadratic spline approximation: in the vicinity of extreme points, the surface is approximated by second-order surfaces. In this case, the parameters θ_k give the positions of extreme points and the values of the function describing the surface, as well as its second derivatives, at each of these points. According to the general principles of the theory of decisions, in order to obtain information about the scattering object, one should form the PDF of the realization of the random noise field $E_n(\boldsymbol{\rho}, t) = E_t(\boldsymbol{\rho}, t) - E(\boldsymbol{\rho}, t, \boldsymbol{\alpha}, \boldsymbol{\theta})$, where $\boldsymbol{\theta}(\theta_1, \ldots, \theta_m)$ is the set of additional unnecessary parameters of object surface roughness that also need to be estimated in this case. Then, for instance, the maximum PDF values determine the most probable estimates of the object parameters. In the case of a deterministically described surface, according to Eq. (1.16) and under the condition that the noise field has a Gaussian distribution and the PDF of the scattered field E is $P[E(\boldsymbol{\rho}, t, \boldsymbol{\alpha}, \boldsymbol{\theta})] \sim \exp(-L)$, then

$$L = -\frac{1}{2} \iiiint W_n(\boldsymbol{\rho}_1, t_1, \boldsymbol{\rho}_2, t_2)[E_t(\boldsymbol{\rho}, t) - E(\boldsymbol{\rho}, t, \boldsymbol{\alpha}, \boldsymbol{\theta})] \times [E_t^*(\boldsymbol{\rho}, t) - E^*(\boldsymbol{\rho}, t, \boldsymbol{\alpha}, \boldsymbol{\theta})] d\boldsymbol{\rho}_1 dt_1 d\boldsymbol{\rho}_2 dt_2,$$

where $W_n(\boldsymbol{\rho}_1, t_1, \boldsymbol{\rho}_2, t_2)$ is the inverse correlation function satisfying the integral equation $\iint W_n(\boldsymbol{\rho}_1, t_1, \boldsymbol{\rho}_2, t_2) B_n(\boldsymbol{\rho}_2, t_2, \boldsymbol{\rho}_3, t_3) d\boldsymbol{\rho}_2 dt_2 = \delta(\boldsymbol{\rho}_1 - \boldsymbol{\rho}_3)\delta(t_1 - t_3)$, and $B_n(\boldsymbol{\rho}_1, t_1, \boldsymbol{\rho}_2, t_2) = \langle E_n(\boldsymbol{\rho}_1, t_1) E_n^*(\boldsymbol{\rho}_2, t_2)\rangle - \langle E_n(\boldsymbol{\rho}_1, t_1)\rangle \langle E_n^*(\boldsymbol{\rho}_2, t_2)\rangle$ is the noise correlation function.

The estimates for the parameters α_j and θ_k satisfy the system of differential equations determining the maximum PDF,

$$\frac{\partial L}{\partial \alpha_j} = 0, \qquad \frac{\partial L}{\partial \theta_k} = 0, \quad j = 1, 2, \ldots, n; \; k = 1, 2, \ldots, m.$$

We see that due to the detailed description of the rough surface of the object under study in the considered case, the number of these equations exceeds by far the number of key parameters α_j. This makes it impossible to determine the parameters of the object in practice.

The solution to the problem is to assume that the field scattered by a rough surface of the object under study is random, since this field is formed by random roughness of the scattering surface. Therefore, the field E_t analyzed by the observer [see relation (1.29)] is the sum of the random field and the noise field. The probability density function for such a field can be found under the assumption that the

scattered field E has a Gaussian distribution. In this case, it follows from Eq. (1.16) that the PDF can be written in the form

$$P[E(\boldsymbol{\rho}, t, \boldsymbol{\alpha})] \sim \exp L,$$

where

$$L = -\frac{1}{2}\iiiint W(\boldsymbol{\rho}_1, t_1, \boldsymbol{\rho}_2, t_2)[E_t(\boldsymbol{\rho}_2, t_2) - \langle E_t(\boldsymbol{\rho}_2, t_2, \alpha)\rangle] \times [E_t(\boldsymbol{\rho}_2, t_2) - \langle E_t(\boldsymbol{\rho}_2, t_2, \alpha)\rangle]^* d\boldsymbol{\rho}_1, dt_1, d\boldsymbol{\rho}_2 dt_2, \tag{1.30}$$

and $W(\boldsymbol{\rho}_1, t_1, \boldsymbol{\rho}_2, t_2)$ is the inverse correlation function, which is found from the integral equation

$$\iint W(\boldsymbol{\rho}_1, t_1, \boldsymbol{\rho}_2, t_2) B_t(\boldsymbol{\rho}_2, t_2, \boldsymbol{\rho}_3, t_3) d\boldsymbol{\rho}_2 dt_2 = \delta(\boldsymbol{\rho}_1 - \boldsymbol{\rho}_3)\delta(t_1 - t_3). \tag{1.31}$$

$B_n(\boldsymbol{\rho}_1, t_1, \boldsymbol{\rho}_2, t_2) = \langle E_n(\boldsymbol{\rho}_1, t_1)E_n^*(\boldsymbol{\rho}_2, t_2)\rangle - \langle E_n(\boldsymbol{\rho}_1, t_1)\rangle\langle E_n^*(\boldsymbol{\rho}_2, t_2)\rangle$ is the noise correlation function, $B_t(\boldsymbol{\rho}_1, t_1, \boldsymbol{\rho}_2, t_2) = \langle E_t(\boldsymbol{\rho}_1, t_1)E_t^*(\boldsymbol{\rho}_2, t_2)\rangle - \langle E_t(\boldsymbol{\rho}_1, t_1)\rangle \times \langle E_t^*(\boldsymbol{\rho}_2, t_2)\rangle = B_n + B$ is the correlation function for the total observed field equal to the sum of the scattered field and the noise field, and

$$B(\boldsymbol{\rho}_1, t_1, \boldsymbol{\rho}_2, t_2) = \langle E(\boldsymbol{\rho}_1, t_1)E^*(\boldsymbol{\rho}_2, t_2)\rangle - \langle E(\boldsymbol{\rho}_1, t_1)\rangle\langle E^*(\boldsymbol{\rho}_2, t_2)\rangle.$$

The mean values used here, according to Eqs. (1.9) and (1.12), are uniquely determined by the correlation function B_{12} of the roughness height distribution of an object's surface. Taking into account that B_{12} depends on the roughness height deviation σ^2, correlation radii ℓ_u and ℓ_v, and correlation time τ_0, one can note that the PDF of the sum field E_t also depends on these four parameters, σ, ℓ_u, ℓ_v, and τ_0, as well as on the key parameters α_j of the object and noise field parameters. Since $P[E_t(\boldsymbol{\rho}, t, \boldsymbol{\alpha})]$ depends on only four statistical parameters of the random surface of the object under study, it becomes possible to estimate all key parameters α_j of the object by means of the statistical theory of decisions.[12,27] We see that for obtaining the information about the object under study, we must know the statistical characteristics of the scattered and noise fields, including the correlation function B of the scattered field and the correlation function B_n of the noise field.

Taking into account that the statistics of the scattered field are mainly determined by the parameters σ, ℓ_u, ℓ_v, and τ_0 of the roughness height distribution $\xi(\mathbf{r})$, it is reasonable to represent the spectral amplitude E_0 of the scattered field as an explicit function of ξ. It has been shown[12] that after assuming that the observation point is close to the optical axis, $\rho \ll r_c$, and the degree of surface roughness is much smaller than the observation distance, $\xi(\mathbf{r}) \ll |\boldsymbol{\rho} - \mathbf{r}_c|$, much smaller than the source–object distance, $\xi(\mathbf{r}) \ll |\mathbf{r}_c - \boldsymbol{\rho}_s|$, and much smaller than R_u and R_v,

i.e., the curvature radii for normal sections that cross the coordinate lines $u = 0$ and $v = 0$ at point (u, v), $\xi(\mathbf{r}) \ll R_u, R_v$, then the field E_0 scattered by the object is

$$E_0(\boldsymbol{\rho}, \omega) \approx -\frac{\omega^2 E_s S_s S_r(\omega)}{2c^2 r_c |\mathbf{r}_c - \boldsymbol{\rho}_s|} \iint \left(\mathbf{q} \cdot \mathbf{N} - \frac{\mathbf{n}_u \cdot \mathbf{q}}{r_u} \frac{\partial \xi}{\partial u} - \frac{\mathbf{n}_v \cdot \mathbf{q}}{r_v} \frac{\partial \xi}{\partial v} \right) k(\mathbf{r}) \times \exp\left[-i \frac{\omega}{c} (|\mathbf{r} - \boldsymbol{\rho}_s| + |\mathbf{r} - \boldsymbol{\rho}|) \right] \exp\left[i \frac{\omega \mathbf{q} \cdot \mathbf{N} \xi(\mathbf{r})}{c} \right] r_u r_v du dv, \tag{1.32}$$

where $\mathbf{n}_u = \mathbf{r}_u / r_u$, $\mathbf{n}_v = \mathbf{r}_v / r_v$, $\mathbf{r}_u = (\partial x/\partial u, \partial y/\partial u, \partial z/\partial u)$, and $\mathbf{r}_v = (\partial x/\partial v, \partial y/\partial v, \partial z/\partial v)$. Here, we do not take into account that the reflection coefficient k depends on ω since the width of the function $S_r(\omega)$, $\Delta\omega$, is, as a rule, much less than the mean frequency ω_0. Substituting this relation into Eq. (1.18), one can obtain the scattered field amplitude $E(\boldsymbol{\rho}, t)$.

In what follows, the analysis of the scattered fields will be carried out under the assumption that the object under study is illuminated by a cw radiation source with coherence length $L_c = c/\Delta\omega > 10L_s$, where L_s is the depth of the scattering surface. Here, the depth of the scattering surface is the distance between the two points that are the furthest and the closest, respectively, to the observation point. In this case, the amplitude of the scattered field at each point of the observation area is given by a sum of amplitudes (interference) of all waves scattered by the object surface and reaching this point. Such a scattered field will be called *coherent* (see Appendix 4). In practice, a lot of elements of a rough surface scatter fields to the same observation point. As a result, the scattered field has a Gaussian distribution, and its intensity distribution forms a speckle pattern with unity contrast (see Sec. 1.3). If the coherence length of the source $L_c = c/\Delta\omega$ is less than twice the depth of the scattering surface, $2L_s$, then the interference pattern at each point of the observation area is formed by waves scattered by a single part of the scattering rough surface with the depth $\sim L_c$. In this case, the resulting field scattered by the surface is a sum of statistically independent fields scattered by all of its parts. As a result, the intensity distribution in the scattered field is a speckle pattern with contrast less than unity. It is reasonable to define this field as a *partially coherent field*. If $L_c < 10\lambda$, where $\lambda = (2\pi c)/\omega_0$, then the scattered field is *noncoherent* (see Appendix 4).

As an example of a coherent field, one can consider the field $E(\boldsymbol{\rho}, t)$ scattered by a large surface area of an object illuminated by a pointlike source that is "almost monochromatic" (see Appendix 4), in the sense that its coherence length exceeds by far any typical depth of the object's scattering surface. In this case, the function $S_r(\omega)$ is concentrated within a narrow frequency interval around the mean frequency ω_0 and can be approximated by a δ-function. Then, it follows from Eq. (1.18) that

$$E(\boldsymbol{\rho}, t) = E_0(\boldsymbol{\rho}) \exp i\omega_0 t, \tag{1.33}$$

where

$$E_0(\boldsymbol{\rho}) \approx -\frac{E_s S_s}{2\lambda^2 r_c |\mathbf{r}_c - \boldsymbol{\rho}_s|} \iint \left(\mathbf{q} \cdot \mathbf{N} - \frac{\mathbf{n}_u \cdot \mathbf{q}}{r_u} \frac{\partial \xi}{\partial u} - \frac{\mathbf{n}_v \cdot \mathbf{q}}{r_v} \frac{\partial \xi}{\partial v} \right) k(\mathbf{r}) \times \exp\left[-i \frac{2\pi}{\lambda} (|\mathbf{r} - \boldsymbol{\rho}_s| + |\mathbf{r} - \boldsymbol{\rho}|) \right] \exp\left[i \frac{2\pi \mathbf{q} \cdot \mathbf{N} \xi(\mathbf{r})}{\lambda} \right] r_u r_v du dv. \quad (1.34)$$

In some problems, such as those of Fourier telescopy (see Chapter 4), information about the object under study can be considerably altered because of a small coherence length of the testing radiation. Still, in this book, the analysis and discussion of applications will mostly concern coherent scattered fields that are formed when rough objects are illuminated by cw pointlike monochromatic sources.

1.3 Statistical characteristics of a field scattered by a stationary object of finite size

In this section, we consider for the Kirchhoff approximation the statistical characteristics of fields scattered by a finite-sized object with a random surface illuminated by a pointlike monochromatic source with wavelength $\lambda = (2\pi c)/\omega_0$. We assume here that the object is stable; namely, that object displacement during the observation time is much less than the wavelength λ.

Let us return to Eq. (1.33), which is convenient for the analysis since it contains explicit dependencies of the scattered field on the directions toward the source $\boldsymbol{\rho}_s$ and the observation point $\boldsymbol{\rho}$. Note that it is also valid for cases where the observation point or the illuminating source is far from the object under study (see Fig. 1.3). The term $[-i(2\pi/\lambda)(|\mathbf{r} - \boldsymbol{\rho}_s| + |\mathbf{r} - \boldsymbol{\rho}|)]$ in Eq. (1.33) describes total phase shifts appearing due to wave propagation from the source to the points of the mean surface and then to the observation point. The term $[-i(2\pi/\lambda)\mathbf{q} \cdot \mathbf{N}\xi(\mathbf{r})]$ describes additional phase shifts due to the propagation from the mean surface to the real random surface of the object.

Let us find the mean value of the field scattered by the object. Due to the statistical independence of the parameters $\partial\xi/\partial u$, $\partial\xi/\partial v$, and ξ, [see expression (1.15)], according to Eq. (1.32), we find that

$$\langle E_0(\boldsymbol{\rho}) \rangle = -\frac{E_s S_s}{2\lambda^2 r_c |\mathbf{r}_c - \boldsymbol{\rho}_s|} \iint \left(\mathbf{q} \cdot \mathbf{N} - \frac{\mathbf{n}_u \cdot \mathbf{q}}{r_u} \left\langle \frac{\partial \xi}{\partial v} \right\rangle - \frac{\mathbf{n}_v \cdot \mathbf{q}}{r_v} \left\langle \frac{\partial \xi}{\partial v} \right\rangle \right) k(\mathbf{r}) \times \exp\left[-i \frac{2\pi}{\lambda} (|\mathbf{r} - \boldsymbol{\rho}_s| + |\mathbf{r} - \boldsymbol{\rho}|) \right] \left\langle \exp\left[i \frac{2\pi \mathbf{q} \cdot \mathbf{N} \xi(\mathbf{r})}{\lambda} \right] \right\rangle r_u r_v du dv.$$

From the definition of the mean surface, $\langle \xi(\mathbf{r}) \rangle = 0$. Then, assuming that ξ has a Gaussian distribution and using relations (1.2) and (1.12), the variance $\sigma^2 =$

$\langle \xi^2(\mathbf{r}) \rangle$, and

$$\langle \exp(-i\varphi) \rangle = \int_{-\infty}^{\infty} \exp(-i\alpha\varphi) w_1(\varphi) d\varphi = \exp\left(-\frac{\sigma_\varphi^2}{2} \right),$$

where $\varphi = 2\pi\xi(\mathbf{q} \cdot \mathbf{N})/\lambda$ and $w_1(\varphi) = (1/\sqrt{2\pi\sigma_\varphi}) \exp(-\varphi^2/2\sigma_\varphi^2)$, we obtain

$$\begin{aligned} E_0(\boldsymbol{\rho}) = -\frac{E_s S_s}{2\lambda^2 r_c |\mathbf{r}_c - \boldsymbol{\rho}_s|} \iint \mathbf{q} \cdot \mathbf{N} k(\mathbf{r}) \\ \times \exp\left[-i\frac{2\pi}{\lambda} (|\mathbf{r} - \boldsymbol{\rho}_s| + |\mathbf{r} - \boldsymbol{\rho}|) \right] \\ \times \exp -\left[\frac{2\pi\sigma(\mathbf{q} \cdot \mathbf{N})}{\lambda} \right]^2 r_u r_v du dv. \end{aligned} \tag{1.35}$$

One can see from Eq. (1.35) that in the case where the roughness height standard deviation $\sigma \ll \lambda$, $\langle E_0(\boldsymbol{\rho}) \rangle = E_m(\boldsymbol{\rho})\{1 - [(2\mathbf{q} \cdot \mathbf{N}\pi\sigma)/\lambda]^2\}$, where

$$\begin{aligned} E_m(\boldsymbol{\rho}) = -\frac{E_s S_s}{2\lambda^2 r_c |\mathbf{r}_c - \boldsymbol{\rho}_s|} \iint \mathbf{q} \cdot \mathbf{N} k(\mathbf{r}) \\ \times \exp\left[-i\frac{2\pi}{\lambda} (|\mathbf{r} - \boldsymbol{\rho}_s| + |\mathbf{r} - \boldsymbol{\rho}|) \right] r_u r_v du dv \end{aligned}$$

is the field that would be scattered by an object with the surface coinciding with the mean surface of the object under study. In the literature, this field is referred to as the *specular component of the scattered field*.[12] We can also use this relation for calculating the field formed by a smooth surface.

Under a weaker condition, $\mathbf{q} \cdot \mathbf{N}\sigma \ll \lambda$, the approximate equality $\langle E_0(\boldsymbol{\rho}) \rangle \approx E_m(\boldsymbol{\rho})$ holds. This describes the well-known fact that beams incident at grazing angles are almost totally reflected; the condition $\mathbf{q} \cdot \mathbf{N}\sigma \ll \lambda$ corresponds to the grazing incidence of the beams at steep parts of the surface. The last statement should be formulated with caution, since the surface of a real object is a complicated superposition of microscopic roughness elements of different scales. This means that in addition to large-scale roughness, with the standard deviation of the object surface roughness height $\sigma \gg \lambda$, there is also small-scale roughness, with $\sigma \ll \lambda$. Because of this, even steep parts of the surface do not totally reflect the incident radiation, and only at points of very steep slope is the reflection specular.

Returning to Eq. (1.35), we see that at $\sigma \gg \lambda$, most of the surface (with the exception of small areas where $\mathbf{q} \cdot \mathbf{N}\sigma \ll \lambda$) satisfies the inequality $\exp\{-[(2\pi\sigma\mathbf{q} \cdot \mathbf{N})/\lambda^2]\} \ll 1$, from which it follows that if $\sigma \gg \lambda$, then $|\langle E_0(\boldsymbol{\rho}) \rangle| \ll |E_m(\boldsymbol{\rho})|$. The last relation shows that for objects having a rough surface with a roughness height standard deviation of $\sigma \gg \lambda$, there is no specular component in the scattered field, and the mean value of the scattered field very rapidly tends toward zero with an increase of the ratio σ/λ. This means that the scattered field contains no distinct

peak. The fact that at $\sigma \gg \lambda$ the mean value of the field scattered by an object with random surface is very small can be explained as follows. In this case, the field E_0 is the sum of a large number of fields with uniform phases distributions within a range that exceeds 2π. As a result, approximately half of these fields have a phase shift of π relative to the other fields. Hence, the resulting field at the observation point is the sum of the fields with opposite signs, which is close to zero.

In practice, there are problems that require the mean intensity of the randomly scattered field to be known; an example is calculation of the area of a backscattering surface. In some applications, it is necessary to know moments of random fields or random intensities of higher orders (i.e., second, third, and fourth). This is necessary, for instance, for determining the relative variance of the intensity of the scattered field in the observation area. In the literature, this parameter is also called *contrast of the intensity distribution*[12] or the *blinking index*.[29]

Finally, there are problems that require information on the joint field moments of the second, third, and fourth orders. For instance, under the assumption that a scattered field has Gaussian distribution, the second joint moment or, more precisely, the correlation function of the scattered field together with the first moment (the mean value of the scattered field) completely describe the statistical distribution of the field, which is given by the PDF [see expression (1.30)]. In turn, the PDF determines the optimal procedures for field processing.[12] The fourth joint moments of the field allow us to find the intensity correlation functions.

Let us now analyze the correlation function of the scattered coherent field $E(\boldsymbol{\rho}, t)$ given by relation (1.33):

$$B(\boldsymbol{\rho}_1, t_1, \boldsymbol{\rho}_2, t_2) = \langle E(\boldsymbol{\rho}_1, t_1) E^*(\boldsymbol{\rho}_2, t_2)\rangle = \exp[i\omega_0(t_1 - t_2)]\langle E_0(\boldsymbol{\rho}_1) E_0^*(\boldsymbol{\rho}_2)\rangle.$$

Taking into account that $\langle \xi(\partial\xi/\partial u)\rangle = 0$ [see Eq. (1.15)] and hence, the averaging over the surface roughness and over its derivatives can be performed separately, we first consider the case $\sigma \gg \lambda$. Suppose that the following conditions also hold: σ/ℓ_u, $\sigma/\ell_v \gg d_\rho/r_c$, d_o/r_c, $\sqrt{\lambda/r_c}$, where d_o is the size of the illuminating surface of an object under study and d_ρ is the size of the observation area. In the case of gaining an image of the object, then d_ρ is the imaging system aperture. Then, approximating the correlation function of the surface roughness by a Gaussian function [see relation (1.10)], we obtain for the correlation function of the scattered field

$$B(\boldsymbol{\rho}_1, t_1, \boldsymbol{\rho}_2, t_2) = \exp[i\omega_0(t_1 - t_2)] \times \iint V(\mathbf{r}) \left[-i\frac{2\pi}{\lambda}(|\mathbf{r} - \boldsymbol{\rho}_1| - |\mathbf{r} - \boldsymbol{\rho}_2|)\right] du dv, \tag{1.36}$$

where

$$V(\mathbf{r}) = \frac{E_s^2 S_s^2 |k(\mathbf{r})|^2 \ell_u \ell_v r_u r_v}{4\pi\lambda^4 r_c^2 |\mathbf{r}_c - \boldsymbol{\rho}_s|^2 (\mathbf{q}\cdot\mathbf{N})^2 \sigma^2} \exp\left[-\frac{(\mathbf{q}\cdot\mathbf{n}_u)^2 \ell_u^2 + (\mathbf{q}\cdot\mathbf{n}_v)^2 \ell_v^2}{(\mathbf{q}\cdot\mathbf{N})^2 \sigma^2}\right] \times \left[(\mathbf{q}\cdot\mathbf{N})^2 + (\mathbf{q}\cdot\mathbf{n}_u)^2 \left(\frac{\sigma}{\ell_u}\right)^2 + (\mathbf{q}\cdot\mathbf{n}_v)^2 \left(\frac{\sigma}{\ell_v}\right)^2\right],$$

and

$$\mathbf{n}_u = \frac{\mathbf{r}_u}{r_u},\ \mathbf{n}_v = \frac{\mathbf{r}_v}{r_v}.$$

Equation (1.36) is considerably simplified in the case of isotropic random surfaces, i.e., for $\ell_u = \ell_v = \ell$, where ℓ is the correlation radius of isotropic roughness. In this case,

$$V(\mathbf{r}) = \frac{E_s^2 S_s^2 \ell^2 r_u r_v}{4\pi\lambda^4 r_c^2 |\mathbf{r}_c - \boldsymbol{\rho}_s|^2 \sigma^2} k_i(\mathbf{r}),$$

where

$$k_i(\mathbf{r}) = \left[1 + \left(\frac{q_t \sigma}{q_N \ell}\right)^2\right] \exp\left[-\left(\frac{q_t \ell}{q_N \sigma}\right)^2\right] |k(\mathbf{r})|^2, \tag{1.37}$$

$q_N = \mathbf{q} \cdot \mathbf{N}$ is the projection of the vector $\mathbf{q}$ on the normal $\mathbf{N}$ to the mean surface of the object under study, and $q_t = [(\mathbf{q} \cdot \mathbf{n}_u)^2 + (\mathbf{q} \cdot \mathbf{n}_v)^2]^{1/2}$ is the length of the projection of $\mathbf{q}$ on the plane tangent to the mean surface. In the next chapter, we will show that the function $k_i(\mathbf{r})$ is proportional to the averaged intensity distribution in the coherent image of the object. Furthermore, without loss of generality and to simplify the final results, we will deal only with the objects having surfaces with isotropic roughness.

Let the field be observed in the Fresnel (near-field) zone, for which $(2\pi\rho^3)/(\lambda r_c^2) \ll 1$. In this case,

$$B(\boldsymbol{\rho}_1, t_1, \boldsymbol{\rho}_2, t_2) = \exp[i\omega_0(t_1 - t_2)] C_0 \iint k_i(\mathbf{r}) \times \exp\left\{-i\frac{2\pi}{\lambda r_c}\left[\mathbf{r}(\boldsymbol{\rho}_1 - \boldsymbol{\rho}_2) - \frac{\rho_1^2 - \rho_2^2}{r_c}\right]\right\} r_u r_v du dv, \tag{1.38}$$

where

$$C_0 = \frac{E_s^2 S_s^2 \ell^2}{4\pi\lambda^4 r_c^2 |\mathbf{r}_c - \boldsymbol{\rho}_s|^2 \sigma^2}.$$

For instance, for a flat object placed on the axis that is orthogonal to the observation plane, and for a illuminating source placed close to the observer,

$$\begin{aligned} B(\boldsymbol{\rho}_1, t_1, \boldsymbol{\rho}_2, t_2) &= \langle E(\boldsymbol{\rho}_1, t_1) E^*(\boldsymbol{\rho}_2, t_2) \rangle \\ &= \frac{E_s^2 S_s^2 \ell^2}{4\pi\lambda^4 r_c^4 \sigma^2} \exp[i\omega_0(t_1 - t_2)] \iint |k(\mathbf{r})|^2 \exp\left\{-i\frac{2\pi}{\lambda r_c}[\mathbf{r}(\boldsymbol{\rho}_1 - \boldsymbol{\rho}_2)]\right\} r_u r_v du dv \\ &\sim \sin c\left[\frac{2\pi d_o(\rho_{1x} - \rho_{2x})}{\lambda r_c}\right]. \end{aligned} \tag{1.39}$$

Of considerable practical interest is the problem of determining the averaged intensity of a field scattered by a nonflat object with random surface. Clearly,

$$\langle I(\boldsymbol{\rho})\rangle \sim \frac{E_s^2 S_s^2 \ell^2}{4\pi\lambda^4 r_c^4 \sigma^2} \iint k_i(\mathbf{r}) r_u r_v du dv, \tag{1.40}$$

where $I(\boldsymbol{\rho}) = |E_0(\boldsymbol{\rho})|^2$ is an intensity realization. One can see from this relation that an increase in the surface roughness steepness σ/ℓ leads to a decrease in the scattered field intensity. The reason is that a surface with steep roughness scatters radiation into a broad angular cone.

Consider, for instance, the intensity of the field scattered by a flat object oriented at an angle θ to the observation plane normal for the case where the positions of the source and the observer coincide:

$$\langle I(\theta)\rangle = \frac{E_s^2 S_s^2 \ell^2 S_o}{4\pi\lambda^4 r_c^4 \sigma^2}\left[1 + \left(\frac{\sigma \tan\theta}{\ell}\right)^2\right] \exp\left[-\left(\frac{\ell \tan\theta}{q_N \sigma}\right)^2\right] |k(\mathbf{r}_p)|^2,$$

where S_o is the area of the illuminating surface of the object. One can see that at $\theta_1 \approx \sigma/\ell$, $I(\theta)$ decreases 2.7 times. A simple geometric consideration of scattering shows that at $\theta \approx 3\sigma/\ell$, radiation $I(\theta)$ scattered by the object almost does not reach the observer.

It is well known that the field scattered by a rough object has a speckle pattern consisting of approximately identical bright speckles (see Fig. 1.4). Usually in the literature these speckles are referred to as correlation domains of the scattered field in the observation plane.[10–12] The area of the correlation domain is

$$S_c(\boldsymbol{\rho}) = \frac{1}{\langle I(\boldsymbol{\rho})\rangle} \int \langle E(\boldsymbol{\rho}, t) E^*(\boldsymbol{\rho}_1, t)\rangle d\boldsymbol{\rho}_1.$$

For example, for a round flat object placed in the Fresnel zone on the axis orthogonal to the observation plane, and for an illuminating source placed close to the observer, it is not difficult to obtain, using Eq. (1.39), that the correlation domain is a circle with diameter $d_c \approx (\lambda r_c)/d_o$ and the area $S_c(\boldsymbol{\rho}) \approx \pi d_c^2$.

It is convenient to determine the correlation radii of the scattered field in each direction of the observation plane (Fig. 1.4); for instance, along the coordinates X and Y on this plane:

$$\rho_{cx} = \frac{1}{\langle I(\boldsymbol{\rho})\rangle} \int \langle E(\boldsymbol{\rho}, t) E^*(\boldsymbol{\rho}_x, \boldsymbol{\rho}_y, t)\rangle d\boldsymbol{\rho}_y,$$

and

$$\rho_{cy} = \frac{1}{\langle I(\boldsymbol{\rho})\rangle} \int \langle E(\boldsymbol{\rho}, t) E^*(\boldsymbol{\rho}_x, \boldsymbol{\rho}_y, t)\rangle d\boldsymbol{\rho}_x.$$

The correlation radii ρ_{cx} and ρ_{cy} are approximately equal to the width KL and the height MN of the correlation domain, respectively. For an elliptical (see Fig. 1.4) or flat rectangular rough object placed in the Fresnel zone on the axis orthogonal to the observation plane, from Eq. (1.39) we obtain

$$\rho_{cx} \approx \frac{\lambda r_c}{d_x \rho_{cy}} \approx \frac{\lambda r_c}{d_y}, \tag{1.41}$$

where d_x and d_y are the sizes of the ellipse (or the rectangle) axes AB and CD, respectively (Fig. 1.4). For a square flat object, $d_x = d_y = d_o$, and

$$\rho_{cx} = \rho_{cy} = \rho_c \approx \frac{\lambda r_c}{d_o}. \tag{1.41a}$$

Knowing relation (1.40), one can find the effective area of the backscattering surface of the object under study, determined as

$$S_e = \frac{\langle I(\boldsymbol{\rho}) \rangle}{\overline{K} C_o} = \iint \frac{k_i(\mathbf{r}) r_u r_v du dv}{\overline{K}},$$

where

$$\overline{K} = \frac{1}{S_o} \iint |k(\mathbf{r})|^2 r_u r_v du dv.$$

For a mostly smooth surface, when $\sigma/\ell < 0.3$, and for a constant reflection coefficient $k(\mathbf{r})$,

$$S_e \approx \iint \exp\left[-\left(\frac{q_t \ell}{q_N \sigma} \right)^2 \right] r_u r_v du dv.$$

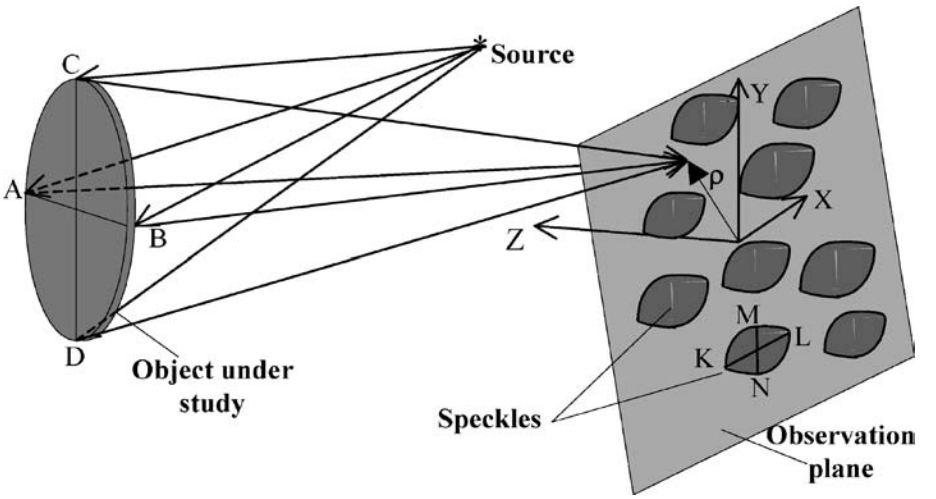

Figure 1.4 The speckle pattern of a coherent field scattered by a rough object.

In this case, the effective scattering surface of a flat object placed at angle θ, $q_N = 2\cos\theta$, $q_t = 2\sin\theta$, and

$$S_e \approx S_o \exp\left[-\left(\frac{\ell \tan\theta}{\sigma}\right)^2\right].$$

From this expression, one can see that the effective scattering surface decreases dramatically with an increase of θ. In practice, this decrease is not large, since for $\tan\theta \gg \sigma/\ell$, the main contribution to $S_e(\theta)$ is given by small-scale roughness.[12] For the same case $\sigma/\ell < 0.3$, the effective scattering surface of a spherical object is

$$S_e \approx \iint \exp\left\{-\left[\frac{(x^2+y^2)\ell^2}{d_o^2\sigma^2}\right]\right\} dxdy = \frac{\pi d_o^2 \sigma^2}{\ell^2}.$$

Let us now pass from the analysis of first- and second-order moments of the scattered field to the consideration of the fourth-order correlation function of the scattered field, for instance, the fourth-order moments of the scattered field real part E_r. Such a correlation function can be represented by the form

$$\begin{aligned}
&\Gamma(\boldsymbol{\rho}_1, \boldsymbol{\rho}_2, \boldsymbol{\rho}_3, \boldsymbol{\rho}_4) \\
&\quad = \langle E_r(\boldsymbol{\rho}_1)E_r(\boldsymbol{\rho}_2)E_r(\boldsymbol{\rho}_3)E_r(\boldsymbol{\rho}_4)\rangle - \langle E_r(\boldsymbol{\rho}_1)E_r(\boldsymbol{\rho}_2)\rangle\langle E_r(\boldsymbol{\rho}_3)E_r(\boldsymbol{\rho}_4)\rangle \\
&\qquad - \langle E_r(\boldsymbol{\rho}_1)E_r(\boldsymbol{\rho}_3)\rangle\langle E_r(\boldsymbol{\rho}_2)E_r(\boldsymbol{\rho}_4)\rangle - \langle E_r(\boldsymbol{\rho}_1)E_r(\boldsymbol{\rho}_4)\rangle\langle E_r(\boldsymbol{\rho}_2)E_r(\boldsymbol{\rho}_3)\rangle,
\end{aligned}$$

where $E_r(\boldsymbol{\rho}) = \mathrm{Re}\, E(\boldsymbol{\rho}, t)$.

Generally speaking, it is difficult to analyze this relation. However, it can be estimated for certain applications-oriented cases. Yet, if the object under study is a flat object placed in the Fresnel zone and illuminated by a plane wave directed normally to its surface and $\ell^2 \ll S_e = S_o$, then $\Gamma(\boldsymbol{\rho}_1, \boldsymbol{\rho}_2, \boldsymbol{\rho}_3, \boldsymbol{\rho}_4) = A_1 + A_2 + A_3$, where

$$\begin{aligned}
A_1 &= C_\Gamma \iint |k(\mathbf{r})|^4 \exp\left[i\frac{2\pi\mathbf{r}(\boldsymbol{\rho}_1 - \boldsymbol{\rho}_2 + \boldsymbol{\rho}_3 - \boldsymbol{\rho}_4)}{\lambda r_c}\right] r_u r_v du dv, \\
A_2 &= C_\Gamma \iint |k(\mathbf{r})|^4 \exp\left[i\frac{2\pi\mathbf{r}(-\boldsymbol{\rho}_1 - \boldsymbol{\rho}_2 + \boldsymbol{\rho}_3 + \boldsymbol{\rho}_4)}{\lambda r_c}\right] r_u r_v du dv, \\
A_3 &= C_\Gamma \iint |k(\mathbf{r})|^4 \exp\left[i\frac{2\pi\mathbf{r}(-\boldsymbol{\rho}_1 + \boldsymbol{\rho}_2 - \boldsymbol{\rho}_3 + \boldsymbol{\rho}_4)}{\lambda r_c}\right] r_u r_v du dv,
\end{aligned}$$

and

$$C_\Gamma = \frac{3\ell^4 E_i^4}{\sigma^2 r_c^2 \lambda^2}.$$

If the correlation radius $\ell \to 0$, then $\Gamma(\boldsymbol{\rho}_1, \boldsymbol{\rho}_2, \boldsymbol{\rho}_3, \boldsymbol{\rho}_4) \to 0$. This is quite a natural result: the decrease of ℓ increases the number of independent contributions to the scattered field, and hence, the scattered field distribution becomes Gaussian. Here, as it is known, $\Gamma(\boldsymbol{\rho}_1, \boldsymbol{\rho}_2, \boldsymbol{\rho}_3, \boldsymbol{\rho}_4) = 0$.[12,29]

It is interesting to estimate the normalized fourth-order correlation function, which gives quantitative information about the deviation of the real scattered field distribution from the Gaussian one:

$$\chi_d = \frac{\Gamma(\boldsymbol{\rho}_1, \boldsymbol{\rho}_2, \boldsymbol{\rho}_3, \boldsymbol{\rho}_4)}{\langle |E_r(\boldsymbol{\rho}_1)|^2 \rangle \langle |E_r(\boldsymbol{\rho}_2)|^2 \rangle}.$$

If $\ell^2 \ll S_p$, then $\chi_d = 1/N_c \ll 1$, where $N_c = S_o/\ell^2$ is the number of independent contributions to the scattered field, which is approximately equal to the number of separate elements of the rough surface. This means that the scattered field $E(\boldsymbol{\rho}, t)$ is the sum of a large number N_c of statistically independent fields scattered by these elements. In this case, the condition $N_c \gg 1$ of the central limit theorem is satisfied, and $E(\boldsymbol{\rho}, t)$ has essentially Gaussian distribution.

Let us write another useful relation, which is valid for $\ell^2 \ll S_o$ and $\sigma \gg \lambda$, when the scattered field distribution is also approximately Gaussian:[12]

$$\langle I(\boldsymbol{\rho}_1) I(\boldsymbol{\rho}_2) \rangle - \langle I(\boldsymbol{\rho}_1) \rangle \langle I(\boldsymbol{\rho}_2) \rangle = |\langle E(\boldsymbol{\rho}_2) E^*(\boldsymbol{\rho}_2) \rangle|^2 \left(1 + \frac{\ell^2}{S_o}\right)$$

$$\approx |\langle E(\boldsymbol{\rho}_2) E^*(\boldsymbol{\rho}_2)|^2. \tag{1.42}$$

For $\boldsymbol{\rho}_1 = \boldsymbol{\rho}_2 = \boldsymbol{\rho}$,

$$\left\langle I^2(\boldsymbol{\rho}) \right\rangle - \left\langle I(\boldsymbol{\rho}) \right\rangle^2 = \left\langle I(\boldsymbol{\rho}) \right\rangle^2 \left(1 + \frac{\ell^2}{S_o}\right). \tag{1.42a}$$

These last results are often used in optics. They indicate that for $\ell^2/S_o \ll 1$, the scattered field has a Gaussian distribution and there is a relationship between the intensity correlation function and the field correlation function. The value ℓ^2/S_o describes deviation of the scattered field distribution from a Gaussian one. Hence, the intensity distribution $I(\boldsymbol{\rho}) = |E(\boldsymbol{\rho})|^2$ with $\ell^2/S_o \ll 1$ is a speckle pattern, with an average speckle size approximately equal to the average size $\rho_c = (\lambda r_c)/d_o$ of speckles in the scattered field $E(\boldsymbol{\rho})$ (see Fig. 1.4). The intensity distribution $I(\boldsymbol{\rho})$ is called in the literature the *intensity hologram*.[11] One can show[11] that the intensity distribution in the image reconstructed with this hologram is $H(\boldsymbol{\delta}) \sim \int I(\boldsymbol{\rho}) \exp[(i2\pi\boldsymbol{\rho} \cdot \boldsymbol{\delta})/(\lambda_r z_i)] d\boldsymbol{\rho}$, where z_i is the distance between the hologram and the image plane, λ_r is the wavelength of the reconstruction radiation, and that the mean intensity distribution in the reconstructed image is the autocorrelation function of $k_i(\mathbf{r})$, $\langle H(\boldsymbol{\delta}) \rangle \sim \int k_i(\mathbf{r}) k_i(\mathbf{r} + \mu\boldsymbol{\delta}) d\mathbf{r}$. Here, $\boldsymbol{\delta}$ is the radius vector in the reconstructed image plane, and $\mu = r_c/z_i$ is a scaling factor.[11] The reconstructed

image is a speckle pattern with speckle size $\sim(\lambda_r z_i)/d_h$, where d_h is the hologram size. Figure 1.5 presents the reconstructed images of rough, flat, triangular-shaped objects for several hologram sizes.

We see that decreasing the hologram size leads to an increase in speckle size in the reconstructed image. The size of a reconstructed image is equal to twice the object size. In our case it is $\sim$20 mm. Intensity holography can be used as a simple method for obtaining data about remote objects in a turbulent atmosphere.[11] The image reconstructed with the help of intensity holography is the autocorrelation of the object image, which enables one to measure object size. It has a speckle pattern, with speckle size depending on the hologram size.

The parameter $C = [\langle I^2\rangle - \langle I\rangle^2]/\langle I\rangle^2$ describes relative intensity fluctuations for the scattered field (the blinking index or the contrast). In Ref. 29, the relation for the blinking index is given. References 31 and 32 contain expressions for the normalized intensity correlation function and the intensity contrast in the case of plane wave scattering by an infinite, flat, chaotic phase screen. This case is identical to the case of plane wave scattering by a flat rough object under the condition of normal incidence of the illuminating wave. In this case, phase modulation of the incident wave by the chaotic screen is equivalent to the modulation of the radiation due to its penetration into the hollows of the object's surface and the resulting phase shift variation, $\varphi(\mathbf{r}) \approx (4\pi/\lambda)\xi(\mathbf{r})$.

In Ref. 29, relations for the blinking index (contrast) of the intensity distribution in the scattered field in the Fresnel zone are given for the case of plane wave scattering by a flat rough object. In our notation,

$$C = \frac{1}{\lambda^2 r_c^2}\iiiint\left\langle \exp\left\{ i\frac{2\pi}{\lambda}\left[\xi(\mathbf{r}_1) - \xi(\mathbf{r}_2) + \xi(\mathbf{r}_3) - \xi(\mathbf{r}_4)\right]\right\}\right\rangle$$
$$\times \exp\left[i\frac{\pi}{\lambda r_c}\left(r_1^2 - r_2^2 + r_3^2 - r_4^2\right)\right] d\mathbf{r}_1 d\mathbf{r}_2 d\mathbf{r}_3 d\mathbf{r}_4.$$

As shown in Ref. 29, the blinking index is maximal at $r_c \approx \ell^2/\sigma$, and its maximum value is approximately $2\log_2(\sigma/\lambda)$. It is considerably different from unity if $\sigma/\lambda \gg 1$. Such a high blinking index causes an interesting effect of amplifying the

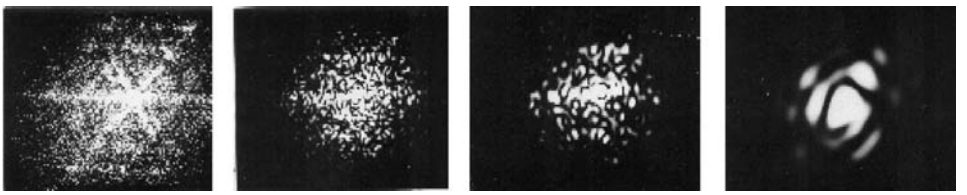

Figure 1.5 Reconstructed images of a rough, flat object of triangular shape. The distance from the object is $r_c = 2$ m, the distance from the image plane is $z_i = 2$ m, $\lambda = 0.63\,\mu$, the object size is $d_o \approx 10$ mm, and the hologram size from left to right is $d_h = 2$ mm, 1 mm, 510^{-2} mm, and 210^{-2} mm.

backscattered field.[40] This effect occurs when, for example, a narrow laser beam illuminates a sea wave. It can be explained by the focusing properties of this wave, which can be represented as a separate element of the wavy sea surface forming a lens with the focal distance $f \sim \ell^2/\sigma$.

The increase of the blinking index above unity is caused by the focusing effect of the scattering surface roughness. In fact, a single element of the rough surface can be approximately represented as a fragment of a collecting mirror with the diameter $d_f \sim \ell$ and bending approximately equal to σ; hence, its focus is of the order of ℓ^2/σ (see Appendix 5). At $r_c \gg \ell^2/\sigma$, intensity fluctuations, according to Ref. 29, correspond to $C = 1$. However, one can show that at $r_c \gg \ell^2/\sigma$, condition (1.42) is satisfied. It follows that if the correlation radius of surface roughness is smaller than the size of the scattering surface by more than one order of magnitude, then the blinking index (contrast) is close to unity; it is equal to

$$C \approx 1 + \frac{\ell^2}{S_\rho}. \tag{1.43}$$

1.4 Statistical characteristics of fields scattered by a moving object

The structure of a scattered field is rather complicated and cannot be fully described by means of a statistical approach, even in the case of radiation scattering by a fixed object with rough surface. In the general case, the scattering object can be moved and deformed simultaneously, so that both its mean surface and the deviations from this surface would vary in time. Here, even for a monochromatic source, the scattered field would have a complicated time dependence in addition to the time multiplier $\exp(i\omega t)$.

Let us first show that for velocities and deformation rates much smaller than the speed of light and for sufficiently small observation times, this field can be calculated by fixing certain positions of the object and calculating the fields scattered at each fixed position. This method is called the *quasi-static principle*.[12] Here, we restrict consideration to the statistical properties of fields scattered by a moving object illuminated by a pointlike monochromatic source with frequency ω_0. In Ref. 12, it was shown that under the condition when the relativistic phase shift is small,

$$\varphi_r = \frac{2\omega_0 v_c^2 T}{c^2} \ll 1, \tag{1.44}$$

where v_c is the velocity of the moving object's center of mass, and the field E scattered by this object at time t can be expressed as

$$E(\boldsymbol{\rho}, t) = \frac{\exp(i\omega_0 t)}{2\lambda r_c(t)} \int \frac{\mathbf{n}(t) \cdot \mathbf{q}(t)}{\mathbf{n}(t) \cdot \mathbf{N}(t)} k(u, v, t) E_i(u, v, t) \times \exp\left[-i \frac{w_0}{c} (|\mathbf{r}_\Sigma - \boldsymbol{\rho}_s| + |\mathbf{r}_\Sigma - \boldsymbol{\rho}|) \right] r_u(t) r_v(t) du dv, \tag{1.45}$$

where

$$\mathbf{q}(t) \approx -\frac{\mathbf{r}(t)-\boldsymbol{\rho}}{|\mathbf{r}(t)-\boldsymbol{\rho}|} - \frac{\mathbf{r}(t)-\boldsymbol{\rho}_s}{|\mathbf{r}(t)-\boldsymbol{\rho}_s|},$$

and

$$\mathbf{r}_\Sigma(u,v,t) = \mathbf{r}(u,v,t) + \mathbf{N}(u,v,t)\xi(u,v,t),$$

$\boldsymbol{\rho}_s$ is the radius vector of the source, $\mathbf{r}(u,v,t)$ is the radius vector of the mean surface, $\mathbf{N}(u,v,t)$ is the normal to the mean surface, $\xi(u,v,t)$ is the surface roughness height distribution, namely, random deviations from the mean surface along the normal [see Eq. (1.1)], and $E_i(u,v,t)$ is the illuminating source field amplitude on the object's surface.

The condition (1.44) is of relativistic origin but can manifest itself at rather low velocities. This can be demonstrated with a simple example. Let the object under study move from (or to) the source and an observer situated near the source, with the constant velocity v_c. One can show[12] that the phase variation of the field scattered by this object is $\varphi(t) = (2v_c t\omega_o)/c + (2v_c^2 t\omega_o)/c$. The first term determines the Doppler frequency shift $\nu_d = 2v_c/\lambda$. We shall discuss this term later. The second term has a relativistic origin. If, for instance, $v_c = 1$ m/s for the observation time $T \ll (\lambda c)/v_c^2 \approx 1.5$ s, then the relativistic term $\varphi_r \ll \pi$. It has practically no influence on the phase time variation. Yet, this example also shows that for a sufficiently long observation time, relativistic effects can make a considerable contribution to the time variation of the observed field even for velocities much slower than the speed of light. In this example, the observation time should be of the order of 1 s. At rather high velocities, relativistic effects can be easily observed, as one can see from Eq. (1.44), even at very short observation times. In the example considered here, at $v_c \sim 10^4$ m/s and $T \sim 10^{-6}$ s, the relativistic term is $\varphi_r \approx \pi$.

In what follows, we consider the condition (1.44) to be satisfied. Then, expression (1.45) gives a quasi-static approximation of the field E scattered by the moving object.[12] Let us discuss its physical essence (Fig. 1.6). Comparing relations (1.44) and (1.27), we can make the following conclusion: at sufficiently short observation time, when displacement of each point of the moving object is so small that the inequality (1.44) holds, then the scattered field at time t can be calculated just as the field scattered by an object fixed in the position it occupies at t. Figure 1.6 shows two fixed positions of the object (a moving solid) at moments t_1 and t_2.

For $\xi(u,v,t) \ll \rho \ll r_c$, we get

$$\begin{aligned} E(\boldsymbol{\rho},t) = \frac{\exp(i\omega_0 t)}{2\lambda r_c(t)} \int \frac{\mathbf{n}(t)\cdot\mathbf{q}(t)}{\mathbf{n}(t)\cdot\mathbf{N}(t)} k(u,v,t) E_i(u,v,t) \\ \times \exp\left[-i\frac{2\pi}{\lambda}(|\mathbf{r}-\boldsymbol{\rho}_s| + |\mathbf{r}-\boldsymbol{\rho}|)\right] \\ \times \exp\left[i\frac{2\pi}{\lambda}\mathbf{q}(t)\cdot\mathbf{N}(t)\xi(u,v,t)\right] r_u(t) r_v(t)\,du\,dv, \end{aligned} \tag{1.46}$$

where $r_c(t)$ is the radius vector of the object's center of mass (see Fig. 1.6).

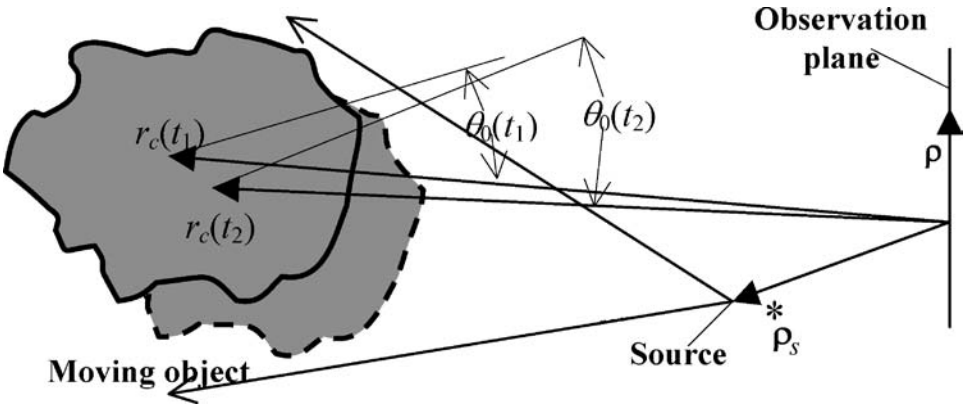

Figure 1.6 The physical essence of the quasi-static approximation for the field E scattered by a moving solid body rotating around its center of mass with the stable axis perpendicular to the figure plane ($\varphi_0(t) = 0$). The solid line shows the position of the object at moment t_1 of observing the scattered field. Dashed line is the object position at time moment t_2. $\theta_0(t_1)$ and $\theta_0(t_2)$ are the rotation angles at moments t_1 and t_2. Here, $\varphi_0(t)$ and $\theta_0(t)$ describe rotations of the solid body around its center of mass. $r_c(t_1)$ and $r_c(t_2)$ are positions of the center of mass at moments t_1 and t_2.

Consider expression (1.46) in the case of a short observation time T of the scattered field, when $T \ll \sqrt{\lambda/a(u,v,t_0)}$, with $a(u,v,t_0)$ being the acceleration of a small object surface part at point (u,v) and t_0 being the initial time of observing the scattered field. Taking into account the relation

$$\left.\frac{d[|\mathbf{r}(t)-\boldsymbol{\rho}|+|\mathbf{r}(t)-\boldsymbol{\rho}_s|]}{dt}\right|_{t=t_0} = \mathbf{v}(t_0)\cdot\mathbf{q}(t_0),$$

which can be easily verified, we obtain

$$\begin{aligned} E(\boldsymbol{\rho},t) = {} & \frac{\exp(i\omega_0 t)}{2\lambda r_c(t_0)}\int \frac{\mathbf{n}(t_0)\cdot\mathbf{q}(t_0)}{\mathbf{n}(t_0)\cdot\mathbf{N}(t_0)} k(u,v,t_0)E_i(u,v,t_0)\exp[-i\nu_d(t-t_0)] \\ & \times \exp\left[i\frac{2\pi}{\lambda}(|\mathbf{r}(t_0)-\boldsymbol{\rho}|+|\mathbf{r}(t_0)-\boldsymbol{\rho}_s|)\right] \\ & \times \exp\left[i\frac{2\pi}{\lambda}\mathbf{q}(t_0)\cdot\mathbf{N}(t_0)\xi(u,v,t_0)\right] r_u(t_0)r_v(t_0)dudv. \end{aligned} \tag{1.47}$$

Here,

$$\nu_d(u,v,t_0) = \frac{[\mathbf{v}(u,v,t_0)\cdot\mathbf{q}(u,v,t_0)]}{\lambda}$$

is the distribution of Doppler frequencies over the object surface at the initial time of observing the scattered field t_0. This distribution is determined by small time

variations of the phases of coherent radiation scattered by small parts of the object surface as the radiation propagates from the source to surface parts and from the surface parts to the observer. In the foregoing, we considered the simple case of a field scattered by an object moving toward the observer with velocity v_c. In this case, $\nu_d = 2v_c/\lambda$.

Let us analyze the statistical characteristics of fields scattered by moving objects. We start from the scattered field averaged value. In this case, using the relation

$$\langle \exp(-i\varphi) \rangle = \int_{-\infty}^{\infty} \exp(-i\alpha\varphi) w_1(\varphi) d\varphi = \exp\left(-\frac{\sigma_\varphi^2}{2}\right),$$

we obtain

$$\begin{aligned} \langle E(\boldsymbol{\rho}, t) \rangle \approx \frac{\exp(i\omega_0 t)}{2\lambda r_c(t)} \int \frac{\mathbf{n}(t) \cdot \mathbf{q}(t)}{\mathbf{n}(t) \cdot \mathbf{N}(t)} k(u, v, t) E_i(u, v, t) \\ \times \exp\left[-i\frac{2\pi}{\lambda}(|\mathbf{r} - \boldsymbol{\rho}_s| + |\mathbf{r} - \boldsymbol{\rho}|)\right] \\ \times \exp\left[-\left(\frac{2\pi\sigma q_N}{\lambda}\right)^2\right] r_u(t) r_v(t) du dv. \end{aligned} \tag{1.47a}$$

We see from this relation that the mean value of the field scattered by a moving rough object with $q_N\sigma \gg \lambda$ very rapidly tends toward zero with an increase of the ratio σ/λ. The same result can be obtained for the field scattered by a fixed rough object with $q_N\sigma \gg \lambda$ [see relation (1.33)].

Let us consider this expression for a flat, square, rough object moving parallel and at a small angle α to the observation plane with constant velocity v_c, under the condition that the illuminating source and the observation point are placed at the center of the laboratory frame of reference and in the Fresnel zone with respect to the object (Fig. 1.7). In this case, $\boldsymbol{\rho}_s = \boldsymbol{\rho} = 0$, and

$$\begin{aligned} \langle E(\boldsymbol{\rho}, t) \rangle \approx \frac{\exp(i\omega_0 t)}{2\lambda r_c(t)} \exp\left[-\left(\frac{4\pi\sigma}{\lambda}\right)^2\right] \\ \times \int_{-d_o/2}^{d_o/2} \int_{-d_o/2}^{d_o/2} k(x, y) E_i(x - v_c t, y) \exp\left(-i\frac{4\pi x\alpha}{\lambda}\right) dx dy, \end{aligned}$$

where α is the angle between the plane and the axis, d_o is the size of the illuminated surface of the object, and $E_i(x, y)$ is the distribution of the illuminating radiation amplitude on an illuminated surface. If this distribution is constant over the object's surface, then the scattered field has no time dependence except $\exp(i\omega_0 t)$. This means that such motion does not lead to the Doppler shift.

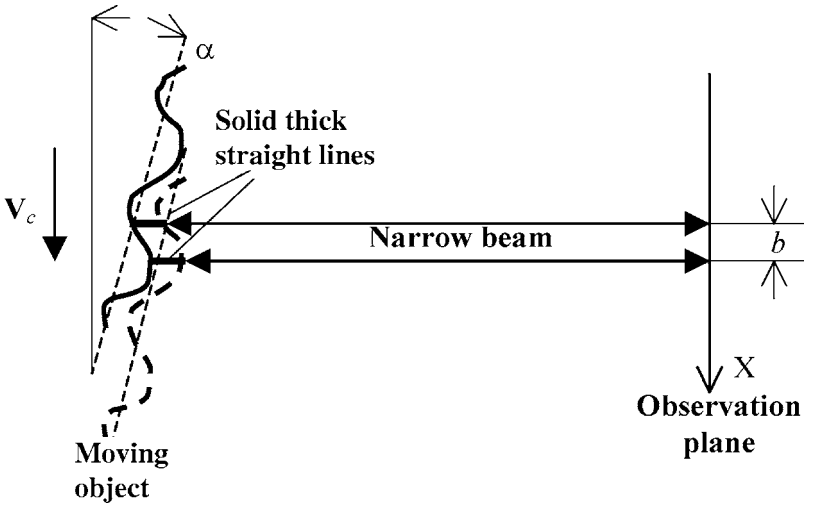

Figure 1.7 Backscattering of the coherent field by a moving rough object with a flat mean surface. The thick dashed curve is the object's surface position at moment t. The two dashed parallel lines show the changing beam path in the course of the object's motion.

The situation is different if this amplitude is limited. Suppose, for example, that the object is illuminated by a very narrow Gaussian beam with width $b < \lambda/\alpha$, and with

$$E_i(x) = E_i(0)\exp\left(-\frac{x^2}{b^2}\right),$$

where E_s is the amplitude of the illuminating source. Then,

$$\langle E(t)\rangle \approx \frac{d_o b\exp(i\omega_0 t)E_i}{2\lambda r_c(t)}\exp\left(-\frac{4\pi^2 b^2\alpha^2}{\lambda^2}\right) \times \exp\left[-\left(\frac{4\pi\sigma}{\lambda}\right)^2\right]k(v_c t)\exp\left(-i\frac{4\pi v_c t\alpha}{\lambda}\right).$$

This result shows that for a moving object illuminated by a narrow beam, the scattered field has a frequency shift equal to $(2v_c t\alpha)/\lambda$ even if the object moves orthogonally to the illuminating beam. It follows that due to the motion of the object, the illuminating beam hits different parts at different distances from the observer, which leads to a variation of the phase shifts in the radiation scattered by the object.

Let us proceed to the analysis of the scattered field correlation function,

$$B(\boldsymbol{\rho}_1, t_1, \boldsymbol{\rho}_2, t_2) = \langle E(\boldsymbol{\rho}_1, t_1)E(\boldsymbol{\rho}_2, t_2)\rangle - \langle E(\boldsymbol{\rho}_1, t_1)\rangle\langle E(\boldsymbol{\rho}_2, t_2)\rangle.$$

We will consider it for the case of rather large-scale surface roughness, where $q_N\sigma = \mathbf{q}\cdot\mathbf{N}\sigma \gg \lambda$ [see relation (1.47a)]. Then, the mean value $\langle E(\boldsymbol{\rho}, t)\rangle$ of the

field E scattered by the moving rough object is close to zero, and

$$B(\boldsymbol{\rho}_1, t_1, \boldsymbol{\rho}_2, t_2) \approx \langle E(\boldsymbol{\rho}_1, t_1) E^*(\boldsymbol{\rho}_2, t_2)\rangle.$$

Assume that the surface roughness is isotropic ($\ell_u = \ell_v = \ell$), and also suppose that the following conditions are satisfied:

$$\frac{\sigma}{\ell} \gg \frac{d_\rho}{r_c}, \frac{d_o}{r_c}, \sqrt{\frac{\lambda}{r_c}},$$

and

$$\Delta t = t_1 - t_2 \ll \frac{\sigma^2}{\ell^2}\left[\frac{\partial(\mathbf{r}_u\mathbf{q})}{\partial t}\right]^{-1}, \frac{\sigma^2}{\ell^2}\left[\frac{\partial(\mathbf{r}_v\mathbf{q})}{\partial t}\right]^{-1}, \frac{\lambda}{\sigma}\left[\frac{\partial(\mathbf{q}\mathbf{N})}{\partial t}\right]^{-1}, \frac{\lambda r_c}{v_c d_\rho}, \frac{\lambda r_c}{v_c d_o},$$

where Δt is the time interval of the correlation function formation. Then, in the quasi-static approximation, allowing us to calculate $E(\boldsymbol{\rho}_1, t_1)$ and $E^*(\boldsymbol{\rho}_2, t_2)$ from relation (1.46), for an arbitrarily deformed and moving object, under the condition that the mean surface of the object has nearly constant orientation during the time interval Δt, we obtain the correlation function in the form

$$\begin{aligned} B(\boldsymbol{\rho}_1, t_1, \boldsymbol{\rho}_2, t_2) &= \langle E(\boldsymbol{\rho}_1, t_1) E^*(\boldsymbol{\rho}_2, t_2)\rangle \\ &= \frac{\ell^2}{\sigma^2 r_c^2} \exp[i\omega_0(t_1 - t_2)] \iint k_i(u, v, t_1) |E_i(u, v, t_1)|^2 \\ &\quad \times \exp i\psi(u, v, t_1) \exp[i2\pi\nu_d(t_2 - t_1)] r_u^2(t_1) r_v^2(t_1) du dv, \quad (1.48) \end{aligned}$$

where $\psi(u, v, t) = 2\pi/\lambda(|\mathbf{r}(u, v, t) - \boldsymbol{\rho}_1| - |\mathbf{r}(u, v, t) - \boldsymbol{\rho}_2|)$, $\mathbf{r}(u, v, t)$ is the radius vector of the instant mean object surface at time t, $\nu_d = (\mathbf{v} \cdot \mathbf{q})/\lambda$, and $\mathbf{v}(u, v, t)$ is the vector of instantaneous velocity of a point (u, v) on the mean surface.

For the case of a moving solid nondeformable body (see Fig. 1.6), it is convenient to rewrite the correlation function of the field scattered by this object in spherical coordinates, with the origin at the center of mass of the solid body:

$$\begin{aligned} B(\boldsymbol{\rho}_1, t_1, \boldsymbol{\rho}_2, t_2) &= \langle E(\boldsymbol{\rho}_1, t_1) E^*(\boldsymbol{\rho}_2, t_2)\rangle \\ &= \frac{\ell^2}{\sigma^2 r_c^2} \exp[i\omega_0(t_1 - t_2)] \iint k_i(\theta, \varphi, t_1) |E_i(\theta, \varphi, t_1)|^2 \\ &\quad \times \exp i\psi(\theta, \varphi, t_1) \exp[i2\pi\nu_d(t_1)(t_2 - t_1)] R^2(\theta, \varphi) \cos^2\theta d\theta d\varphi, \end{aligned} \quad (1.48a)$$

where

$$\nu_d(t) = \frac{[\mathbf{v}(\theta, \varphi, t) \cdot \mathbf{q}(\theta, \varphi, t)]}{\lambda}, \ \mathbf{v}(\theta, \varphi, t) = \mathbf{v}_c(t) + \{\boldsymbol{\Omega} \times [\mathbf{r}(t) - \mathbf{r}_c(t)]\}$$

is the instantaneous velocity of the point on the solid-body surface; $\mathbf{\Omega}(t)$ is the vector of instantaneous angular velocity of the solid body; $\mathbf{v}_c(t)$ is the instantaneous velocity of the solid body's center of mass; R, θ, and φ are spherical coordinates of the solid body's surface; $\varphi_0(t)$ and $\theta_0(t)$ describe the rotations of the solid body around its center of mass (Fig. 1.6);

$$\psi(u, v, t) = \left(\frac{2\pi}{\lambda}\right)(|\mathbf{r}(\theta, \varphi, t) - \boldsymbol{\rho}_1| - |\mathbf{r}(\theta, \varphi, t) - \boldsymbol{\rho}_2|),$$

$$\mathbf{r}(t) = \mathbf{r}(\theta, \varphi, t) = (X, Y, Z),$$

$$X = R(\theta, \varphi)\sin[\theta + \theta_0(t)]\cos[\varphi + \varphi_0(t)] + x_c(t),$$

$$Y = R(\theta, \varphi)\sin[\theta + \theta_0(t)]\sin[\varphi + \varphi_0(t)] + y_c(t),$$

and

$$Z = R(\theta, \varphi)\sin[\theta + \theta_0(t)] + z_c(t)$$

are components of the radius vector of the instant mean object surface at time t; and $x_c(t)$, $y_c(t)$, $z_c(t)$ are components of the radius vector $\mathbf{r}_c(t)$.

Expression (1.48a) transforms into expression (1.36) for the correlation function of the field scattered by a fixed object. If $\mathbf{v}(\theta, \varphi, t) \neq 0$, with the increase of the time interval $\Delta t = t_1 - t_2$, the correlation function $B(\boldsymbol{\rho}_1, t_1, \boldsymbol{\rho}_2, t_2)$ of the field scattered by the moving solid body rapidly decreases; and after a rather large time interval, full decorrelation results. The correlation time is given by

$$t_c = \frac{1}{I(\boldsymbol{\rho}, t)} \int_{t_0}^{t_0+T} \langle E(\boldsymbol{\rho}, t)E^*(\boldsymbol{\rho}, t_1)\rangle dt_1,$$

where $I(\boldsymbol{\rho}, t) = |E(\boldsymbol{\rho}, t)|^2$.

Let us consider two examples. In the first example, a flat, rough, square object placed in the Fresnel zone moves along the X axis orthogonally to the beam illuminating the object as a whole, and the observer is close to the source. In this case, where E_i and k are constant, it follows from Eq. (1.48a) that

$$\begin{aligned} B(\boldsymbol{\rho}_1, t_1, \boldsymbol{\rho}_2, t_2) &= \langle E(\boldsymbol{\rho}, t_1)E^*(\boldsymbol{\rho}, t_2)\rangle \\ &= \frac{|E_i|^2\ell^2}{\sigma^2} \int_{-d_o/2}^{d_o/2} \int_{-d_o/2}^{d_o/2} |k(x, y)|^2 \exp\left[i\frac{4\pi x v_c(t_2 - t_1)}{\lambda r_c}\right] dxdy \\ &= \frac{|E_s|^2\ell^2 d_o^2}{\sigma^2 r_c^2} \sin c\left[\frac{2\pi d_o v_c(t_2 - t_1)}{\lambda r_c}\right], \end{aligned} \tag{1.49}$$

where v_c is the object velocity, and r_c is the distance from the object.

From the last expression, one can easily see that the correlation time is $t_c \approx (\lambda r_c)/(d_o v_c)$. One can see from this relation that a complete decorrelation occurs as the object is displaced by $\Delta x_c = v_c(t_1 - t_2) = \rho_c \approx (\lambda r_c)/d_o$, where ρ_c is the correlation radius of the field scattered by a fixed square object [see Eq. (1.40a)]. Such a decorrelation can be explained by comparing Eq. (1.47) with Eq. (1.37) for the correlation function of the field scattered by a fixed object but observed at different points in space $\boldsymbol{\rho}_1$ and $\boldsymbol{\rho}_2$ [see Fig. 1.8(a)]. One can show that at small displacements Δx of the solid body and for small distances $|\boldsymbol{\rho}_1 - \boldsymbol{\rho}_2|$ between the observation points, these relations have a similar structure. This means that a field scattered by a moving object and registered by a fixed observer at space points $\boldsymbol{\rho}_1$ and $\boldsymbol{\rho}_2$ varies the same way as the field scattered by a fixed object but registered by an observer moving with velocity v_o. If $v_o = v_c$ and $|\boldsymbol{\rho}_1 - \boldsymbol{\rho}_2| = \Delta x$, relations (1.37) and (1.47) become identical. As a result, displacement of the object causes a simultaneous displacement of the scattered field and of its speckle pattern. Hence, the correlation time t_c is the time of this displacement by a distance equal to the size of the correlation radius ρ_c of the field scattered by fixed object. This displacement is equal to the speckle size $d_r \approx (\lambda r_c)/d_o$ [see (1.40a)]. Therefore,

$$t_c = \frac{d_r}{v_c} \approx \frac{\lambda r_c}{d_o v_c}.$$

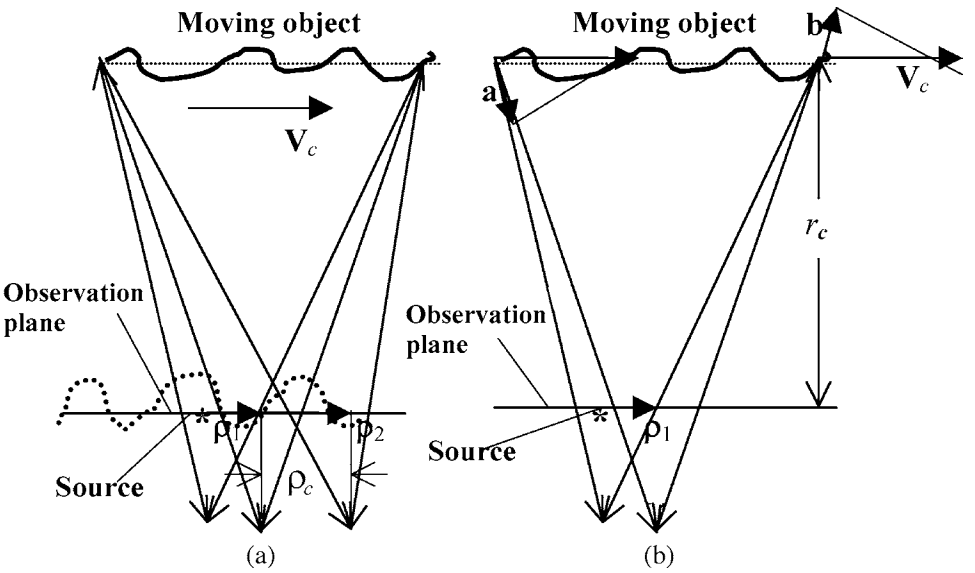

Figure 1.8 Two explanations of the correlation time $t_c \approx (\lambda r_c)/(d_o v_c)$ of the field scattered by a moving object: (a) the correlation time is the time of the scattered field displacement at the distance equal to the speckle size $\rho_c \approx (\lambda r_c)/d_o$ (the dashed line is the speckle pattern formed by the fixed object); (b) the correlation time is determined by the spread $\Delta\nu_d = (a + b)/\lambda$ of the Doppler frequencies: $t_c \approx 1/\Delta\nu_d$. Here, **a** and **b** are projections of the vector $\mathbf{v}_c$ on lines connecting the edge points of the object, with the observer placed at point $\boldsymbol{\rho}_1$.

Another explanation of the correlation time $t_c \approx (\lambda r_c)/(d_o v_c)$ of the field scattered by a moving object is based on the spread of the Doppler frequencies caused by the object's motion. This spread is $\Delta\nu_d = (\mathrm{a}+\mathrm{b})/\lambda$, where a and b are projections of the vector $\mathbf{v}_c$ on lines connecting the edge points of the object with the observer placed at point $\boldsymbol{\rho}_1$. From Fig. 1.8(b) it is easy to see that $\mathbf{a}+\mathbf{b} \approx (\mathbf{v}_c d_o)/r_c$. Hence, $\Delta\nu_d \approx (d_o v_c)/(\lambda r_c)$, and the correlation time of the scattered field is $t_c = 1/\Delta\nu_d \approx (\lambda r_c)/(d_o v_c)$.

In the second example, a flat, square, rough object placed in the Fresnel zone rotates around a fixed axis parallel to the observation plane (Fig. 1.9). In this case, if the observer is placed adjacent to the illuminating source and $E_i(x,y)$ and $k(x,y)$ are constant, it follows from Eq. (1.48a) that

$$\langle E(\boldsymbol{\rho},t_1)E^*(\boldsymbol{\rho},t_2)\rangle = \frac{\ell^2}{\sigma^2}\int\limits_{-d_o/2}^{d_o/2}\int\limits_{-d_o/2}^{d_o/2}|E_i(x,y)k(x,y)|^2\exp\left[i\frac{4\pi x\Omega(t_2-t_1)}{\lambda}\right]dxdy$$

$$= \frac{|E_i(0,0)k(0,0)|^2\ell^2 d_o^2}{\sigma^2 r_c^2}\sin c\left[\frac{2\pi d_o\Omega(t_1-t_2)}{\lambda}\right]. \qquad (1.50)$$

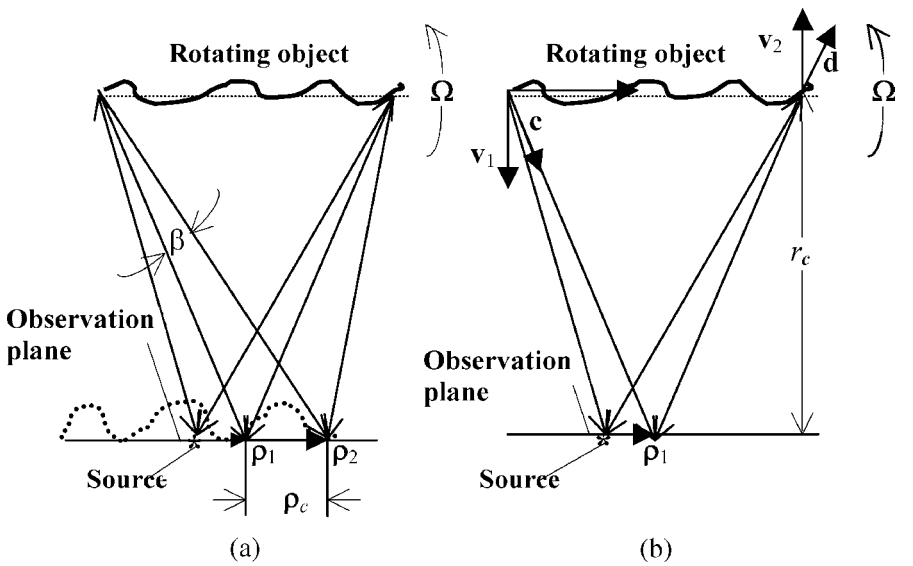

Figure 1.9 Two explanations of the correlation time $t_c \approx \lambda/(d_o\Omega)$ of the field scattered by a rotating object. In (a) the correlation time is the time of the scattered field rotation by angle λ/d_o, which is equal to the speckle angular size $\beta_c \approx \rho_c/r_c$; in (b) the correlation time is the time determined by the spread $\Delta\nu = (\mathrm{c}+\mathrm{d})/\lambda$ of the Doppler frequencies: $t_c \approx 1/\Delta\nu_\Omega$. Here, c and d are projections of the vectors $\mathbf{v}_1$ and $\mathbf{v}_2$ of the edge points of the rotating object on lines connecting these points, with the observer placed at point $\boldsymbol{\rho}_1$.

From this expression, we see that a complete decorrelation occurs as the object rotates by the angle $\Delta\alpha_c = \Omega(t_1 - t_2)$ equal to $\rho_c/r_c = \lambda/d_o$, where $\rho_c = (\lambda r_c)/d_o$ is the correlation radius ρ_c of the field scattered by a stable square object placed at distance r_c. Hence, $\Delta\alpha_c$ is equal to the angular size β of the speckle in this field [see Eq. (1.40a)]. Such a decorrelation can be explained by comparing Eq. (1.48) with relation (1.37) for the correlation function of fields scattered by a fixed object but observed in different directions [see Fig. 1.9(a)], which can be rewritten as

$$\langle E(\boldsymbol{\rho}_1, t)E^*(\boldsymbol{\rho}_2, t)\rangle \sim \operatorname{sinc}\left[\frac{2\pi d_o \Delta\psi}{\lambda}\right], \tag{1.51}$$

where $\Delta\psi$ is the angle between the directions. If the observer moves relative to the fixed object with the angular velocity Ω, $\Delta\psi = \Omega(t_1 - t_2)$, the correlation function of the field scattered by the fixed object and observed at different points $\boldsymbol{\rho}_1$ and $\boldsymbol{\rho}_2$ coincides, after replacing $|\boldsymbol{\rho}_1 - \boldsymbol{\rho}_2|/r_c = \Delta\psi$, with correlation function (1.50). One can also see that rotation of the object leads to a decorrelation of the scattered fields, and displacement of the observer synchronously to this rotation leads to the same decorrelation of the fields scattered by a fixed object. Hence, decorrelation can be interpreted as a complete change of fields caused by the rotation of the scattered field as a whole by the angle β_c, and the correlation time of the scattered field is $t_c \approx \beta_c/\Omega = \lambda/(d_o\Omega)$.

Another explanation of the correlation time t_c of the field scattered by the rotating object consists of the spread of the Doppler frequencies caused by the object rotation [see Fig. 1.9(b)]. This spread is $\Delta\nu_d = (\mathrm{c} + \mathrm{d})/\lambda$, where c and d are projections of the vector velocities $\mathbf{v}_1$ and $\mathbf{v}_2$ of the edge points of the object on the lines connecting these points, with the observer placed at point $\boldsymbol{\rho}_1$. From Fig. 1.9(b) it is easy to see that $\mathrm{c} + \mathrm{d} \approx \Omega d_o$. Hence, $\Delta\nu_d \approx (d_o\Omega)/\lambda$, and the correlation time of the scattered field is $t_c = 1/\Delta\nu_d \approx \lambda/(d_o\Omega)$.

Consider now how illuminating a moving object by a narrow beam affects the correlation function of the field scattered by the object. In order to find out the physical origin of this effect, it is reasonable to consider it in the case of a flat square object moving parallel to the observation plane with velocity v_c. Let the object be illuminated by a beam directed normal to the object surface. In this case, from the relation

$$\langle (E(\boldsymbol{\rho}, t_1)E^*(\boldsymbol{\rho}, t_2)\rangle = \left(\frac{\ell^2}{\sigma^2}\right)\iint |E_i(x,y)k(x,y)|^2 \exp\left[i\frac{2\pi x \mathrm{v}_c(t_2 - t_1)}{\lambda r_c}\right]dxdy,$$

where $\boldsymbol{\rho}$ is the radius vector of the observer, we obtain, for the case of a Gaussian illuminating beam, $E_i(x,y) = E_i(0,0)\exp(-x^2/b^2)$, where b is the beam width under conditions $(\lambda\ell)/\sigma \ll b \ll d_o$,

$$\langle |E(\boldsymbol{\rho}, t_1)E^*(\boldsymbol{\rho}, t_2)|\rangle = \frac{|E_i(0,0)k(0,0)|^2\ell^2 d_o b}{\sigma^2 r_c^2}\exp\left\{-\left[\frac{\pi \mathrm{v}_c(t_1 - t_2)b}{\lambda r_c}\right]^2\right\}. \tag{1.52}$$

We see from this equation that in this case, the correlation time $t_c \approx (\lambda r_c)/(2bv_c)$. Comparing Eq. (1.52) with relation (1.49), one can see that in the considered case, the correlation time increases with a decrease of the illuminating beam width.

1.5 Conclusions

1. For the description of a rough object surface, it is convenient to consider a smooth, deterministic average (mean) surface and a random, nonsmooth surface differing from the mean surface by a small value. Deviations from the mean surface are called the object surface roughness height. The roughness height distribution is a space–time random process, which can be represented by a Gaussian probability density function. Each realization of roughness height is determined by four parameters: the standard deviation, σ; correlation radii in orthogonal directions, ℓ_u and ℓ_v; and the correlation time, τ_0.
2. The field scattered by a rough surface can be described by the Kirchhoff approximation and in terms of local plane waves incident at each surface point and reflected from the tangential plane at the same point. As a rule, the field in the observation plane is the sum of two random processes, the noise field and the field scattered by rough surfaces.
3. A sufficiently complete description of this field can be given by the Gaussian probability density function. Each realization of the field scattered by rough surfaces is determined by the shape of the mean surface as well as by the four parameters characterizing the random surface: the standard deviation, σ; correlation radii of the object surface roughness height in orthogonal directions, ℓ_u and ℓ_v; and the correlation time, τ_0, of the object surface roughness height.
4. The average intensity of the field scattered by a rough surface is determined by the shape of the mean surface, the standard deviation σ, and the correlation radii of roughness height in orthogonal directions, ℓ_u and ℓ_v. The correlation radii of the scattered field in the orthogonal directions on the observation plane, ρ_{cx} and ρ_{cy} (the average dimensions of a single speckle in the scattered field), are inversely proportional to the dimensions of the object scattering area in the same directions. Relative fluctuations (also called the contrast or blinking index) of the intensity of the field scattered by a rough surface in the vicinity of the object surface can exceed unity. Far from the surface, the contrast is close to unity.
5. Intensity of the field scattered by a rough surface is the object intensity hologram. Intensity holography can be used as a simple method for obtaining data about remote rough objects in a turbulent atmosphere.[11] The object pattern reconstructed with the help of an intensity hologram is described by the autocorrelation function of the intensity distribution in the object's undistorted image, which, in particular, allows one to measure object size. The reconstructed pattern has a speckle structure, where the speckle size depends on the hologram size.
6. When an object moves at sufficiently low velocity compared to the speed of light, which is usually the case in practice, the quasi-static principle is

realized: the field scattered by a moving object at each moment is the same as if the object were stationary.

7. The space–time correlation function and the correlation time t_c for a field scattered by a moving rough object have a rather complicated dependence on the object's motion, the shape of its surface, and the intensity distribution for the illuminating radiation. In particular, for the case of a rotating object and constant intensity distribution of the illuminating radiation on the object surface, the field correlation time is determined by the ratio of the scattered field correlation radius to the angular rotation rate.

Chapter 2

Statistical Description of Coherent Images

2.1 Introduction

In this chapter, we use the models of coherent fields scattered by extended objects, which were studied in Chapter 1, for the statistical description of coherent images. According to our definition, an image will be called coherent if each point of it is formed by interfering contributions of all waves coming from the smallest part of the object's surface that is resolvable by the imaging system. In this case, a speckle pattern is formed in the image plane. The conditions for the formation of coherent images will be considered in detail in Sec. 2.5. We consider the general theory of remote object coherent imaging, which takes into account the correlation properties of roughness height distribution on the object's surface as well as the spectrum $S_r(\omega)$ of the illuminating radiation. The interest in coherent images lies in their wide use in remote sensing,[12] and because the formation of coherent images provides the most complete information about an object in the presence of additional noise. This was first shown in Ref. 11 from the viewpoint of the theory of statistical decisions, by means of processing the fields scattered by rough objects and calculating the probability density function for these fields (see Sec. 1.2).

In most works on coherent images, one considers flat rough objects placed on the axis of the optical system (the lens), which forms coherent images in monochromatic light. At each point of the image, the field is assumed to have Gaussian distribution. However, in practice, the objects are usually not flat and their positions with respect to the optical system are arbitrary. In addition, sometimes it is necessary to use images formed in quasi-monochromatic light. For these reasons, one should take into account that the correlation properties of the object surface and the spectral properties of the illuminating source influence the properties of coherent images. In this chapter, this influence is studied in detail, which provides a more accurate and complete description of coherent images of objects with arbitrary shapes. In particular, the contrast and the correlation radius of the speckle patterns are defined more accurately. If the imaging system resolves the object surface roughness, then, as we will show, the field distribution in the coherent image is essentially non-Gaussian. We dealt with such deviations in the previous chapter when we analyzed fluctuation characteristics of the scattered radiation in the case of illumination with a narrow monochromatic beam. Deviations from Gaussian

statistics are related to certain peculiarities in the fluctuation and correlation properties of images, which also will be considered in detail below. This chapter is closely connected with Appendix 5, where detailed semi-qualitative explanations of speckle pattern formation in the images of rough objects are given and calculations for the contrast are presented.

2.2 Statistical properties of fields in coherent images

In this section, we analyze the statistical properties of coherent images of nonflat objects formed by their illumination by pointlike monochromatic sources. The following characteristics will be studied: the first, second, third, and fourth moments of real and imaginary parts of the fields in the image, and the first and second moments of the intensity distribution in the image. Much of the analysis will be devoted to coherent images of flat rough objects since they provide an explicit example of using coherent images for remote sensing. To start, we will analyze the field in a coherent image and the mean value of this field. Using relations (1.24)–(1.28) and the Kirchhoff approximation, we can write the field in a coherent image in the form[12] (see Fig. 2.1)

$$E(\boldsymbol{\delta}) = A_i \int \frac{\mathbf{n}\cdot\mathbf{q}}{\mathbf{n}\cdot\mathbf{N}} k(\mathbf{r}) \exp\left[i\frac{2\pi}{\lambda}\mathbf{q}\cdot\mathbf{N}\xi(\mathbf{r})\right] \exp\left[i\frac{2\pi(|\mathbf{r}-\boldsymbol{\rho}_s|+\mathbf{r})}{\lambda}\right] h_\omega(\mathbf{r},\boldsymbol{\delta})d\mathbf{r}, \tag{2.1}$$

where $\mathbf{q} = -\boldsymbol{\nu}_i + \boldsymbol{\nu}_o$, with $\boldsymbol{\nu}_i = (\mathbf{r}-\boldsymbol{\rho}_s)/|\mathbf{r}-\boldsymbol{\rho}_s|$, $\boldsymbol{\nu}_o = -(\mathbf{r}-\boldsymbol{\rho})/|\mathbf{r}-\boldsymbol{\rho}|$, $\boldsymbol{\delta}$ is the radius vector in the image plane, $\mathbf{r} = \mathbf{r}(u, v)$ is the radius vector of the mean surface of the object, $\xi(\mathbf{r})$ is the distribution of surface roughness height, $\boldsymbol{\rho}_s$ is the radius vector of the illuminating monochromatic pointlike source, $A_i = [(S_\rho E_i)/(\lambda^2 r_c z_i)]$, $E_i = (E_s S_s)/(\lambda r_c)$ is the amplitude of the illuminating radiation on the object under study, E_s is the source amplitude, S_s is the source area, $r_c = |\mathbf{r}_c|$, $\mathbf{r}_c$ is the radius vector of the object's center of mass, z_i is the distance from the imaging system aperture plane to the image plane, which satisfies the lens formula $1/r_c + 1/z_i =$

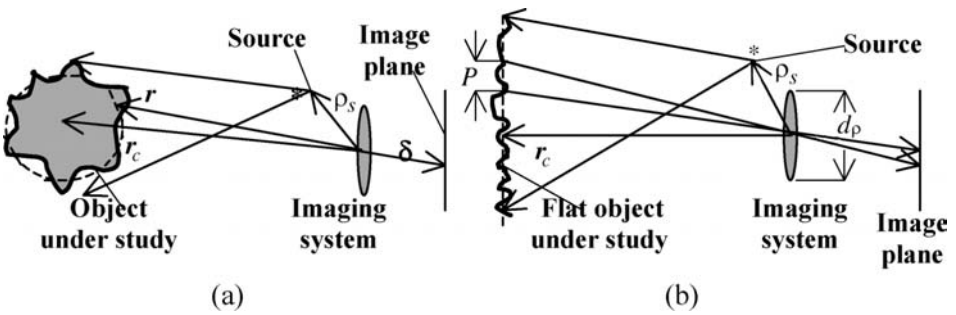

Figure 2.1 Geometry of image formation. The dashed line is the mean surface of the rough object. $P_r = (r_c\lambda)/d_\rho$ is the size of the minimally resolved domain on the object surface.

$1/f$, $\lambda = (2\pi c)/\omega$, f is the imaging system focal length, and

$$h_\omega(\mathbf{r}, \delta) = \frac{1}{S_\rho} \int \Lambda(\boldsymbol{\rho}) \exp\left[i \frac{\omega}{c} \boldsymbol{\rho} \cdot \left(\frac{\mathbf{r}}{r_c} + \frac{\delta}{z_i} \right) \right] d\boldsymbol{\rho} \tag{2.2}$$

is the pulse response of the imaging system describing the field distribution in the image of a single point of the object at the frequency of the illuminating source. In Eq. (2.2), $\Lambda(\boldsymbol{\rho})$ is the pupil function. Integration in Eq. (2.1) runs over the illuminated surface of the object, and integration in Eq. (2.2) runs over the imaging system aperture with the area S_ρ.

Let us demonstrate explicitly how the statistical properties of an object, including correlations between different surface points, influence the statistical characteristics of coherent images. We begin the analysis by considering the image of a simple rough object that has a flat mean surface orthogonal to the axis of the imaging system.[34] The pointlike illuminating source is placed almost exactly at the center of the imaging system aperture ($\boldsymbol{\rho}_s = 0$). At first we assume that the imaging system does not resolve separate elements of the rough surface of the object and the object is illuminated by a plane wave propagating along the imaging system axis. Then, the following relation holds:

$$E(\delta) = A_i \int k(\mathbf{r}) \exp[i\varphi(\mathbf{r})] \exp\left[i \left(\frac{4\pi r}{\lambda} \right) \right] h_\omega(\mathbf{r}, \delta) d\mathbf{r},$$

where $\varphi(\mathbf{r}) = (4\pi\xi(\mathbf{r})/\lambda)$. Assuming some particular random distribution $W(\varphi)$ for the function $\varphi(\mathbf{r})$ for the mean value of the field, we obtain

$$\langle E(\delta) \rangle = A_i \int k(\mathbf{r}) \langle \exp[i\varphi(\mathbf{r})] \rangle \exp\left[i \left(\frac{4\pi r}{\lambda} \right) \right] h_\omega(\mathbf{r}, \delta) d\mathbf{r},$$

where $\langle \exp[i\varphi(\mathbf{r})] \rangle = \int \exp[i\varphi(\mathbf{r})] W(\varphi) d\varphi$. Assuming that the roughness height for the objects under study have Gaussian distribution,

$$W(\varphi) = \frac{1}{\sqrt{\pi \langle \varphi^2 \rangle}} \exp - \frac{\varphi^2}{\langle \varphi^2 \rangle},$$

and taking into account that $\langle \varphi \rangle^2 = 16\pi^2 \langle \xi^2(\mathbf{r}) \rangle / \lambda^2$, we obtain

$$\langle E(\delta) \rangle = A_i \exp\left[\frac{-(16\pi^2 \sigma^2)}{\lambda^2} \right] \int k(\mathbf{r}) \exp\left[i \left(\frac{4\pi r}{\lambda} \right) \right] h_\omega(\mathbf{r}, \delta) d\mathbf{r},$$

where $\sigma^2 = \langle \xi^2(\mathbf{r}) \rangle$ is the variance of the surface roughness height.

In the case of sufficiently high resolution of the imaging system, which corresponds to the condition $\Lambda_d \gg P_r \approx (r_c \lambda)/d_\rho$, where Λ_d is the size of minimal detail of the function $k(\mathbf{r})$ and P_r is the size of the minimally resolved domain

of the object's surface (see Fig. 2.1), the function $h_\omega(\mathbf{r}, \boldsymbol{\delta})$ can be considered a δ-function in comparison with $k(\mathbf{r})$,[12] and

$$\langle E(\boldsymbol{\delta})\rangle = \mu \exp\left[\frac{-(16\pi^2\sigma^2)}{\lambda^2}\right] k(\mathbf{r} = -\mu\boldsymbol{\delta}), \tag{2.3}$$

where $\mu = r_c/z_i$ is a scaling factor.

From Eq. (2.3) it follows that for large-scale roughness of an object's surface, when $\sigma \gg \lambda$, $I_r(\boldsymbol{\delta}) = |\langle E(\boldsymbol{\delta})\rangle|^2 \ll I_s(\boldsymbol{\delta}) = \mu|E_i k(\mathbf{r} = -\mu\boldsymbol{\delta})|^2$, where $I_r(\boldsymbol{\delta})$ is the intensity of the average field, and $I_s(\boldsymbol{\delta})$ is the intensity of the object's image for the case where $\sigma = 0$ (the image specular component for $\sigma \ll \lambda$; see Sec. 2.5). The reason is that in the case of roughness much larger than the wavelength ($\sigma \gg \lambda$) but resolvable by the optical system, the field E at each point of the image is a sum of a large number of random fields with phases uniformly distributed within the interval $6\pi \gg 1$. In this case, the contribution of each separate element of the rough surface in the nonresolvable domain of the object surface can be both positive and negative; and if the resolution domain (see Fig. 2.1) includes a large number of such elements, then the total field is close to zero.

2.2.1 Mean value and contrast of the intensity distribution in a coherent image

Let us now analyze the mean value (the first moment) of the intensity $I(\boldsymbol{\delta}) = |E(\boldsymbol{\delta})|^2$ in the coherent image of a flat rough object. Assuming $\sigma \gg \lambda$, we obtain[12]

$$\langle I(\boldsymbol{\delta})\rangle = A_i^2 \iint k(\mathbf{r}_1)k^*(\mathbf{r}_2) \times \exp\left\{-\frac{16\pi^2}{\lambda^2}\left[\sigma^2 - B_{12}(\mathbf{r}_1, \mathbf{r}_2)\right]\right\} h_\omega(\mathbf{r}_1, \boldsymbol{\delta})h_\omega^*(\mathbf{r}_2, \boldsymbol{\delta})d\mathbf{r}_1 d\mathbf{r}_2,$$

where $B_{12}(\mathbf{r}_1, \mathbf{r}_2) = \langle \xi(\mathbf{r}_1)\xi(\mathbf{r}_2)\rangle$ is the correlation function of surface roughness height distribution. In what follows, we will have to assume that surface roughness is isotropic and approximate this function by a Gaussian function

$$B_{12}(\mathbf{r}_1, \mathbf{r}_2) = \sigma^2 \exp\left[-\frac{(\mathbf{r}_1 - \mathbf{r}_2)^2}{\ell^2}\right].$$

One can show that if $\sigma \gg \lambda$, then $(\lambda\ell)/\sigma \ll d_o$, where d_o is the object size and ℓ is the correlation radius of the surface roughness of the object under study. Then, from the two previous equations, one can gain

$$\langle I(\boldsymbol{\delta})\rangle = |A_i|^2 \iint k(\mathbf{r}_1)k^*(\mathbf{r}_2) \times \exp\left[-\frac{16\pi^2\sigma^2(\mathbf{r}_1 - \mathbf{r}_2)^2}{\lambda^2\ell^2}\right] h_\omega(\mathbf{r}_1, \boldsymbol{\delta})h_\omega^*(\mathbf{r}_2, \boldsymbol{\delta})d\mathbf{r}_1 d\mathbf{r}_2. \tag{2.4}$$

Now consider two limiting cases:[12]

(1) $\sigma^2/\ell^2 \gg S_\rho/r_c^2$, where S_ρ is the imaging system aperture area; i.e., the Gaussian peak in Eq. (2.4) is narrower in $\mathbf{r}$ than other functions under the integral. In this case,

$$\langle I(\delta)\rangle = A_i^2\rho_p^2\int |k(\mathbf{r})h_\omega(\mathbf{r},\delta)|^2 d\mathbf{r}, \tag{2.5}$$

where $\rho_p = (\lambda\ell)/\sigma$ is the correlation radius in the phase distribution of the scattered field on the object surface. In the case of high resolution, $\Lambda_d \gg P_r \approx (\lambda r_c)/d_\rho$,

$$\langle I(\delta)\rangle = \left[\frac{S_\rho\ell^2}{(\sigma z_i)^2}\right]|E_i k(\mathbf{r}=-\mu\delta)|^2. \tag{2.5a}$$

This is a natural result that demonstrates that at high resolution, the coherent image of a flat object is its exact copy. However, in what follows we show that for nonflat objects, coherent images are not identical to the original. It should also be mentioned that at high resolution, the average intensity distribution in the image does not depend on the wavelength of the illuminating radiation. This conclusion is also natural since, in the case of high resolution, the image is formed according to geometric optics.

(2) $\sigma^2/\ell^2 \ll S_\rho/r_c^2$; i.e., the Gaussian peak in Eq. (2.4) is broader in $\mathbf{r}$ than other functions under the integral. Physically, this means that the radiation scattered by each part of the rough surface occupies a small solid angle. Then, $\langle I(\delta)\rangle \sim |k(\mathbf{r}=-\mu\delta)\Lambda(\mu\delta)|^2$, where $\Lambda(\mu\delta)$ is the pupil function of the imaging system.[12]

It is undoubtedly interesting to analyze the third field moment and the second intensity moment (mean square intensity), $\langle I^2\rangle$, in the coherent image. Such an analysis allows the study of deviations of the image field distribution from a Gaussian distribution. The analysis of higher-order moments is rather complicated. At $\sigma \gg \lambda$, the third field moments as well as the first field moments (mean values) in the image are approximately equal to zero.[12] One can show (see Appendix 1) that if $\ell^2 \ll (\lambda r_c)^2/S_\rho$ (in this case, separate elements of the rough surface are not resolvable by the imaging system), the mean square intensity is

$$\left\langle I(\delta)^2\right\rangle = 2\langle I(\delta)\rangle^2\left(1+\frac{\varepsilon}{N_i}\right),$$

where $\varepsilon \sim 1$; and in the case of a high-resolution imaging system, $N_i = S_i/\ell^2$, $S_i \approx P_r^2 \approx (\lambda r_c)^2/S_\rho$.

In the case of a low-resolution imaging system, $N_i = S_e/\ell^2$, where $S_e = (\int |k(\mathbf{r})|^2 d\mathbf{r})^2/(\int |k(\mathbf{r})|^4 d\mathbf{r})$ is the effective area of the rough object backscattering. The physical meaning of this parameter will be explained below. Then, $N_i = S_e/\ell^2$ is the number of correlation pixels within a single resolution domain.[34] In the case of a low-resolution imaging system, N_i is the number of roughness correlation pixels on the backscattering surface of the object under study. If $|k(\mathbf{r})|$ is constant, then $S_e = S_o$, which is the area of the flat object.

The contrast of the intensity distribution in the object image is

$$C = \frac{\langle I^2 \rangle - \langle I \rangle^2}{\langle I \rangle^2} = 1 + \frac{\varepsilon}{N_i}. \tag{2.6}$$

If $N_i \gg 1$, then $C \approx 1$. The unity contrast demonstrates in this case that the field distribution in the coherent image is Gaussian. In the case of a low-resolution imaging system, relation (2.6) coincides with relation (1.43) for the contrast of the intensity distribution in the coherent radiation scattered by a rough object.[30,35,36] It should be mentioned that the estimates of N_i by different authors are considerably different. Indeed, in Ref. 30, the estimate of N_i for the second case was in fact heuristic, which made unclear the physical essence of this number. In Ref. 33, rather clumsy expressions for N_i have been obtained. This is first of all connected with additional artificial postulates imposed on the distributions of the field's real and imaginary parts; according to the assumptions made in Ref. 33, they have joint Gaussian distribution.

2.2.2 Non-Gaussian statistics of the field in a coherent image formed by the imaging system with very high resolution and the contrast of the intensity distribution in this image[12]

From Eq. (2.6), it follows that at $N_i < 10$, C differs noticeably from unity, which indicates that the field distribution in the coherent image is non-Gaussian. Therefore, let us analyze intensity fluctuations in the coherent image for the case where $\ell^2 \ll S_i \approx P_r^2 \approx (\lambda^2 r_c^2)/S_\rho$; i.e., each separate element of the rough surface is well resolved by the imaging system. As we show below, in this case the contrast in the image can differ considerably from unity, which indicates that the statistics of the field in the coherent image is non-Gaussian. Therefore, relatively simple asymptotic approximations for the contrast C can be obtained for the Gaussian pupil function of the imaging system,

$$\Lambda(\boldsymbol{\rho}) = \exp\left(-\frac{4\boldsymbol{\rho}^2}{d_\rho^2}\right),$$

using the Taylor expansion for the function $\xi(\mathbf{r})$ in the vicinity of the point $\mathbf{r} = -\mu\boldsymbol{\delta}$. In this expansion, let us keep only derivatives of the second order and lower;

up to inessential factors, we obtain $E(\delta) \sim E_x, E_y$, where

$$E_x = \int \exp\left(i\frac{2\pi x^2}{r_c\lambda}\right)\exp\left[i\frac{4\pi(\xi'_x x + \xi''_{xx}x^2)}{\lambda}\right]\exp\left(-\frac{x^2}{4S_i}\right)dx,$$
$$E_y = \int \exp\left(i\frac{2\pi y^2}{r_c\lambda}\right)\exp\left[i\frac{4\pi(\xi'_y y^2 + \xi''_{yy}y^2)}{\lambda}\right]\exp\left(-\frac{y^2}{4S_i}\right)dy.$$

Here all derivatives are taken at point $\mathbf{r} = -\mu\delta$.

Assuming that the random function $\xi(\mathbf{r})$ has Gaussian distribution, after calculating the integrals in the last expression and averaging the obtained result over the derivatives of the function $\xi(\mathbf{r})$, we get the following relations:

$$\langle I(\delta)\rangle \sim \frac{|k(\mathbf{r}=-\mu\delta)|^2}{(1+2\alpha)^2},\ \langle I^2(\delta)\rangle \sim \frac{|k(\mathbf{r}=-\mu\delta)|^4 v^2\left(\frac{1}{2},1,\frac{1}{\beta}\right)}{(1+4\alpha)\beta}, \tag{2.7}$$

where $\alpha = (8r_c^2\sigma^2)/(S_\rho\ell^2)$, $\beta = (\lambda\sigma r_c^2)/d_\rho^2\ell^2)$, and $v(1/2, 1, 1/\beta)$ is the degenerate hypergeometric function. Using Eq. (2.7) and taking into account relation (2.6), for the contrast of the coherent image we obtain $d_\rho/r_c \approx 0.4$:

$$C = \frac{\langle I^2\rangle - \langle I\rangle^2}{\langle I\rangle^2} \approx \begin{cases} 1+\varepsilon/N_i & \text{for } d_\rho/r_c \ll \lambda/d_o, \\ (\sigma/\beta\lambda)\ln^2 2\beta^2 & \text{for } d_\rho/r_c \sim \sqrt{\lambda\sigma}/\ell, \\ \alpha^2 & \text{for } d_\rho/r_c \gg \sigma/\ell. \end{cases} \tag{2.8}$$

The contrast C has a maximum $C_m \approx 1.2\sigma/\lambda$ at $d_\rho/r_c \approx 0.4\sqrt{\lambda\sigma}/\ell$. Under the condition that $\sigma \gg \lambda$, C_m can considerably exceed unity. This is caused by the fact that each separate element of the rough surface can be considered as a focusing element with focal length $\sim\ell^2/\sigma$. As a result, at $d_\rho/r_c \approx 0.4\sqrt{\lambda\sigma}/\ell$, only beams coming from the domain of small size $\sim\ell\sqrt{\lambda/\sigma} \ll \ell$ of each element of the rough surface reach the input aperture of the imaging system. Hence, the image consists of separate isolated speckles with the size $\ell/\mu\sqrt{\lambda/\sigma} \ll \ell/\mu$, and it is for this reason that the intensity distribution in the coherent image has such a high contrast.

2.2.3 Correlation properties of fields and intensities in the coherent image of a flat rough object for fields with Gaussian statistics

Now, let us analyze the correlation properties of fields in the coherent image of a flat rough object placed orthogonally to the imaging system axis. Under the condition $\sigma \gg \lambda$, the field correlation function in the coherent image has the form

$$B_f(\delta_1, \delta_2) = \langle E(\delta_1)E^*(\delta_2)\rangle = |A_i|^2 \iint k(\mathbf{r}_1)k^*(\mathbf{r}_2)$$
$$\times \exp\left\{-\frac{[4\pi\sigma(\mathbf{r}_1-\mathbf{r}_2)]^2}{(\lambda\ell)^2}\right\} h_\omega(\mathbf{r}_1, \delta_1)h_\omega(\mathbf{r}_2, \delta_2)d\mathbf{r}_1 d\mathbf{r}_2.$$

Here, two limiting cases are possible:[12]

(1) $\sigma^2/\ell^2 \gg S_\rho/r_c^2$. Then,

$$B_f(\boldsymbol{\delta}_1, \boldsymbol{\delta}_2) = |A_i|^2 \rho_p^2 |k(\boldsymbol{\delta}_1)|^2 \int \Lambda(\boldsymbol{\rho}) \exp\left\{ \frac{i[2\pi(\boldsymbol{\delta}_1 - \boldsymbol{\delta}_2) \cdot \boldsymbol{\rho}]}{\lambda z_i} \right\} d\boldsymbol{\rho}, \tag{2.9}$$

where $\rho_p = (\lambda\ell)/\sigma$.

(2) $\sigma^2/\ell^2 \ll S_\rho/r_c^2$. Then,

$$B_f(\boldsymbol{\delta}_1, \boldsymbol{\delta}_2) = \left(\frac{S_\rho \ell^2}{z_i^2} \right) |E_i k(\mathbf{r} = -\mu\boldsymbol{\delta})|^2 \exp\left\{ -\frac{[4\pi\sigma\mu(\boldsymbol{\delta}_1 - \boldsymbol{\delta}_2)]^2}{(\lambda\ell)^2} \right\}.$$

One can study the correlation function $B_f(\boldsymbol{\delta}_1, \boldsymbol{\delta}_2)$ behavior in the image plane. A simple calculation based on the approximation $\Lambda(\boldsymbol{\rho}) = \exp(-4\boldsymbol{\rho}^2/d_\rho^2)$ shows that with a high-resolution imaging system, where $M_r = S_o/P_r^2 \approx S_o/S_i = (S_o S_\rho)/(\lambda^2 r_c^2) \gg 1$, and $P_r = (\lambda r_c)/d_\rho$ is the size of the Rayleigh resolution domain, the correlation radius of the field distribution is

$$\rho_f \approx \begin{cases} \lambda z_i/d_\rho & \text{for } d_\rho/r_c \ll \sigma/\ell, \\ \lambda\ell/\sigma\mu & \text{for } d_\rho/r_c \gg \sigma/\ell. \end{cases} \tag{2.10}$$

This can be verified experimentally by means of the scheme shown in Fig. 2.2(a). A flat rough object is illuminated by a monochromatic source. The image of the object is formed by lens 1 in the plane orthogonal to the reference wave, with a flat wavefront coming from the beam splitter and lens 2. Interference of the reference

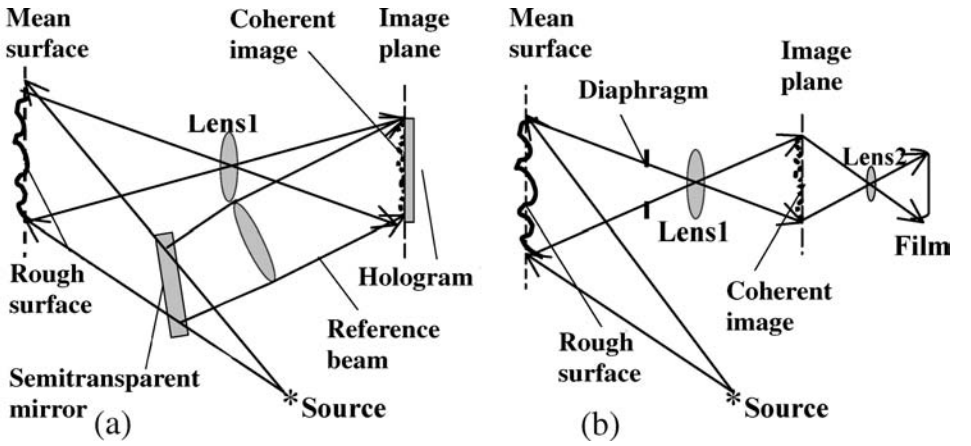

Figure 2.2 Experimental setups for analyzing the correlation characteristics of the rough surface coherent image: (a) with the reference wave, and (b) without the reference wave. The coherent image is displayed as a speckle pattern.

wave and the coherent image results in a hologram of the focused image[37] placed in the image plane. The intensity distribution in the hologram is registered, and the result can be used for estimating the correlation function and hence, the correlation radius ρ_f.

However, if the image of a Rayleigh resolution domain on the object surface contains a large number N_i of correlation pixels, i.e., separate elements of the rough surface ($N_i \gg 1$), then the correlation properties of the field $E(\delta)$ forming the coherent image can be rather easily estimated directly from the intensity distribution in the image. Indeed, one can show that under the condition $N_i \gg 1$, the field $E(\delta)$ in the image has Gaussian distribution, for which the following known equation is valid for the intensity correlation function:[12,38]

$$B_i(\delta_1, \delta_2) = \langle I(\delta_1)I(\delta_2)\rangle - \langle I(\delta_1)\rangle\langle I(\delta_2)\rangle$$
$$= |\langle E(\delta_1)E^*(\delta_2)\rangle|^2 = |B_f(\delta_1, \delta_2)|^2. \tag{2.11}$$

In this case, if $N_i \gg 1$, then for $\sigma \gg \lambda$ and $d_\rho/r_c \ll \sigma/\ell$, it follows from Eqs. (2.10) and (2.11) that the intensity correlation radius

$$\rho_i \approx \frac{\lambda z_i}{d_\rho}. \tag{2.11a}$$

For the object under study, an image fragment of a size comparable to the intensity correlation radius is optically conjugated to the Rayleigh resolution domains of the object surface with size $P_r = \mu\rho_i \approx (\lambda r_c)/d_\rho$. It is interesting to note that the least resolvable domain of the object surface is of the same size; its area is $S_i \approx P_r^2$, and the number of such areas is $M_r = S_o/S_i = (S_o S_\rho)/(\lambda r_c)^2$. Approximately the same is the number of correlation pixels M_r in the object image. If $M_r \gg 1$, then one says that the imaging system has high resolution. If $M_r \leq 1$, then one says that the imaging system has low resolution. This is according to the Rayleigh criterion.

If the image is formed with high resolution, then at $M_r \gg 1$ and $N_i \gg 1$, the image's intensity fluctuates considerably, so that the relative fluctuations (the contrast) in the image are $C \approx 1$ [see Eq. (2.6)]. In this case, the intensity distribution in each correlation pixel of the image drops fast with the increase in the distance from the pixel center. Hence, for an object that is highly resolved according to the Rayleigh criterion, the coherent image is a set of random bright domains (speckles). Their number can be estimated from the relation[11]

$$M = \frac{[\int I(\delta)d\delta]^2}{\int B_i(\delta_1, \delta_2)d\delta_1 d\delta_2}. \tag{2.12}$$

Taking into account Eqs. (2.9) and (2.11), one can show that

$$M = \frac{S_e S_\rho}{(\lambda r_c)^2}; \tag{2.13}$$

hence, the coherent image has a speckle structure. For a uniformly illuminated object with a constant reflection coefficient,[38]

$$M \approx M_r. \tag{2.14}$$

These conclusions are confirmed by the experiment shown in Fig. 2.2(b). The object under study was a flat square sheet of fine-grained sandpaper with the area $S_e = S_o = 9\ \text{m}^2$. The average grain size (the correlation radius of the sheet's rough surface) was $\ell \approx 20\ \mu\text{m}$. The size was chosen so that a single resolution domain included a large number of grains. The object was placed on the axis of the image-forming objective lens (lens 1) at a distance $r_c = 5470$ mm. The objective lens focal length was chosen to be $f = 300$ mm. The object was illuminated by green coherent radiation with wavelength $\lambda = 0.488\ \mu\text{m}$, and the objective lens had a square aperture with side dimension $d_\rho = 5$ mm. Under these conditions, the number of correlation pixels in a single resolution domain, given by the equation $N_i = (\lambda r_c)^2/(d_\rho \ell)^2$, was approximately 200. This ensured that the field distribution in the image was Gaussian. A coherent image of the object consisted of a small ($M \sim 10$) number of speckles, which led to a considerable decrease in image quality and object contour distortion [Fig. 2.3(a)]. Magnification of the number of Rayleigh resolution domains $M_r = (S_o d_\rho^2)/(\lambda^2 r_c^2)$ improved the image quality. We see this phenomenon from Fig. 2.3(b), which presents the image of the same object with $d_\rho = 15$ mm.

Figure 2.3(c) presents the image of a wooden 3-mm-diameter screwhead made at different aperture sizes d_ρ. Figure 2.3(d) presents an image of the same object obtained under the same conditions but in white light. We see that the quality of this image is much better than the coherent image quality. For instance, the image of the slot is more distinct than the one in Fig. 2.3(c).

Suppose that the number of speckles in the image is large (i.e., more than 100) and that there is no need to determine the dynamic parameters of the object using the speckle pattern, which is very sensitive to such parameters (see Chapter 3).

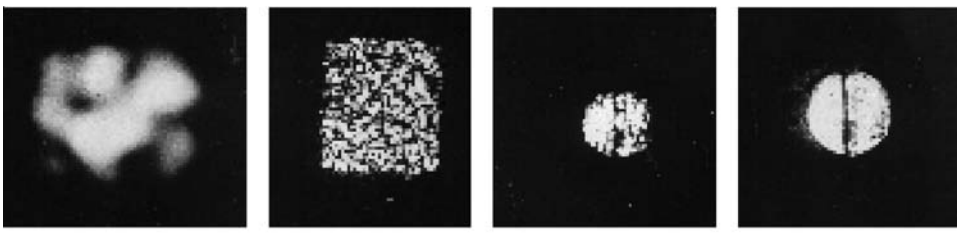

Figure 2.3 Coherent images of flat objects: (a) and (b) a square with rough surface; (c) a wooden screwhead imaged in coherent light; (d) a wooden screwhead imaged in white light.

Under these circumstances, it is preferable to form the image in white light, i.e., a noncoherent image. The contrast of the speckle pattern in such an image is practically equal to zero. This means that the speckle pattern disappears due to the summation of coherent images of the object formed at different wavelengths. Although in this case the quality of the image is good, the image is much less sensitive to the dynamic parameters of the object than a coherent image. If the number of speckles in the image is small (less than 100), then the quality of the image in white light is low. However, in Sec. 2.4 we show that even in this case one can obtain a high-quality image by summing statistically independent coherent images of the object formed at a single wavelength.

Figure 2.4(a) shows the theoretical and experimental dependencies of the number of speckles M on the number of Rayleigh resolution domains M_r in the images of a rough 5×5 mm square surface obtained with various aperture sizes d_ρ. The experimental data are rather close to the theoretical curve. It demonstrates that relation (2.14), which follows from the Gaussian field distribution in the image, holds true to a good accuracy.

2.2.4 The probability density function of coherent image intensity confirming the chosen model of coherent fields scattered by surfaces with large-scale roughness

Consider now the probability density function of the intensity at each point of a coherent image for objects with large-scale surface roughness ($\sigma \gg \lambda$). If the field distribution in the image is Gaussian, then the intensity at each image point is described by a negative-exponential probability density functional; i.e., $W_i = (1/\langle I \rangle) \exp(-I/\langle I \rangle)$. Figure 2.4(b) shows the histogram of the optical density D obtained experimentally from a photographically registered image. The photograph

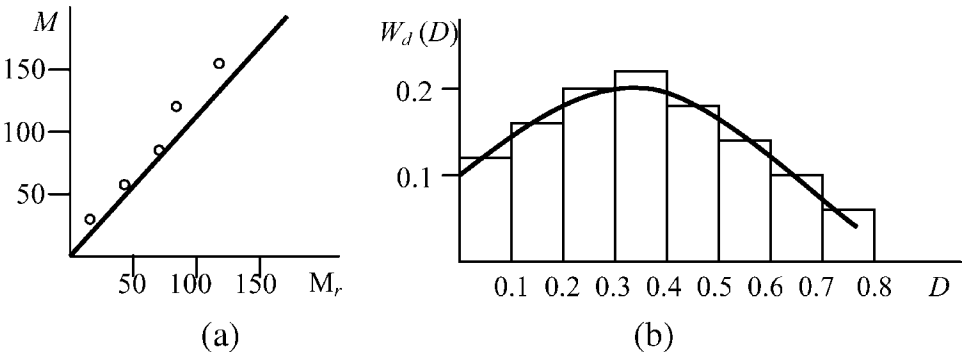

Figure 2.4 (a) Theoretical (solid line) and experimental (circles) dependences of the number of speckles M on the number of resolution domains M_r in the images of a rough 5×5 mm square surface obtained with various aperture sizes d_ρ. (b) The histogram of the optical density D obtained experimentally from a photographically registered image.

was obtained at $d_\rho = 12$ mm; the corresponding number N was rather high. The optical density was measured experimentally at the center of each speckle. The large number of speckles ensures high image quality and good accuracy of the optical density measurement.

Taking into account that $D = \gamma \ln(I/I_0)$, where $\gamma = 1.6$ is the contrast coefficient of the film and I_0 is a parameter giving the fogging level, we obtain for the optical density

$$W_d = \frac{I_0}{\gamma \langle I \rangle} \exp\left[\frac{D}{\gamma} - \frac{I_0}{\langle I \rangle} \exp\left(-\frac{D}{\gamma}\right)\right].$$

From the results of measurement, the area-normalized histogram $W_d(D)$ of the number of speckles with approximately equal central density was plotted [Fig. 2.4(b)]. The solid line in the same figure shows the theoretical probability density function of the intensity. A small deviation of this curve from the experimental histogram indicates that the real optical density distribution $W_d(D)$, which follows from the Gaussian distribution of the field in the image of the object under study, is rather precise at $N_i \gg 1$. This experimental fact confirms our model of coherent fields scattered by surfaces with large-scale roughness ($\sigma \gg \lambda$) and their coherent images, valid under the condition that a single resolution domain contains a large number of separate elements of the rough surface.

2.2.5 Correlation properties of the intensity in the case of non-Gaussian statistics of the field in the coherent image formed by a very high resolution imaging system

Consider now the correlation properties of the intensity distribution in a coherent image in the case where the field in the coherent image has non-Gaussian distribution. This is the case of very high resolution, where $\ell \gg P_r \approx (\lambda r_c)/d_\rho$; i.e., each separate element of the rough surface is well resolved by the imaging system and, hence, a single resolution domain contains only a small degree of roughness. Here, at each point of the coherent image, the field is not an additive combination of a large number of fields coming from a separate element of the rough surface, and therefore, it cannot be considered as having Gaussian distribution. In particular, the intensity correlation function does not satisfy relation (2.11). For simplicity, we restrict consideration to the analysis of the correlation properties of the intensity distribution in the coherent image of a flat rough object for the Gaussian pupil function of the imaging system $\Lambda(\boldsymbol{\rho}) = \exp(-4\boldsymbol{\rho}^2/d_\rho^2)$. In Ref. 12, it was shown that with $\ell^2 \gg S_i$ and $\mu = 1$, the normalized intensity correlation function is

$$\frac{B_i(\boldsymbol{\delta}_1, \boldsymbol{\delta}_2)}{\langle I(\boldsymbol{\delta}) \rangle^2} \approx C\left(1 - \frac{\boldsymbol{\delta}_1 - \boldsymbol{\delta}_2}{\rho_i^2}\right),$$

where C is the intensity contrast in the image [see Eq. (2.8)], and

$$\rho_i \approx \begin{cases} \dfrac{\sqrt{2} r_c \lambda}{\pi d}\left(1 - \dfrac{1}{\ln \beta}\right) & \text{for } \beta > 1, \\ \dfrac{d\ell^2}{2\sqrt{2}\sigma r_c}\left(1 + \dfrac{\beta^2}{2}\right) & \text{for } \beta < 1, \\ \ell & \text{for } \alpha < 1, \end{cases} \tag{2.15}$$

is the correlation radius of the intensity speckle pattern in the coherent image.

One can see from relation (2.15) that for small values of the angular aperture d_ρ/r_c, the intensity correlation radius is determined by the size of the resolution domain $P_r \approx (\lambda r_c)/d_\rho$ of the imaging system on the object's surface. It decreases to $\rho_i \sim \ell\sqrt{\lambda/\sigma}$ with an increase in angular aperture, and then increases again as $(d_\rho \ell^2)/(\sigma r_c)$. This parameter can be interpreted geometrically as follows:[39] each separate element of the rough surface focuses the incident light into the domain placed at the distance ℓ^2/σ from the mean surface.

One can find from the perspective of geometric optics that in the plane of the mean surface image, the image of the focusing part is blurred. For instance, for unity magnification of the imaging system, the size of the blurring is $\Delta = (\ell^2/4\sigma)(d_\rho/r_c)$. If $\Delta \ll \ell$, the image consists of separate bright domains—speckles of size $\rho_i \sim \Delta$. These are exactly those speckles that were mentioned in the analysis of the contrast C [see Eq. (2.8)] of coherent images. For a smaller blurring size (speckle size), Δ is also smaller and hence, the contrast of the image speckle pattern, d_ρ/r_c, is higher. As one can see from Eq. (2.15), Δ is equal to the correlation radius in the coherent image.

With a further decrease of d_ρ/r_c, the contrast and correlation radius are determined by diffraction effects caused by the finite size d_ρ of the imaging system aperture. For $d_\rho < (\lambda r_c)/\ell$, the correlation radius (speckle size) is given by the size of the Airy spot of the imaging system, and is $\rho_i \sim (\lambda r_c)/\ell$; and the contrast, as one can see from relation (2.15), is approximately equal to unity. Thus, the intensity correlation radius ρ_i in a coherent image depends on the angular aperture d_ρ/r_c of the imaging system and on the roughness parameters of the surface under study. In the vicinity of the contrast maximum, $d_\rho/r_c \sim \sqrt{\lambda\sigma}/\ell$; i.e., this value is much smaller than the correlation radius ℓ of the object surface roughness. In the case where $d_\rho/r_c \gg \sigma/\ell$, then $\rho_i \sim \ell$. This result follows from the fact that under the condition d_ρ/r_c, images of separate elements of the rough surface can overlap each other. This leads, on the one hand, to lower contrast [see relation (2.8)], and on the other hand, to an increase of the correlation radius in the image, up to the size of roughness. In other words, under this condition the imaging system "traces" every separate element of the rough surface.

Thus, at fixed statistical surface roughness parameters σ and ℓ, the growth of the imaging system angular aperture d_ρ/r_c leads to an increase of the coherent

image contrast from unity to $\sim\sigma/\lambda$. Further, it drops down to almost zero value when $d_\rho/r_c > \sigma/\ell$; i.e., the surface behaves as if it were smooth, while the correlation radius decreases to its minimum value, $\rho_i \sim \ell\sqrt{\lambda/\sigma}$, at which the contrast is maximum ($C \approx 1.2\sigma/\lambda$), and then increases up to $\rho_i \sim \ell$.

In Fig. 2.5 the contrast and correlation radius obtained above are plotted versus the angular aperture for the coherent image of a rough metal surface with the parameters $\sigma = 1.6$ μm and $\ell = 16.1$ μ, and under the condition that $\lambda = 0.63$ μ, $d_\rho = 1 \ldots 75$ mm, and $r_c = z_i = 500$ mm ($\mu = 1$). In the same plot, experimental values of these dependencies are given. Small deviations of the experimental points from the theoretical dependencies are explained by the fact that the dependencies are calculated for an imaging system with the pupil function $\Lambda(\boldsymbol{\rho}) = \exp(-4\boldsymbol{\rho}^2/d_\rho^2)$, while the experimental values are obtained for coherent images formed by an imaging system with the rectangular pupil function. According to the data of Ref. 40, the dashed line in Fig. 2.5(a) shows the dependence of the coherent image contrast on the size of the angular aperture of the imaging system with the pupil function $\Lambda(\boldsymbol{\rho}) = \exp(-4\boldsymbol{\rho}^2/d_\rho^2)$ calculated numerically under the condition that the surface roughness height of the object has Gaussian distribution. Since the curve calculated from the asymptotic formulas (2.8) coincides, for a broad range of angular apertures, with the curve calculated numerically, the conclusion follows that relations (2.8) are correct.

It is interesting to note that non-Gaussian statistics of the field distribution $E(\boldsymbol{\delta})$ in speckle patterns of coherent images can be used effectively to determine mean height and length of ocean waves by measuring the contrast and correlation radius of ocean surface coherent images. Here, we use the effect of double passing a laser beam through the ocean surface waves and the top layers by means of a laser air probing process, which leads to an image contrast that essentially exceeds unity.[33]

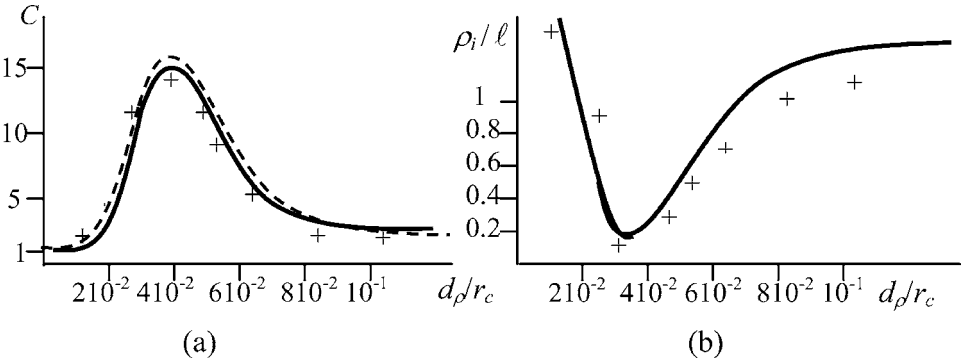

Figure 2.5 (a) The contrast and (b) the correlation radius plotted versus the angular aperture for the coherent image of a rough metal surface. Solid lines are theoretical curves. The dashed line is the contrast calculated numerically. The crosses (+) are experimental data.

2.3 Statistical characteristics of coherent image intensity in nonflat rough objects

We now consider the statistical characteristics of intensity spatial distribution in the coherent images of nonflat rough objects placed arbitrarily with respect to the imaging system.[41] One can show that when the field statistics in an image are non-Gaussian, then the statistical characteristics of the intensity distribution are practically the same as for the corresponding characteristics of a flat rough object's coherent image. Therefore, we restrict ourselves to the case where the field distribution in the coherent image of a nonflat rough object is near-Gaussian. In this case, according to relation (2.1) and under the assumptions that the observer is placed close to the illuminating source, the factor $(\mathbf{n}\cdot\mathbf{q})/(\mathbf{n}\cdot\mathbf{N})$ is sufficiently smooth, and d_o/r_c, then the field distribution in the coherent image of the object can be represented as

$$E(\boldsymbol{\delta}) = A_i \int k(\mathbf{r}) \exp[i\varphi_n(\mathbf{r})] \exp\left[i\left(\frac{4\pi r}{\lambda}\right)\right] h_\omega(\mathbf{r}, \boldsymbol{\delta}) d\mathbf{r},$$

where $\varphi_n(\mathbf{r}) = [2\pi\mathbf{q}\cdot\mathbf{N}\xi(\mathbf{r})]/\lambda$. Similar to the case of the coherent image of a flat object, at $\sigma \gg \lambda$, for the mean field value in the coherent image of a nonflat object we obtain that the averaged field in the coherent image $\langle E(\boldsymbol{\delta})\rangle \sim \exp[-(4\pi\sigma/\lambda)^2] \approx 0$.

The average intensity in this image[12,41] is $\exp[-(q_\perp^2 \ell^2)/(\sigma^2 q_N^2)]$

$$\langle I(\boldsymbol{\delta})\rangle = |A_i|^2 \rho_p^2 \int k_i(\mathbf{r}) h_\omega(\mathbf{r}, \boldsymbol{\delta}) d\mathbf{r},\ q_N = \mathbf{q}\cdot\mathbf{N}, \tag{2.16}$$

where $A_i = (E_i S_\rho)/(\lambda^2 r_c z_i)$, $k_i(\mathbf{r}) = |k(\mathbf{r})^2| \exp[-(q_\perp^2 \ell^2)/(\sigma^2 q_N^2)]$, $q_\perp = \sqrt{q^2 - q_N^2}$, and $\rho_p = (\lambda\ell)/\sigma$. At high angular resolution, when the function $h_\omega(\mathbf{r}, \boldsymbol{\delta})$ is narrower than the function $k_i(\mathbf{r})$,

$$\langle I(\boldsymbol{\delta})\rangle = k_i(\mathbf{r} = -\mu\boldsymbol{\delta}) \frac{\ell^2 S_\rho |E_i|^2}{(\sigma z_i)^2}. \tag{2.16a}$$

Relations (2.16) and (2.16a) differ from Eqs. (2.5) and (2.5a)—which were obtained for a flat object placed orthogonally to the imaging system's axis and illuminated normally to the surface—by the factor $\exp[-(q_t \ell/\sigma q_N)^2]$, the physical meaning of which will be explained at the end of this section. With the assumption that the roughness correlation radius ℓ is small compared to the size of the resolution domain image $\ell \ll \rho_i = (\lambda z_i)/d_\rho$, where d_ρ is the imaging system aperture size, and that $d_\rho/r_c \ll \sigma/\ell$, then the mean square intensity in the coherent image of a nonflat rough object is

$$\langle I^2\rangle = 2\langle I\rangle - 2|A_i^2|\rho_p^4 \int k_i^2(\mathbf{r}) h_\omega(\mathbf{r}, \boldsymbol{\delta}) d\mathbf{r},$$

where $\rho_p = (\lambda\ell/\sigma)$. Substituting the expression for $\langle I\rangle$ into Eq. (2.16), we obtain

$$C = 1 - \frac{1}{N_i^*}, \tag{2.17}$$

where $N_i^* = N_i \exp[-(q_t\ell/\sigma q_N)^2]$.

Physically, this result means that in the case of oblique incidence and scattering of radiation, the number of points with mirrorlike reflection on the object surface[11] decreases. Equation (2.17) can be interpreted as the relation for calculating the number of mirror-reflecting points in the case of an object placed arbitrarily with respect to the lens' optical axis. One can see from Eq. (2.16a) that the brightest spots of the image are determined from conditions $q_t(\mathbf{r}_j) = 0$.[41] These are what we will refer to here as the "shine domains" of the illuminated surface, with j numerating the points. Taking into account Eq. (2.12), one can show that under the condition $(\ell/\sigma)^2 \ll r_c^2/S_\rho$, which is usually satisfied in practice, the speckle number M in the image of a nonflat object is

$$M = \frac{S_e S_\rho}{\lambda^2 r_c^2}, \tag{2.18}$$

where $S_e = (\int k_i(\mathbf{r})d\mathbf{r})^2 / \int (k_i^2(\mathbf{r})d\mathbf{r})$ is the effective area of the backscattering surface.

Using the example of a spherical, uniformly illuminated object, let us estimate the effective backscattering area S_e. This will give us an opportunity to estimate the effect of the nonflatness of the object on the speckle number in its image. In this case, $S_e \approx (S_o\sigma^2)/\ell^2$, where S_o is the area of the principal section of the object. For a flat rough object, $S_e = S_o$. We see that the deviation from flatness of the object surface leads to a decrease in S_e. In this case, the speckle number in the image also decreases, according to relation (2.18). The correlation radius of the intensity distribution in the coherent image of a nonflat object can be determined by the same relation (2.11a) as for a flat object: $\rho_i = (\lambda z_i)/d_\rho$.

The influence of the surface shape of a nonflat object on the intensity distribution and on the speckle number M in the speckle pattern of a coherent image manifests itself most clearly in the case of imaging the side of a rough disk placed on the axis of an imaging lens (see Fig. 2.6). In this case,[12] $S_e \approx (w_d\rho_d\sigma)/\ell$, and $M = (\sigma_d\rho_d S_\rho)/(\ell\lambda^2 r_c^2)$, where w_d is the disk width, and ρ_d is the disk radius; $q_N = \mathbf{q}\cdot\mathbf{N} = 2\cos\varphi$, $q_\perp = (q^2 - q_N^2)^{-1/2} = 2\sin\varphi$, where φ is the polar coordinate of a point on the disk side; and

$$\langle I(\delta_x, \delta_y)\rangle = \frac{\ell^2 S_\rho |E_i|^2}{\sigma^2 z_i^2} |k(x = -\mu\delta_x, y = -\mu\delta_y)|^2 \exp\left(-\frac{\ell^2 tg^2\varphi}{\sigma^2}\right). \tag{2.19}$$

The shine domain on top of the cylinder surface has the coordinate $x = 0$. For steep roughness, $\sigma/\ell \approx 1$, as one can see from Eq. (2.19), and the shape of the surface has almost no influence on the image.

Figure 2.7 presents photographs of a 5-mm screw nut, which were obtained for various imaging system aperture diameters d_ρ: (a) $d_\rho = 4$ mm, (b) $d_\rho = 8$ mm, (c) and (d) $d_\rho = 16$ mm. The outer surface of the nut consists of flat rough surfaces (faces). In Fig. 2.7, the image is brightest for the faces oriented so that the angles between the normal **N** and the scattering vector **q** are small, $\alpha < 15$ deg. The brightest face is the front one. One of the side faces ($\alpha > 30$ deg) is imaged poorly. The same photographs demonstrate that coherent image speckle size has a strong influence on image quality. One can see that a decrease of diaphragm size d_ρ leads to increased speckle size and, hence, to decreased image quality. At $d_\rho = 4$ mm [Fig. 2.7(a)], the nut's hole hardly can be recognized. The best image is obtained when illuminating with white light [Fig. 2.7(d)]; this is due to the overlap of coherent images of the same object at different wavelengths, which results in an image with improved quality. The method of overlapping coherent images will be discussed in detail below.

Figures 2.8 and 2.9 illustrate how, with different speckle quantities M, the surface shape influences coherent images of a signal lamp. In the photographs, by

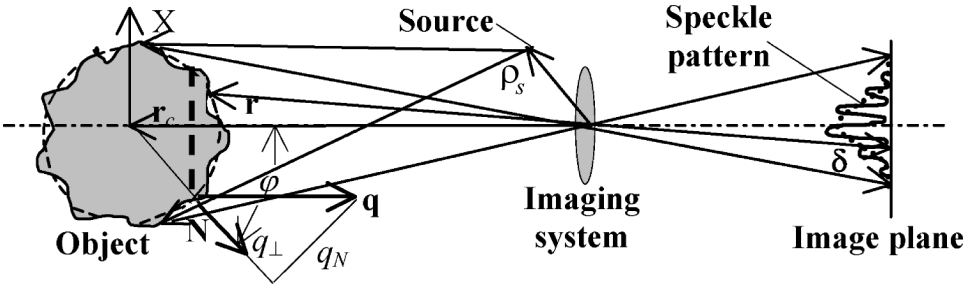

Figure 2.6 Coherent imaging of the side of a rough disk. The thin dashed line is the mean disk surface. The dashed line is the mean intensity distribution $\langle I(\delta_x, \delta_y)\rangle$. The thick dashed line restricts the "shine domain" (the backscattering surface) with the size $d_s \sim (\rho_d \sigma)/\ell$, where ρ_d is the disk radius.

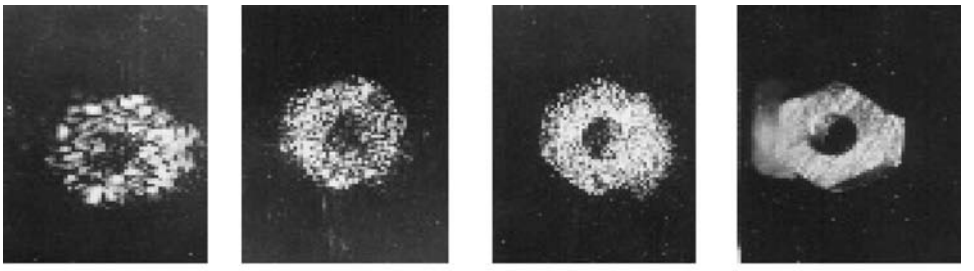

Figure 2.7 Coherent images of a screw nut obtained for various diameters of imaging system aperture d_ρ: (a) $d_\rho = 4$ mm, $M \approx 30$; (b) $d_\rho = 8$ mm, $M \approx 120$; (c) $d_\rho = 16$ mm, $M \approx 480$; (d) $d_\rho = 16$ mm.

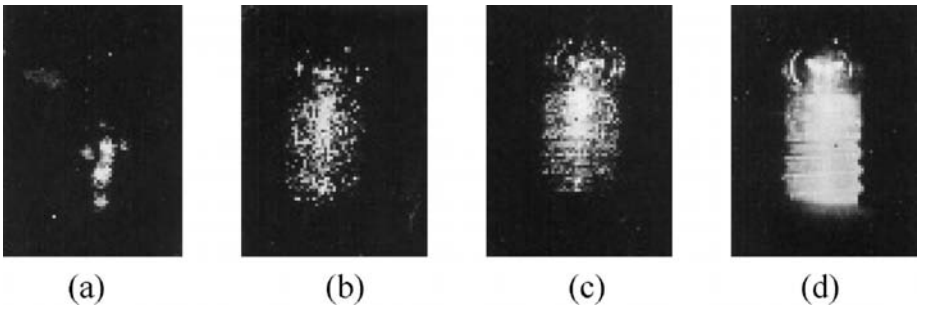

Figure 2.8 Coherent images of the signal lamp: (a) $M = 6$; (b) $M \sim 100$; (c) $M \sim 400$; (d) photograph in white light.

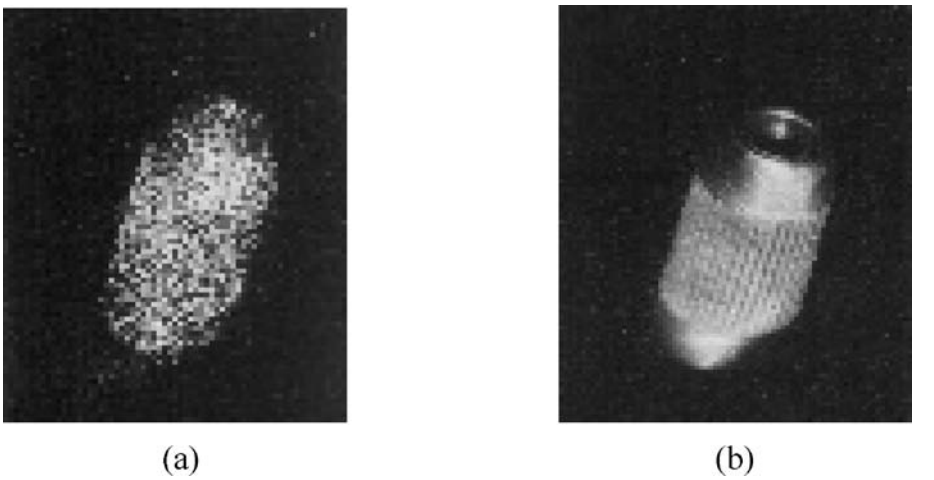

Figure 2.9 Coherent images of a cylindrical object: (a) $M \sim 240$; (b) photograph in white light. The speckle pattern hides the side stripes on the surface.

using the scheme shown in Fig. 2.7, one can see shine domains satisfying the condition $(q_\perp^2 \ell^2)/(q_N^2 \sigma^2) \leq 0.3$. The edges of smooth parts are not distinct because, in this case, the sizes of shine domains $d_s = (\sigma d_o)/\ell$ are rather small. Here, d_o is the signal lamp.

2.4 Methods of estimating and improving the quality of coherent images

We see that coherent images of rough objects have a strongly fluctuating structure, i.e., the speckle pattern. There are at least two ways of improving the quality of such images. The first way is to increase the size d_ρ of the imaging system aperture. This leads to a decrease in speckle size in the coherent image and, hence, each detail of the object is represented by a larger number of speckles. The parameter d_ρ is chosen based on the size Λ_d of the smallest detail of the object's surface.

The sizes of the smallest details along the X and Y axes are calculated from the formulas[12]

$$\Lambda_{dx} = \left| k_i\left(\mathbf{r} = -\frac{\delta r_c}{z_i}\right)\right| \left[\mathrm{Re}(k''_{ixx} + k^{*\prime\prime}_{ixx})k_i + 2|k'_{ix}|^2\right]^{-1/2},$$

and (2.20)

$$\Lambda_{dy} = \left| k_i\left(\mathbf{r} = -\frac{\delta r_c}{z_i}\right)\right| \left[\mathrm{Re}(k''_{iyy} + k^{*\prime\prime}_{iyy})k_i + 2|k'_{iy}|^2\right]^{-1/2}.$$

Here, all derivatives are taken at point $\mathbf{r} = -\mu\boldsymbol{\delta}$. The conditions for a high-quality image are $d_\rho \gg (\lambda r_c)/\Lambda_x$ and $d_\rho \gg (\lambda r_c)/\Lambda_y$. For instance, in the case of a flat rough object having a periodic reflection coefficient, the mean intensity distribution is

$$\langle I(\delta_x, \delta_y)\rangle \sim 1 + \cos\left(\frac{2\pi\mu\delta_x}{\Lambda_{ox}}\right)\cos\left(\frac{2\pi\mu\delta_y}{\Lambda_{oy}}\right),$$

and the smallest detail sizes are $\Lambda_x = \Lambda_{ox}$, $\Lambda_y = \Lambda_{oy}$. Under conditions where $d_\rho \gg (\lambda r_c)/\Lambda_{ox}$ and $d_\rho \gg (\lambda r_c)/\Lambda_{oy}$, details having sizes $\Lambda_{ox} \times \Lambda_{oy}$ are reproduced very well, since in this case the image of the detail contains a large number of speckles; i.e., the imaging system resolves these details.

The second way to improve coherent image quality is to accumulate statistically independent realizations of images, which leads to a decrease in the intensity fluctuations in the accumulated image. As an integral criterion of the image quality, which characterizes the similarity between the accumulated image and the mean nonfluctuating image, we will consider the correlation criterion. It can be estimated as

$$K = \frac{\int I_a(\boldsymbol{\delta})\langle I(\boldsymbol{\delta})\rangle d\boldsymbol{\delta}}{\int \langle \mathbf{I}(\boldsymbol{\delta})\rangle^2 d\boldsymbol{\delta}},$$

where

$$I_a(\boldsymbol{\delta}) = \frac{1}{N_a}\sum_{n=1}^{n=N_a} I_n(\boldsymbol{\delta})$$

is the intensity distribution in the accumulated image normalized as $\int I_a^2 d\boldsymbol{\delta} = \int \langle I\rangle^2 d\boldsymbol{\delta}$, and N_a is the number of accumulated images.[34,42] Assume that the image I_a is close to $\langle I\rangle$ when the value K takes its maximum value. The efficiency of this criterion, i.e., the accuracy η_c to which the accumulated image I_a coincides with $\langle I\rangle$, can be estimated from relative fluctuations of K,

$$\eta_c = \frac{\langle K^2\rangle - \langle K\rangle^2}{\langle K\rangle^2}. \tag{2.21}$$

If statistically independent realizations of images are accumulated, when $B_{mn}(\delta_1, \delta_2) = \langle I_m(\delta_1) I_n(\delta_2)\rangle - \langle I_m(\delta_1)\rangle\langle I_n(\delta_2)\rangle = B_i(\delta_1, \delta_2)\delta_{mn}$, where $B_i(\delta_1, \delta_2) = \langle I_m(\delta_1) I_m(\delta_2)\rangle - \langle I_m(\delta_1)\rangle\langle I_m(\delta_2)\rangle$ is the correlation function of the intensity distribution in the m-th coherent image, $\delta_{mn} = 1$, for $m = n$, $\delta_{mn} = 0$, for $m \neq n$, then we obtain

$$\eta_c = \frac{\iint \langle I(\delta_1)\rangle\langle I(\delta_2)\rangle B_i(\delta_1, \delta_2) d\delta}{N_a(\int \langle I(\delta)\rangle^4)}.$$

On an order of magnitude, $\eta_c \approx 1/(MN_a)$, where M is the number of speckles in the image realization. An increase of M and N_a reduces the relative fluctuations of K, since at large M and N_a the criterion is more stable. Hence, the accuracy η_c to which the accumulated image I_a coincides with $\langle I\rangle$ is very high.

Let us consider the possibility of accumulating coherent images for various directions of object illumination. We can perform this by changing the position of the illuminating monochromatic source (Fig. 2.10). Let, for simplicity, all sources be placed in the imaging system's aperture plane at different distances d_j from the aperture center, where j is the source number, and let the object under study be a flat rough object. In this case,[12] at $M \gg 1$,

$$B_{mn}(\delta_1, \delta_2) = B_i(\delta_1, \delta_2) J_{mn},$$

where

$$J_{mn} \approx \begin{cases} 1 - (d_m - d_n)^2/S_\rho, & \text{for } d_m - d_n \leq d_\rho, \\ 0, & \text{for } d_m - d_n > d_\rho. \end{cases}$$

Hence, under the condition $d_m - d_n > d_\rho$ and $J_{mn} \approx \delta_{mn}$, accumulated coherent images become statistically independent (Fig. 2.11). This independence is connected with the fact that any change of the illumination direction leads to the simultaneous rotation of the scattered field in the opposite direction, since in the first

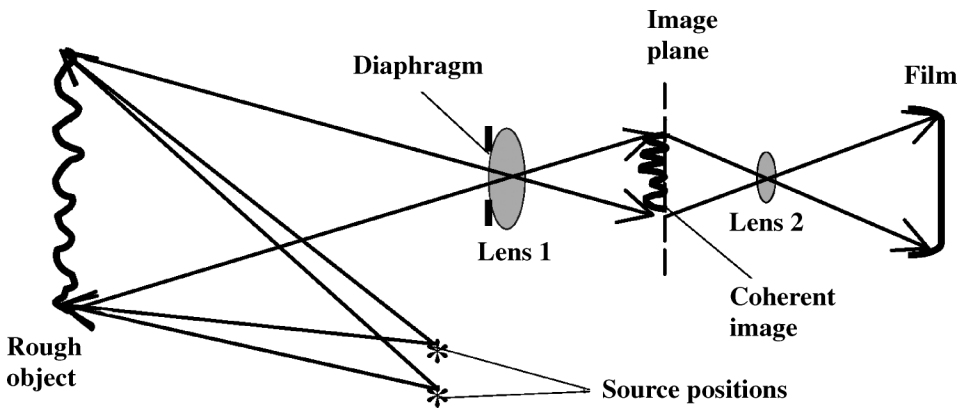

Figure 2.10 Schematic of experiments for accumulating statistically independent coherent images by changing the position of the illuminating coherent source.

approximation, a rough surface can be considered as a strongly distorted mirror. Hence, changing the illumination direction leads to the simultaneous rotation of the rays reflected by this mirror's rays. Rotating the scattered field leads to the formation of new independent realizations of the object's coherent images.

Rotation of the field is accompanied by displacement of the scattered field speckle pattern on the aperture of the imaging system. As a result, if the source is displaced by the aperture size d_ρ (Fig. 2.11), then the illumination direction varies by the angle $\sim d_\rho / r_c$, the speckle pattern is displaced on the aperture plane by the same distance d_ρ, and a new speckle pattern appears on the aperture. Hence, the initial speckle pattern is completely changed and there occurs a complete change in the scattered field realizations. As a result, the initial realization of the object's coherent image is replaced by a new, statistically independent realization; and in the image plane, new speckles appear between the old speckles. As the direction of the object illumination varies further, new speckles fill the contour of its ideal image and, hence, the quality of the accumulated image tends toward the ideal image quality.

The improvement in the resulting image quality with the accumulation of statistically independent images is accompanied by a decrease of contrast in the image. Taking into account that $\langle I_m I_n \rangle = \delta_{mn}$, we obtain that $C = 1/N_a$. As shown in the schematic in Fig. 2.10, 10 statistically independent coherent images of a flat triangular rough object made of sandpaper were obtained by changing the position of the illumination source so that the condition $d_m - d_n > d_\rho$ was satisfied. In Fig. 2.12(a), a single realization of the coherent image consisting of $M = 7$ speckles is shown. The image quality is very low. After accumulating the coherent im-

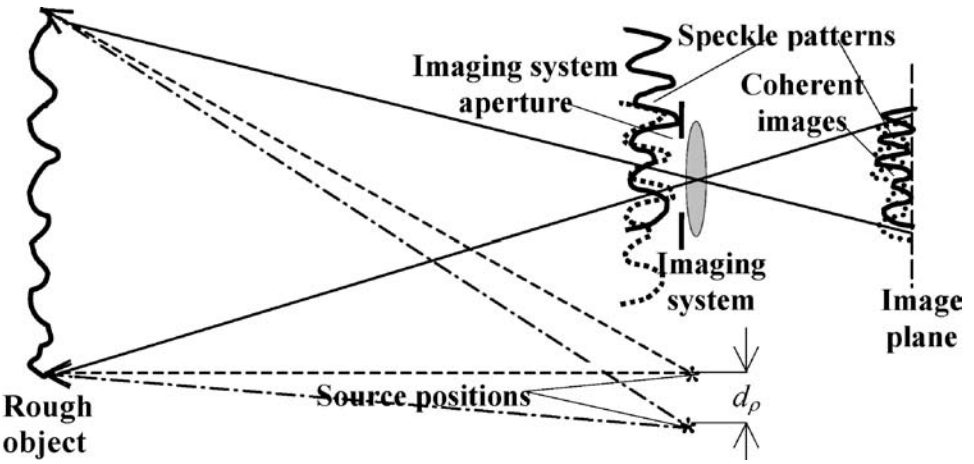

Figure 2.11 Improving image quality using the accumulation of statistically independent coherent images by changing the position of the illuminating monochromatic source. The two dashed lines are rays from the first source position. The square-point line is the first speckle pattern position in the aperture and image planes. The two dash-dot lines are rays from the second source position. The solid line is the second speckle pattern position in the aperture and image planes.

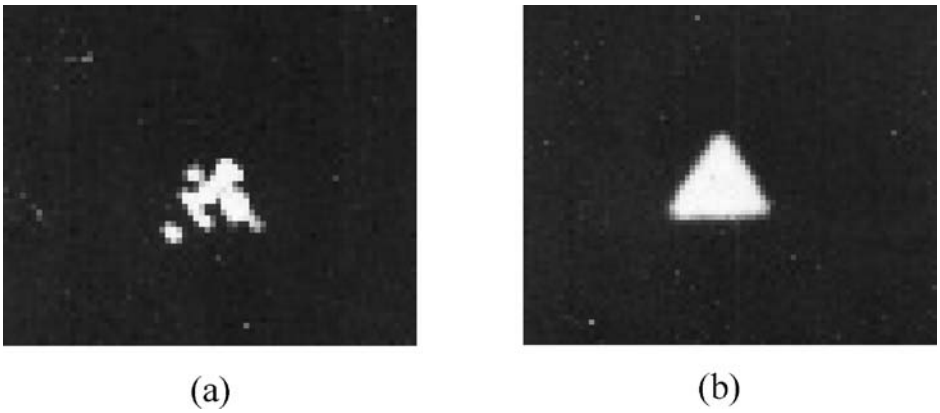

Figure 2.12 Experimental results of accumulating coherent images for a triangular rough object obtained by changing the position of the illumination source: (a) a single realization of the coherent image; (b) the accumulated image.

ages, the speckled structure disappeared almost completely, and the image quality increased dramatically [see Fig. 2.12(b)]. According to the criterion K introduced above, in this case the accuracy is $\eta_c \approx 1.5\%$ and the contrast of the intensity distribution in the accumulated image is small ($C \approx 0.1 \ll 1$).

The coherent image quality also can be improved by accumulating statistically independent images of a rough object at various wavelengths. This will be discussed in detail in the next section.

2.5 Statistical characteristics of images of an object illuminated by quasi-monochromatic and polychromatic light

In the previous section we analyzed the statistical characteristics of rough-surface object images. It was shown that in monochromatic light the image has a rather contrasted structure. For instance, if the imaging system does not resolve separate elements of the object's rough surface, the contrast of the image speckle pattern is equal to unity. It is interesting to analyze the image where the object is illuminated by quasi-monochromatic and polychromatic radiation.[43] In this case, one should expect a decrease in image contrast. Below, we analyze the statistical characteristics of the intensity distributions in images obtained in quasi-monochromatic and polychromatic radiation. From these characteristics, we estimate the contrast, i.e., relative intensity fluctuations in the images. Let the object be illuminated by quasi-monochromatic radiation with mean frequency ω_0. Then, taking into account Eqs. (1.18) and (1.27), and assuming that the object is in the Fresnel zone, we represent the field in the image plane as

$$E(\boldsymbol{\delta}, t) \sim \int E_\omega(\boldsymbol{\delta}) \exp(-i\omega t) d\omega, \tag{2.22}$$

where

$$E_\omega(\delta) = A_i S_r(\omega) \int \frac{\mathbf{n}\cdot\mathbf{q}}{\mathbf{n}\cdot\mathbf{N}} k(\mathbf{r}) \exp\left[i\frac{\omega}{c}\mathbf{q}\cdot\mathbf{N}\xi(\mathbf{r})\right] \times \exp\left[i\frac{\omega(|\mathbf{r}-\boldsymbol{\rho}_s| + r)}{c}\right] h_\omega(\mathbf{r}, \delta) d\mathbf{r}$$

is the field scattered by the object at one of the frequencies [see expression (2.1)], $S_r(\omega)$ is the illuminating radiation spectrum, $A_i = (E_i S_\rho \omega^2)/(c^2 r_c z_i)$, $\mathbf{N}$ is the normal to the mean object surface, $\mathbf{q} = \boldsymbol{\nu}_o - \boldsymbol{\nu}_i$, $\boldsymbol{\nu}_i \approx (\mathbf{r}_c - \boldsymbol{\rho}_s)/|\mathbf{r}_c - \boldsymbol{\rho}_s|$, and $\boldsymbol{\nu}_o \approx \mathbf{r}_c/r_c$.

Furthermore, when finding the statistical characteristics of the image we will take into account that detectors are inertial and therefore, register time-averaged intensity distribution:

$$\bar{I}(\delta) = \frac{1}{T}\int_{t_0}^{t_0+T} |E(\delta, t)|^2 dt,$$

where t_0 is the initial time and T is the registration time. Approximating the intensity spectrum by a Gaussian function, $S_r(\omega) = (1/\Delta\omega)\exp[-(\omega-\omega_0)^2/(\Delta\omega)^2]$, where $\Delta\omega$ and ω_0 are the width and mean frequency of the illuminating source spectrum, respectively, let us find the intensity distribution in the image averaged over various realizations of roughness height $\xi(\mathbf{r})$. Assuming $T\Delta\omega \gg 1$, in the case of a high-resolution imaging system we obtain for the mean intensity distribution in the image

$$\langle \bar{I}(\delta)\rangle = \frac{\ell^2 S_\rho |E_i|^2}{\sigma^2 z_i^2} k_i(\mathbf{r} = -\mu\delta), \tag{2.23}$$

which coincides with expression (2.16a) for the mean intensity in the coherent image. Here, angle brackets $\langle\rangle$ denote averaging over various realizations of the roughness height distribution $\xi(\mathbf{r})$.

Consider now the correlation function of the time-averaged intensity distribution in the image. Assuming that the field distribution in the image is Gaussian, we obtain for this correlation function[12]

$$B_t(\delta_1, \delta_2) = \langle \bar{I}(\delta_1)\bar{I}(\delta_2)\rangle - \langle \bar{I}(\delta_1)\rangle\langle \bar{I}(\delta_2)\rangle = \frac{1}{T^2}\int_{t_0}^{t_0+T}\int_{t_0}^{t_0+T} |\langle \mathrm{E}(\delta_1, t_1)\mathrm{E}^*(\delta_2, t_2)\rangle|^2 dt_1 dt_2.$$

Under the condition $L_p \ll L_c$, where L_c is the source coherence length (see Fig. 2.13), $L_p = (cr_c q_t)/(q_N \omega_0 d_\rho)$, the size of projection of the least-resolvable

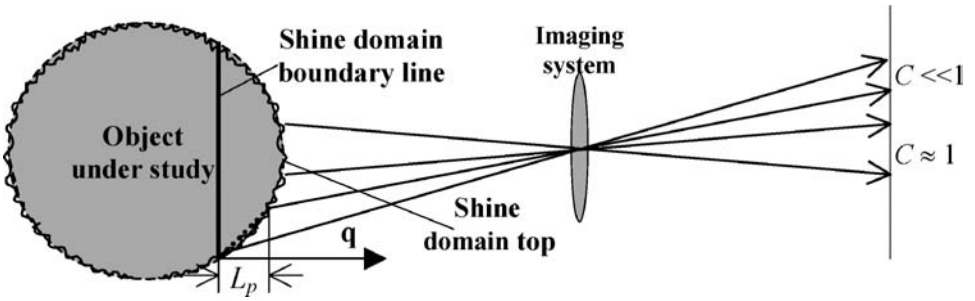

Figure 2.13 Optical images in the case of illuminating the object by quasi-monochromatic light with $L_p \gg L_c \gg \sigma$. The dotted line restricts the resolvable area of the object surface, which we display at the boundary line of the shine domain (backscattering surface), where its projection L_p is maximal and the image contrast $C = L_c/L_p$ is minimal.

area of the object surface on the direction **q**, equal to the depth of this area, $q_N = \mathbf{q} \cdot \mathbf{N}$, $q_t = (q^2 - q_N^2)^{0.5}$, for the contrast of the speckle pattern in the image of a rough object we obtain[12]

$$C = \frac{B_t(\delta, \delta)}{\langle \bar{I}(\delta) \rangle^2} \approx 1. \tag{2.24}$$

This situation is similar to the case of illumination with a monochromatic source having infinite coherence length, where the contrast speckle pattern in the image of a rough object is unity. The relation $L_p \ll L_c$ is the condition for the formation of coherent images of the rough objects. Under this condition, each point of the image is formed by interfering contributions of all waves coming from the minimal domain of the object surface resolvable by the imaging system and according to the definition formulated in the Preface, such an image will be called *coherent*.

Assuming that the imaging system has high resolution, under the opposite condition of quasi-monochromatic illumination, $L_p \gg L_c$, and $L_c \gg q_N\sigma$ (see Fig. 2.13), then

$$C = \frac{1}{N_s}, \tag{2.25}$$

where $N_s = L_p/L_c$ is the number of statistically independent contributions of the scattered radiation to the image of the minimally resolved domain of the object surface. In this case, interference takes place only for waves scattered by a small part of the resolvable area of the object surface. Therefore, at each point of the image of a minimally resolved domain, there is an overlap of several statistically independent interference patterns. As a result, the contrast of the image is significantly lower than the contrast of the speckle pattern for a coherent image, which is equal to unity.

In the case $q_N\sigma \gg L_c$, which is realized for polychromatic object illumination, for instance, for the case of illumination by sunlight or by a heat source[43] (Fig. 2.14),

$$C = \frac{1}{N_s'}, \tag{2.26}$$

where $N_s' = (q_N\sigma)/L_c$ is the number of statistically independent contributions of the scattered radiation to the image within a single separate element of the rough surface. If we take into account that the shine domain of the object surface provides the most important contribution to the object image, then as a rule, $1 < q_N < 2$; and, hence, when $\sigma \gg L_c$, then $C \ll 1$ within the whole shine domain image.

According to relations (2.24)–(2.26), one can imagine the following scenario. Let an object be placed on the imaging system axis, L_p being the projection of the least-resolvable area of the object's surface on this axis (see Fig. 2.13). For a large source coherence length, $L_c \gg L_p$, the contrast in each part of the image is unity [see Eq. (2.24)]. In this case, the whole image is coherent. For the intermediate case, $L_p \gg L_c \gg \sigma$ (see Fig. 2.13), the image of the top of the shine domain is coherent in the sense that it has unity contrast. Outside of this area, the contrast is equal to $C = L_c/L_p$ [see Eq. (2.25)], i.e., the ratio of the coherence length to the projection of the least-resolvable area of the object surface in the direction **q** (for an object placed on the imaging system axis, this is the projection onto this axis); and this contrast is small.

For a source with small coherence length, $L_c \ll \sigma$ (see Fig. 2.14), the contrast of the speckle pattern in the image is equal to $C \approx L_c/\sigma$. This contrast is very small, which corresponds to the case of imaging with polychromatic white light [see Figs. 2.7(d) and 2.8(d)] or thermal source light. Let us restrict the range of the roughness height for the object under study by the condition $\sigma < 100\lambda$, where λ is the mean wavelength of the radiation scattered by the object. Then, the last inequality $L_c \ll \sigma$ can be replaced by the inequality $L_c < 10\lambda$.

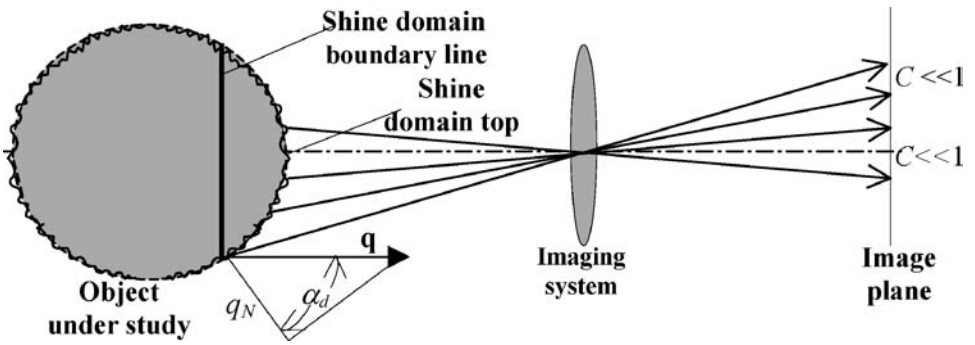

Figure 2.14 The optical image in the case of illuminating the object by polychromatic light. Here, α_d is the angle width of the shine domain. At the shine domain boundary line, $q_N = q\cos\alpha_d = 2\cos\alpha_d$ is minimal.

2.6 Coherent images of small-scale surface roughness

2.6.1 Introduction

In previous sections we analyzed coherent images of rough objects with relatively large-scale surface roughness. Here, we will analyze coherent images of rough objects with rather small-scale surface roughness. Let the roughness height be less than the wavelength λ of the radiation used for obtaining the images, i.e., the roughness standard deviation $\sigma \ll \lambda$. For example, in the optical range this is the case for mirror surfaces and other polished surfaces; in the radio range, for sea and ocean surfaces, and so on. Here we consider statistical characteristics of the coherent images of surfaces with small-scale roughness and devices for determining the roughness standard deviation and correlation radius of mirror surfaces by using their coherent images.

For simplicity, we will restrict calculations to the field correlation function in the coherent images of objects with small-scale roughness and flat mean surfaces, with the correlation radius of the surface roughness height distribution $\ell \gg \lambda$. This is sufficient for analyzing the properties of coherent images for objects with arbitrary shape. A good example of an object surface with small-scale roughness is the surface of a mirror.

2.6.2 Field correlation function of coherent images of surfaces with small-scale roughness

Consider the field correlation function of a coherent image of a surface with small-scale roughness. Let this surface—for instance, the surface of a mirror—have a flat mean surface (Fig. 2.l5), and let it be illuminated by a monochromatic plane wave

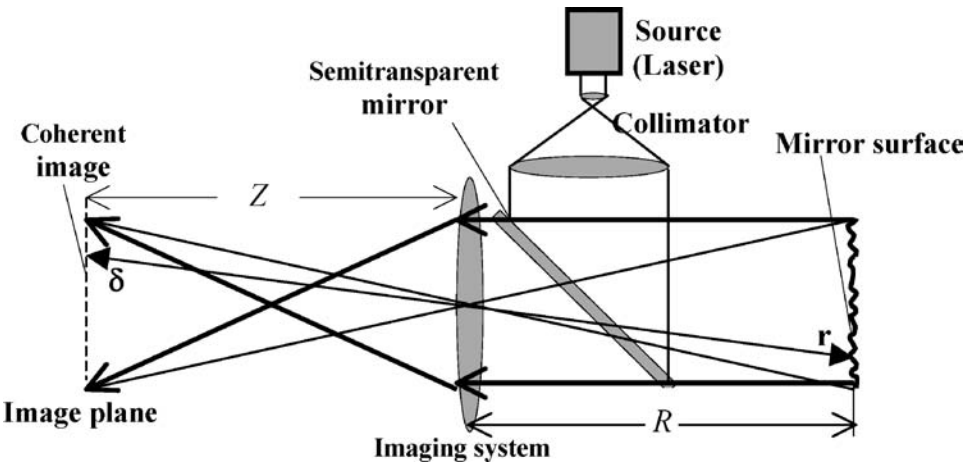

Figure 2.15 Coherent image of a mirror surface. Thin lines denote rays forming the image in the diffuse component; thick lines denote rays forming the image in the specular component.

directed orthogonally to the surface. Let us introduce a coordinate system with the origin at the center of the imaging system. In this case, the field in the surface image is

$$E(\boldsymbol{\delta}) = \left(\frac{1}{\lambda R}\right) \iint E_i(\mathbf{r}) k(\mathbf{r}) h(\mathbf{r}, \boldsymbol{\delta}) \exp\left[\frac{i4\pi\xi(\mathbf{r})}{\lambda}\right] dxdy, \tag{2.27}$$

where $E_i(\mathbf{r})$ is the amplitude distribution for the plane wave illuminating the mirror surface; $\boldsymbol{\delta}$ is the radius vector of the image plane with the components δ_x, δ_y, Z (here, Z is the distance between the mirror surface and the image plane, and δ_x and δ_y are the image plane coordinates); R is the distance between the mirror surface and the imaging system; x and y are mirror surface coordinates; $\xi(\mathbf{r}) = \xi(x, y)$ is a random function describing the surface roughness height distribution; $k(\mathbf{r}) = k(x, y)$ is the reflection factor distribution; and $h(\mathbf{r}, \boldsymbol{\delta}) = h(x, y, \boldsymbol{\delta})$ is the pulse response function of the imaging system. If the imaging system has high resolution, then the field correlation function is

$$B_f(\boldsymbol{\delta}_1, \boldsymbol{\delta}_2) = \langle E(\boldsymbol{\delta}_1) E^*(\boldsymbol{\delta}_2) \rangle - \langle E(\boldsymbol{\delta}_1) \rangle \langle E^*(\boldsymbol{\delta}_2) \rangle, \tag{2.28}$$

where the brackets $\langle\rangle$ denote averaging over all realizations of the random function $\xi(\mathbf{r})$.

Let, for simplicity, the random function ξ have a Gaussian distribution with the Gaussian correlation function

$$\langle \xi(x_1, y_1) \xi(x_2, y_2) \rangle = \sigma^2(x_1, y_1) \exp\left[-\frac{(x_1 - x_2) + (y_1 - y_2)^2}{\ell^2}\right]. \tag{2.29}$$

Then, for $\sigma \ll \lambda$, it follows from Eqs. (2.27) and (2.28) that in the case of a high-resolution imaging system, where $P_r \sim (\lambda R)/d_\rho \ll d_o$ (d_ρ is the imaging system aperture size and d_o is the size of the illuminated area of the mirror surface), we obtain $B_f(\boldsymbol{\delta}_1, \boldsymbol{\delta}_2) \approx [|E_i(\boldsymbol{\delta}) k(\boldsymbol{\delta})|^2/(\lambda R)^2] B_d(\boldsymbol{\delta}_1, \boldsymbol{\delta}_2)$, where

$$B_d(\boldsymbol{\delta}_1, \boldsymbol{\delta}_2) = \left[\frac{4\pi\sigma(\boldsymbol{\delta})}{\lambda}\right]^2 \iiiint \exp\left[-\frac{(x_1 - x_2) + (y_1 - y_2)^2}{\ell^2}\right] \times h(x_1, y_1, \boldsymbol{\delta}) h^*(x_2, y_2, \boldsymbol{\delta}) dx_1 dy_1 dx_2 dy_2.$$

The correlation radius of the field distribution E in the image of the mirror surface is determined from the relation $\rho_f(\boldsymbol{\delta}) = [\int B_d(\boldsymbol{\delta}, \boldsymbol{\delta}_1) d\boldsymbol{\delta}_1]/B_d(\boldsymbol{\delta}, \boldsymbol{\delta})$. Mean intensity in the mirror surface image is equal to

$$\langle I(\boldsymbol{\delta}) \rangle = \langle |E(\boldsymbol{\delta})| \rangle^2 = I_s(\boldsymbol{\delta}) + I_d(\boldsymbol{\delta}),$$

where $I_s(\boldsymbol{\delta}) = [|RE_i(\boldsymbol{\delta}) k(\boldsymbol{\delta})|^2/Z^2]$, $I_d(\boldsymbol{\delta}) \approx [|E_i(\boldsymbol{\delta}) k(\boldsymbol{\delta})|^2/(\lambda R)^2] B_d(\boldsymbol{\delta}, \boldsymbol{\delta})$; $\boldsymbol{\delta} = -Z\mathbf{r}/R$ is the radius vector of the point in the image plane optically conjugated to the radius vector $\mathbf{r}$ of the point on the mirror surface.

We notice that the image intensity is a sum of two terms: the first term I_s is the specular component; the second term I_d is the diffuse component formed by diffraction of the illuminating light by the mirror surface roughness. We select the second term I_d with the help of a very small light trap placed in the imaging system focus (Fig. 2.15) that absorbs specular reflected rays and, hence, suppresses the specular component of the field. The imaging system, together with the light trap, conserves in the image plane only the diffuse component $E_d(\boldsymbol{\delta})$ of the field $E(\boldsymbol{\delta})$. It is easy to show that when $\sigma \ll \lambda$, the mean intensity and correlation function of this component are I_d and $B_f(\boldsymbol{\delta}_1, \boldsymbol{\delta}_2)$.

It is useful to present the statistical characteristics of the field distribution $E_d(\boldsymbol{\delta})$ in a mirror surface image formed by diffuse light in the two limiting cases:

(1) The case where $\ell \gg P_r$. Under this condition, the imaging system aperture is large enough to collect all diffuse light diffracted by each particular element of the mirror surface. This light propagates within the cone with an angle $\alpha \approx \lambda/\ell$ (see Fig. 2.15). In this case $B_f(\boldsymbol{\delta}_1, \boldsymbol{\delta}_2) \approx I_d(\boldsymbol{\delta}_1) \exp[-(\boldsymbol{\delta}_1 - \boldsymbol{\delta}_2)^2/\ell^2]$, where

$$I_d(\boldsymbol{\delta}) = \frac{16\pi^2 |E_i|^2 |k(\boldsymbol{\delta})|^2 \sigma^2(\boldsymbol{\delta}) P_r^4}{\lambda^4 R^2}. \tag{2.30}$$

We see that in this case, the correlation radius of the field distribution $E_d(\boldsymbol{\delta})$ is approximately equal to the correlation radius of the mirror surface roughness: $\rho_f(\boldsymbol{\delta}) \approx \ell(\boldsymbol{\delta})$. Hence, in this case the imaging system resolves separate elements of the mirror surface.

(2) $\ell \ll P_r$. In this case the imaging system collects only some of the diffuse components of the scattered radiation. Then,

$$B_f(\boldsymbol{\delta}_1, \boldsymbol{\delta}_2) \approx I_d(\boldsymbol{\delta}_1) S_c(\boldsymbol{\delta}_1, \boldsymbol{\delta}_2), \tag{2.31}$$

where $S_c(\boldsymbol{\delta}_1, \boldsymbol{\delta}_2) = \int h(\mathbf{r}, \boldsymbol{\delta}_1) h^*(\mathbf{r}, \boldsymbol{\delta}_2) d\mathbf{r}$, and

$$I_d(\boldsymbol{\delta}) = \frac{16\pi^2 I_s(\boldsymbol{\delta}) \sigma^2(\boldsymbol{\delta})}{\lambda^2} = \frac{16\pi^2 |E_i|^2 k(\boldsymbol{\delta}) \sigma^2(\boldsymbol{\delta}) \ell^2(\boldsymbol{\delta}) P_r^2}{\lambda^4 R^2}.$$

In this case, the correlation radius of the field distribution E_d in the mirror surface image is approximately equal to the imaging system resolution, $\rho_f(\boldsymbol{\delta}) = P_r \approx (\lambda R)/d_\rho$. This result coincides with the expression for the correlation radius of the field distribution in the coherent image of a surface with large-scale roughness, when the standard deviation of roughness height is much greater than the wavelength of light illuminating the surface, $\sigma \gg \lambda$, and the imaging system does not resolve separate elements of the rough surface. Hence, in this case, coherent images of surfaces with small-scale roughness, as well as coherent images of surfaces with rather large-scale roughness, manifest a speckle pattern with speckle size $\sim(\lambda R)/d_\rho$.

For the case of an imaging system with a circular aperture and constant pupil function, we can derive an analytical expression for the intensity of the diffuse component of the coherent image of a surface with small-scale roughness. Then, the imaging system pulse response is $h(x, y, \delta_x, \delta_y) = J_1(\Re)/\Re$, where $\Re = (2\pi d_\rho w)/\lambda$,

$$w = \sqrt{\left(\frac{x}{R} + \frac{\delta_x}{Z}\right)^2 + \left(\frac{y}{R} + \frac{\delta_y}{Z}\right)^2},$$

$J_1(\Re)$ is the Bessel function of the first order, d_ρ is the system's aperture diameter, and the intensity in the coherent image in diffuse light for arbitrary relations between ℓ and P_r is

$$I_d(\delta) \approx \frac{16\pi^2 I_s(\delta)\sigma^2(\delta)}{\lambda^2}\left[1 - \exp -\frac{d_\rho^2 \ell^2(\delta)}{R^2\lambda^2}\right]. \tag{2.32}$$

Relation (2.32) can be explained by using the energy approach. Let us turn to Fig. 2.16, which describes the formation of a mirror surface image in diffuse light with the help of a very small light trap; and let, for simplicity, $\mu = 1$ and $k = 1$.

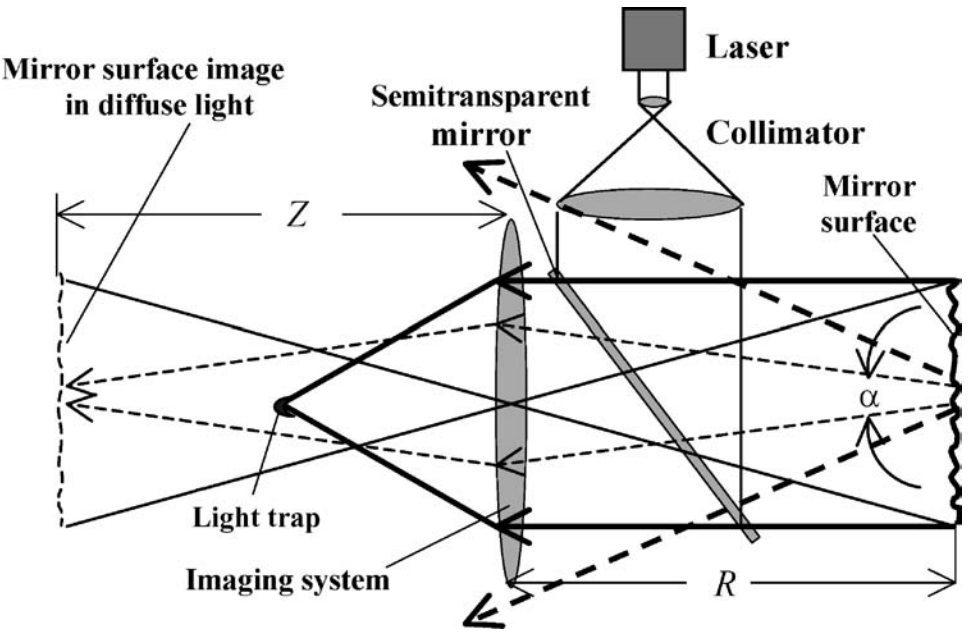

Figure 2.16 Formation of a mirror surface image in diffuse light with the help of a very small light trap. The dashed lines show the rays restricting most of the light diffracted by a small part of the mirror surface, which occupies the cone with an angle $\alpha \approx \lambda/\ell$. The thin and thick dashed lines demonstrate the cases $\ell > P_r$ and $\ell < P_r$, respectively, where $P_r \approx (\lambda R)/d_\rho$ is the imaging system resolution.

Then, relation (2.32) has the following form:

$$I_d(\delta) \approx \frac{16\pi^2|E_i|^2\sigma^2}{\lambda^2}\left[1 - \exp -\frac{d_\rho^2\ell^2(\delta)}{R^2\lambda^2}\right]. \tag{2.33}$$

If $P_r \approx (\lambda R)/d_\rho \ll \ell$, then

$$I_d \approx \frac{16\pi^2|E_i|^2\sigma^2}{\lambda^2}. \tag{2.34}$$

Let us explain this relation. If $(\lambda R)/d_\rho \ll \ell$, all energy Q_d of the diffuse component of light diffracted by a small area of the mirror surface gets into the imaging system. For $\xi \ll \lambda$ it is not difficult to obtain

$$Q_d = \langle|E_d'|^2\rangle S_b = \frac{16\pi^2|E_i|^2\sigma^2 S_b}{\lambda^2}, \tag{2.35}$$

where $E_d' = 2 \times (E_i 2\pi\xi)/\lambda$ is the scattered field component formed by the surface roughness close to the mirror surface, and S_b is the small illuminated area on the mirror surface. The factor 2 appears since each ray passes the rough surface twice. Taking into account the energy conservation law, we can represent the scattered energy of the diffuse component in the image plane as $Q_d = I_d S_b$. From Eq. (2.35) we obtain the required relation (2.33):

$$I_d \approx \frac{Q_d}{S_b} = \frac{16\pi^2|E_i|^2\sigma^2}{\lambda^2}.$$

For the intermediate case $(\lambda R)/d_\rho \sim \ell$ and for the case $(\lambda R)/d_\rho \gg \ell$, taking into account that most of the light diffracted by the small part of the mirror surface occupies a cone with angle $\alpha \approx \lambda/\ell$, we can approximate the mean intensity of the diffuse component in the imaging system aperture by the exponential function $I_a = I_0 \exp\{-[\ell^2(\rho_x^2 + \rho_y^2)/\lambda^2]\}$, where ρ_x and ρ_y are coordinates in the aperture plane of the imaging system, and I_0 is the mean intensity at the aperture center. This result can be obtained by taking into account that when $\sigma \ll \lambda$, then $I_a = \langle|E_a(\rho_x, \rho_y)|^2\rangle$, where

$$E_a = \left(\frac{4\pi i E_0}{\lambda R}\right)\iint \xi(x, y)\exp\left[\frac{2\pi i(\rho_x x + \rho_y y)}{\lambda R}\right]dxdy. \tag{2.36}$$

The energy of the diffuse component passing through the imaging system aperture is then calculated by integrating over the aperture plane: $Q_p = \iint I_a dudv = \iint \langle|E_a(\rho_x, \rho_y)|^2\rangle dudv$. For a circular imaging system aperture, $Q_p = Q_d$, and using Eqs. (2.29) and (2.36), we obtain Eq. (2.33):

$$I_d(\delta) = \frac{Q_p}{S_b} \approx \left(\frac{16\pi^2|E_0|^2\sigma^2}{\lambda^2}\right)\left\{1 - \exp\left[-\left(\frac{d_\rho \ell}{\lambda R}\right)^2\right]\right\}.$$

2.6.3 Determining the roughness standard deviation and correlation radius of mirror surfaces by means of their coherent images

The roughness standard deviation σ and correlation radius ℓ of (polished) mirror surfaces, for which σ is smaller than the wavelength λ, are usually determined by measuring the diffuse and reflected specular components of monochromatic radiation scattered by this surface. As a rule, these measurements are carried out by using low-energy lasers with continuous radiation. One can apply such lasers for unmoving and stable surfaces, since the radiation energy needed for measurements can be accumulated over a long time period. Yet, there are real-life situations that require a rapid determination of σ and ℓ. For solving such problems, it is necessary to use high-energy pulsed lasers. This is the case, for instance, when the surface under study is moving or unstable, in particular during the process of mirror production by metal surface sharpening with a diamond-tipped cutting tool. In this case, the necessary radiation energy scattered by a fixed surface area is accumulated during the short time when the surface parts under study are practically immobile.

Now we will consider a device that can be applied for measuring the roughness standard deviation σ and correlation radius ℓ of mirror surfaces (Fig. 2.17). A thin laser beam illuminates a small part of the mirror surface. The imaging system forms two images of the mirror surface in diffuse light. Detector 1 detects all diffuse scattered radiation $I_{d1}(\delta)$ passing through the imaging system whose aperture diameter is $d_{\rho 1}$; and detector 2 detects radiation that passes through an aperture $I_{d2}(\delta)$ with an equivalent diameter equal to $d_{\rho 2}$. Here, $\boldsymbol{\delta} = -\mathbf{r}/\mu$ ($\mu = R/Z$ is the scale factor) is the radius vector of the area in the image plane optically conjugated to the radius vector $\mathbf{r}$ of the small illuminated area of the mirror surface. For

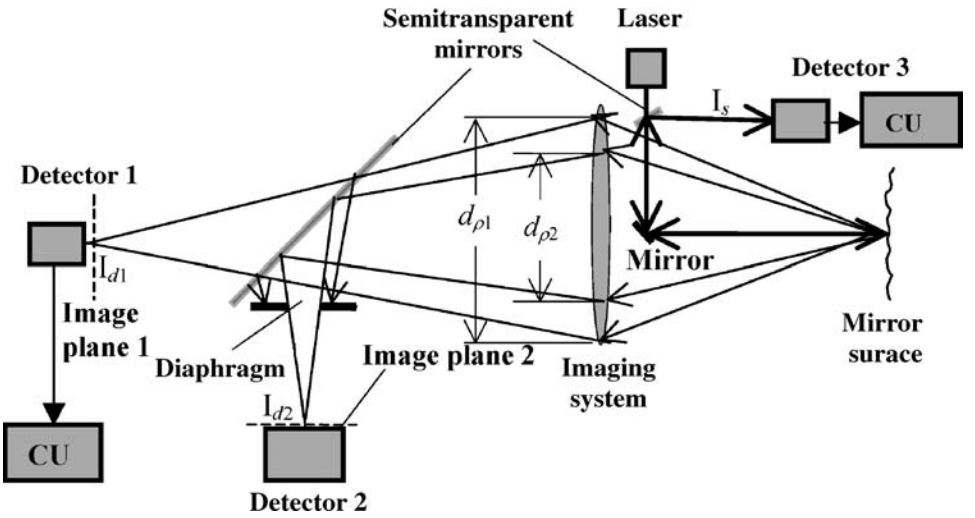

Figure 2.17 A device for measuring the roughness standard deviation σ and correlation radius ℓ of a mirror surface. CU is the calculating unit.

instance, in Fig. 2.17, $\mathbf{r}$ has components $0, 0, R$, and $\boldsymbol{\delta}$ has components $0, 0, Z$. Detector 3 detects the specular component of the radiation with intensity I_s by means of two mirrors, a highly reflecting one and a semitransparent one (the thick rays in Fig. 2.17). Finally, the calculating unit (CU) computes the roughness standard deviation σ and the correlation radius ℓ of the mirror surface roughness.

We used the device depicted in Fig. 2.17 to determine roughness parameters with the help of Eq. (2.36). The mirror surface was illuminated by a pulsed ruby laser, and three values were measured: the energy diffuse components Q_{p1} and Q_{p2} passing through imaging system's apertures with diameters d_{p1} and $d_{p2} \approx 0.7d_{p1}$, respectively, and the energy Q_s of the specularly reflected component. The roughness parameters are determined from the formulas

$$\sigma = \frac{\lambda}{4\pi}\sqrt{\frac{Q_{\rho 1}}{Q_s(1-\alpha^2)}}$$

and

$$\ell = \frac{\lambda R}{d_{\rho 2}}\sqrt{-2\ln\alpha},$$

where $\alpha = 1 - Q_{\rho 1}/Q_{\rho 2}$. The device ensured mirror roughness measurements to approximately 10 nm with ~10% accuracy. The proposed device can be used to measure these parameters during mirror production by metal surface sharpening with a diamond-tipped cutting tool.

2.7 Speckle structure of the time spectrum of a coherent field scattered by a moving rough object

In the previous section we analyzed time dependencies for the correlation function of a coherent field scattered by a moving object.[12,44] Let us analyze the time–frequency spectrum $S(\omega)$ of such fields. This can be achieved by heterodyning the scattered field with a reference signal $\exp(-i\omega_0 t)$, where ω_0 is the frequency of the illuminating radiation, and analyzing the resulting signal by means of a spectrum analyzer:

$$S(\omega) = \frac{1}{T}\int_{t_0}^{t_0+T} E(\boldsymbol{\rho}, t)\exp(-i\omega_0 t + i\omega t)dt, \tag{2.37}$$

where t_0 and T are the initial time and the processing time, respectively, and $\boldsymbol{\rho}$ is the radius vector of the receiving aperture. With a spectrum analyzer one obtains the field intensity spectrum, $I(\omega) = |S(\omega)|^2$, and analyzes its mean value over all realizations of surface roughness height, $\langle I(\omega)\rangle$. Consider, for simplicity, the intensity spectrum of a field scattered by a rotating rough narrow stripe at the point

$\boldsymbol{\rho} = 0$ and the coherent image of the stable stripe, $I(\delta_x)$. In this case, within a small stripe domain, the reflection coefficient and the surface roughness height are functions of the coordinate x on the stripe domain, $k(\mathbf{r}) \approx k(x)$ and $\xi(\mathbf{r}) \approx \xi(x)$. Taking into account relation (2.37) for the spectrum of the field scattered by this object, we obtain[12]

$$S(\omega) \sim \int_{-d_s/2}^{d_s/2} k(x) \exp\left[\frac{i4\pi\xi,(x)}{\lambda}\right] \operatorname{sinc}\left[T\left(\frac{2\pi\Omega x}{\lambda - \omega}\right)\right] dx, \tag{2.38}$$

where d_s is the stripe size.

If $\sigma/(\ell\Omega) \gg T \gg \lambda/(\Lambda\Omega)$, where Λ is the size of the smallest detail of the object, then σ and ℓ are the standard deviation and the correlation radius of the object's surface roughness, respectively, and the function $\operatorname{sinc}\{T[(2\pi\Omega x)/\lambda - \omega]\}$ is narrower in x than Λ, but broader than the correlation radius of the scattered field phase distribution close to the object surface, $\rho_\varphi = (\lambda\ell)/\sigma$. We then obtain

$$\langle I(\omega)\rangle \sim \left|k\left(x = -\frac{\lambda\omega}{2\pi\Omega}\right)\right|^2. \tag{2.39}$$

On the other hand, it is not difficult to show that in the case of a high-resolution imaging system, the averaged intensity in the coherent image of a stable stripe is $\langle I(\delta_x)\rangle \sim |k(x = -\mu\delta_x)|^2$, where μ is a scaling factor. Comparing the expressions for $\langle I(\omega)\rangle$ and $\langle I(\delta_x)\rangle$, we see that they are identical. This is not surprising since in the linear approximation in t, the field $E(0, t)$ coincides, after a certain scaling, with the field $E(u, 0)$ scattered by a stable stripe, where u is a coordinate of the imaging system's aperture. Indeed, from a physics viewpoint, rotation of the stripe leads to a simultaneous rotation of the scattered field (see Sec. 1.4). Let us take into account that spectrum formation and image formation are mathematically quite similar, in the sense that the first operation consists of a Fourier time transform and the second a Fourier space transform. Then we arrive at the result that the spectral intensity pattern coincides with the intensity distribution in the image of a stable stripe.

Consider the relative variance of $I(\omega)$ and its correlation function. After calculations similar to the ones used when deriving relation (A1.4) of Appendix 1, one can show that under the condition $T \gg \lambda/(\Lambda\Omega)$, the relative variance of $I(\omega)$ and its correlation function can be represented as

$$\frac{\langle I^2(\omega)\rangle - \langle I(\omega)\rangle^2}{\langle I(\omega)\rangle^2} \approx 1$$

and

$$\langle I(\omega_1)I(\omega_2)\rangle - \langle I(\omega_1)\rangle\langle I(\omega_2)\rangle \sim \operatorname{sinc}^2[T(\omega_1 - \omega_2)].$$

These expressions show that the intensity spectrum $I(\omega)$ has unity contrast and correlation angular frequency $\omega_f = 2\pi/T$. Taking into account that, according to Eq. (2.36), the spectrum's width is $(2\pi d_s\Omega)/\lambda$, we obtain that each realization of the intensity spectrum consists of $M_\Omega = (\Omega T d_s)/\lambda$ lobes. We see a close analogy between the intensity spectrum and the coherent image. For this reason, we can consider the intensity spectrum as a one-dimensional frequency–time-coherent image formed by means of the Fourier time transform. The processing time T in the case of a frequency–time image can be considered as the time aperture of the spectrum analyzer, and the spectrum lobes can be considered as frequency speckles with mean size $f_c = 1/T$. Hence, the intensity spectrum $I(\omega)$ is a speckle pattern. In Chapter 5, we consider a more general Fourier–Fresnel transform of the field scattered by a moving rough object. Such a transformation allows one to form two-dimensional images of objects. The intensity distribution in this image is the two-dimensional speckle pattern.

Analysis of scattered field spectra is also useful for explaining the effects relating to the scattering of small-width beams by various objects. For instance, in the case of a rough object moving in a single plane and illuminated by a Gaussian beam with width b, such as $d_o \gg b \gg (\lambda\ell)/\sigma$, where d_o is the object size, the average intensity spectrum of the scattered light is[12]

$$\langle I(\omega)\rangle \sim \left(\frac{\ell}{\sigma}\right)\exp\left(-\frac{\ell^2\tan^2\theta}{\sigma^2}\right)\exp\left[-\left(\frac{\omega b}{v}\right)^2\right],$$

where θ is the angle of incidence of the illuminating beam. One can see that there is a spectral broadening by $\omega_b = v/b$, which can be explained as follows: In the course of the object's motion, the illuminating beam hits new elements of the rough surface. As the illuminated part of the rough surface is completely replaced by a new part, the scattered field is also replaced by its new realization. The correlation time of this process is equal to the roughness shift time $t_i = b/v$, which corresponds to the frequency range $\omega_b = 1/t_i = v/b$.

2.8 Conclusions

1. A coherent image of a rough object has the form of a speckle pattern with $M = (S_e S_\rho)/(\lambda r_c)^2$ number of speckles, where S_e is the effective shine (backscattering) domain of the object surface giving the main contribution to the image, S_ρ is the area of the imaging system aperture, λ is the illuminating radiation wavelength, and r_c is the distance from the object to the imaging system. For a spherical rough object, $S_e = (\pi\rho_o^2\sigma^2)/\ell^2$, where σ and ℓ are the standard deviation and the correlation radius of the object surface roughness, respectively, and ρ_o is the sphere radius.
2. The average field intensity in the coherent image of an object with surface roughness height much greater than wavelength λ of the illuminating radiation consists of several distinct bright spots, which are the images of the object

surface's shine (backscattering) domain, whose tops have tangential planes orthogonal to the imaging system's optical axis and whose sizes are determined by the average roughness slope σ/ℓ.

3. For a coherent image of an object with surface roughness height much larger than λ, the contrast in the intensity distribution I is close to unity. In the case of very high resolution imaging, the contrast can exceed unity considerably. In this case, the intensity distribution correlation radius is much smaller than $\mu\ell$, μ being the scaling factor. For a very large imaging system aperture, the contrast is close to zero and the correlation radius is close to ℓ.
4. The quality of a coherent image can be estimated by means of two criteria, one that is local and one that is integral. The local criterion determines the imaging quality for a small detail of the object's surface, which will be high quality if the speckle number in the image of the detail $M_d = (S_d S_\rho)/(\lambda r_c)^2 \gg 1$, where S_d is the area of the surface detail. The integral criterion relates to the quality of the whole image. The quality of a coherent image is high if the relative fluctuations η_c of the parameter

$$K = \frac{\int I_a(\delta)\langle I(\delta)\rangle d\delta}{\int \langle \mathbf{I}(\delta)\rangle^2 d\delta}$$

are small. Here, I and $\langle I\rangle$ denote the real and average intensity distributions in the image, respectively. One of the ways to increase image quality is to accumulate statistically independent realizations of a coherent image. In this case,

$$I_a(\delta) = \frac{1}{N_a}\sum_{n=1}^{n=N_a} I_n(\delta),$$

and $\eta_c \approx 1/(MN_a)$, where N_a is the number of accumulated images, M is the speckle number in the realization of the coherent image, and I_n is the intensity distribution in the nth realization of the coherent image. For $N_a \gg 1$ and $M \gg 1$, η_c is very small. The contrast in the accumulated image is $C = 1/(MN_a)$. For $N_a \gg 1$, the contrast is very low.
5. A rough object's image is partially coherent if it is formed by means of illuminating the object with quasi-monochromatic radiation having a coherence length $10L_p > L_c > 10\lambda$, where L_p is the projection of the resolvable domain of the object's surface on the optical axis. In this case, the contrast C of the intensity distribution depends on the orientation of the resolvable domain of the object's surface with respect to the imaging system's optical axis. If the projection of this domain $L_c \ll L_p$, then $C \sim L_c/L_p \ll 1$. An image is incoherent if it is formed by means of polychromatic radiation, such as natural light, that has a coherence length $L_c \ll 10\lambda$. In this case, the contrast in any part of the image is small: $C \sim L_c/\sigma \ll 1$.

6. A coherent image of a surface with small-scale roughness ($\sigma \ll \lambda$), e.g., a mirror surface, contains a high-intensity specular and low-intensity diffuse components (speckle pattern). If the imaging system does not resolve separate elements of the rough surface, then the correlation radius (the average speckle size) of the speckle pattern is $(\lambda r_c)/d_\rho$. In the opposite case, the average speckle size is $\sim\ell$. The standard deviation σ and the correlation radius ℓ of mirror surface roughness are determined by measuring separately the specular and diffuse components of the mirror's coherent image.
7. The time spectrum of a coherent field scattered by a moving rough object has the form of a speckle pattern in frequency coordinates with the speckle size $f_c \approx 1/T$, where T is the time of the scattered field Fourier transform.

2.9 General conclusions to Chapters 1 and 2

1. For a coherent field scattered by a rough object, the fields at points close to the object and far from it are related via the Fourier–Fresnel space transform, and the intensity distribution of the scattered field far from the object has the form of a space speckle pattern.
2. For coherent fields scattered by rough objects, fields on the imaging system's aperture and in the coherent image are related via the inverse Fourier–Fresnel space transform, and the intensity distribution in the coherent image also forms a space speckle pattern.
3. For a coherent field scattered by a moving rough object, the fields at points far from the object and close to it are related via the Fourier time transformation, and the scattered field intensity distribution at a fixed point far from the scattering object forms a time speckle pattern.
4. The object image reconstructed with an intensity hologram (obtained with the help of the Fourier space transformation of the intensity distribution of the field scattered by the rough object) has a speckle structure, with speckle size depending on the size of the hologram. The reconstructed image of the object is given by the space autocorrelation function of its coherent image.
5. A Fourier time transform (the spectrum) of a coherent scattered field at a fixed point far from the scattering moving object also forms a time speckle pattern that is analogous to a typical coherent image. The average speckle size is $\sim 1/T$, T being the time of the spectrum formation. Similarly, it is shown in Chapter 5 that the Fourier–Fresnel time transform of the coherent scattered field at a fixed point far from the scattering moving object forms a two-dimensional object pattern with a speckle structure.

The results obtained in Chapters 1 and 2 reveal the universal nature of speckle patterns of fields scattered by rough objects, which manifest themselves both in space and time.

Chapter 3

Use of Coherent Fields and Images to Determine the Dynamic Parameters of Remote Objects

3.1 Introduction

This chapter describes particular methods of obtaining information about the motion and deformation of objects that use coherent fields scattered by these objects and their coherent images. The object under investigation should have a statistically rough surface. The result is that the field at particular points of the reception plane and the image plane is produced by waves coming from different surface points. If the object is illuminated by monochromatic radiation, then interference of these waves forms scattered coherent fields and coherent images with random speckle structure—the speckle pattern. This structure can give us information about the parameters that describe the object's motion. Indeed, the motion of the object changes the phase difference between the waves coming from adjacent surface areas. This, in turn, brings to motion some fragments of the speckle pattern in the reception plane of the scattered field and the image plane. As a result, the speckle pattern brightness is varied. We will use this to estimate the parameters of the object's motion: the vector of linear velocity and the angular velocity of rotation. We will also use these variations to estimate the parameters of surface deformations, such as changes of components of unit vectors normal to particular areas of the object's surface.

The concept of using coherent fields and images to determine the dynamic parameters of remote objects has drawn considerable interest.[13,44–48] However, investigators dealing with the subject usually give neither explicit algorithms for estimating these parameters nor relationships for determining the accuracy of the estimation. In this chapter we will fill that information gap. The approach we suggest here is applicable to most of the known coherent-image methods for estimating the parameters of remote objects, and it allows us to estimate the parameters with high accuracy by relatively simple and reliable technical means. The methods considered in this chapter use no reference beam and therefore can be used with short-coherence-length sources, e.g., less than 1 m.

3.2 Methods of determining the linear velocity of a remote rough object

The well-known method of determining the radial component v_R of the linear velocity vector of an object that is used to locate remote objects is based on the interference of a reference beam with a coherent field scattered by the moving object. A detector registers the interference fringes, and the Doppler beat frequency f_R is determined. It is known that $v_R = f_R\lambda$, where λ is the wavelength of the illuminating beam. The drawback of this method is the necessity to form a stable reference beam and to satisfy the condition that the path difference between the reference and signal beams is less than the coherence length of the light source. In the case of a moving remote object, this condition requires that special light sources with large coherence length be used. Another strict limitation is that the arrangement used for velocity measurement must be vibration-proof. Moreover, such a scheme does not allow one to determine the tangential component of the linear velocity vector of a remote object.

Figure 3.1 is a schematic that shows how to determine the tangential component v_{tA} of the linear velocity $\mathbf{v}_A$ for a selected area A of an object's surface. The method does not have the above-mentioned drawbacks of the previous methods. A monochromatic light source illuminates the moving object. A two-aperture screen covers the imaging system, whose optical axis is directed toward the object under investigation. The two apertures are placed symmetrically with respect to the optical axis of the lens.

The distance between the apertures, s_H, is assumed to be much larger than the aperture size d_H. Light scattered by area A, after passing through the two apertures,

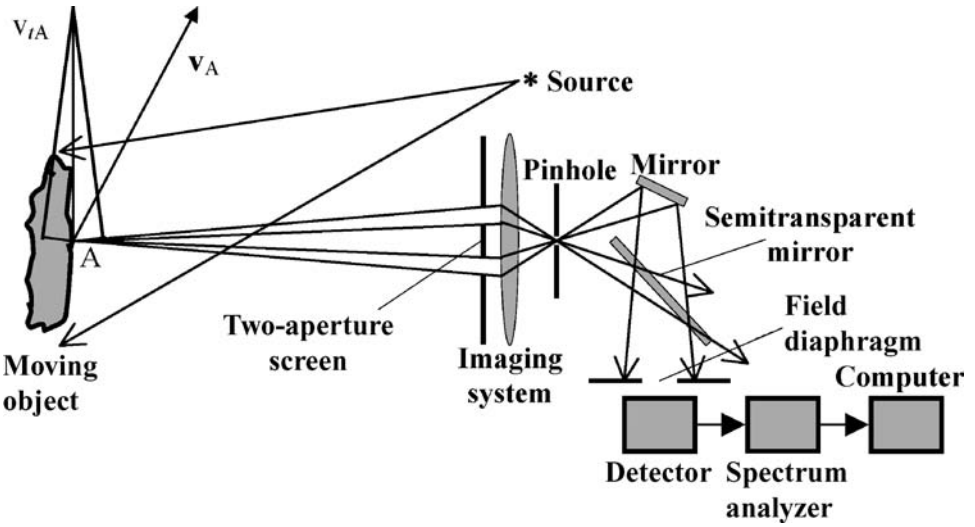

Figure 3.1 The arrangement for determining the tangential components of velocities for a selected area of an object's surface.

is focused in the image plane and selected by the pinhole. Mirrors direct the two beams with different frequencies to the field diaphragm and to the detector. The electrical signal from the detector is fed to the spectrum analyzer, and the output spectral curve is analyzed by the computer to determine the frequency difference f_D and to obtain the estimate for the tangential component v_{tA} of the linear velocity for a particular area of the object's surface.

To simplify the calculations, we assume that the remote object has a flat surface orthogonal to the imaging system axis and moves with a constant velocity. With sufficient accuracy, the distribution of the light field in the image plane can be written as

$$E(x_H, y_H, t) \sim \int k(x - V_{tA}t, y) \exp\left[\frac{2\pi i}{\lambda}(r_c + |\mathbf{r} - \boldsymbol{\rho}_S|)\right] \exp\frac{4i\pi\xi(x - V_{tA}t, y)}{\lambda} \times h(x_H, y_H, \mathbf{r})d\mathbf{r}, \tag{3.1}$$

where x_H and y_H are coordinates of the pinhole optically conjugated to the coordinates $x_A = -(r_c x_H)/z_i$ and $y_A = -(r_c y_H)/z_i$ of the area A; r_c is the distance between the two-aperture screen and the object's center of gravity; z_i is the distance between the two-aperture screen and the image plane; the Z axis is directed along the optical axis of the imaging system; t is time; $\mathbf{r}(x, y, z)$ is the radius vector of the object surface; $k(\mathbf{r})$ is the distribution of field reflection coefficients on the object surface; $\boldsymbol{\rho}_s$ is the radius vector of the illuminated source;

$$h(x_H, y_H, \mathbf{r}) = \operatorname{sinc}\left[\frac{2\pi d_H}{\lambda}\left(\frac{x}{r_c} + \frac{x_H}{z_i}\right)\right] \operatorname{sinc}\left[\frac{2\pi d_H}{\lambda}\left(\frac{y}{r_c} + \frac{y_H}{z_i}\right)\right] \times \cos\left[\frac{2\pi s_N}{\lambda}\left(\frac{x}{r_c} + \frac{x_H}{z_i}\right)\right] \cos\left[\frac{2\pi s_N}{\lambda}\left(\frac{y}{r_c} + \frac{y_H}{z_i}\right)\right]$$

is the pulse response (point spread function) of the imaging optics consisting of a screen with two apertures of square shape $d_H \times d_H$ and the lens; and $\xi(x, y)$ is the roughness height distribution on the object surface. In Fig. 3.1, $x_H = y_H = 0$. The spectrum analyzer gives the spectral curve

$$S_H(f) = \frac{1}{T}\left|\int_{t_0}^{t_0+T} |E(x_H, y_H, t)|^2 \exp(2\pi i f t)dt\right|^2,$$

where t_0 is the initial time and T is the spectrum formation time. Using Eq. (3.1), we obtain $S_H(f) = S_L(-f_D) + S_0 + S_L(f_D)$. One can see from this expression that the spectrum has three lobes (a central one and two side ones) with maximums at $f_{-1} \approx f_i - f_D$, $f_0 = f_i$, $f_1 \approx f_i + f_D$, where f_i is the intermediate frequency, and $f_D = (s_H v_{tA})/(\lambda r_c)$. Under the assumption that $\mathrm{E}(x_H, y_H, t)$ has a Gaussian distribution, one can show that the spectrum $S(f)$ is a random function with the correlation

frequency $f_c = 1/T$, and the spectral curve is presented by time speckle pattern with the speckle width about $f_c = 1/T$ and the average spectrum (see Sec. 2.7)

$$\langle S(x_H, y_H, f)\rangle = \int_{t_0}^{t_0+T}\int_{t_0}^{t_0+T} \left|\langle E(x_H, y_H, t_1)E*(x_H, y_H, t_2)\rangle\right|^2 \times \exp[i2\pi f(t_1 - t_2)]dt_1 dt_2, \tag{3.2}$$

where f is the spectral frequency and $\langle\rangle$ denotes averaging over different realizations of the roughness height distribution $\xi(x, y)$.

Approximating the point spread function of the imaging system by a Gaussian function and assuming that the roughness height spatial distribution $\xi(x, y)$ has a Gaussian correlation function, with the help of expression (3.2) it can be shown that the averaged spectrum in the side lobes is

$$\langle S_L(f \pm f_D)\rangle \sim \frac{\ell^4}{\sigma^4}\,\mathrm{sinc}^2\left[\frac{2\pi}{\Delta f_D}(f \pm f_D)\right]\left[\int |k(\mathbf{r})h(\mathbf{r}, x_H, y_H)|^2 d\mathbf{r}\right]^2. \tag{3.3}$$

Here, $\Delta f_D = M_V f_c$ is the width of the spectrum side lobes,

$$M_V = \begin{cases} \dfrac{vTd_o}{r_c\lambda}, & \text{if } d_H \ll \dfrac{r_c\lambda}{d_o} \\ \dfrac{vT}{d_H}, & \text{if } \dfrac{r_c\lambda}{d_o} \ll d_H \ll \sqrt{\lambda r_c} \\ \dfrac{vTd_H}{r_c\lambda}, & \text{if } d_H \gg \sqrt{\lambda r_c} \end{cases}$$

is the number of correlation cells (time speckles with the speckle width $f_c = 1/T$; see Sec. 2.7) in the spectrum side lobe; σ and ℓ are the standard deviation and the correlation radius of the roughness height spatial distribution; and d_o is the size of an illuminated surface of the object under study.

Let us now evaluate the accuracy of the method. The estimate of the object linear velocity can be expressed analytically as

$$\hat{v} = \frac{\lambda r_c \int (f - f_i)S_L(f \pm f_D)df}{s_H \int S_L(f \pm f_D)df}.$$

From the last expression, we obtain

$$\langle\hat{v}\rangle = v = f_D\frac{\lambda r_c}{s_H}. \tag{3.4}$$

Formula (3.4) has a simple geometric interpretation (Fig. 3.1). The tangential component of the object velocity has two projections, $v_1 = -(s_H v)/2r_c$ and $v_2 =$

$(s_H v)/2r_c$, on the rays connecting the two apertures in the two-aperture screen with the object surface point A. These projections cause the difference between the frequencies of the beams selected by the two apertures, $f_D \approx (v_2 - v_1)/\lambda = s_H/(\lambda r_c)$. The standard deviation σ_V of the estimate (the error in the object velocity measurement) is determined by the number of time speckles:

$$\sigma_V = \sqrt{\langle \hat{v}^2 \rangle - \langle \hat{v} \rangle^2} = \frac{v}{\sqrt{M_V}}. \tag{3.5}$$

Hence, the accuracy of the velocity estimate σ_v is determined by the characteristics of the time speckle pattern of the spectral curve $S(f)$ and the width of the spectrum side lobes Δf_D. Therefore, it is important to give a physical explanation for the frequency spread around the spectrum maxima.

For the case $\sqrt{r_c\lambda} \ll d_H$, the spectrum width $\Delta f_D = (v d_H)/(\lambda r_c)$ can be explained by the spread of the Doppler beats between the frequencies of rays going from a certain small area of the object surface to different points of the two apertures. The spread is equal to $\Delta f_D = (v_1 - v_2)/\lambda = (v d_H)/(\lambda r_c)$, where $v_1 = (v d_H)/2r$ and $v_2 = -(v d_H)/2r_c$ are projections of the object's velocity on the peripheral rays [Fig. 3.2(a)].

For the case $\sqrt{r_c\lambda} \gg d_H \gg (\lambda r_c)/d_o$, only rays coming from the smallest area of the object surface resolved by the imaging system with the aperture size d_H hit the pinhole (see Fig. 3.1). As a result, the width of the spectrum side lobes Δf_D is determined by the Doppler beats between the frequencies of peripheral rays from this area, $\Delta f_D = (v_1 - v_2)/\lambda = v/d_H$, where $v_1 = (v\lambda)/2d_H$, and $v_2 = -(v\lambda)/2d_H$ are projections of the object's velocity on the peripheral rays [Fig. 3.2(b)]. Another explanation is based on the synchronous motion of the scattered field speckles due to the object motion; a full change in the speckle pattern within the two apertures of

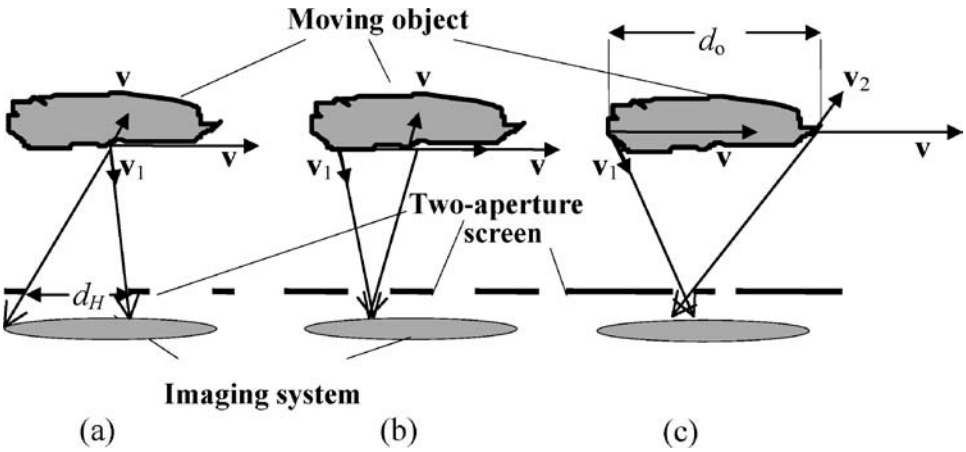

Figure 3.2 Explanation of the spectrum spreading around the side lobe maximums of the spectral curve.

the screen (see Fig. 3.1) occurs in time $\tau = d_H/v$. Hence, the width of the spectrum side lobes is $\Delta f_D = 1/\tau = v/d_H$.

In the case $d_H \ll (\lambda r_c)/d_o$ [Fig. 3.2(c)], the width of the spectrum side lobe $\Delta f_D = (vd_o/(\lambda r_c)$ can be explained by the spread of the Doppler frequency beats of all rays going from the object surface to the two apertures in the screen (see Fig. 3.1), including peripheral rays. The spread is equal to $\Delta f_D = (v_1 - v_2)/\lambda = (d_o v)/(\lambda r_c)$, where $v_1 = (d_o v)/2r_c$, $v_2 = -(d_o v)/2r_c$ are projections of the object's velocity on the peripheral rays [Fig. 3.2(c)]. We can present another explanation: the width of the side lobe spectrum $\Delta f_D = (d_o v)/r_c$ is inversely proportional to the time during which a single speckle of size $\sim(\lambda r_c)/d_o$ moves along one of the two apertures during object motion. The plots in Fig. 3.3 show dependence of the frequency difference f_D on the velocity v for different s_H for the case $\sqrt{r_c\lambda} \ll d_H$ and for $r_c = 1$ m, $\lambda = 0.63$ μm. The measurements are performed using the arrangement presented in Fig. 3.1.

In the case $d_H \ll (\lambda r_c)/d_o$, the object's velocity can be measured directly with the help of a very simple arrangement (Fig. 3.4) using the scattered coherent field

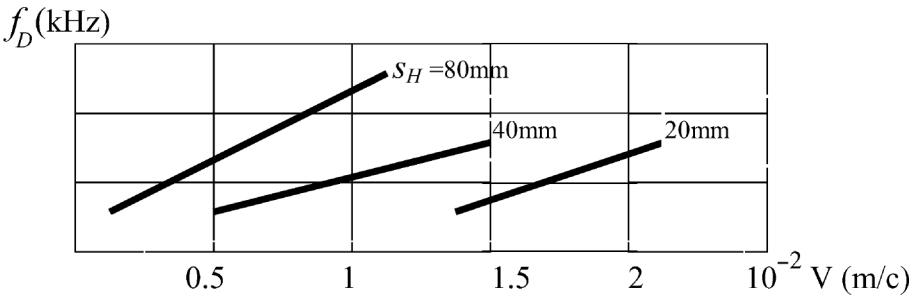

Figure 3.3 The relative Doppler shift f_D as a function of the tangential component v of the object's linear velocity measured for different s_H. Straight lines correspond to the relation $f_D = (s_H v)/(\lambda r_c)$.

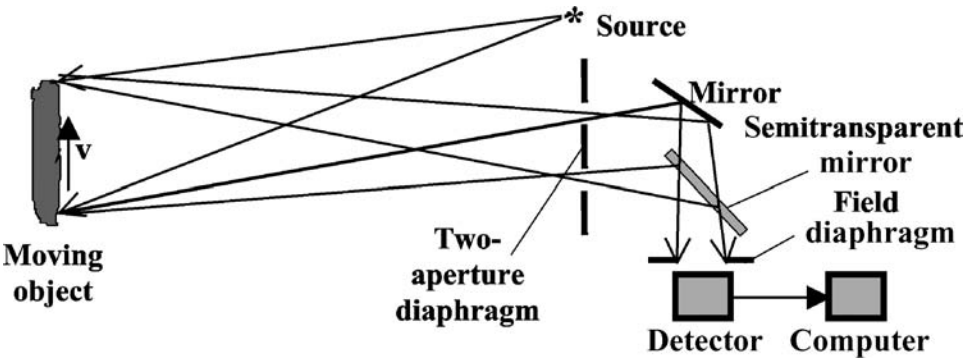

Figure 3.4 The arrangement for determining the tangential component of an object's velocity using a coherent scattered field.

passing through the two-aperture screen. Mirrors on the field diaphragm and the input of the detector bring together the beams transmitted through the two apertures. The object's velocity is measured using the side lobe spectrum S_L [see Eq. (3.3)]. The main drawback of this method is a very low signal-to-noise ratio, which is due to the small size of the apertures. Another drawback is the impossibility of measuring the linear velocity of each area of the object surface when the points of the surface move at different rates.

For estimating the Cartesian components v_x, v_y, and v_z of the linear velocity vector $\mathbf{v}_A$ of a selected area A on the object surface, one can use three receiving arrangements (see Fig. 3.5) equivalent to the arrangement in Fig. 3.1. The two-aperture screen is placed in the reception aperture plane of each arrangement.

The double apertures of the first and second receiving arrangements are placed side by side in one plane. The center of the double aperture of the third receiv-

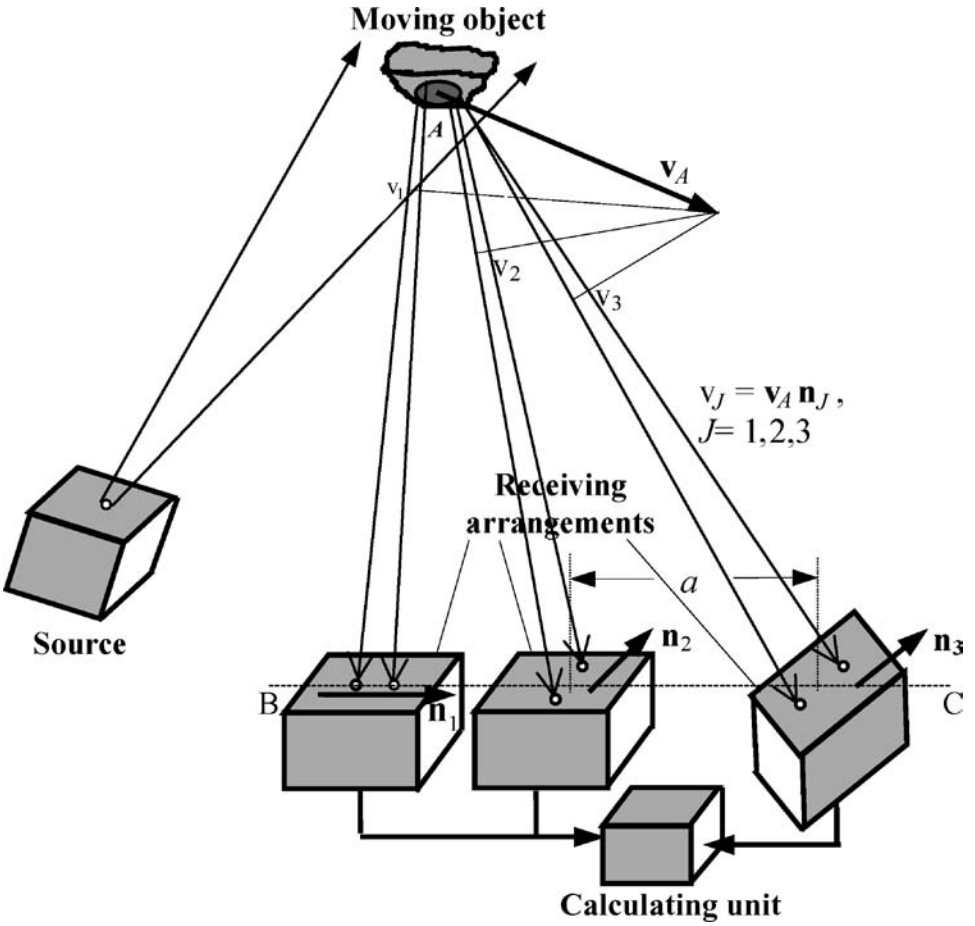

Figure 3.5 Conceptual schematic of the method of determining Cartesian components of the linear velocity vector for selected areas of the object surface.

ing arrangement is placed on the line BC connecting the two apertures of the first arrangement at the distance a from the center of the double aperture of the second and third arrangements. The Jth arrangement ($J = 1, 2, 3$) determines the projection v_J of the vector $\mathbf{v}_A$ on the line connecting the two apertures of the Jth arrangement by using expression (3.4). The estimates of the three Cartesian components v_x, v_y, and v_z are determined in the calculating unit (Fig. 3.5) from three equations $\mathbf{v}_A \cdot \mathbf{n}_J = v_J$, where $J = 1, 2, 3$; $\mathbf{n}_J$ is the unit vector in the direction of the lines connecting the apertures of the Jth arrangement. If the double apertures of the arrangements 1 and 2 are oriented so that the vectors $\mathbf{n}_J$ have the components $n_1 = (1, 0, 0)$, $n_2 = (0, 1, 0)$, $n_3 = (1, 0, -a/r_c)$, then from three equations $\mathbf{v}_A \cdot \mathbf{n}_J = v_J$, we obtain the three Cartesian components of the linear velocity vector of the object's surface area:

$$v_x = v_1,$$

$$v_y = v_2,$$

and

$$v_z = \frac{(v_1 - v_3)r_c}{a}. \tag{3.6}$$

For a solid moving object, the linear velocity vector of a selected area A (see Fig. 3.5) on the object's surface is $\mathbf{v}_A = \mathbf{v}_c + \boldsymbol{\Omega} \times (\mathbf{r}_c - \mathbf{r}_A)$, where $\mathbf{v}_c$ is the vector of the object's center of gravity, $\boldsymbol{\Omega}$ is the angular velocity vector of the object rotation, $\mathbf{r}_c$ is the radius vector of the object's center of gravity, and $\mathbf{r}_A$ is the radius vector of the area A with the components $x_A = (r_c x_H)/z_i$, $y_A = (r_c y_H)/z_i$, $z_A = r_c$. If the angular velocity of rotation is small enough, $\boldsymbol{\Omega} \ll v_x/d_o, v_y/d_o, v_z/d_o, d_o$ is then $\mathbf{v}_c = \mathbf{v}_A$ and relations (3.6) can be used for determining the Cartesian components of the linear velocity vector $\mathbf{v}_c$, which are calculated as

$$v_{xc} = v_1,$$

$$v_{yc} = v_2,$$

and

$$v_{zc} = \frac{(v_1 - v_3)r_c}{a}.$$

The arrangement represented in Fig. 3.5 can be used for an arbitrarily moving, deformed three-dimensional remote object. If the points of the object surface move at different rates, we can measure the three components of linear velocities of each area A on the object's surface by placing diaphragms with several pinholes in the planes of the coherent images built by the three arrangements, and detecting light passing through each pinhole. A method for determining the components of angular velocity vector $\boldsymbol{\Omega}$ will be considered in the next section.

3.3 Method of determining the angular velocity of a rotating object

There are different optical methods of determining the rotation parameters of a solid object. In particular, the stroboscopic method[49] uses pulsed illumination of a mark put on the surface of a rotating object. Illuminated this way, a stationary mark means that the angular rotation velocity of the object is equal to the pulse repetition rate. However, this method cannot be used for measuring small angular velocities or variations of angular velocity. As a rule, for optical measurements of the rotation velocity, one applies methods based on measuring the Doppler frequency shift of monochromatic light scattered by the moving object. A typical arrangement for implementing this approach is described in Ref. 50. In this arrangement, coherent light is split into two beams: the reference beam and the signal beam. The signal beam is focused on a small area of the rotating object surface. Then it is scattered by the object and arrives at the detector, where it interferes with the reference beam. An electronic unit, which consists of a spectrum analyzer and a frequency meter, determines the Doppler beat frequency ω_D. One can show that the number n of rotations the object completes in a second is related to ω_D as $n = (\lambda\omega_D)/(4\pi d_o \sin\varphi_\upsilon)$, where d_o is the object diameter, λ is the wavelength of coherent light, and φ_υ is the angle between the direction of incidence of the signal beam on the object surface and the local linear velocity at the signal beam's focus. The angular rotation velocity is

$$\Omega = 2\pi n = \frac{\lambda\omega_D}{2d_o \sin\varphi_\upsilon}.$$

The basic drawback of such a method is the necessity to form a stable reference beam and to satisfy the condition that the path-length difference between the reference beam and the signal beam is less than the coherence length of the light source. In the case of a remote rotating object, these conditions require the use of special light sources with large coherence length. Another strict limitation is that the arrangement must be vibration-proof. Besides, this technique does not determine the direction of the axis of rotation.

Figure 3.6 shows a setup for determining angular velocity that is free from the above-mentioned drawbacks.[51] A rotating object is illuminated by a monochromatic light source. The scattered light passes through the imaging system and apertures A* and B* in a two-aperture diaphragm placed in the image plane and optically conjugated to the small areas A and B of the object surface. The diaphragm can rotate around the optical axis of the imaging system. The frequency of the beam formed by aperture A* is equal to the frequency of the radiation scattered by the center point of area A in the direction of the imaging system; i.e., $f_1 = 2v_1/\lambda$, where $v_1 = \mathbf{v}_A \cdot \mathbf{k}$ is the projection of the linear velocity vector $\mathbf{v}_A$ of the center of area A on the imaging system's optical axis (Fig. 3.6), and $\mathbf{k}$ is the unit vector directed along the optical axis. Analogously, the beam formed by aperture B* has the central frequency $f_2 = 2v_2/\lambda = -2v_1/\lambda$, where $v_2 = \mathbf{v}_B \cdot \mathbf{k}$ is the projection of the linear velocity vector of the center of area B on the imaging lens' optical axis.

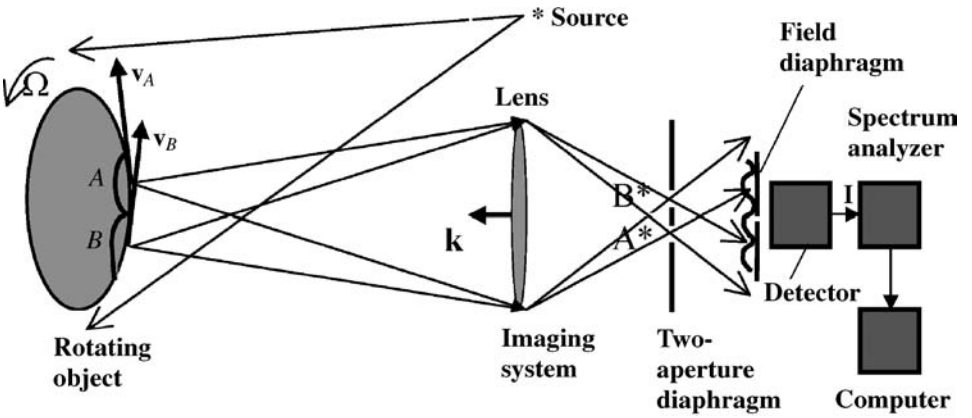

Figure 3.6 Setup for determining the angular velocity of a rotating object. In the plane of the field diaphragm, moving sinusoidal interference fringes are formed, which cause a periodic electrical detector signal, $J(t)$, at the frequency of the relative Doppler shift $f_S = f_1 - f_2 = 4v_1/\lambda$.

Their difference is the relative Doppler shift, $f_S = f_1 - f_2 = 4v_1/\lambda$. Having different frequencies, the beams produce interference fringes that move along the field diaphragm. Motion of the interference fringes causes a periodic electrical signal $J(t)$ in the detector. This signal is fed to the spectrum analyzer. From the resulting spectrum, the computer calculates the angular velocity of the object's rotation.

Using the well-known relations for a moving solid object, $\mathbf{v}_A = \mathbf{v}_c + \boldsymbol{\Omega} \times (\mathbf{r}_c - \mathbf{r}_A)$ and $\mathbf{v}_B = \mathbf{v}_c + \Omega \times (\mathbf{r}_c - \mathbf{r}_B)$, where $\mathbf{v}_c$ is the linear velocity vector of the object gravity center, $\boldsymbol{\Omega}$ is the angular velocity vector of the object's rotation, $\mathbf{r}_c$ is the radius vector of the object's gravity center, and $\mathbf{r}_A$ and $\mathbf{r}_B$ are radius vectors of the centers of areas A and B on the object surface, which are conjugated to the centers of apertures A* and B*, for the relative Doppler shift f_S we obtain

$$f_S = \frac{2}{\lambda}[\boldsymbol{\Omega} \times (\mathbf{r}_A - \mathbf{r}_B)]\mathbf{k} = \frac{2r_c}{\lambda z_i}[\Omega_y(x_1 - x_2) + \Omega_x(y_1 - y_2)], \qquad (3.7)$$

where r_c is the distance between the lens and the object's gravity center; z_i is the distance between the lens and the image plane; and x_1, y_1 and x_2, y_2 are coordinates of the centers of the first and second apertures in the two-aperture diaphragm. As we will show later, the spectral curve at the output of the spectrum analyzer (Fig. 3.6) has three lobes with principal maxima[12] at frequencies $f_{-1} = f_i - f_S, f_0 = f_i$, and $f_1 = f_i + f_S$, where f_i is the intermediate frequency. The measurements are controlled by means of a stroboscope, which can determine the rotation velocity of the drive shaft that rotates the object. The use of a reduction gear makes the object rotate 182 times slower than the shaft.

It is interesting that expressions (3.7) for the relative Doppler shift f_S do not depend on the geometric parameters of the rotating solid. In particular, if the apertures A* and B* (Fig. 3.6) are placed symmetrical to the optical system axis ($x_2 = -x_1$

and $y_2 = -y_1$), from Eq. (3.7) we have

$$f_S = \left(\frac{2r_c}{\lambda z_i}\right)(-\Omega_y x_1 + \Omega_y y_1) = \frac{r_c s_D}{\lambda z_i}(-\Omega_y \cos\psi_r + \Omega_y \sin\psi_r), \tag{3.8}$$

where ψ_r is the angle between the object's axis of rotation and the line connecting the centers of the apertures, and s_D is the distance between the apertures.

In the experiment, cylindrical and spherical objects 10 to 30 mm in diameter, placed 1000 mm from a lens with a 3-mm focal length, began rotating at the rates of 0.01 to 0.25 rotations per second. The axis of rotation was orthogonal to the line connecting the centers of the apertures (in this case, $\psi_r = \pi/2$, $\Omega_x = 0$, $x_1 = s_D/2$, and $y_1 = 0$). From relation (3.8) it follows that the true angular velocity of the object's rotation is $\Omega = \Omega_y = (f_S \lambda z_i)/(s_D r_c)$. The experimental spectrum $S(f)$ of the electrical signal $J(t)$ obtained at the detector output (Fig. 3.6) has principal maxima at frequencies $f_{-1} = f_i - f_S$, $f_0 = f_i$, $f_1 = f_i + f_S$. This spectrum was used for measuring the relative Doppler shift f_S and estimating the angular velocity of the object's rotation by computer (Fig. 3.6) by using the relation $\Omega = (f_S \lambda z_i)/(s_D r_c)$. The resulting estimate of the angular velocity agreed with the data obtained by measuring Ω by means of the stroboscopic method to within 1%. Figure 3.7 shows a calibration plot that helps to determine, for this particular experimental arrangement, the angular velocity of rotation within 1% accuracy.

After this, the angle ψ_r is changed from $\pi/2$ to 0 by rotating the two-aperture diaphragm around the optical axis of the lens (Fig. 3.6). The experimental dependence (Fig. 3.8) of the relative Doppler shift on the angle ψ_r between the axis of rotation and the line connecting the centers of the two apertures (see Fig 3.6) agrees with relation (3.8). The relative Doppler shift is maximal in the case $\psi_r = \pi/2$. This fact allows one to determine the direction of the rotation axis: the rotation axis is directed orthogonal to the position of the line connecting the centers of the apertures in which the maximal Doppler shift is achieved.

The experimental data show that the spectrum $S(f)$ has a time speckle structure (many narrow lobes), a wide central lobe, and two wide side lobes. The width of a single narrow lobe (of time speckles in the spectrum time speckle pattern) is about $1/T$, where T is the spectrum formation time. As we will show later, the side lobe

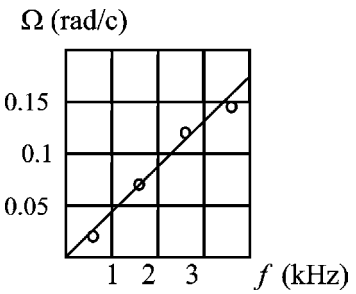

Figure 3.7 Calibration plot. The small circles are calibration data.

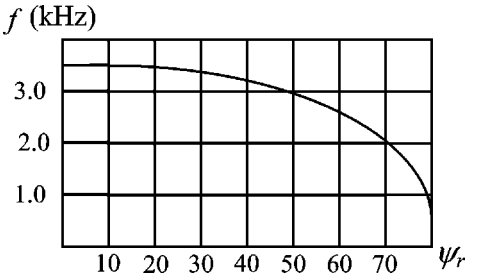

Figure 3.8 Dependence of the relative Doppler shift on the angular position ψ_r of the two-aperture diaphragm.

width depends on the angular velocity of the object rotation Ω, and the estimation error of Ω depends on the number of narrow lobes in the side lobes. To analyze these dependencies, we consider the relatively simple case $\psi_r = \pi/2$, where the axis of a cylindrical object is perpendicular to the axis of the optical system and to the line connecting the apertures in the two-aperture diaphragm. One can show that up to a constant factor, the electrical signal at the detector output is

$$J(t) = |A_1 + A_2|^2, \tag{3.9}$$

where

$$A_j(\varphi_j, \chi) \sim \int_{-\gamma}^{\gamma}\int_{-\gamma}^{\gamma}\iint k(\varphi, y) \times \exp i\Phi_j(\varphi_j, \varphi)h(\varphi, y, \delta_x, \delta_y, \varphi_j)d\varphi dy d\delta_x d\delta_y$$

$$\gamma = \frac{d_D}{2},\ \Phi(\varphi_j, \varphi) = i\frac{2\pi}{\lambda}\left[\xi_j(\varphi - \Omega t, y) + \frac{d_o}{2}\cos(\varphi + \varphi_j) + y\right],$$

$$h(\varphi, y, \delta_x, \delta_y, \varphi_j) = h\left[\frac{\pi d_\rho d_0}{\lambda r_c}\sin(\varphi + \varphi_j) + \frac{\pi d_\rho \delta_x}{\lambda z_i}, \frac{y}{r_c} + \frac{\delta_y}{z_i}\right]$$

is the pulse response (the point spread function) of the imaging system (Fig. 3.6), $j = 1, 2$; $k(\varphi, y)$ is the reflection coefficient spatial distribution in cylindrical coordinates $x = \rho\cos\varphi$, $y = \rho\sin\varphi$, with the origin O placed on the rotation axis (see Fig. 3.6); d_o is the diameter of the cylindrical object; d_ρ is the diameter of the imaging system aperture;

$$\varphi_1 = \frac{\varphi_0}{2},$$

$$\varphi_2 = -\frac{\varphi_0}{2},$$

and

$$\varphi_0 = \arcsin\left[\frac{r_c(d_D + s_D)}{2d_o z_i}\right];$$

d_D is the aperture diameter; $\xi_1(\varphi)$ and $\xi_2(\varphi)$ are roughness height distributions on object surface areas A and B, optically conjugated with the apertures A* and B*; and δ_x, δ_y are image plane coordinates. The spectral curve is

$$S(f) \sim \left| \frac{1}{T} \int_{t_o}^{t_o+T} J(t) \exp(2\pi i f t) dt \right|^2, \tag{3.10}$$

where t_0 is the initial time. Taking into account the last expression, we will show that if the lens has a sufficiently sharp pulse response, $h(\varphi, \varphi_j)$, and $\xi_1(\varphi)$ and $\xi_2(\varphi)$ have a Gaussian distribution with a Gaussian correlation function, the expression for the spectrum can be calculated analytically.[52] The analysis using expressions (3.9) and (3.10) shows that the expression for the averaged spectral curve is given by the sum of three symmetrical components:

$$\langle S(f) \rangle = \langle S_1(f) \rangle + \langle S_0(f) \rangle + \langle S_{-1}(f) \rangle,$$

and that the spectrum $S(f)$ has the correlation frequency $f_c = 1/T$. This correlation frequency is equal to the average width of a narrow lobe (time speckle; see Sec. 2.7) of the spectrum time speckle pattern. The term $\langle S_0(f) \rangle$ gives the central lobe of the spectral curve, and terms $\langle S_1(f) \rangle$ and $\langle S_{-1}(f) \rangle$ give the side lobes of the spectral curve. This is a full analog of the speckle patterns in the two first orders and the one zero order known in holography in connection with image reconstruction.

The principal maxima of the three components are placed at frequencies $f_1 = f_i - f_S$, $f_0 = f_i$, and $f_1 = f_i + f_S$.[12] Here, $f_S = (8\pi n s_D r_c)/(\lambda z_i) = (2\Omega s_D r_c)/(\lambda z_i)$, and $\Omega = 2\pi n$ is the magnitude of the angular velocity of the object rotation. Approximating transmission of the apertures A* and B* by Gaussian functions, we obtain the averaged spectra of the spectral curve side lobes in the form[12]

$$\langle S_1(f) \rangle \sim \exp - \left(\frac{f - f_i - f_D}{\Delta f_S} \right)^2,$$

and

$$\langle S_{-1}(f) \rangle \sim \exp - \left(\frac{f - f_i + f_D}{\Delta f_S} \right),$$

where the width of the spectrum side lobes is

$$\Delta f_S = \frac{\Omega r_c}{d_\rho}, \quad \text{if } d_D \ll \frac{\lambda z_i}{d_\rho},$$

and

$$\Delta f_S = \frac{\Omega d_D r_c}{\lambda z_i} = \frac{f_S d_D}{s_D}, \quad \text{if } d_D \gg \frac{\lambda z_i}{d_\rho}. \tag{3.11}$$

The last relation was checked experimentally for $s_D = 0.5$ mm and $d_D = 0.08$ mm to be accurate to within 10%.

Let us now consider the minimal coherence length of light sources required for the realization of this method. It is not difficult to show that the coherence length should not exceed the size of the object. Moreover, if the apertures in the two-aperture diaphragm are placed symmetrically with respect to the object's axis of rotation (Fig. 3.6), the coherence length can be of the order of 10 standard deviations of surface roughness height. For sufficiently smooth surfaces, this length can be several tens of microns. We see that it is possible to determine the rotational velocity of a symmetric solid object using light sources with a small coherence length.

For applications of this method, it is very important to evaluate the method's accuracy. It is clear from general physical reasoning that error in the rotation velocity estimate, σ_Ω, is determined by the number of time speckles in the side lobes $S_{\pm 1}(f)$ of the spectral curve $S(f)$. Under the assumption that $s_D \gg (\lambda z_i)/d_\rho$, the estimate for the angular velocity of the object rotation can be expressed analytically as

$$\widehat{\Omega} = \frac{2\lambda z_i}{r_c s_D} \hat{f}_S,$$

where $\hat{f}_S = \int (f - f_i) S_1(f) df / \int S_1(f) df$ is the estimate of the principal maximum f_S of the spectrum side lobe. From the last expression, we obtain $\langle \widehat{\Omega} \rangle = \Omega = (f_S \lambda z_i)/(s_D r_c)(2\Omega s_D r_c)/(\lambda z_i)$; and so

$$\sigma_\Omega = \sqrt{\langle \widehat{\Omega}^2 \rangle - \langle \widehat{\Omega} \rangle^2} = \frac{\Omega}{M_\Omega}, \tag{3.12}$$

where Ω is the true angular velocity of rotation, $M_\Omega = \Delta f_S / f_c$, with $f_c = 1/T$, is the number of correlation cells (time speckles; see Sec. 2.7) in the side lobes $S_{\pm 1}(f)$ of the spectral curve; $s_D \gg (\lambda z_i)/d_\rho$; $M_\Omega = (\Omega r_c)/(d_\rho f_c) = \Omega r_c T / d_\rho$, if $d_D \ll (\lambda z_i)/d_\rho$; and $M_\Omega = (\Omega r_c d_D)/(\lambda z_i f_c) = (\Omega r_c T d_D)/(\lambda z_i)$, if $d_D \gg \lambda z_i / d_\rho$.

Let us try to give a physical interpretation of expressions (3.11) for the width of the side lobes of the spectrum. At the beginning, consider the case where $d_D \ll \lambda z_i / d_\rho$. In this case, $\Delta f_S = (2\Omega r_c)/d_\rho$. Let us take the minimally resolved area A of the object surface, optically conjugated with aperture A* in the image plane (Fig. 3.9). For each point of this area, projection of the velocity on the direction of the imaging system's optical axis is given by the relation $v = [\mathbf{v}_c + \boldsymbol{\Omega} \times (\mathbf{r}_c - \mathbf{r})] \cdot \mathbf{k}$. We see that velocities of the points of area A have different projections on the direction of the optical axis. Therefore, they scatter rays in this direction with different Doppler frequency beats. As a result, the Doppler beats between the rays scattered by different points of area A and passing through aperture A* vary within the range $\Delta f_S = 2|v_1 - v_2|/\lambda = (2\Omega r_c)/d_\rho$, where $|v_1 - v_2| = (2\Omega r_c)/d_\rho$. Here, v_1 and v_2 are projections of linear velocities $\mathbf{v}_{L2}$ and $\mathbf{v}_{L1}$, the peripheral points of area A on the imaging lens' optical axis (Fig. 3.9). Taking into account

expression (3.12) and the fact that the correlation frequency of the spectrum is $f_c = 1/T$, we obtain that the relative Doppler shift f_S and the angular velocity Ω of the object rotation can be estimated with high accuracy if the number of correlation cells (narrow lobes or time speckles) in the side lobes $S_{\pm 1}(f)$ of the spectral curve $M_\Omega = \Delta f_S / f_c = (\Omega T d_D r_c)/(\lambda z_i) \gg 1$.

If $d_D \gg (\lambda z_i)/d_\rho$, then $\Delta f_S = (\Omega r_c d_D)/(\lambda z_i)$. This is the case in the experiment presented here. Let us take the area A of the object surface optically conjugated to the aperture A* (Fig. 3.10). For the points of this area, maximal variation of the velocity projections on the optical axis of the imaging system is $|v_1 - v_2| = (2\Omega d_D r_c)/z_i$, where v_1 and v_2 are projections of linear velocities $\mathbf{v}_{L2}$ and $\mathbf{v}_{L1}$ of area A's peripheral points. From expression (3.12) it follows that the estimation

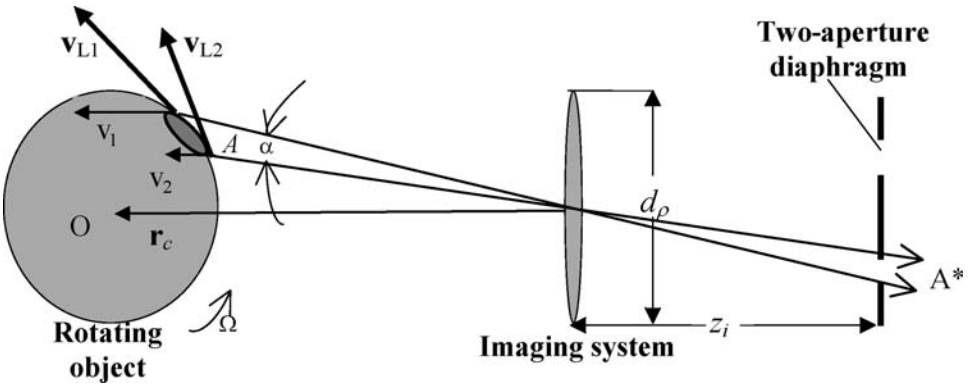

Figure 3.9 The case $d_D \ll \lambda z_i / d_\rho$. For a rotating object, finite angular resolution $\alpha = \lambda / d_\rho$ of the imaging system causes frequency variations of light scattered by the minimally resolved area A and passing the aperture A* placed in the image plane equal to $|v_1 - v_2|/\lambda = (\Omega \lambda r_c)/d_\rho$, where v_1 and v_2 are projections of velocities of the peripheral points of area A on the imaging lens' optical axis. Point O is the object's center of mass.

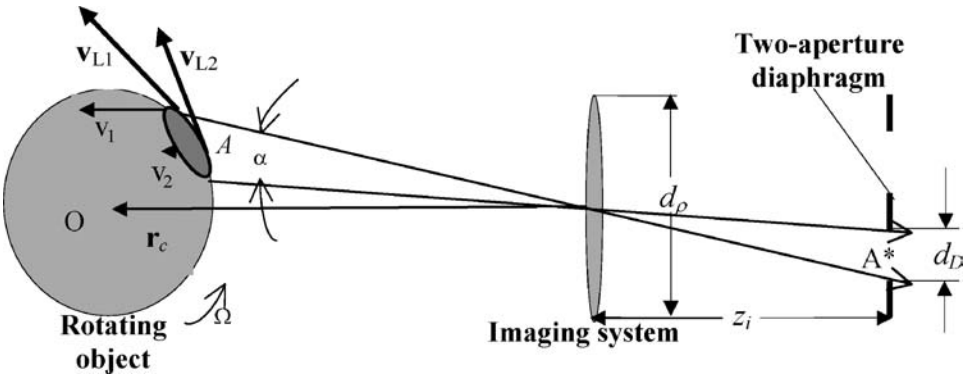

Figure 3.10 The case $d_D \gg (\lambda z_i)/d_\rho$. Values v_1 and v_2 are projections of velocities for the peripheral points of the object surface area A, which is optically conjugated to the aperture A* on the imaging lens' optical axis.

error of the angular velocity of rotation can be reduced either by decreasing the diameter of the imaging system aperture or by increasing the size d_D of the two apertures A* and B* in the image plane. In the latter case, increasing the size d_D is limited by the asymmetry of the averaged intensity distribution in the object image plane within the two apertures (Fig. 3.11), which, as one can show, causes the asymmetry of the spectrum side lobe and additional error $\sigma_{D\Omega}$ in the estimate for the angular rotation velocity. If $d_D/s_D \ll 1$, then

$$\sigma_{D\Omega} \approx \frac{\Omega d_D^2[\partial k_i(s_D, 0)\partial\delta_x]}{k_i(s_D, 0)s_D}, \tag{3.13}$$

where $k_i(\delta_x, \delta_y) = (\ell^2/\sigma^2)|k(\delta_x, \delta_y)|^2 \exp[-(\ell\delta)/(\sigma z_i)^2]$ is a function proportional to the averaged intensity distribution in the object image plane (for the two-aperture diaphragm plane in Fig. 3.6, σ and ℓ are the standard deviation and the correlation radius of the surface roughness height distribution, respectively). Taking into account that within the small areas A and B of the object surface, the module of the reflection coefficient distribution $k(\mathbf{r})$ is approximately constant, then from Eq. (3.13) we obtain $\sigma_{D\Omega} = \Omega[(d_D\ell)/(\sigma z_i s_D)]^2$.

However, it should be noted that in the case of rotating objects with sufficiently smooth surfaces, the peripheral areas of the object image are considerably dimmer and the greatly increased distance between the two apertures can lead to a considerable decrease in the intensity in the plane of one aperture proportionally to the factor $\exp[-(\ell s_D r_c/2z_i\sigma d_o)^2]$ [see expression (3.13)]. Therefore, the rotation velocity estimation error drops considerably even in the presence of low additional noise.

For determining the three components Ω_x, Ω_y, Ω_z of the angular velocity vector of the object's rotation, we can use a system consisting of three arrangements (Fig. 3.12) equivalent to the setup in Fig. 3.6. The relative positions of the key system elements are presented in Fig. 3.12 in the reference frame XYZ with the origin

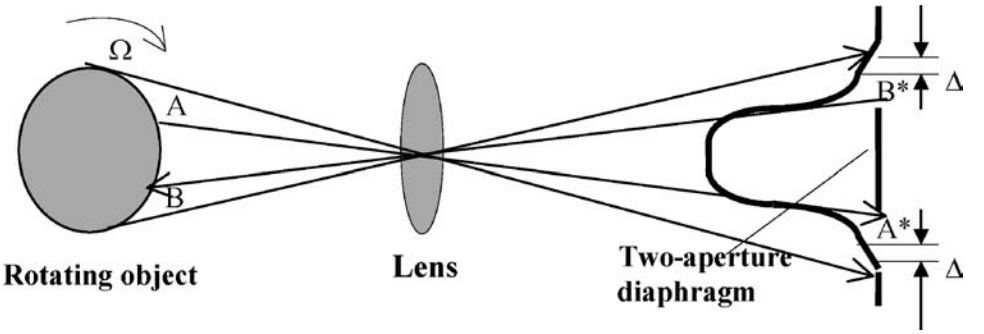

Figure 3.11 The asymmetry Δ of the averaged intensity distribution (solid line) of the object image within the two apertures A* and B* displaces the energy center of the spectral curve side lobes and causes additional error $\sigma_{D\Omega}$ in the estimate for the angular rotation velocity.

at center O of the imaging system's input aperture of the first arrangement and the Z axis directed along the imaging system's optical axis. The input apertures of the imaging systems of the first and the second arrangements are placed side by side in the $X0Y$ plane, with the X axis directed along the line OC connecting the aperture centers.

The center C of the imaging system's input aperture in the third arrangement is placed on the X axis at a distance a from origin 0 (a is much larger than the input aperture). The optical axis in the third arrangement is placed in the $X0Z$ plane at the angle $\vartheta \cong a/r_c$ to the Z axis. The Jth arrangement detects radiation scattered by the corresponding Jth pair of adjacent areas A_J and B_J of the solid surface.

All apertures in the three two-aperture diaphragms are placed in the image planes symmetrically with respect to the optical axes of the imaging systems. The Jth pair of apertures is optically conjugated to the Jth pair of adjacent areas A_J and B_J of the solid surface. The distance between the apertures in the two-aperture diaphragms is equal to s_D. The two apertures in the diaphragm of the first arrangement are placed on the lines parallel to the X axis (the unit vector of the aperture's

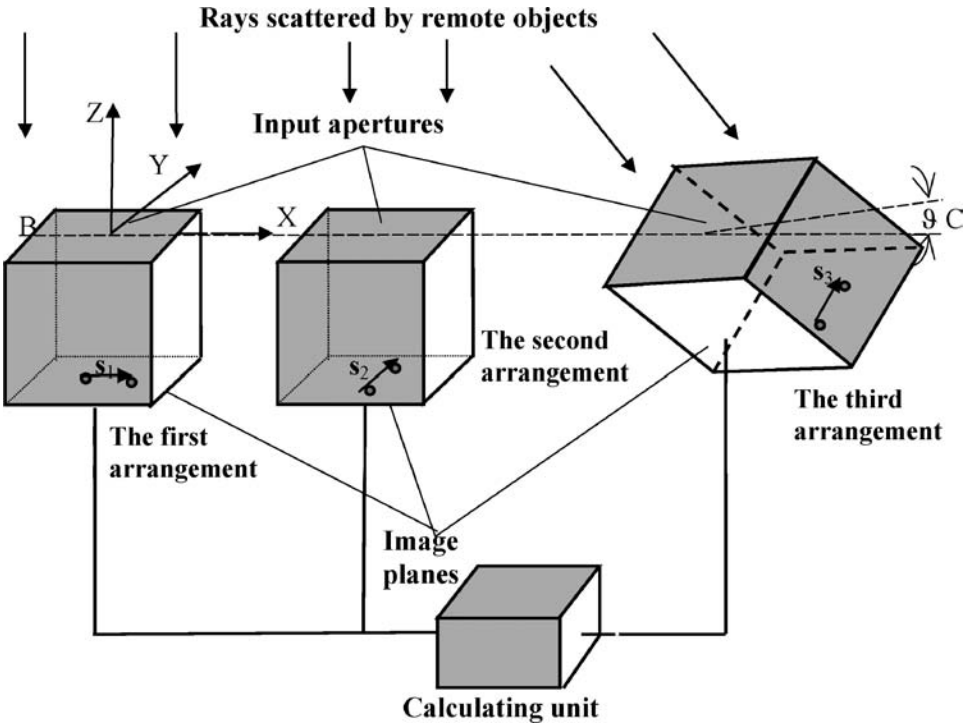

Figure 3.12 Conceptual schematic of the method of determining components of the angular velocity vector of the object rotation. Unit vectors $\mathbf{s}_J$ determine orientations of apertures in two-aperture diaphragms installed in the image plane of each arrangement (small dark spots in each image plane). The angle $\vartheta \cong a/r_c$, where r_c is the distance to the object, and a is the distance between the centers O and C of the input apertures of the first and third arrangements.

orientation $\mathbf{s}_1$ has the components $1, 0, 0$). The two apertures in the diaphragm of the second arrangement and the two apertures in the diaphragm of the third arrangement are placed on the lines parallel to the Y axis (the unit vectors of the apertures' orientations $\mathbf{s}_2$ and $\mathbf{s}_3$ have the components $0, 1, 0$). The Jth arrangement measures the relative Doppler shift f_{SJ} $(J = 1, 2, 3)$. The calculating unit determines the three components Ω_x, Ω_y, Ω_z according to the following relations:

$$\Omega_x = \frac{f_{S2}\lambda z_i}{r_c s_D},$$
$$\Omega_y = \frac{f_{S1}\lambda z_i}{r_c s_D},$$

and

$$\Omega_z = \frac{(f_{S3} - f_{S2})\lambda z_i}{a s_D}. \tag{3.14}$$

3.4 Determining object surface deformation parameters

In the previous section, we considered methods of determining the linear velocity vector of a remote object and the vector of the object's rotation velocity that are based on changes in the speckle pattern brightness in the reception plane of the scattered field and the image plane. Here we will use these changes to estimate the parameters of an object's surface deformations, namely, variations of the unit vectors normal to the fixed small areas of the object's surface.[44,52,53]

Before discussing the coherent methods of determining the variations of vectors normal to a particular area of an object's surface, let us consider the joint correlation function of their coherent images. Approximating the chosen area of an object's mean surface by a small section of its tangential plane, we can describe the field in the image plane as

$$E(\boldsymbol{\delta}, \mathbf{n}) \sim \int k(\mathbf{r}) \exp\left[\frac{2\pi i}{\lambda}(r + |\mathbf{r} - \boldsymbol{\rho}_s|)\right] \exp\left\{i\frac{4\pi[\xi(x, y) + \alpha x + \beta y]}{\lambda}\right\} h(\mathbf{r}, \boldsymbol{\delta}) d\mathbf{r}, \tag{3.15}$$

where integration runs over the chosen area, and α and β are the parameters of the unit vector normal to the small area,

$$\mathbf{n}(\alpha, \beta) = \left(\frac{-\alpha}{\sqrt{1 + \alpha^2 + \beta^2}}, \frac{-\beta}{\sqrt{1 + \alpha^2 + \beta^2}}, \frac{1}{\sqrt{1 + \alpha^2 + \beta^2}}\right),$$

and

$$h(\boldsymbol{\delta}, \mathbf{r}) = \frac{1}{S_\rho} \int \boldsymbol{\Lambda}(\boldsymbol{\rho}) \exp\left[\frac{i2\pi\boldsymbol{\rho}}{\lambda}\left(\frac{\boldsymbol{\delta}}{z_i} + \frac{\mathbf{r}}{r_c}\right)\right] d\boldsymbol{\rho}$$

is the pulse response of the imaging system, $\boldsymbol{\rho}$ is the radius vector of the imaging system aperture, S_ρ is the area of the imaging system aperture, $\boldsymbol{\Lambda}(\boldsymbol{\rho})$ is the pupil function of the imaging system, $\boldsymbol{\delta}$ is the radius vector of a point in the image of the chosen area, $\mathbf{r}$ is the radius vector of the object's mean (envelope) surface, r_c is the distance between the imaging system aperture and the object, and z_i is the distance between the imaging system aperture and the image plane.

To describe the surface deformation, let us introduce the initial, $\mathbf{n}_1 = \mathbf{n}(\alpha_1, \beta_1)$, and the final, $\mathbf{n}_2 = \mathbf{n}(\alpha_2, \beta_2)$, unit vectors normal to the selected area before and after its deformation, and the joint correlation function,

$$B_T(\mathbf{n}_1, \mathbf{n}_2) = \langle E(\boldsymbol{\delta}, \mathbf{n}_1) E^*(\boldsymbol{\delta}, \mathbf{n}_2) \rangle,$$

where the symbol $\langle\rangle$ denotes averaging over different realizations of surface roughness height distribution $\xi(x, y)$. Furthermore, we will assume that $\alpha, \beta < 0.3$. Then,

$$\mathbf{n}(\alpha_1, \beta_1) \approx (-\alpha_1, -\beta_1, 1),$$

and

$$\mathbf{n}(\alpha_2, \beta_2) \approx (-\alpha_2, -\beta_2, 1).$$

Our aim now is to determine the variations $\Delta\alpha = \alpha_1 - \alpha_2$ and $\Delta\beta = \beta_1 - \beta_2$ of the parameters α, β of the unit vector normal to the small area of the object surface optically conjugated with the point $\boldsymbol{\delta}$ in the image plane, by means of the joint correlation function $B_T(\mathbf{n}_1, \mathbf{n}_2)$. These variations describe deformation of the selected area. The general expression for this correlation function is rather cumbersome, so we present here a normalized joint correlation function for a very narrow object extended along the X axis (a narrow stripe), which is not resolved by the imaging system along the Y axis and whose coherent image has a large number of speckles $M \gg 1$. The narrow stripe is rotating around the axis parallel to the Y axis. Here, $\mathbf{n}_1(\alpha_1, \beta_1) \approx (-\alpha_1, 0, 1)$ and $\mathbf{n}_2(\alpha_2, \beta_2) \approx (-\alpha_2, 0, 1)$, where α_1 and α_2 are the initial and the final angles of light incidence on the narrow stripe surface. Using relation (3.15), under the assumption that the spatial distribution of the reflection coefficient $k(\mathbf{r})$ is constant within the selected area, we obtain the normalized joint correlation function

$$K(\alpha) = \frac{B_T(\alpha_1, \alpha_2)}{B_T(\alpha_1, \alpha_1)} \approx \begin{cases} 1 - \gamma & \text{for } \gamma < 1 - \dfrac{1}{M}, \\ \dfrac{\cos[2(1-\gamma)]}{M} & \text{for } \gamma \geq 1 - \dfrac{1}{M}. \end{cases} \tag{3.16}$$

Here, $M = (d_o d_\rho)/(\lambda r_c)$, $\gamma = (r_c \Delta\alpha)/d_\rho$ is the stripe rotation angle, d_o is the object size, and d_ρ is the size of the imaging system aperture. We see from Eq. (3.16) that full decorrelation occurs when the rotation angle of the narrow

stripe $\Delta\alpha > d_\rho/r_c$. The value d_ρ/r_c of the decorrelation angle can be explained as follows: the speckle pattern of the scattered field is shifted in the aperture size d_ρ when the stripe turns by an angle of $\Delta\alpha = d_\rho/r_c$. As a result, new speckles fully replace the old speckles in the imaging system's aperture plane.

Let us dwell on the experimental testing of relation (3.16). The experiment is carried out with the setup shown in Fig. 3.13. The object is a narrow stripe 0.5 mm $\times$ 5 mm metal sheet cutout fixed onto a neutral filter. It is illuminated by a monochromatic light source. An imaging system with a varying aperture builds the image of the stripe, and a matrix detector connected to a computer, which determines the rotation angle $\Delta\alpha$ of the narrow stripe, registers the intensity in the image plane. The image is recorded for different angular positions α of the neutral filter and the object, which is equivalent to changing the angle of incidence of the illuminating light. Magnification of the imaging system is chosen to provide about five readings of intensity for each speckle of the object image. The coherent image is read out line by line, and the quantized output electrical signal is fed into the computer. Instead of the normalized joint correlation function, the computer calculates the following expression:

$$K_E(\alpha_1, \alpha_2) = \frac{\int |E(\delta, \alpha_1)E^*(\delta, \alpha_2)|^2 d\delta}{\int |E(\delta, \alpha_1)|^4 d\delta}. \tag{3.17}$$

One can show that for $M \gg 1$,

$$K_E(\alpha_1, \alpha_2) \cong \frac{1 + |K(\Delta\alpha)|^2}{2} = \begin{cases} \dfrac{1 + (1-\gamma)^2}{2} & \text{for } \gamma < 1 - \dfrac{1}{M}, \\ \dfrac{\cos^2[2(1-\gamma)]}{M^2} & \text{for } \gamma \geq 1 - \dfrac{1}{M}. \end{cases} \tag{3.18}$$

For $M \gg 1$, the last relation agrees with the result obtained in Ref. 53. From this it follows that for $M \gg 1$, $K_E(\alpha_1, \alpha_2)$ depends on the normalized joint correlation function K and does not depend on surface roughness parameters.[12] Figure 3.14

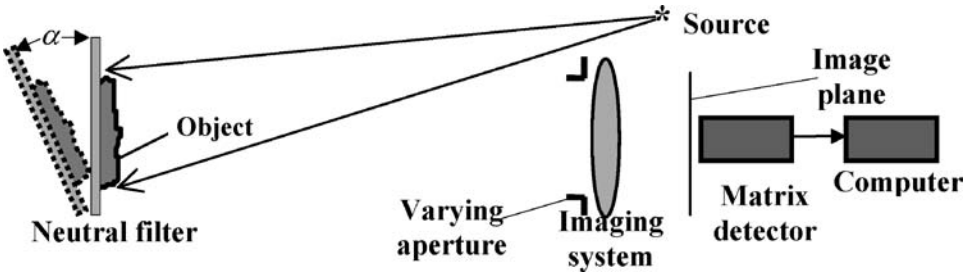

Figure 3.13 Experimental setup for determining the rotation angle of an object using its coherent speckle image. The dotted lines show the variation of the angular position of the neutral optical filter and the object fixed to the neutral filter.

gives the plot of the function K_E versus the angle difference. One can see that the dashed line goes a little above the solid one and the theoretical and experimental curves agree quite well, especially for $\Delta\alpha < d_\rho/r_c$. The difference between the two curves is caused by the fact that formula (3.18) may not be exact for $M < 10$. Knowledge of the function K_E ($\Delta\alpha = \alpha_1 - \alpha_2$) allows use of the schematic presented in Fig. 3.13 to determine the rotation angle $\Delta\alpha$ of the object with sufficiently high accuracy. To calculate the accuracy of the method, we must determine the relation for estimating the rotation angle $\Delta\alpha$. From expression (3.18), we obtain this estimate:

$$\bar{\Delta}\alpha = \frac{d_\rho}{r_c\sqrt{2K_E - 1}}. \tag{3.19}$$

For the case of $\Delta\alpha < d_\rho/r_c$, simple though somewhat cumbersome calculations give us the following expression for the estimation variance:

$$\sigma_\alpha^2 = \left\langle \bar{\Delta}\alpha^2 \right\rangle - \langle \bar{\Delta}\alpha \rangle^2 = \frac{d_\rho^2}{\mathrm{M} r_c^2}. \tag{3.20}$$

From relation (3.20) we see that if the coherent image of the object consists of a large number of speckles M, i.e., if the resolution of the imaging system is high, then the accuracy σ_α of the rotation angle estimation is very good.

In the case of a low-resolution imaging system where $M \leq 1$, we have $K_E(\Delta\alpha) \sim \mathrm{sinc}(\Delta\alpha d_o/\lambda)$. In this case, only a single speckle is contained in the imaging system aperture (see Fig. 3.13) and in the image plane, and as we see from expression (3.20), the estimation error $\sigma_\alpha = d_\rho/r_c$ is larger than the true rotation angle $\Delta\alpha$, which is less than d_ρ/r_c. Hence, when $M \leq 1$, the previous method

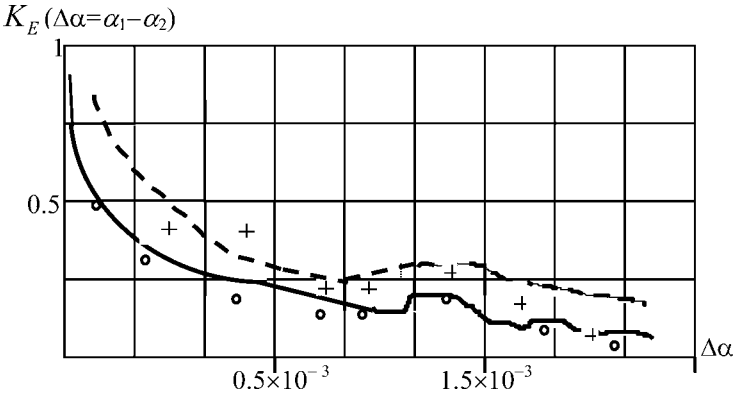

Figure 3.14 The function K_E ($\Delta\alpha = \alpha_1 - \alpha_2$) plotted versus the rotation angle $\Delta\alpha = \alpha_1 - \alpha_2$ of the narrow stripe. The crosses correspond to the case of diaphragm diameter $d_\rho = 1.3$ mm, stripe length $d_o = 9.5$ mm, and $M \approx 5$; the circles correspond to $d_\rho = 3$ mm, $d_o = 9.5$ mm, and $M \approx 8$. The dashed and solid lines are theoretical curves for $M \approx 5$ and $M \approx 8$, respectively.

of measuring the rotation angle based on the correlation properties of coherent images is not correct. From the relation $K_E(\Delta\alpha) \sim \mathrm{sinc}(\Delta\alpha d_o/\lambda)$, we see that a full decorrelation occurs when the object rotation angle $\Delta\alpha$ is larger than the correlation angle $\alpha_c = 2\lambda/d_o$. The last value can be explained by the speckle motion in the aperture plane during object rotation: the initial single speckle is replaced in the aperture plane by its neighboring speckle (speckles are shifted synchronously along this plane by the speckle size $\sim r_c\lambda/d_o$ when the object turns by an angle of $\alpha_c = 2\lambda/d_o$). This shift may be applied to determine the rotation angle estimate using the intensity spectrum $S_L(f)$ of a coherent field scattered by the rotating object.

In Fig. 3.15 a simple setup is presented that determines the rotation angle in this case. A rotating object is illuminated by a monochromatic light source, and a detector reads the intensity of the scattered field. The electrical signal is fed to a spectrum analyzer connected to a computer. The rotation angle estimate $\bar{\Delta}\alpha$ is performed according to the formula

$$\bar{\Delta}\alpha = \left[\frac{\lambda T \int (f - f_i)^2 S_L(f) df}{d_o \int S_L(f) df}\right]^{1/2},$$

where T is the spectrum formation time. The estimation variance is

$$\sigma_\alpha^2 = \left\langle \bar{\Delta}\alpha^2 \right\rangle - \langle \bar{\Delta}\alpha \rangle^2 = \frac{\alpha^2}{M_\alpha}, \tag{3.20a}$$

where $M_\alpha = (\alpha d_o)/2\lambda = \alpha/\alpha_c$ is the number of correlation cells in the spectrum $S_L(f)$ and $\alpha_c = 2\lambda/d_o$ is the correlation angle. For $M_\alpha \gg 1$, the ratio σ_α/α is small. Thus, in the case of a low-resolution imaging system, we can determine the object rotation angle $\Delta\alpha$ with sufficiently high precision using the time variation of the speckle pattern in the scattered coherent radiation. It is important to note that the method of measuring the rotation angle of particular areas of the object surface proposed in Fig. 3.15 cannot be used.

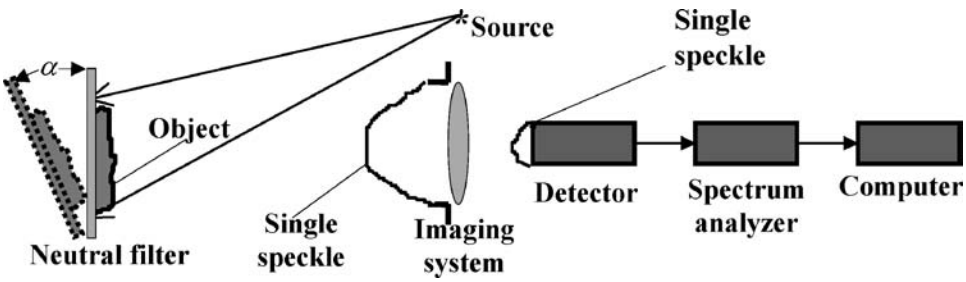

Figure 3.15 Schematic of a setup that determines the object rotation angle in a low-resolution imaging system using the time variation of the speckle pattern in the coherent scattered field. The detector in the image plane reads the image intensity.

To determine the two parameters $\Delta\alpha = \alpha_1 - \alpha_2$ and $\Delta\beta = \beta_1 - \beta_2$ describing deformations of small areas of an arbitrarily shaped object, we will use the correlation properties of coherent images formed by a system consisting of two closely placed arrangements (Fig. 3.16). Each arrangement contains two imaging systems with different aperture shapes; the first imaging system aperture has a square shape $d_\rho \times d_\rho$, and the second imaging system aperture has a rectangular shape $d_\rho \times d_\rho/2$ (the short side of the rectangle is oriented along the Y axis). The intensity in the image planes is read by matrix detectors connected to a computer that calculates the deformation parameters. They can be determined with the help of two joint correlation functions,

$$B_{mT}(\mathbf{n}_1, \mathbf{n}_2) = \langle E_m(\boldsymbol{\delta}, \mathbf{n}_1) E_m^*(\boldsymbol{\delta}, \mathbf{n}_2) \rangle,$$

where $m = 1, 2$; E_m are complex amplitudes of the fields in the image planes (see Fig. 3.16); and $\boldsymbol{\delta}$ is the radius vector of a small area of the object image optically conjugated to the chosen area of the object surface. Under conditions $\Delta\alpha < d_\rho/2r_c$ and $\Delta\beta < d_\rho/2r_c$, the normalized joint correlation functions are

$$K_m = \frac{B_{mT}(\mathbf{n}_1, \mathbf{n}_2)}{B_{mT}(\mathbf{n}_1, \mathbf{n}_1)} \sim \left(1 - \frac{r_c \Delta\alpha}{d_\rho}\right)\left(1 - \frac{r_c \Delta\beta}{d_\rho}\right), \quad \text{where } m = 1, 2.$$

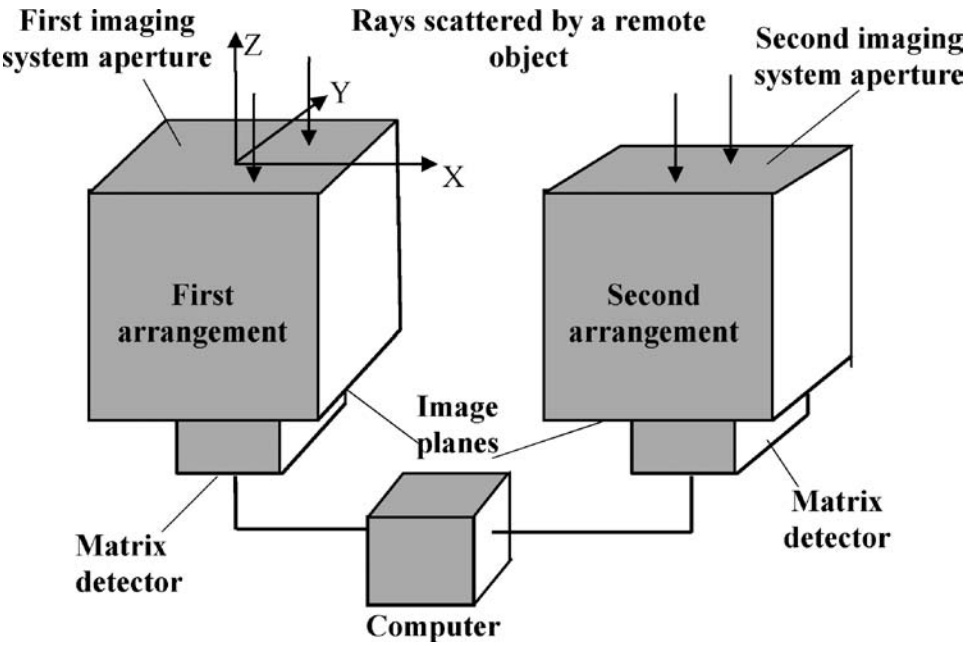

Figure 3.16 Device for determining the deformation parameters of particular areas of an arbitrarily shaped object.

From these two relations we can calculate two deformation parameters $\Delta\alpha$ and $\Delta\beta$:

$$\Delta\alpha = \frac{d_\rho(2K_1' - K_2')}{r_c},$$

and

$$\Delta\beta = \frac{d_\rho(K_1' - K_2')}{r_c(2K_1' - K_2')}, \tag{3.21}$$

where $K_m' = \sqrt{2K_{mE} - 1}$ $(m = 1, 2)$ are the estimates for two normalized joint correlation functions,

$$K_{mE}(\mathbf{n}_1, \mathbf{n}_2) = \frac{\int |E_m(\delta, \mathbf{n}_1)E_m^*(\delta, \mathbf{n}_2)|^2 d\delta}{\int |E_m(\delta, \mathbf{n}_1)|^4 d\delta}, \tag{3.22}$$

calculated by the computer (see Fig. 3.16). For the case where $\Delta\beta = \beta_1 = \beta_2 = 0$, from Eqs. (3.21) and (3.22) we obtain $\Delta\alpha = \sqrt{2K_E - 1}$ and $\Delta\beta = 0$. For the standard deviations of these parameters, we have $\sigma_\alpha \approx (d_\rho/r_c)/\sqrt{M_T}$ and $\sigma_\beta \approx (d_\rho/r_c)/\sqrt{M_T}$, where $M_T = S_A[d_\rho/(\lambda r_c)^2]$ and S_A is the area of a deformed small piece of the object surface.

3.5 Combined method of determining the motion and deformation parameters of an object

Now we consider a combined method of determining all dynamic parameters (deformation and motion parameters) of a remote object. First, we must note that the vector $\mathbf{\Omega}$ of the angular velocity of the object's rotation and the vector $\mathbf{v}_c$ of the linear velocity of the object's center of mass satisfy the equation $\mathbf{v}_A = \mathbf{v}_c + \mathbf{\Omega} \times (\mathbf{r}_c - \mathbf{r}_A)$, where $\mathbf{v}_A$ is the linear velocity vector of the center of a selected area A on the object surface. As a rule, the angular velocity of rotation is small enough: $\mathbf{\Omega} \ll v_{cx}/d_o, v_{cy}/d_o, v_{cz}/d_o$. Therefore, we restrict ourselves to the determination of the components v_{cx}, v_{cy}, v_{cz} of the vector $\mathbf{v}_c$ instead of determining the components of linear velocity vectors for each area.

The combined method provides simultaneous determination of eight estimates, namely, two parameters $\Delta\alpha$ and $\Delta\beta$ describing the deformations of small areas of the object surface, three components $\Omega_x, \Omega_y, \Omega_z$ of the vector Ω and three components v_{cx}, v_{cy}, v_{cz}. To determine the six components of the vectors $\mathbf{\Omega}$ and $\mathbf{v}_c$ and the parameters $\Delta\alpha$ and $\Delta\beta$, we can use a system consisting of four devices (Fig. 3.17). The first three devices are the arrangements used for determining the six components of the vectors $\mathbf{\Omega}$ and $\mathbf{v}_c$: the Jth arrangement $(J = 1, 2, 3)$ measures tangential components v_J of the vector $\mathbf{v}_c$ and the relative Doppler shift f_{SJ} $(J = 1, 2, 3)$.

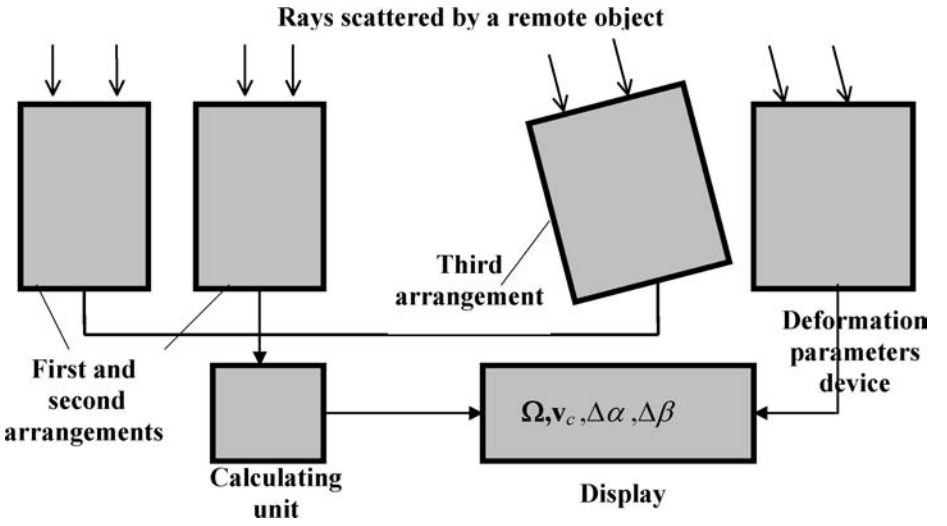

Figure 3.17 Conceptual schematic of a combined system for determining the deformation and motion parameters of remote objects.

The first and the second arrangements are placed side by side. The third arrangement is placed at the angle $\vartheta \cong a/r_c \ll 1$ to the first and the second arrangements; here, a is the distance between the second and the third arrangements, and r_c is the distance to the object. The calculating unit determines the three components Ω_x, Ω_y, Ω_z of the vector $\mathbf{\Omega}$ and the three components v_{cx}, v_{cy}, v_{cz} of the vector $\mathbf{v}_c$ by using the values v_J and f_{SJ}. Two parameters $\Delta\alpha$ and $\Delta\beta$ describing deformations of small selected areas of the object surface are determined with the help of the estimates [Eq. (3.21)] for the normalized joint correlation functions K_1' and K_2' in the device presented in detail in Fig. 3.16. The data about the object's dynamic parameters $\mathbf{\Omega}$, $\mathbf{v}_c$, and $\Delta\alpha$ and $\Delta\beta$ are also displayed.

Each one of the three arrangements used for determining the components of the vectors $\mathbf{\Omega}$ and $\mathbf{v}_c$ contains two coaxial imaging systems, the internal one and the external one. For instance, Fig. 3.18 shows the second arrangement ($J = 2$) containing two coaxial imaging systems, placed behind the three-aperture screen: the central large aperture is the aperture of the internal imaging lens, and the two small side apertures are the apertures of the external imaging lens.

The internal and the external imaging lenses form the object image in parallel image planes, namely, the plane of the two-aperture diaphragm and the plane of the field diaphragm. The first unit calculates the relative Doppler shift f_{S2}, and the second unit calculates the tangential component v_2 of the vector $\mathbf{v}_c$ equal to the projection of the vector $\mathbf{v}_c$ on the line connecting the apertures in the two-aperture diaphragm.

The combined system presented in Fig. 3.17 allows simultaneous determination of the three components Ω_x, Ω_y, Ω_z of the angular velocity of the object rotation, three components v_{cx}, v_{cy}, v_{cz} of the linear velocity of the object's center

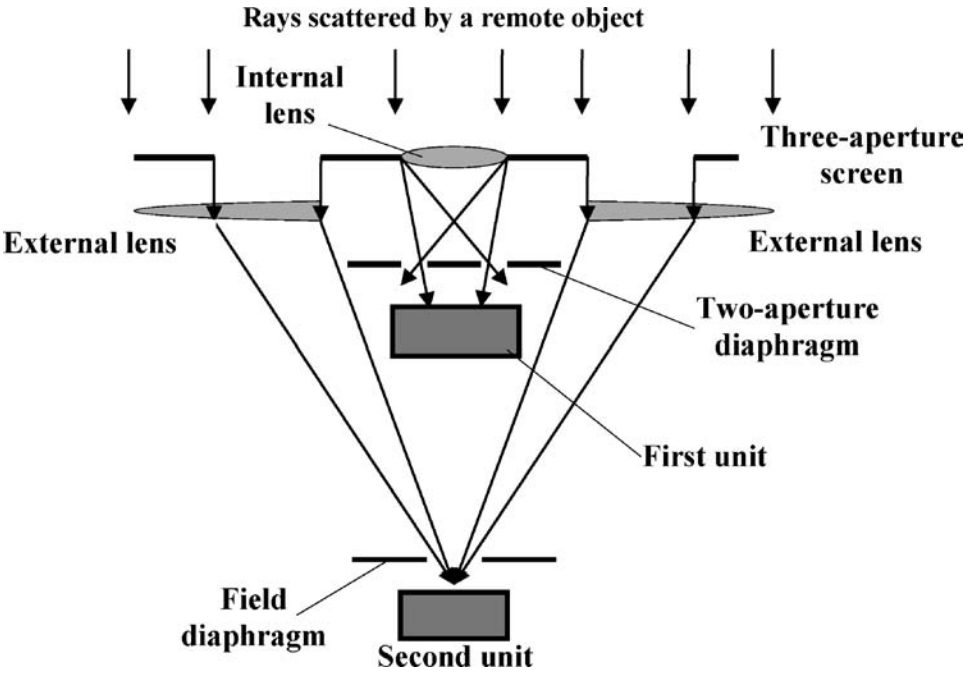

Figure 3.18 The second arrangement, which calculates the relative Doppler shift f_{S2} equal to the difference of frequencies of the radiation scattered by adjoining small areas of the object surface and the tangential components v_2 of the vector $\mathbf{v}_c$ of the object's center of mass.

of mass, and two parameters $\Delta\alpha$ and $\Delta\beta$ describing the deformations of different areas of the object surface. These parameters are calculated with the help of expressions (3.6), (3.14), and (3.21):

$$\Omega_x = \frac{f_{S2}\lambda z_i}{r_c s_D}, \quad \Omega_y = \frac{f_{S1}\lambda z_i}{r_c s_D}, \quad \Omega_z = \frac{(f_{S3} - f_{S2})\lambda z_i}{a s_D};$$

$$v_{cx} = v_1, \quad v_{cy} = v_2, \quad v_{cz} = \frac{(v_1 - v_2) r_c}{a};$$

and

$$\Delta\alpha = \frac{d_\rho(2K_1' - K_2')}{r_c}, \quad \Delta\beta = \frac{d_\rho(K_1' - K_2')}{r_c(2K_1' - K_2')}.$$

3.6 Conclusions

1. Dynamic parameters of remote objects with rough surfaces can be determined with sufficiently high accuracy by illuminating the object's surfaces by monochromatic radiation and determining time variations of the speckle pattern of a

scattered coherent field in the plane of the scattered field and the object image plane without using a reference beam.

2. An object's linear velocity can be found by putting a two-aperture screen in the aperture plane of the imaging system and determining in the image plane the frequency difference between the two interfering scattered beams passing through the two apertures.
3. The method of using a two-aperture diaphragm placed in the image plane is most efficient for determining the magnitude and direction of the rotation velocity of a remote object. The method can be realized without using a reference beam and with the help of small-coherence-length sources, and it relies on finding the spectrum of the scattered coherent field.
4. The parameters of selected small areas of a deformed object surface can be obtained by determining the correlation characteristics between the speckle patterns of coherent images of these areas formed before and after deformation, and by determining the time variations of the speckle patterns in the scattered coherent field during deformation.

Chapter 4

Fourier Telescopy

4.1 Introduction

The problem of distortion-free imaging of distant objects in a turbulent medium has a long history. However, most of the schemes used for this purpose are based on adaptive methods of compensating for phase distortions that appear as radiation propagates from an object to a registration device. Recently, considerable interest has been drawn to the systems that remove phase distortions with the help of active aperture synthesis. They are based on illuminating the object by means of a transmitting aperture, which consists of transmitters with controlled positions that emit monochromatic or quasi-monochromatic radiation (Fig. 4.1).[54–70] The transmitters are controlled in such a way that interference of radiation from various pairs of transmitters forms sinusoidal interference fringes with different periods and different orientations on the object surface. Furthermore, the receiving system registers contributions to the scattered radiation from the sinusoidal pattern formed by different fixed pairs of transmitters. In Ref. 56, these are assumed to be proportional to different spatial Fourier components of the object's optical image and different multipliers $\exp\{i\psi\}$, where ψ is the difference between the phase distortions due to the radiation propagation from both transmitters of each pair. After removing the factor $\exp\{i\psi\}$ by means of an inverse Fourier transform, the object image is reconstructed. This method is called Fourier telescopy. In Ref. 56, an interesting algorithm is suggested for compensating for phase distortions. It is proposed to place the transmitters so that they form a square equidistant matrix in the transmitting aperture; different pairs of transmitters should be sorted successively in time. In addition, one takes the product of energies registered from neighboring transmitters. In Ref. 57, it is proposed that the number of transmitters is reduced considerably, placing them so that they form orthogonal arrays, their size being comparable with that of the square matrix suggested in Ref. 56. The number of different spatial Fourier components formed this way is the same as in the case of transmitters forming a square matrix.

References 60–62 suggest using transmitters radiating at different frequencies and to illuminating an object simultaneously by all the transmitters. In this case, the received signal contains information about instantaneous Fourier components of the optical image and about instantaneous phase distortions. References 60–62

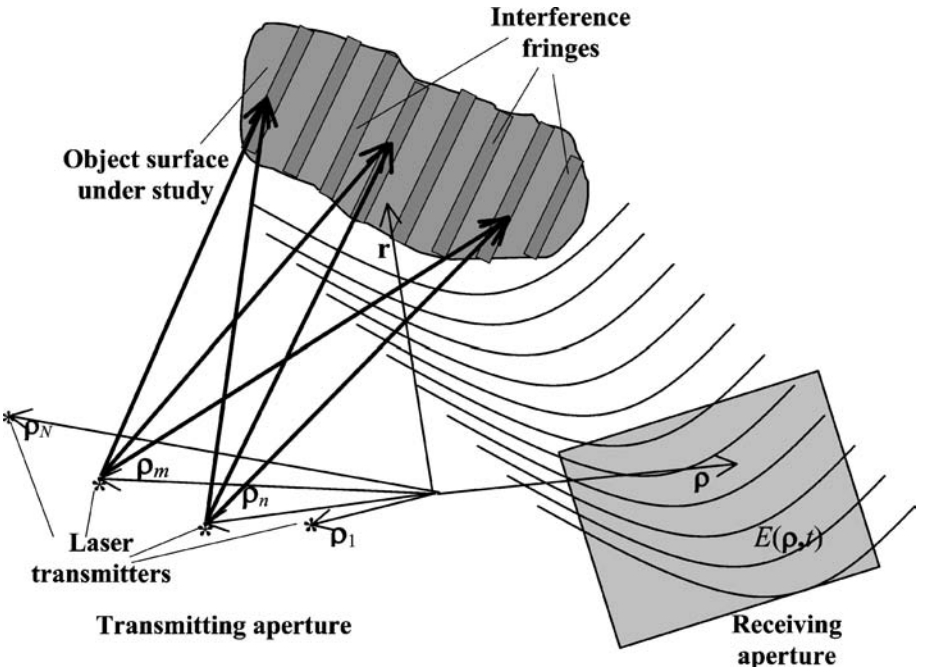

Figure 4.1 Geometry of Fourier telescopy. Thick arrows denote the rays illuminating the object.

propose to select a fixed Fourier component by filtering the signal at the difference frequency appearing due to the radiation interference from two transmitters. Reference 60 suggests that before filtering the signal, the receiving system measures all the radiation of the energy scattered by the object. Evidently, in this case, the linear size d_r of the receiving aperture that registers the scattered energy should exceed $r_c\gamma$, where r_c is the distance from the object, and γ is the angle of the cone into which the energy is scattered. It can be found from the relation $\gamma = \sigma/\ell$, where σ is the standard deviation of the surface roughness and ℓ is its correlation radius.[12] This means that for an object placed at a distance of 10 km, for the usual case $\gamma = \sigma/\ell \approx 0.1$, r_c should exceed 1 km. However, such a size of scattered energy detector is impossible in practice.

Hence, the following important problems should be analyzed for the practical realization of Fourier telescopy. First, what is the minimum size of the transmitting aperture and what is the minimum number of transmitters that is necessary for the realization of Fourier-telescopic imaging with sufficiently high quality of the image reproduced from the spatial Fourier components? Second, what is the minimum size of the receiving aperture registering the scattered energy that will maintain this quality? Third, how do the shape and roughness parameters of the surface of the object under study influence the quality of its image? Fourth, what is the effect of the laser radiation time instability on the quality of the Fourier-telescopic image?

These problems will be considered in detail in this chapter. First, we will introduce the statistical model of the received signal for the case where laser transmitters

illuminate the object with arbitrary coordinates and with different frequencies. The dependence of the received signal on the direction diagram of transmitters will be taken into account. Also, Fourier-telescopic imaging will be described for the case where atmospheric phase fluctuations in the path of the laser radiation are absent or completely compensated. The dependence of the Fourier-telescopic image on the object's shape and the parameters of its surface roughness, and the dependence of the resolving power on the sizes of the transmitting and receiving apertures, will be analyzed in detail. We will take into account that the quality of a Fourier-telescopic image depends on the frequency difference between the transmitters, as well as on the coherence length and the linear time shift of the illuminating radiation's basic frequency, caused by the source's instability. Next, as an example of Fourier telescopy in the absence of phase fluctuations, we will describe a panoramic microscope for Fourier-telescopic imaging of an extended object having a size of up to 10 cm with resolution approximating the illuminating radiation wavelength ($\sim$1 μm in the visible range).

At the end of the chapter, we introduce the integral and local measures of the relationship between the Fourier-telescopic image of an object and the averaged undistorted image. Fourier-telescopic imaging in an inhomogeneous atmosphere will be discussed in Appendix 3, where we will consider the problem of compensating for atmospheric phase fluctuations by means of the phase closure algorithm, the basic principles of which are described in Ref. 56.

4.2 Statistical model of the received signal in Fourier telescopy and the Fourier-telescopic image

First, let us analyze the received signal when pulsed, monochromatic, mutually coherent transmitters of different frequencies simultaneously illuminate the object. The transmitters are placed arbitrarily in the plane of the transmitting aperture. Without the loss of generality, assume that the transmitters are numbered in the order of frequency increase (Fig. 4.1).

Assuming that the object is distant from the Earth's surface, we approximate the influence of atmosphere on laser radiation propagation using the model of an infinitely thin phase screen placed on the transmitting and receiving apertures. In this case, using Eqs. (1.18), (1.28), (1.32), and (1.34), one can write the complex amplitude of the field scattered by the object to the receiving aperture in the Fresnel approximation, which is valid for remote objects,

$$E(\boldsymbol{\rho}, t) = \exp[i\psi_r(\boldsymbol{\rho})]\frac{E_t S_t}{\lambda^2 r_c^2}\int \frac{\mathbf{q}\cdot\mathbf{n}}{\mathbf{q}\cdot\mathbf{N}} k(\mathbf{r}) \exp\left[\frac{2\pi i \xi(\mathbf{r})\mathbf{q}\cdot\mathbf{N}}{\lambda}\right] u(\mathbf{r}, t)d\mathbf{r}, \quad (4.1)$$

where

$$u(\mathbf{r}, t) = \sum_{n=1}^{n=N} u_n\left(t - \frac{2r_c}{c}\right) D_n(\mathbf{r}) \exp i\left[\omega_n t - 2\frac{\omega_n r}{c} + \frac{\omega_n \mathbf{r}(\boldsymbol{\rho}_n + \boldsymbol{\rho})}{2r_c c}\right],$$

N is the number of transmitters, E_t and S_t are the complex amplitude of the transmitter and the area of its aperture, respectively, $\omega_n = \omega_0 + \Delta\omega_n$ is the nth transmitter frequency, c is the velocity of light, $\Delta\omega_n = C(n)\Delta\omega$, $\Delta\omega = \omega_2 - \omega_1$, where $C(n)$ is an integer-valued function depending on the transmitter number n, $C(1) = 1$, $\psi_r(\boldsymbol{\rho})$ are random phase shifts on the path from the object to the receiving aperture, $\mathbf{N}(\mathbf{r})$ is the normal to the object's mean surface, $\mathbf{n}(\mathbf{r})$ is the normal to the object surface, $k(\mathbf{r})$ is the reflection coefficient distribution over the object's surface, $\boldsymbol{\rho}$ is the radius vector in the plane of the receiving aperture, $\xi(\mathbf{r})$ is the roughness height distribution over the object's surface, $\mathbf{r}$ is the radius vector of the mean surface of the object, $\mathbf{r}_c$ is the radius vector of the object's center of mass, r_c is the distance from the object, $\mathbf{q} = 2\mathbf{r}_c/r_c$, $D_n(\mathbf{r})$ is the direction diagram for the nth transmitter, and $u_n(t)$ is the pulse profile of the radiation from the nth transmitter. Integration is performed over the illuminated area S_o of the object's surface. We further assume the roughness height on the object surface to have a Gaussian distribution and Gaussian correlation function.[12] If the atmospheric inhomogeneities are smooth, the transmitters are similar; and $(\lambda r_c)/d_t \gg d_o$, where d_t is the transmitter size, d_o is the object's size, then $D_n(\mathbf{r}) \approx D(\mathbf{r}_c)\exp(i\psi_n)$, where ψ_n are phase errors on the path from the nth transmitter to the object, and $D(\mathbf{r}_c)$ is the value of the transmitter direction diagram on the object's surface in the absence of atmospheric influence on radiation propagation (see Appendix 3). By filtering the scattered field intensity averaged over the area S_ρ of the receiving aperture,

$$\mathrm{Q}(t) = \frac{1}{S_\rho}\int |E(\boldsymbol{\rho}, t)|^2 d\boldsymbol{\rho},$$

performed as

$$G_{mn} = \frac{1}{T}\int_{t_0}^{t_0+T} \mathrm{Q}(t)\exp[i(\omega_m - \omega_n)t]dt,$$

where T is the signal processing time satisfying the inequalities $(\omega_m - \omega_n)T \geq 1$ and t_0 is the processing start time, we extract from all received radiation the part that is determined by the sinusoidal interference fringes produced by the interference of radiation propagating from the mth and nth transmitters. Under the conditions $c\Delta\omega_N \ll \lambda$ and $q_\perp/q_N \gg \sigma/\ell \gg \lambda/d_o$, where d_o is the object size, $q_N = \mathbf{q}\cdot\mathbf{N}$, $q_\perp = (\mathbf{q}^2 - q_N^2)^{1/2}$, and under the assumptions that all pulse shapes are equal $[u_n(t) = u_1(t)]$, the pulse lengths for all transmitters considerably exceed the depth of the illuminated surface, but the pulse duration is much less than the signal processing time T,

$$G_{mn} = \exp[i(\psi_m - \psi_n)]F_{mn}, \tag{4.2}$$

where

$$F_{mn} = \frac{S_t^2 |E_t^2|}{\lambda^2 r_c^2} |D(\mathbf{r}_c)|^2 u_1^2 \left(t_0 q - \frac{2r_c}{c} \right) \times \iint |k(\mathbf{r}_1)|^2 \exp i \frac{4\pi}{\lambda} \left\{ \mathbf{r}_1 - \mathbf{r}_2 + \frac{2\mathbf{r}_c \cdot \mathbf{N}(\mathbf{r}_1)[\xi(\mathbf{r}_1) - \xi(\mathbf{r}_2)]}{r_c} \right\} \times w(\mathbf{r}_1, \mathbf{r}_2) \exp \left[\frac{i(\omega_m \mathbf{r}_1 \boldsymbol{\rho}_m - \omega_n \mathbf{r}_2 \boldsymbol{\rho}_n)}{2r_c c} \right] d\mathbf{r}_1 d\mathbf{r}_2$$

is an estimate for the m, nth Fourier component of the undistorted image of the object,

$$w(\mathbf{r}_1, \mathbf{r}_2) = \frac{1}{S\rho} \int \exp \left\{ \frac{i[\boldsymbol{\rho}(\omega_m \mathbf{r}_1 - \omega_n \mathbf{r}_2)]}{2\mathbf{r}_c c} \right\} d\boldsymbol{\rho}.$$

Further in our investigations of Fourier telescopy we will focus on the choice of a transmitting aperture in the shape of two orthogonal linear arrays of transmitters placed at equal distances along the X and Y axes in the plane of the receiving aperture (Fig. 4.2). In the X-array, there are N_{1x} transmitters on the left of

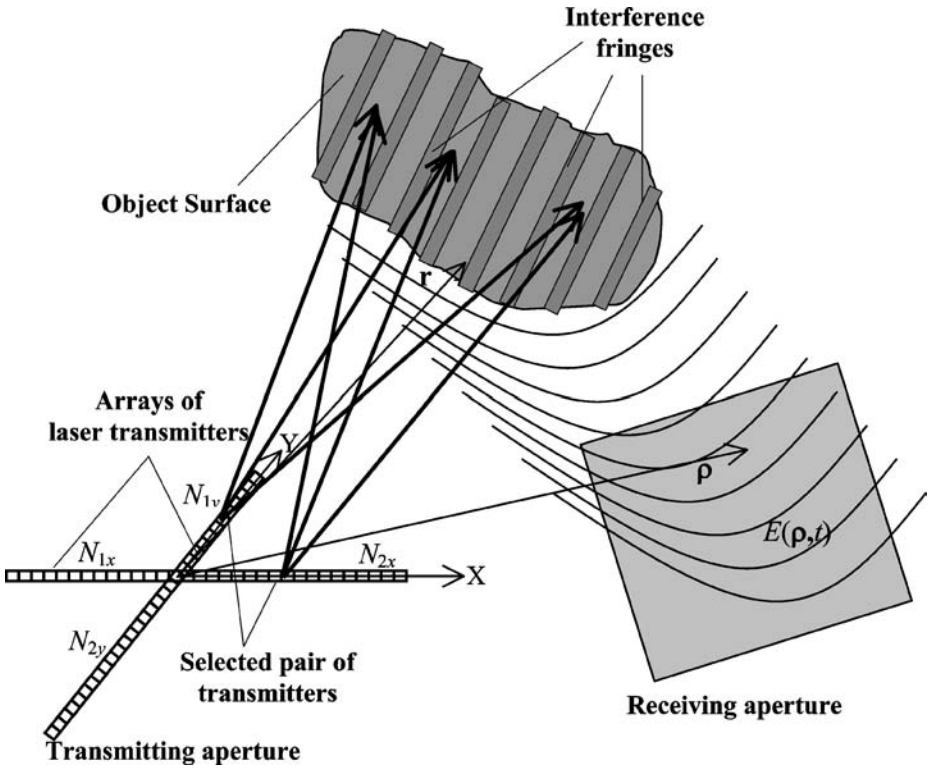

Figure 4.2 Geometry of Fourier telescopy in the case of two orthogonal linear arrays of transmitters in the plane of the transmitting aperture.

the array cross-section and N_{2x} on the right; in the Y-array, N_{1y} transmitters are below the cross-section and N_{2y} are above. The total number of transmitters is $N = N_x + N_y$, where $N_x = N_{1x} + N_{2x}$ and $N_y = N_{1y} + N_{2y}$. The integer-valued function $C(n)$ is chosen in such a way that two conditions are satisfied. First, transmitter frequencies should increase from ω_0 (the left-hand transmitter of the X-array) to $\omega_0 + C(N_x)\Delta\omega$ (the right-hand transmitter of the X-array), and then from $\omega_0 + C(N_x+1)\Delta\omega$ (the bottom transmitter of the Y-array) to $\omega_0 + C(N_x+N_y)\Delta\omega$ (the top transmitter of the Y-array). Second, the frequency differences between any pair of transmitters from either the same array or from different arrays should not coincide. According to the chosen space and frequency configurations of the transmitters from Eq. (4.2), we obtain

$$G_{mn} = \frac{1}{T}\int_{t_0}^{t_0+T} \mathrm{Q}(t)\exp[i(\omega_m - \omega_n)t]dt = \exp[i(\psi_m - \psi_n)]F_{mn}, \tag{4.2a}$$

where

$$F_{mn} = \frac{S_r^2|E_t^2|}{\lambda^2 r_c^2}|D(\mathbf{r}_c)|^2 u_1^2\left(t_0 - \frac{2r_c}{\mathrm{c}}\right)$$
$$\times \iint |k(\mathbf{r}_1)|^2 \exp i\frac{4\pi}{\lambda}\left\{\mathbf{r}_1 - \mathbf{r}_2 + \frac{2\mathbf{r}_c\cdot\mathbf{N}(\mathbf{r}_1)[\xi(\mathbf{r}_1) - \xi(\mathbf{r}_2)]}{r_c}\right\} w(\mathbf{r}_1, \mathbf{r}_2)$$
$$\times \exp\left[\frac{i(d_x x_1 \omega_m m/N_x - d_y y_2 \omega_n n/N_x)}{2r_c c}\right] d\mathbf{r}_1 d\mathbf{r}_2, \tag{4.2b}$$

d_x is the length of the X-array, d_y is the length of the Y-array, E_t is the transmitter complex amplitude, ψ_{xm} is the random phase shift (phase errors) on the path from the mth transmitter of the X-array to the object, ψ_{yn} is the random phase shift on the path from the nth transmitter of the Y-array to the object, and $\omega_{xm} = \omega_0 + \Delta\omega C(N_{1x}+m)$, $\omega_{yn} = \omega_0 + \Delta\omega C(N_{1y}+n)$. Here, G_{mn} is the part of the received radiation connected with the sinusoidal interference fringes produced by interference of radiation propagating from the selected couple of transmitters, the mth and nth transmitters (Fig. 4.2). To simplify the calculation, assume the following conditions are satisfied:

$$\frac{\Delta\omega C(N_{1x}+m)d_o d_x}{cr_c} \ll 1,$$
$$\frac{\Delta\omega C(N_{1y}+n)d_o d_y}{cr_c} \ll 1,$$
$$\frac{\Delta\omega C(N_{1x}+m)d_\rho d_x}{cr_c} \ll 1,$$

and

$$\frac{\Delta\omega C(N_{1y}+n)d_\rho d_y}{cr_c} \ll 1. \tag{4.3}$$

A very large receiving aperture with area $S_\rho \gg (r_c\sigma)^2/\ell^2$ collects all of the scattered radiation energy, and the correlation radius of phase inhomogeneities for the scattered field in the vicinity of the surface,[12] $\ell_\varphi \approx (\lambda\ell)/\sigma$, exceeds in this case the width $(r_c\lambda)/d_\rho$ of the function $w(\mathbf{r})$. Then, taking into account conditions (4.3), one can write $w(\mathbf{r}_1, \mathbf{r}_2)$ as a function proportional to the δ-function: $w(\mathbf{r}_1, \mathbf{r}_2) \approx (\lambda^2 r_c^2/S_\rho)\delta(\mathbf{r}_1 - \mathbf{r}_2)$. In this case, the first integration in Eq. (4.2b) over the object surface yields, under the same conditions,

$$F_{mn} = \left[\frac{|D(\mathbf{r}_c)|^2}{S_e}\right] \int k(\mathbf{r}) \exp\left[\frac{i(d_x x\omega_m m/N_x - d_y y\omega_n n/N_x)}{2r_c c}\right] d\mathbf{r},$$

where S_e is the backscattering surface area of the object under study. One can see that when the orthogonal arrays are placed at equal distances between the transmitters, G_{mn} is proportional, under conditions indicated in Eq. (4.3), to the (m, n)-th Fourier component of the intensity reflection coefficient $|k(\mathbf{r})|^2$ distribution on the object's surface, which determines its contour. This means that regardless of the object's surface shape, even the rays scattered by the edges get into the receiving aperture if the aperture size $d_\rho \gg (r_c\sigma)/\ell$. Hence, if the receiving aperture collects all the scattered energy, Fourier components F_{mn} and coefficients G_{mn} do not depend on the shape of the object surface. This can also be seen from the above relation.

4.2.1 Influence of an object's surface shape on Fourier telescopy

In practice, the receiving aperture size is usually not large, i.e., $d_\rho < (r_c\sigma)/\ell$. The registered signals and G_{mn} depend on the shape and roughness parameters of the object's surface. In the case of a smoother surface, the receiving aperture collects a larger part of the energy. Considering these problems in more detail, let us define the mean values of the Fourier components F_{mn}, which are calculated the same way as in the derivation of the scattered field correlation function [Eq. (1.36)]. Taking into account the last condition, after averaging Eq. (4.2b) over realizations $\xi(\mathbf{r})$ of the object surface roughness height, we obtain that under conditions of Eq. (4.3) and for $N_x N_y \gg M$, where M is the number of domains on the object surface resolvable according to Rayleigh's criterion, i.e., the number of speckles in the Fourier-telescopic image (see Appendix 2), for $S_\rho \geq d_x d_y$ we

obtain

$$\langle F_{mn}\rangle = \left[\frac{|D(\mathbf{r}_c)|^2}{S_e}\right]\int k_i(\mathbf{r})\exp\left[\frac{i(d_x x\omega_m m/N_x - d_y y\omega_n n/N_x)}{2rc}\right]d\mathbf{r}, \qquad (4.4)$$

where $k_i(\mathbf{r}) = (\ell/\sigma)^2|k(\mathbf{r})|^2\exp\{-[(\ell q_\perp)/(q_N\sigma)]^2\}$.

Here, $\langle F_{mn}\rangle$ is the (m, n)-th Fourier component of the function $k_i(\mathbf{r})$ (Fig. 4.3). This function is proportional to the averaged value (the envelope) of the intensity distribution in the image obtained by a high-resolution system in the absence of turbulent distortions.[12] It follows that under the condition $\sqrt{S_r} \ll r_c\gamma$, where $\gamma = \sigma/\ell$, both $\langle F_{mn}\rangle$ and $\langle G_{mn}\rangle$ are on the average proportional to the discrete Fourier transform of the function $k_i(\mathbf{r})$, which, in turn, was shown in Sec. 2.3 to be proportional to the mean intensity of the speckled image in coherent light. Hence, these parameters are estimates of the Fourier components of this function. In practice, the transmitting aperture should be placed so that the object is close to its normal $\mathbf{n}_t$. In this case, the object's direction is parallel to the normal to the transmitting aperture. Then, for a flat object

$$k(\mathbf{r}) = \left(\frac{\ell}{\sigma}\right)^2|k(\mathbf{r})|^2\exp\left\{-\left[\frac{\ell\tan\theta(\mathbf{r})}{\sigma}\right]^2\right\},$$

where $\theta(\mathbf{r})$ is the angle between the normal to the mean object surface and the normal to the transmitting aperture $\mathbf{n}_t$. If the object is flat and placed orthogonally

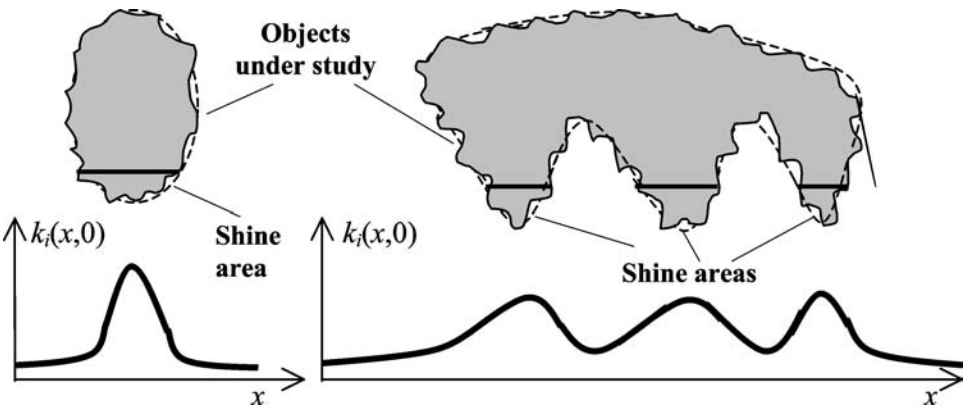

Figure 4.3 The function $k_i(x, 0)$ is proportional to the averaged value of the intensity distribution in the object image of rough objects of simple (left object, a single shine area or, in other words, a single surface of backscattering) and complicated (right object, three shine areas) shapes in the section by the plane $X0Z$ (the plane where $y = 0$). The dashed lines are mean surfaces of the objects; the thick straight lines show the backscattering surface.

to this normal, then $\theta = 0$. The factor $(\ell/\sigma)^2$ is proportional to the amount of energy collected by a finite receiving aperture and depends on the average slope σ/ℓ of the object's surface roughness. If the surface is relatively smooth, i.e., the average slope is small, then a larger amount of radiation is scattered towards the receiving aperture and, hence, Fourier components F_{mn} and coefficients G_{mn} are larger. If the object is flat and its normal forms an angle $\theta > 2\sigma/\ell$ to the object's direction, then $k_i(\mathbf{r}) \cong 0$, since in this case, the axes of the backscattering diagrams for all parts of the object do not hit the receiving aperture, and F_{mn} and G_{mn} are small.

Consider a nonflat object and assume that $\sigma/\ell < 0.3$, which is usually satisfied. First, let the rough object have a simple (ellipsoidal) shape. One can show that under this condition,

$$k_i(\mathbf{r}) = \left(\frac{\ell}{\sigma}\right)^2 |k(\mathbf{r})|^2 \exp -\frac{\ell^2}{\sigma^2}\left(\frac{x^2}{\rho_x^2} + \frac{y^2}{\rho_y^2}\right),$$

where ρ_x and ρ_y are basic curvature radii of the surface.

If $x \geq (2\rho_x\sigma)/\ell$ and $y \geq (2\rho_y\sigma)/\ell$, then $k_i(\mathbf{r})$, the Fourier components F_{mn}, and the coefficients G_{mn} become small. This means that for each part of the object surface, the angle between the scattering diagram axis and the normal to the receiving aperture is larger than σ/ℓ, and hence, the scattered radiation does not get into the receiving aperture. In other words, for each part of this kind, a mirrorlike reflection shows the peak of the scattering diagram far from the receiving aperture. If $x \leq (2\rho_x\sigma)/\ell$ and $y \leq (2\rho_y\sigma)/\ell$, then $k_i(\mathbf{r})$, F_{mn}, and G_{mn} are large; they are maximum at $x = y = 0$, since for this part, almost all scattered radiation enters the receiving aperture. The area selected by this inequality, with its center at $x = y = 0$, is the shine domain (or backscattering surface). If the object's size is greater than the size of this area, then its edges do not contribute to $k_i(\mathbf{r})$, F_{mn}, or G_{mn}. For a nonflat rough object with a complicated shape (Fig. 4.3),

$$k_i(\mathbf{r}) \cong \sum_{j=1}^{j=N_s} \left(\frac{\ell_j}{\sigma_j}\right)^2 |k_j(\mathbf{r})|^2 \exp -\frac{\ell_j^2}{\sigma_j^2}\left(\frac{|x - x_j|^2}{\rho_{jx}^2} + \frac{|y - y_j|^2}{\rho_{jy}^2}\right),$$

where ρ_{jx}, ρ_{jy}, ℓ_j, σ_j, and $k_j(\mathbf{r})$ are curvature and correlation radii, the roughness standard deviation, and the reflection coefficient distribution for the jth shine domain, respectively; x_j, y_j, and N_j are the center coordinates of the jth shine domain and the total number of shine areas, respectively.

4.2.2 Fourier-telescopic image and the resolution of a Fourier-telescopic system

Let us return to Eq. (4.2a) and recall that G_{mn} is proportional to the (m, n)-th Fourier component F_{mn} of the function $k_i(\mathbf{r})$. Taking this into account, one can

propose that the inverse Fourier transform,

$$I(\boldsymbol{\delta}) = \frac{1}{N_x N_y} \sum_{m=-N_{1x},n=-N_{1y}}^{m=N_{2x},n=N_{2y}} F_{mn} \exp i \frac{\pi(\delta_x d_x m/N_x + \delta_y d_y n/N_y)}{z_i \lambda}, \tag{4.5}$$

where z_i is the distance from the receiving aperture plane to the plane of the reconstructed image plane, $\boldsymbol{\delta}$ is the radius vector of a point in this plane, and δ_x and δ_y are coordinates of this point, gives the intensity distribution for the image of an object without the distortions caused by propagation. However, before doing the inverse Fourier transform over G_{mn}, one should first remove the factors $\exp[i(\psi_{xm} - \psi_{yn})]$, which complicate this transform. This problem will be considered in detail in Appendix 3. Increasing the size of the arrays and the number N of transmitters in each array [which is equal to the number of the Fourier components of the function $k_i(\mathbf{r})$], one can make the expression (4.4) tend toward the object's optical image. This can be seen most easily by assuming that the laser transmitters are placed along the X- and Y-arrays continuously. Such an assumption can be made if $N_x N_y \gg M$; and hence, in relations (4.4) and (4.5) we can replace discrete variables by continuous variables: $(md_x)/N_x \cong u$, $(nd_y)/N_y \cong v$. Furthermore, assume that the atmospheric phase fluctuations are compensated, i.e., the factors $\exp[i(\psi_{xm} - \psi_{yn})]$ in G_{mn} are removed. Then, replacing into Eqs. (4.4) and (4.5) $(md_x)/N_x = u$ and $(nd_y)/N_y = v$, we obtain

$$\langle I(\boldsymbol{\delta}) \rangle \sim |D(\mathbf{r}_c)|^2 \iint k_i(x, y) h(x, y, \delta_x, \delta_y) dx dy, \tag{4.6}$$

where $h(x, y, \delta_x, \delta_y) = \operatorname{sinc}^2 \Theta_x \operatorname{sinc}^2 \Theta_y$—given that $\Theta_x = (2\pi d/\lambda)(x/r_c + \delta_x/z_i)$ and $\Theta_y = (2\pi d/\lambda)(y/r_c + \delta_y/z_i)$—is the pulse response of the Fourier-telescopic imaging system.

If this system has high resolving power, then

$$\langle I(\boldsymbol{\delta}) \rangle \sim |D(\mathbf{r}_c)|^2 k_i(x = -\mu\delta_x, y = -\mu\delta_y), \tag{4.6a}$$

where $\mu = r_c/z_i$ is the scaling factor. This means that if the resolution is high, the proposed method allows formation of the object image, the average intensity distribution being the same as for a standard coherent image (see Secs. 2.2 and 2.3). The direction diagram of the laser transmitter, given by the bounding factor $|D(\mathbf{r}_c)|^2$, determines the illuminated area of the object. It follows from the condition $N_x, N_y \gg M$ that if transmitter arrays have an equal number of transmitter $N_x = N_y = N_t$, then the minimum number of transmitters in each array is $N_t = 3M^{1/2}$. Then, if $d_x = d_y$, it follows that $d_t = d/(3M^{1/2})$. If the object is on the edge of the directional diagram $D(\mathbf{r}_c)$, then $\langle I(\boldsymbol{\delta}) \rangle$ is close to zero.

As shown in Appendix 2, the correlation area of the intensity distribution (the speckle area in the Fourier-telescopic image),

$$S_c = \int \frac{B(\delta_1, \delta_2)d\delta_2}{\langle I^2(\delta_2)\rangle},$$

determines the resolution of the Fourier telescopy. Here,

$$B_i(\delta_1, \delta_2) = \langle I(\delta_1)I(\delta_2)\rangle - \langle I(\delta_1)\rangle\langle I(\delta_2)\rangle$$

is the correlation function of the intensity distribution. The number of speckles in the Fourier-telescopic image is $M = [\int \langle I(\delta)\rangle d\delta]^2/[\iint B_i(\delta_1, \delta_2)d\delta_1 d\delta_2]$, as in a normal coherent image (see Chapter 2). Hence, a Fourier-telescopic image has a speckle structure. In Chapter 2, it was shown that M is equal to the number of object surface domains resolved by the imaging system. The contrast in this image, as in a normal coherent image, is defined by the relation $C = (\langle I^2\rangle - \langle I\rangle^2)/\langle I\rangle^2$.

In Appendix 2, we consider Fourier telescopy both for arbitrary positions of transmitters in the transmitting aperture and for an object with an arbitrary surface shape. In addition, relatively simple but explicit examples with orthogonally placed arrays of transmitters and a flat or spherical object are considered. Let us discuss these examples. One can select three cases, based on varying relations between the dimensions of the transmitting arrays and the receiving aperture.

Case 1: Both dimensions of the receiving aperture are larger than the dimensions of the transmitting arrays; i.e., $d_{rx} > d_x$, $d_{ry} > d_y$. Then,

$$B_i(\delta_1, \delta_2) \sim k_i^2(\mathbf{r} = -\mu\delta_1)\,\mathrm{sinc}^2\,\Theta'_x\,\mathrm{sinc}^2\,\Theta'_y,$$

where $\Theta'_x = [(2\pi d_x)/(\lambda z_i)](\delta_{1x} - \delta_{2x})$, and $\Theta'_y = [(2\pi d_y)/(\lambda z_i)](\delta_{1y} - \delta_{2y})$.

The correlation area in this case is $S_i = \rho_{ix}\rho_{iy}$, where $\rho_{ix} = (z_i\lambda)/d_x$ and $\rho_{iy} = (z_i\lambda)/d$ are correlation radii along the X and Y axes, respectively, and the contrast $C \approx (d_x d_y)/(d_{rx}d_{ry}) < 1$. For a flat rectangular object, the number of speckles in the restored image is $M = (d_x d_y d_{ox} d_{oy})/(r_c\lambda)^2$, where d_{ox} and d_{oy} are the object's dimensions, and for a spherical object, $M = (\sigma^2 d_x d_y \rho_o^2)^2/(\ell r_c\lambda)^2$, where ρ_o is the object radius. In the case where $d_{rx} \gg d_x$, $d_{ry} \gg d_y$, $C \ll 1$; and the Fourier telescopic image is analogous to an image obtained by summing a large number of independent coherent images or an image in polychromatic radiation, for instance, in white light (see Sec. 2.5).

Case 2: Both dimensions of the receiving aperture are smaller than the dimensions of the transmitting arrays; i.e., $d_{rx} < d_x$ and $d_{ry} < d_y$. Then,

$$B(\delta_1, \delta_2) \sim k_i^2(\mathbf{r} = -\mu\delta_1)w(\delta_1 - \delta_2) = \mathrm{sinc}\,\Theta_{rx}\,\mathrm{sinc}\,\Theta_{ry},$$

where $w(\boldsymbol{\delta}_1 - \boldsymbol{\delta}_2) = \operatorname{sinc}\Theta_{rx}\operatorname{sinc}\Theta_{ry}$, and

$$\Theta_{rx} = \left(\frac{2\pi d_{rx}}{\lambda z_i}\right)(\delta_{1x} - \delta_{2x}),\ \Theta_{ry} = \left(\frac{2\pi d_{ry}}{\lambda z_i}\right)(\delta_{1y} - \delta_{2y}).$$

The correlation area is $S_c = \rho_{ix}\rho_{iy}$, with $\rho_{ix} = (z_i\lambda)/d_{rx}$ and $\rho_{iy} = (z_i\lambda)/d_{ry}$ being the correlation radii along the X and Y axes, and the contrast $C \approx 1$. For a flat rectangular object, the number of speckles in the image is $M = (d_{rx}d_{ry}d_{ox}d_{oy})/(r_c\lambda)^2$; for a spherical object, $M = (\sigma^2 d_{rx}d_{ry}\rho_o^2)/(\ell r_c\lambda)^2$. In this case, the Fourier telescopic image is the same as a normal coherent image.

Case 3: One of the receiving aperture dimensions, say, the Y-array dimension, is smaller than the dimension of the transmitting array; and the other dimension of the receiving aperture is larger than the dimension of the transmitting array, i.e., $d_{rx} > d_x$, $d_{ry} < d_y$. Then,

$$B(\boldsymbol{\delta}_1, \boldsymbol{\delta}_2) \sim k_i^2(\mathbf{r} = -\mu\boldsymbol{\delta}_1)\operatorname{sinc}\Theta_x\operatorname{sinc}\Theta_{ry},$$

where $\Theta_x = [(2\pi d_x)/(\lambda z_i)](\delta_{1x} - \delta_{2x})$ and $\Theta_{ry} = [(2\pi d_{ry})/(\lambda z_i)](\delta_{1y} - \delta_{2y})$. The correlation area is $S_i = \rho_{ix}\rho_{iy}$, where $\rho_{ix} = (z_i\lambda)/d_x$ and $\rho_{iy} = (z_i\lambda)/d_{ry}$ are correlation radii along the X and Y axes, and the contrast $C \approx d/d_{rx}$. For a flat rectangular object, the number of speckles in the reproduced image is $M = (d_x d_{ry}d_{ox}d_{oy})/(r_c\lambda)^2$; for a spherical object, $M = (\sigma^2 d_x d_{ry}\rho_o^2)/(\ell r_c\lambda)^2$.

Dimensions P_x and P_y of the domain resolvable by Fourier-telescopic imaging on the object surface are, according to the Rayleigh criterion, related to the correlation radii in the plane of the reproduced image as follows (see Appendix 2). For the first case,

$$P_x = \mu\rho_{ix} = \frac{r_c\lambda}{d_x};\quad P_y = \mu\rho_{iy} = \frac{r_c\lambda}{d_y}. \tag{4.7a}$$

Here the resolution of the Fourier telescopy is determined by size d of the X- and Y-arrays.

For the second case,

$$P_x = \mu\rho_{ix} = \frac{r_c\lambda}{d_{rx}};\quad P_y = \mu\rho_{iy} = \frac{r_c\lambda}{d_{ry}}. \tag{4.7b}$$

In this case, the resolution of the Fourier telescopy is limited by sizes d_{rx} and d_{ry} of the receiving aperture. This is due to the fact that under the conditions $d_{rx} < d_x$ and $d_{ry} < d_y$, the numbers of speckles in the scattered field on the receiving aperture and in the image are the same. Therefore, the decrease in d_{rx} and d_{ry} leads to a decrease in the number of speckles in the image. Their sizes ρ_{ix} and ρ_{iy} become larger, which leads to an increase of the sizes P_x and P_y of the minimally resolved domains on the object surface. Hence, the resolution of the Fourier-telescopic method decreases.

For the third case,

$$P_x = \mu\rho_{ix} = \frac{r_c\lambda}{d_x}; \quad P_y = \mu\rho_{iy} = \frac{r_c\lambda}{d_{ry}}. \tag{4.7c}$$

Here, resolution of the Fourier telescopy along the X-axis is determined by the transmitter array size d_x, and the resolution along the Y-axis by the size d_{ry} of the receiving aperture.

It is interesting to note the important fact that follows from the above expressions: the number of speckles in the Fourier telescopic image, as in the case of usual coherent images (see Chapter 2 and Appendix 1) is equal to the number of resolvable domains on the surface of the object under study.

4.2.3 Effect of the laser transmitter's time instability, including low coherence, on the quality of the Fourier-telescopic image

Let us study how time instability of the laser transmitter influences the quality of the Fourier-telescopic image, namely, the intensity distribution in the image, $I(\boldsymbol{\delta})$. This can be estimated with considerable accuracy by assuming that the laser transmitters are placed along the X- and Y-arrays nearly continuously, that the arrays are of equal size ($d_x = d_y = d$) and form a cross, and finally, that atmospheric fluctuations are compensated for. Then, under the assumption that time fluctuations of the laser radiation are stationary and Gaussian, with the spectral width $\Delta\omega \le \omega_{xm} - \omega_{yn}$, we obtain

$$\langle I(\boldsymbol{\delta})\rangle \sim |D(\mathbf{r}_c)|^2 \int_{-\infty}^{\infty}\int_{-\infty}^{\infty}\int_{-\infty}^{\infty}\int_{-\infty}^{\infty}\int_{-\infty}^{\infty} S_r(\omega-\omega_0)k_i(\mathbf{r}) \times \exp i\frac{\omega}{c}\left[u\left(\frac{x}{r_c}+\frac{\delta_x}{z_i}\right)+v\left(\frac{y}{r_c}+\frac{\delta_y}{z_i}\right)\right]d\omega\,du\,dv\,dx\,dy,$$

where $\omega = (2\pi c)/\lambda$ and $\omega_0 = (2\pi c)/\lambda_0$; ω_0 and λ_0 are the central frequency and wavelength of the laser radiation, respectively; and $S_r(\omega - \omega_0)$ is the spectral amplitude of the laser radiation. For simplicity, we further assume that the spectral amplitude has Gaussian shape, $S_r(\omega - \omega_0) \sim \exp[-(\omega-\omega_0)^2/(\Delta\omega)^2]$, and $\Delta\omega T \gg 1$. Then, for $M \gg 1$,

$$\langle I(\boldsymbol{\delta})\rangle \sim |D(\mathbf{r}_c)|^2 k_i(\mathbf{r}=-\boldsymbol{\delta})\left[1+\left(\frac{c_1\boldsymbol{\delta}^2\Delta\omega d}{cz_i^2}\right)\right], \tag{4.8}$$

where c_1 is a constant on the order of unity. One can see from Eq. (4.8) that for an object placed on the axis of a receiving system, the Fourier-telescopic image has the largest distortions on its boundary, where $\delta_x = \delta_{xb} \sim \delta_y = \delta_{yb} \sim d_i$. Here, d_i is the image size; for instance, for a flat square object, $d_i = d_o/\mu$, where d_o is the

object size. For a sphere, $d_i = (\rho_o \sigma)/\ell$, where ρ_o is its radius (see Sec. 2.1). Taking into account the foregoing equations and the relations for the number of speckles M in the Fourier-telescopic image, it is easy to obtain that the instability of laser radiation has almost no effect on the quality of the restored image, provided that $\Delta\omega/\omega \ll 1/M^{1/2}$.

The frequency of the illuminating radiation usually has linear variations in time, $\omega_b = \omega_0 + \beta_d t$, where ω_0 is the initial frequency, and β_d is constant. Assuming for simplicity that the received signal is processed using a narrow Gaussian time window, i.e.,

$$G_{mn} \approx \frac{1}{T} \int_{-\infty}^{\infty} \mathrm{Q}(t) \exp -\left(\frac{t - t_0}{T}\right)^2 \exp it(\omega_{yn} - \omega_{xm}) dt,$$

where t_0 is the received signal processing start time, we obtain

$$\langle \mathbf{I}(\boldsymbol{\delta}) \rangle \sim |D(\mathbf{r}_c)|^2 k_i(\mathbf{r} = -\mu\delta) \left[1 + \frac{\delta^2 \Delta\omega_t d}{(cz_i)^2}\right], \tag{4.8a}$$

where

$$\Delta\omega_t = \sqrt{\frac{\beta_d^2 + \alpha_e^2}{\alpha_e^2}}, \quad \alpha_e = (\Delta\omega)^2 + \frac{1}{\tau_e^2}, \quad \tau_e = \frac{T\tau}{\sqrt{T^2 + \tau^2}},$$

and τ is the duration of the laser pulse also having, for simplicity, Gaussian form. One can see from Eq. (4.8a) that laser radiation instability and its frequency deviations have almost no effect on the quality of the Fourier-telescopic image under the condition

$$\chi = \frac{\Delta\omega_t M^{1/2}}{\omega_b} \ll 1. \tag{4.9}$$

Let us consider two cases:

(1) $\beta \gg \alpha$. If $\Delta\omega\tau_e \gg 1$, then $\Delta\omega_t = \beta/\Delta\omega$; if $\Delta\omega\tau_e \gg 1$, then $\Delta\omega_t = \Delta\omega$.
(2) $\beta \ll \alpha$. If $\Delta\omega_t \ll 1$, then $\Delta\omega_t = 1/\tau_e$. If $\Delta\omega\tau_e \ll 1$, then $\Delta\omega_t = \beta\tau_e$.

Let, for example, the backscattering surface of an object under study contain $M = 10^4$ resolvable domains, and let both dimensions of the receiving aperture be larger than the dimensions of the transmitting arrays, i.e., $d_{rx} > d_x$, $d_{ry} > d_y$. Here, the backscattering surface area $S_e \approx M(\lambda r_c)^2/(d_x d_y)$. Then, for instance, choosing the signal processing time $T \sim 10^{-3}$, which is less than the time of the atmosphere stability $\sim 10^{-2}$, and during which the radiation frequency drift is about 10 GHz, for illuminating an object with cw monochromatic infrared radiation ($\lambda \approx 10^{-6}$ m),

we have the case 1(a): $\Delta\omega_t \approx 10^7$ s^{-1}, $\omega_b \approx 3 \times 10^{13}$ s^{-1}, $\chi \approx 3 \times 10^{-2} \ll 1$. Hence, the frequency drift of 10 GHz has practically no influence on the quality of the Fourier-telescopic image.

Relation (4.8a) has a simple physical interpretation (Fig. 4.4). It is easy to show that $(\delta^2 \Delta\omega_t d)/(cz_i) \leq (dd_e)/r_c$, where d_e is the size of the object shine domain (the backscattering surface area). If the object is placed on the receiving–transmitting system axis, then from Eq. (4.9) we obtain the following restriction for the laser radiation coherence length: $L_c = c/\Delta\omega_t \gg L_d = \mathrm{AC} - \mathrm{CB} \approx (dd_e)/r_c$ [Fig. 4.4(a)].

Here, L_d is the path length difference for the beams coming from the most distant transmitters to the edges of the object's scattering area. This means that the laser radiation instability is small enough so that the coherence length is essentially smaller than L_d. If the object is not on the receiving system axis, then by removing transmitters we can make the path length difference $L_d = \mathrm{A^*C} - \mathrm{CB}$ less than the source coherence length [Fig. 4.4(b)].

Fourier telescopy was proposed mainly for imaging very distant objects. Yet, it can be also applied to obtaining, in the absence of phase fluctuations, the images of relatively extended objects with very small surface details. As an example of the Fourier telescopy of such objects, consider the scheme of a panoramic microscope for imaging extended objects having sizes ~10 cm and a resolution of approximately the wavelength λ of the illuminating radiation.

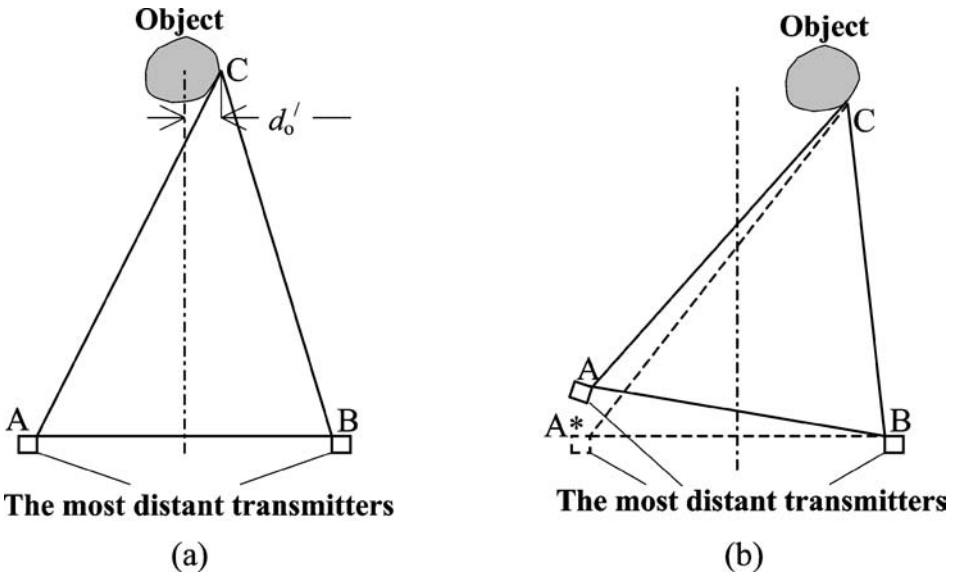

Figure 4.4 Geometry of the effect of the laser transmitter time instability, including low coherence, on the quality of the Fourier-telescopic image. A and B are the most distant transmitters, the dash-dot line is the receiving–transmitting system axis, the dashed square is the initial displacement of the laser transmitter, and the dashed lines connect this displacement (point A*) with the edge of the scattering area of the object (point C).

4.3 Fourier-telescopic panoramic microscope

4.3.1 Introduction

When imaging distant extended objects with a resolution of approximately λ, the mean wavelength of the illuminating light assumes new significance. Particularly, in internal surgery it is often necessary to have a high-resolution image of a large (∼10 cm) area of tissue situated at a distance of more than 10 cm from the imaging system. Yet, most microscopes with ∼λ resolution require that the object is placed near the front focal plane of the imaging system aperture at a distance of less than 10 mm (Ref. 3). This limits the field-of-view of traditional microscopes: the area of tissue that can be imaged this way does not exceed 1 mm^2. This fact makes it difficult to use traditional microscopes in such applications. This section describes a panoramic microscope design that allows simultaneous imaging of different parts of a distant large-area object with ∼λ resolution, by employing the principle of Fourier telescopy.[18,71] The object is illuminated by light from a transmitting aperture with transmitters of monochromatic radiation. The transmitters are controlled in such a way that light coming from various source pairs produces sinusoidal interference patterns with different periods and directions on the object's surface. The part of the scattered energy that corresponds to a fixed pattern formed by each couple of transmitters is detected. This part is proportional to a certain spatial Fourier component of the object's image. Then, the object image is reconstructed using an inverse Fourier transform.

4.3.2 Analysis of image formation in a panoramic microscope

The proposed schematic of the panoramic microscope is as follows (Fig. 4.5). Laser transmitters of different frequencies illuminate an object simultaneously. The transmitters form orthogonal linear arrays, which intersect at the center of the receiving aperture. These arrays, together with the receiving aperture, compose the joint transmitting–receiving aperture. Both dimensions d_{rx} and d_{ry} of the receiving aperture exceed dimensions of transmitting arrays d_x and d_y; i.e., $d_{rx} > d_x$ and $d_{ry} > d_y$.

The object is illuminated by continuous radiation from different-frequency laser transmitters that are located equidistantly on the X and Y linear arrays. If each linear array contains N_t symmetrically placed transmitters of the same size, then dimensions of the transmitting aperture are $d_x = d_y = N_t d_t = d$. The scattered light is focused on the detector. A comb filter selects signals at the difference frequency and sends them to the image-forming unit. The reconstructed image is viewed on a display.

Let us now analyze image formation in a panoramic microscope. The analysis is the same as image formation analysis in the case of Fourier-telescopic imaging through the atmosphere, excluding the influence of phase distortions. The complex amplitude of the scattered light [see relation (4.1)] at the receiving aperture can be

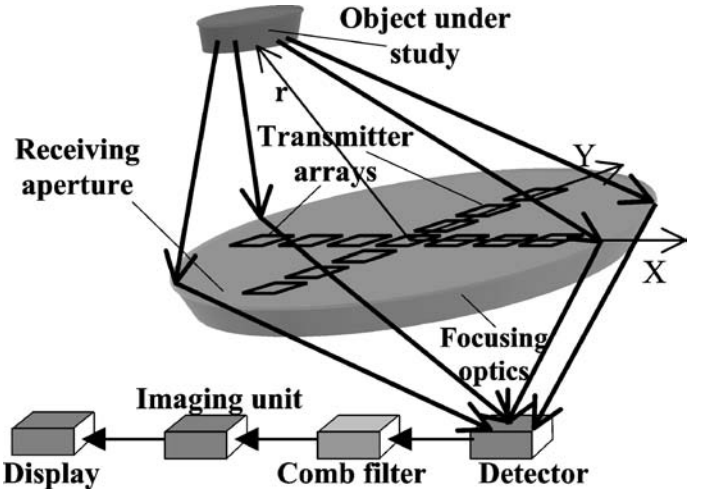

Figure 4.5 Conceptual schematic of a Fourier-telescopic panoramic microscope. Thick arrows denote rays scattered by the object.

rewritten without the phase distortions as

$$E(\boldsymbol{\rho}, t) = \left[\frac{E_t S_t}{(\lambda r_c)^2}\right] \int k(\mathbf{r}) u(\mathbf{r}, t) \exp\left[\frac{4\pi i \xi(\mathbf{r}) \mathbf{r} \cdot \mathbf{N}}{\lambda r_c}\right] d\mathbf{r}, \tag{4.10}$$

where

$$u(\mathbf{r}, t) = \sum_{n=1}^{n=N} u_n\left(t - \frac{2r}{c}\right) D_n(\mathbf{r}) \exp i\left[\omega_n t - 2\frac{\omega_n r}{c} + \frac{\omega_n \mathbf{r} \cdot (\boldsymbol{\rho}_n + \boldsymbol{\rho})}{2 r_c c}\right],$$

and $\xi(\mathbf{r})$ is the roughness height distribution on the surface of the object under study. This formula repeats Eq. (4.1) of Sec. 4.2, including all notations. The power $\mathrm{Q}(t)$ of the scattered light is averaged over the area of the receiving aperture S_ρ,

$$\mathrm{Q}(t) = \left(\frac{1}{S_\rho}\right) \int |E(\boldsymbol{\rho}, t)|^2 d\boldsymbol{\rho}, \tag{4.11}$$

and filtered using the following algorithm: one selects the portion of the detected power that is defined by the sinusoidal distribution produced by the *m*th transmitter of the X-array and the *n*th transmitter of the Y-array,

$$G_{mn} = \frac{1}{T} \int_{t_0}^{t_0+T} \mathrm{Q}(t) \exp[i(\omega_{yn} - \omega_{xm})t] dt.$$

Assuming that the surface roughness height distribution is Gaussian, and using Eqs. (4.10) and (4.11), as a result of the averaging over realizations of $\xi(\mathbf{r})$, we obtain $\langle G_{mn}\rangle = \Theta|D_m(\mathbf{r}_c)D_n^*(\mathbf{r}_c)|\langle F_{mn}\rangle$, where $\Theta = (S_t|E_t|)^2/(\lambda r_c)^2$, and

$$\langle F_{mn}\rangle = \frac{|D(\mathbf{r}_c)|^2}{S_e}\int k_i(\mathbf{r})\exp\left\{\frac{i[(d_x x\omega_m m - d_y y\omega_n n)/N]}{2r_c c}\right\}d\mathbf{r},$$

where

$$k_i(\mathbf{r}) = \left(\frac{\ell}{\sigma}\right)^2 |k(\mathbf{r})|^2 \exp\left[-\left(\frac{\ell q_\perp}{q_N \sigma}\right)^2\right]$$

is the (m, n)-th Fourier component of the function $k_i(\mathbf{r})$, which is proportional to the averaged intensity distribution of the usual coherent image of the object (see Sec. 2.3). By making the inverse Fourier transformation,

$$I(\boldsymbol{\delta}) = \frac{1}{N^2}\sum_{m=-N,n=1}^{m=N,n=N} G_{mn}\exp i\frac{2\pi(d_x\delta_x m + d_y\delta_y n)}{z_i N\lambda},$$

where z_i is the distance from the receiving aperture to the image plane, $\boldsymbol{\delta}$ is the radius vector of a point on this plane, and δ_x and δ_y are the coordinates of this point, we obtain the intensity distribution in the object image,

$$I(\boldsymbol{\delta}) = \frac{\Theta}{N^2}\iint_{ss} k(\mathbf{r}_1)k^*(\mathbf{r}_2) \times \exp i\left\{\frac{4\pi}{\lambda}\left[\mathbf{r}_1 - \mathbf{r}_2 + \frac{\mathbf{r}_1\cdot\mathbf{N}(\mathbf{r}_1)(\xi(\mathbf{r}_1) - \xi(\mathbf{r}_2))}{r_c}\right]\right\} \times h(\mathbf{r}_1, \mathbf{r}_2, \boldsymbol{\delta})d\mathbf{r}_1 d\mathbf{r}_2,$$

where

$$h(\mathbf{r}_1, \mathbf{r}_2, \boldsymbol{\delta}) = \frac{\sin 2\pi d_x[(x_1/r_c) + (\delta_x/z_i)]/\lambda}{\sin 2\pi d_x[(x_1/r_c) + (\delta_x/z_i)]/N\lambda}\cdot\frac{\sin 2\pi d_y[(y_2/r_c) + (\delta_y/z_i)]/\lambda}{\sin 2\pi d_y[(y_2/r_c) + (\delta_y/z_i)]/N\lambda}$$

is the pulse response of the Fourier-telescopic imaging system.

In the case of a high-resolution imaging system, where the number of minimally resolved domains on the object surface $M = (d_x d_y S_e)/(\lambda r_c)^2 \gg 1$, with S_e being the area of the object's backscattering surface, then $I(\boldsymbol{\delta})\rangle \sim k_i(\mathbf{r} = -\mu\boldsymbol{\delta})$ [see also relation (4.6a)]. Hence, the function $\langle I\rangle$, as shown in Chapter 2, gives the brightness distribution in the optical image of the object built by high-resolution optics in natural light.

Let us estimate the resolution of the proposed microscope. For the case considered here, where both dimensions of the receiving aperture exceed the dimensions of the transmitting aperture ($d_{rx} > d_x$, $d_{ry} > d_y$), from relation (4.7a) we determine that the sizes of the minimally resolved domain are $P_x = \lambda/\gamma_x$ and $P_y = \lambda/\gamma_y$, where $\gamma_x = d_x/r_c$ and $\gamma_y = d_y/r_c$. The maximum value of γ_x and γ_y is σ/ℓ, since at larger γ_x and γ_y, rays coming from the edge transmitters and scattered by the object do not overlap on the receiving aperture. Hence, resolution of the Fourier-telescopic panoramic microscope is limited by $P = (\lambda\ell)/\sigma$ and $P_x, P_y \geq (\lambda\ell)/\sigma$.

It should be noted that traditional microscopy (Fig. 4.6) has $\sim\lambda/\gamma$ resolution, where γ is the input angular aperture of the microscope's imaging system.[3] However, in traditional microscopy, $\gamma \geq 0.2$, and therefore, the resolution limit is $P_t = 5\lambda$.

The resolution limit of the Fourier-telescopic panoramic microscope is $P_F = (\lambda\ell)/\sigma$. For instance, at $\sigma/\ell \approx 0.3$, $P_F \approx 3\lambda > P_t$. The size of the imaged area in traditional microscopy is not more than several millimeters. In the case of Fourier-telescopic panoramic microscopy, it is equal to the size of the object's backscattering surface, $(\rho_o\sigma)/\ell$, where ρ_o is the curvature radius of this surface. For instance, if $\rho_o \sim 30$ cm, then at $\sigma/\ell \approx 0.3$ the size of the domain under study is $\sim$10 cm, and the resolution is $P_F \approx 3\lambda$.

Figure 4.7 shows one of the possible designs of a panoramic microscope. This system uses a thin Fresnel lens as the illuminating source and an aperture to detect the scattered light. Two illuminating laser beams of close frequencies ω_1 and ω_2 from a single cw laser are directed at two deflectors, a continuous one and a discrete one, and then at two diverging lenses. The beams are driven by the deflectors, one of them continuously and the other discretely, in an orthogonal direction along the diameters of the Fresnel lens. The number of beam positions in each direction is equal to $3\sqrt{M}$, where M is the number of object surface domains to be resolved. The lens directs both beams onto the object under study and the scattered light on the detector. For smoothing the speckle pattern in the image, the receiving aperture size must exceed the size of the transmitter aperture (see Fig. 4.7 and

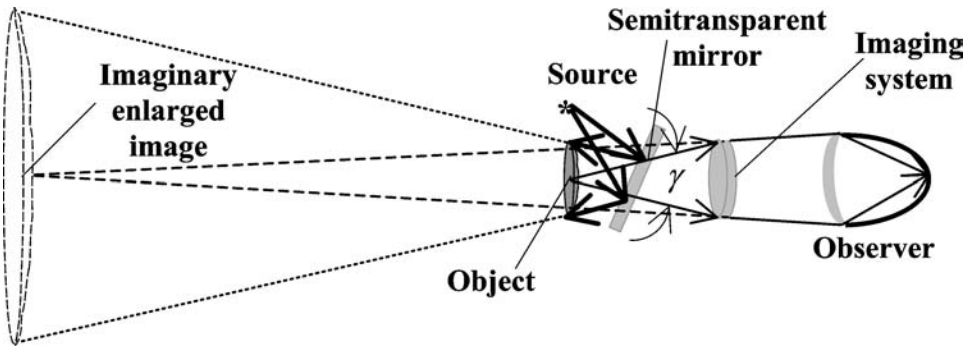

Figure 4.6 A simplified schematic of microscopy for a nontransparent object. The thick arrows denote illuminating rays; the thin arrows denote scattered rays.

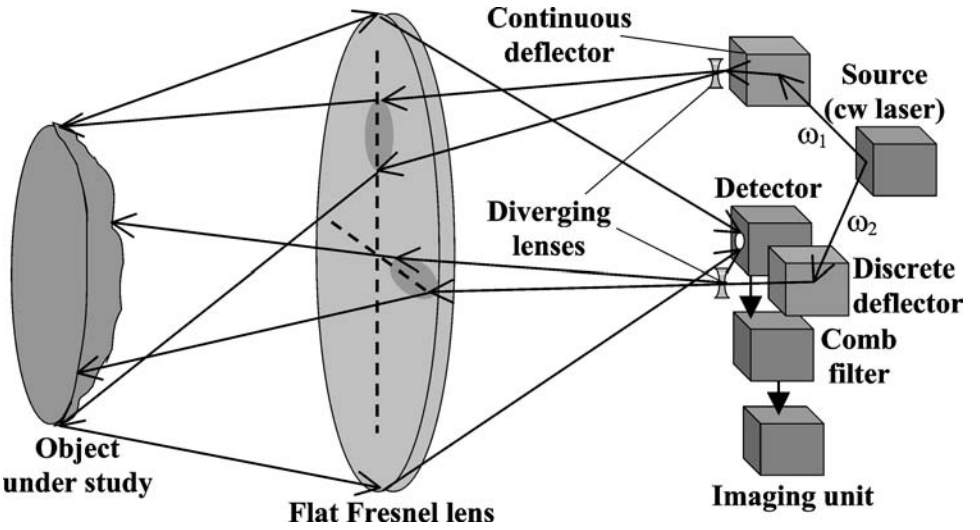

Figure 4.7 Design of the Fourier-telescopic panoramic microscope with a Fresnel lens used as the illuminator of the object under study and a receiving aperture for the radiation scattered by this object. The transmitter aperture (domains scanned by the illuminating laser beams) is shown by dashed lines. For smoothing the speckle pattern in the image, its dimensions are smaller than the Fresnel lens diameter.

Sec. 4.4). The comb filter at the difference frequency filters the electric signal from the detector. The object's image is assembled in the imaging unit using the inverse Fourier transform.

In the next section, we will analyze in detail the integral and local measures of the relationship between an object's Fourier-telescopic image and its averaged undistorted image.

4.4 Integral and local measures of the relationship between the Fourier-telescopic image of an object and its averaged undistorted image

Let us estimate the degree of closeness of a real Fourier-telescopic image of an object in the presence of added noise to its averaged undistorted image as a whole. For this purpose, let us represent the noise component in the real image as the image of an imaginary noise object with the intensity distribution equal to $I_n(\delta)$;[12] and let us introduce the integral correlation measurement of the relationship between the real Fourier-telescopic image and the averaged undistorted image of the object as

$$K = \frac{\int I_i(\delta) I_\Sigma(\delta) d\delta}{\int I_i^2(\delta) d\delta}, \tag{4.12}$$

where $I_\Sigma(\delta) = I(\delta) + I_n(\delta)$ is the intensity distribution in the real image, and $I(\delta)$ and $I_i(\delta) = \langle I(\delta)\rangle$ are intensity distributions in the undistorted Fourier-telescopic image and its averaged image, respectively.

The imaginary noise object can be represented by a flat rough surface placed in the Fresnel zone and having the area S_n, far larger than the backscattering area of the object under study, S_e. This surface can be of various physical origins. In particular, for a noise aerosol cluster, the surface has the same backscattering properties as the cluster itself. The closer the quantity K is to unity, the better the real reconstructed image $I_\Sigma(\delta)$ reproduces the undistorted image $I_i(\delta)$.[12] The accuracy of this relationship can be estimated by relative fluctuations of K defined as $\eta = (\langle K^2\rangle - \langle K\rangle^2)/\langle K\rangle^2$, where brackets $\langle\rangle$ stand for the averaging over various realizations $\xi(\mathbf{r})$ of the surface roughness height.

Let, for simplicity, the size of the transmitter arrays be equal and the area S_ρ of the receiving aperture be big ($S_\rho > d^2$, where d is the size of the transmitter array). Then [see Appendix 2, relation (A2.13)] the correlation function of the intensity distribution $I(\delta)$ in the Fourier-telescopic image in the absence of noise is

$$B(\delta_1, \delta_2) \sim k_i^2(\delta_1)\,\mathrm{sinc}\,\frac{2\pi(\delta_{2x} - \delta_{1x})d}{\lambda z_i}\,\mathrm{sinc}\,\frac{2\pi(\delta_{2y} - \delta_{1y})d}{\lambda z_i},$$

the correlation radii along the X and Y axes are $\rho_i = (\lambda z_i)/d$, and the number of speckles in the object image is $M \approx S_e/(\mu\rho_i)^2$. For example, for a square, flat, rough object, $S_e = d_o^2$, where d_o is its size, and $M \approx d_o^2/(\mu\rho_i)^2 = (d_o d)^2/(\lambda r_c)^2$. When $S_\rho > d^2$, the intensity distribution contrast in the Fourier-telescopic image is $C = d^2/S_\rho < 1$. With an account for the last relations, if $M \gg 1$, then $\eta \approx C/M < 1/M \ll 1$. Hence, $\eta \ll 1$ and $K \approx 1$. This means that under the conditions $S_\rho > d^2$ the Fourier-telescopic image is very close to the true image of the object [$I(\delta)$ differs weakly from $I_i(\delta)$] and has small contrast C. We see that unlike coherent imaging, in which the contrast of a speckled pattern is usually near unity,[12] the Fourier-telescopic imaging method can give much smaller values of the image contrast. For $S_\rho \geq 10d^2$, the method already provides an image quality as good as that formed by high-resolution optics in natural light [see Sec. 2.4, relation (2.26)]. Thus, for smoothing the image speckle pattern , the receiving aperture sizes should considerably exceed the size of the transmitter linear arrays. In this case, the image quality is the same as in traditional optical imaging where polychromatic illuminating radiation is used. Consequently, the value K can be considered as the integral correlation measurement of the relationship between a real Fourier-telescopic image and a true, undistorted image.

The integral correlation measurement K can be also used to identify an object in the presence of noise. For this purpose, we must know the distribution densities for the random value K in the presence of the object, $w_p(K)$ (see Fig. 4.8), and in the absence of the object, $w_a(K)$. In the latter case, only the noise component is present in the Fourier-telescopic image, which may be represented as an imaginary noise object image.[12] Let us approximate these distributions by a gamma distribution; then, the distribution density of the integral measurement K is given by the formula

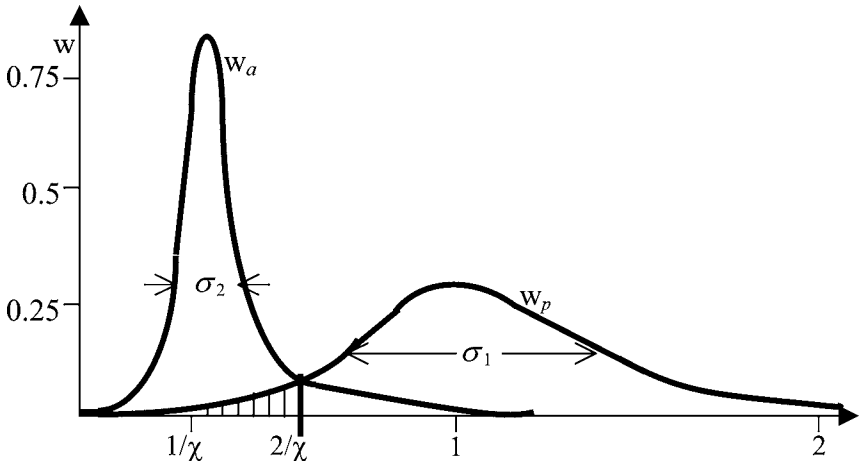

Figure 4.8 Probability densities of distributions for the integral measurement K in the absence and in the presence of the object.

$w(K) = [(\beta^{\alpha})/\Gamma(\alpha)]K^{\alpha-1}\exp(-\beta K)$, where $\Gamma(\alpha)$ is the gamma function, and whose center m and variance D are determined from the relations $m = \langle K\rangle = \alpha/\beta$, $D = \langle K^2\rangle - \langle K\rangle^2 = \alpha/\beta^2$. Then, in the presence of the object, if $M \gg 1$ and the signal-to-noise ratio $\chi = \langle I(\delta)\rangle/\langle I_n(\delta)\rangle \gg 1$, using Eq. (4.12) we obtain

$$\langle K\rangle = m_1 \approx 1, \quad \sigma_1 = D_1^{1/2} = \left(\frac{M}{C}\right)^{-1/2}.$$

Therefore,

$$w_p(K) = \left(\frac{M}{2C\pi}\right)^{1/2} K^{(M/C)-1}\exp\left[-\left(\frac{M}{C}\right)(1-K)\right],$$

where $C = d^2/S_{\rho}$ is the contrast of the speckle pattern in a Fourier-telescopic image. If the object is absent $[I(\delta) = 0]$ and the number of speckles in the imaginary noise object image $M_n \gg \chi^2$, then also using Eq. (4.12) we obtain

$$\langle K\rangle = m_2 = \frac{1}{\chi}, \quad \sigma_2 = D_2^{1/2} = \left(\frac{M_n}{C}\right)^{-1/2}.$$

Then,

$$w_a(K) = \left(\frac{M_n}{2C\pi}\right)^{1/2} (\chi K)^{\alpha_n - 1}\exp\left[-\left(\frac{M_n}{C}\right)\left(\frac{1}{\chi^2} - \frac{K}{\chi}\right)\right],$$

where $\alpha_n = M_n/(C\chi^2)$.

Here, we assume that χ and M_n are known *a priori*.[12] Since $S_n \gg S_e$, then $M_n \gg M$. We assume that the object is recognized if K exceeds a given threshold K_t. For $M > 10$ and a relatively high signal-to-noise ratio $\chi > 6$, the following relations hold: $m_1 \ll m_2$ and $\sigma_1 \ll \sigma_2$. Under these conditions, one can choose a rather low-recognition threshold, $K_t = 2/\chi \approx 0.3$. Then in the case where $M > 10$, $\chi > 6$, a false alarm, i.e., when an imaginary noise object is taken for the object under study, has very low probability:

$$P_f = \int_{K_t}^{\infty} w_a(K)dK \ll 1,$$

and the object recognition probability is $P_o = 1 - P_m$, where

$$P_m = \int_0^{K_t} w_p(K)dK \approx \sqrt{\frac{C}{2\pi M}} \frac{[2^{M/C} \exp(M/C)]}{\chi^{M/C}} \ll 1$$

is the probability that the object is missing. For $M \geq 10$, $C \approx d^2/S_o = 1/2$ and $\chi \geq 6$, $P_m \ll 1$, and P_o is close to unity. Consequently, object recognition is reliable even for the case when the useful signal level does not essentially exceed the additional noise level ($\chi \geq 6$) and the number of speckles in the Fourier-telescopic image is not large ($M \geq 10$).

Integral correlation measurements are useful for estimating to what extent a real Fourier-telescopic image is close to the average undistorted image as a whole. To estimate the degree of similarity between the Fourier-telescopic images of particular details of the object and their undistorted images, we introduce local measures. As local measures, it is convenient to take two numbers: $M_x = \Lambda_x/P_x$ and $M_y = \Lambda_y/P_y$, where P_x and P_y are the sizes of the smallest resolved domain on the surface of an object along the X and Y axes, and Λ_x and Λ_y are the smallest detail sizes along the X and Y axes calculated by the formulas (2.20) of Chapter 2:

$$\Lambda_x = |k_i(\mathbf{r} = -\mu\boldsymbol{\delta})| \left[\left| k_i \frac{\partial^2 k_i}{\partial x^2} + 2\left(\frac{\partial k_i}{\partial y} \right)^2 \right| \right]^{-1/2},$$

and

$$\Lambda_y = |k_i(\mathbf{r} = -\mu\boldsymbol{\delta})| \left[\left| k_i \frac{\partial^2 k_i}{\partial y^2} + 2\left(\frac{\partial k_i}{\partial y} \right)^2 \right| \right]^{-1/2}. \tag{4.13}$$

Here, all derivatives are taken at the point $\mathbf{r} = -\mu\delta$, and $M_d = M_x M_y$ is equal to the number of speckles in the image of the smallest detail. The larger the numbers M_x and M_y, the higher the degree of similarity between the smallest details

and their true, undistorted image. For instance, in the case of a flat object surface having a periodic reflection coefficient $k_i(x, y) \sim \cos(2\pi x/\Lambda_{0x})\cos(2\pi y/\Lambda_{0y})$, the smallest sizes of the details are $\Lambda_x \approx \Lambda_{0x}$ and $\Lambda_y \approx \Lambda_{0y}$. If $M_x = \Lambda_x/P_x \gg 1$ and $M_y = \Lambda_y/P_y \gg 1$, then details with sizes Λ_x and Λ_y are reproduced very well and $M_d \gg 1$. Hence, under these conditions, Fourier telescopy resolves these details and the similarity between the smallest details and their true undistorted images is high. One can show[12] that the standard deviations of estimating the sizes of the object's details are $\sigma_x = \Lambda_x/\sqrt{M_x}$ and $\sigma_y = \Lambda_y/\sqrt{M_y}$. We see that the accuracy of the object's size estimation depends on the local measurements of similarity. Hence, the larger M_x and M_y are, the more the image of a detail resembles its true undistorted image, and the higher the accuracy of the detail estimation parameters.

4.5 Conclusions

1. The transmitting aperture used in Fourier telescopy for illuminating an object can consist of two orthogonal arrays with difference-frequency transmitters, placed equidistantly. The minimum size d of each array is determined by the desired resolution of the method; it is related to the required number of the resolvable domains M on the object's surface and the object's surface shape. For a spherical rough object placed at a distance r_c, then $d = (\sqrt{M} r_c \ell\lambda)/(\sigma\rho_o)$, where ρ_o is the object's radius, and σ and ℓ are the standard deviation and the correlation radius of the object surface roughness, respectively. The minimum number N_t of transmitters on each array should be approximately $3\sqrt{M}$.
2. A Fourier-telescopic image is similar to a coherent image formed by a typical optical system; it depends essentially on the object's surface shape and the parameters σ and ℓ of the object's surface roughness. For instance, for a nonflat rough object, the intensity in the Fourier-telescopic image is proportional to $(\ell/\sigma)^2$ in each part of the image. In addition, the image consists of the images of separate shine domains of the object surface with size $d_j = (\rho_j \sigma z_i)/(r_c \ell)$, where ρ_j is the curvature radius for the jth shine domain and z_i is the distance from the receiving aperture plane to the image plane.
3. Periodic instability of illuminating laser radiation, including the central frequency drift and the initial radiation spectral width, has no influence on the quality of the Fourier-telescopic image if $(\Delta\omega_t\sqrt{\mathrm{M}})/\omega_b \ll 1$, where $\Delta\omega_t$ is the total spectral broadening of the radiation frequency during the signal processing, and ω_b is the initial radiation frequency.
4. After eliminating the effect of turbulent atmosphere, the obtained undistorted image of the object is the same as the usual coherent image gained in the absence of phase distortion.
5. A proposed laser panoramic microscope based on the principles of Fourier telescopy enables imaging of objects as large as 10 cm and located as far as 10 cm away from an imaging system with resolution approximating that of the illuminating radiation wavelength. With a receiving aperture that is much larger than the transmitting arrays, a panoramic microscope can produce an image with

speckle contrast noticeably less than the contrast of a usual coherent image (unity). For this reason, despite the fact that the object is illuminated by monochromatic radiation, the image quality is the same as with a high-resolution white-light microscope.

6. The value

$$K = \frac{\int I_i(\delta) I_\Sigma(\delta) d\delta}{\int I_i^2(\delta) d\delta},$$

where $I_\Sigma(\delta) = I(\delta) + I_n(\delta)$ is the real intensity distribution in a Fourier-telescopic image, $I_n(\delta)$ is the intensity distribution of the noise component of a Fourier-telescopic image, and $I(\delta)$ and $I_i(\delta)$ are the intensity distributions in an undistorted Fourier-telescopic image and in the averaged undistorted Fourier-telescopic image, respectively—can be considered as the integral correlation measurement of the relationship between a real Fourier-telescopic image and the true undistorted image as a whole. If $K \approx 1$, the quality of the Fourier-telescopic image is satisfactory when the size of the receiving aperture exceeds the size of the transmitting aperture, and the speckle pattern in the image is smoothed.

7. The integral correlation measurement K can also be used to recognize an object in the presence of a noise component $I_n(\delta)$. Here, object recognition is reliable even in the case when the useful signal level does not essentially exceed the additional noise level ($\chi = 6$), the number of speckles in the Fourier-telescopic image of the object is not large ($M \approx 10$), and $S_\rho/d^2 = 2$, where S_ρ is the area of the receiving aperture and d is the size of the transmitter array.
8. To estimate the degree of similarity between a Fourier-telescopic image of a surface detail of an object and its undistorted image, one can introduce the local measurement technique. It is convenient to take as the local measurement of similarity $M_x = \Lambda_x/P_x$ and $M_y = \Lambda_y/P_y$, where Λ_x and Λ_y are the smallest detail sizes along mutually orthogonal directions, and P_x and P_y are sizes of the smallest resolved domain along these directions. If M_x and M_y are large ($\gg 1$), then the Fourier-telescopic image has the highest quality. Under those conditions, the number of speckles in the image of the smallest detail, $M_d = M_x M_y$, is large.

Chapter 5

Time Background Holography of Moving Objects

5.1 Introduction

Considerable attention is being given to methods of obtaining information about moving objects from statistical analysis of the space and time structures of coherent fields scattered by these objects as well as their coherent images. These methods enable one to solve certain problems that cannot be solved by other methods, especially with the presence of monochromatic background radiation: measuring velocity and acceleration distributions on an object's surface, which yield a deformation map of the object; determining the roughness parameters for moving surfaces; finding the geometric and dynamic parameters of weakly reflecting and transparent moving objects; detecting, in addition to size and velocity measurement, small, spatially unresolvable objects; and finally, imaging objects that are indistinguishable from the surrounding background.

The known methods for obtaining information about moving objects in the presence of monochromatic background radiation, including the situation where the object has the same scattering characteristics as the background, are based on compensating for the object's motion and increasing the contrast of its image with respect to the background image.[20,74,75] All of these methods involve complex techniques and complicated algorithms for background suppression that can be realized only with fast and powerful computers. Although several researchers have mentioned the effect of increased contrast between the holographic images of moving and stable parts of the same surface, which manifests itself as dark and bright fringes, they did not pay much attention to this effect and used it only for determining the amplitude of surface vibrations.[76,77]

It is likely that E. Feleppa was the first to notice that this effect could be used for gaining information about separately moving objects surrounded by a stable background.[19] While studying the motion of erythrocytes and leukocytes in blood by means of holographic methods, he recorded with a He-Ne laser beam a long-exposure hologram of a thin blood sample placed between two glass plates. While analyzing the reconstructed image, he noticed that against a bright background there were noticeable intensity minima, both at places occupied by moving ery-

throcytes, which have high reflection for laser radiation, and at places occupied by moving leukocytes, which have weak contrast and are usually invisible. The intensity minima became more pronounced with the increase in the hologram exposure time and, hence, with the increase of particle displacement. As a result, separate shadow images of the moving particles appeared. In this way, Feleppa managed to increase considerably the contrast for particles that had been initially invisible. In Ref. 78, the effect is explained by the fact that during hologram exposure, coherent fields scattered by the moving object and by the surrounding background are averaged in time. If object displacement during the exposure considerably exceeds the illuminating radiation wavelength, then the intensity of the averaged field scattered by the object drops almost to zero due to a phase shift by more than 2π, while the intensity of the averaged radiation scattered by the background does not change. Hence, using monochromatic radiation scattered by a stable background and an arbitrarily reflecting moving object, one can form the image of the object as dark spots against a bright background.

In the beginning of the 1990s, it was discovered that the time-averaged intensity of a field scattered by a complex object consisting of a stable, randomly inhomogeneous background and a moving object decreases if the scattered field is registered by a low-resolution system. This effect was observed for even an almost completely absorbing moving object,[79] and therefore, it could be related only to the time dynamics of the field scattered by the background. It follows that even in this case, monochromatic radiation of the surrounding background provides useful information about moving objects. In Sec. 5.5, we give a detailed analysis and explanation of this effect.

The discovered effect forms a basis for a new field in holography: time background holography.[21] Within its framework, one can analyze such effects and suggest prominent coherent methods of gaining information about a moving object based on utilizing coherent radiation from the surrounding background and on the statistical analysis of the temporal and spatial structure of coherent fields scattered by the background and by the moving object.[21] This chapter deals with the study of time background holography, which is realized by the Fourier–Fresnel time transform of the sum of coherent fields scattered by a moving object and the stable, randomly inhomogeneous background that surrounds the object. The transform is performed, as a rule, in the image plane of the object.

In this chapter, we will explain the general theory of time background holography, and will present experimental results that confirm its applicability to the detection of moving objects in the presence of noise. We will also consider a method for the reliable detection of the parameters of arbitrarily reflecting moving objects, including those that are reflecting, transparent, or absorbing. Finally, we will consider time background-intensity holography, which allows detection of a moving object that is illuminated by a quasi-monochromatic source with small coherence length.

For the purposes of these discussions, we will simplify the analysis by representing the background surrounding a moving object as a randomly inhomogeneous stable background surface. We will also assume the object to be flat.

5.2 General theory of time background holography

Consider a stable background surface and an object moving along it, where both are illuminated by a monochromatic pointlike source placed close to the center of the domain of the scattered field observation (Fig. 5.1). The field scattered by this complex object can be represented as

$$E(\boldsymbol{\rho}, t) = \frac{\exp i\omega_0 t}{z_t \lambda} \int E_t(\mathbf{r}_t, t) \exp\left(\frac{2\pi i |\mathbf{r}_t - \boldsymbol{\rho}|}{\lambda}\right) d\boldsymbol{\rho}. \tag{5.1}$$

Here, $E_t(x, y, t) = E_o(x, y) + E_b(x, y)[1 - R(x - v_{xt}t, y - v_{yt}t)]$ is the scattered field complex amplitude in the intermediate plane, which is parallel to the observation plane and placed very close to the moving object; E_o and E_b are the parts of this distribution that are scattered by the object and by the background, accounting for the contribution of the illuminating radiation; $R(x, y)$ is the function that describes shading of the background surface by the moving object; λ is the wavelength of the illuminating radiation; $\omega_0 = (2\pi c)/\lambda$, with c being the velocity of light, is the angular frequency of the illuminating radiation; $\mathbf{r}$ with components x, y, z_t, is the radius vector of a point in the intermediate plane; $z_t \approx r_c$ is the distance between the observation and intermediate planes; and v_{xt} and v_{yt} are the velocity tangential components for the object's center of mass.

To calculate the scattered field complex amplitude distribution in the intermediate plane in the framework of geometric optics, one can consider reflected beams parallel to the MN axis (see Fig. 5.1), which is orthogonal to the observation plane.

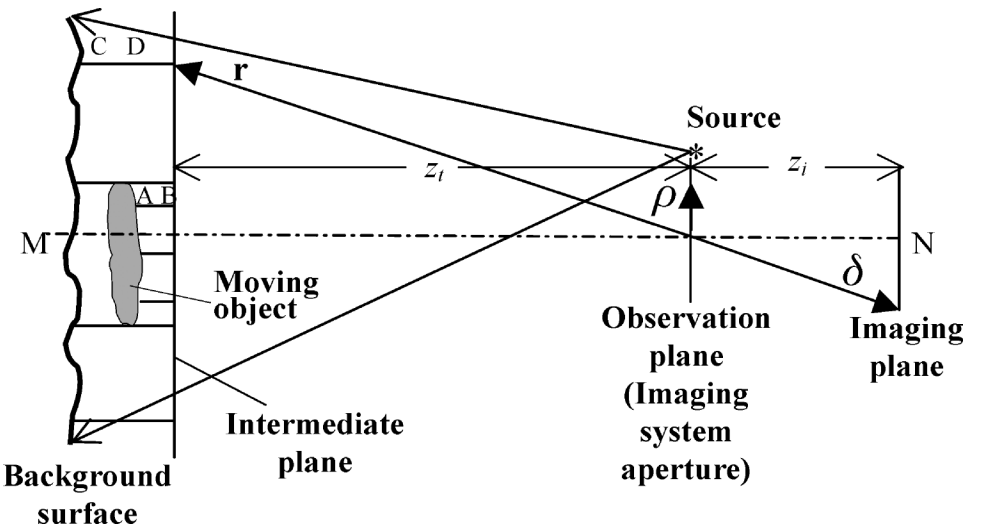

Figure 5.1 Description of the field scattered by a complex object consisting of a stable background surface and an object moving along it, with the help of an intermediate plane. The dash-dot line shows the axis orthogonal to the observation plane.

The modulo of this distribution is given by the reflection coefficient of the background surface of the moving object, and its phase is determined by the phase shifts of the beams reflected from these objects. Seven beams of this kind are shown in Fig. 5.1, two of them being reflected from the background surface and tangential to the moving object boundary. For example, the field at point D on the intermediate plane is $E_t(\mathbf{r}, t) = E_i k_c \exp(i\varphi_{\mathrm{CD}})$, where $E_i = (S_s E_s)/(\lambda r_c)$ is the amplitude of the incident field, S_s and E_s are the aperture area and the complex amplitude of the illuminating source, respectively, k_c is the reflection coefficient of the background surface at point C, $\varphi_{\mathrm{CD}} = (2\pi l_{\mathrm{CD}})/\lambda$ is the phase shift along the reflected beam CD, and l_{CD} is the distance from the point D to the intermediate plane (length of the segment CD). At point B on the intermediate plane, $E_t(\mathbf{r}_t, t) = E_i k_{\mathrm{A}} \exp(i\varphi_{\mathrm{AB}})$, where k_{A} is the reflection coefficient of the moving object surface at point A, $\varphi_{\mathrm{AB}} = (2\pi l_{\mathrm{AB}})/\lambda$ is the phase shift along the reflected beam AB, and l_{AB} is the distance from point A to the intermediate plane (i.e., length of segment AB). This simplified picture, on the one hand, gives an overview of time background holography and, on the other hand, provides a rather precise example of time background holography in the case where the moving object is close to the background surface. The case where the moving object is far from the background surface and hence, the role of diffraction is considerably increased, will be considered in detail below.

Suppose that the additive random noise field $E_n(\boldsymbol{\rho}, t)$, which, as a rule, exists together with the scattered field, has a correlation time and radius essentially smaller than the corresponding parameters of the scattered field. Then, the resulting (sum) field $E_\Sigma(\boldsymbol{\rho}, t) = E(\boldsymbol{\rho}, t) + E_n(\boldsymbol{\rho}, t)$ can be calculated with the help of the statistical theory of solutions,[12] which defines the probability density function for this field, $P[E_\Sigma(\boldsymbol{\rho}, t)] \sim \exp[-(L_d + L)]$, where

$$L_d = \frac{1}{N_n} \int_{t_0}^{t_0+T} \int |E_\Sigma(\boldsymbol{\rho}, t)|^2 d\boldsymbol{\rho} dt$$

is proportional to the energy of the processed field, N_n is the noise field spectral density,

$$L = \int_{t_0}^{t_0+T} \int W(\mathbf{r}, t) |E_g(\mathbf{r}, t)|^2 d\mathbf{r} dt$$

is the statistics of the scattered field, $W(\mathbf{r}, t)$ is a function depending on the expected properties of the complex object and on N_n,

$$E_g(\mathbf{r}, t) = \left(\frac{1}{\lambda r_c T}\right) \int E_\Sigma(\boldsymbol{\rho}, t) \exp\left(\frac{2\pi i |\mathbf{r} - \boldsymbol{\rho}|}{\lambda}\right) d\boldsymbol{\rho}$$

is the generalized image of the object,[12] $\mathbf{r}$ is the expected radius vector of the intermediate plane, and t_0 and T are the starting time and duration of the sum field

processing, respectively. The second integral is performed one over the observation domain. The functional $P[E_\Sigma(\boldsymbol{\rho}, t)]$ contains complete information about the complex object under study and thus can be used for the detection, recognition, and measurement of its parameters. In particular, detection of the object can be performed by comparing the function

$$L_d = \frac{1}{N_n} \int_{t_0}^{t_0+T} \int |E_\Sigma(\boldsymbol{\rho}, t)|^2 d\boldsymbol{\rho} dt$$

with a given threshold. In what follows, we consider a modification of this function, which allows one to detect an object moving along the background surface even in the case of very weak reflectivity of the object surface. In this method, detection is based on the analysis of monochromatic radiation scattered by the background surface. In Ref. 12 it is shown in detail how the field scattered by the object under study can be processed using the statistics of the scattered field, $L = \int_{t_0}^{t_0+T} \int W(\mathbf{r}, t)|E_g(\mathbf{r}, t)|^2 d\mathbf{r} dt$. This method of processing requires a large number of operations. However, for a small noise field, determination of the object parameters can be simplified.

Let the intermediate plane be close to the object under study and far from the observation plane. Under these conditions, the intermediate plane is often called the picture plane,[11] and $\mathbf{r}$ is the radius vector of the intermediate plane (see Fig. 5.1) with components x, y, z_t, where $z_t \approx r_c$. Then, after the change of variables $\mathbf{r}/r = \boldsymbol{\delta}/\delta$, $1/r = 1/\delta - 1/f$, one can show that if the terms $\sim t^3$ are neglected, for a relatively small size d_ρ of the observation domain,[80]

$$E_g[\mathbf{r}(\boldsymbol{\delta})] = \frac{1}{T} \int_{t_0}^{t_0+T} E_m(\boldsymbol{\delta}, t) \exp\left(i\omega t + i\beta t^2\right) dt, \tag{5.2}$$

where

$$E_m[\mathbf{r}(\boldsymbol{\delta}), t] = \frac{1}{\lambda z_i} \int E_\Sigma(\boldsymbol{\rho}, t) \exp\left(i \frac{2\pi \boldsymbol{\delta}\boldsymbol{\rho}}{\lambda \delta}\right) \exp\left[i \frac{\pi \rho^2}{\lambda} \left(\frac{1}{f} + \frac{1}{\delta}\right)\right] d\boldsymbol{\rho}$$
$$= \int E_t(x, y, t) h(x, y, \boldsymbol{\delta}) dx dy + \Phi[E_n(\boldsymbol{\rho}, t)]$$

is the instantaneous field distribution in the coherent image of the complex object formed by the imaging system, which is placed in the observation plane; $h(x, y, \boldsymbol{\delta})$ is the pulse response of the imaging system, f is its focal length; $\boldsymbol{\delta}$ is the radius vector of the point in the image plane that is optically conjugate to the point with radius vector $\mathbf{r}$ on the intermediate plane; ω is the spectrum frequency, β is the spectrum deviation, and $\Phi[E_n(\boldsymbol{\rho}, t)]$ is a functional, determined only by the noise field. The radius vector $\boldsymbol{\delta}$ has components δ_x, δ_y, z_i, where z_i is the distance between the object image and the imaging system aperture. The generalized image of

the object is related to the instant coherent image by means of the Fourier–Fresnel time transform with the kernel $\exp(i\omega t + i\beta t^2)$.

Furthermore, under the condition that the influence of the noise field E_n can be neglected, consider the two cases of the scattered field processing. These are the cases of high and low imaging system resolution.

5.2.1 Time background holography in the case of a high-resolution imaging system

Consider the case of a high-resolution imaging system, $d_\rho \gg (\lambda r_c)/d_o$, where d_o is the size of the moving object and d_ρ is the imaging system aperture size. Then, the following operations can be used to process the scattered field (Fig. 5.2). The object is illuminated by a monochromatic source with a coherence length more than twice the distance between the background surface and the observation plane. The detector detects radiation scattered by the object and the background surface. After this, the image is formed. Then, with the help of the reference wave created by the illuminating source, a dynamic hologram of the focused object image having the field distribution E_m is formed in the image plane. According to Eq. (5.2), a Fourier–Fresnel time transform is performed in each small domain of the image (Fig. 5.2), and the resulting field distribution E_m is analyzed. Furthermore, for each domain, using a filter matrix one finds the maximum absolute value of the

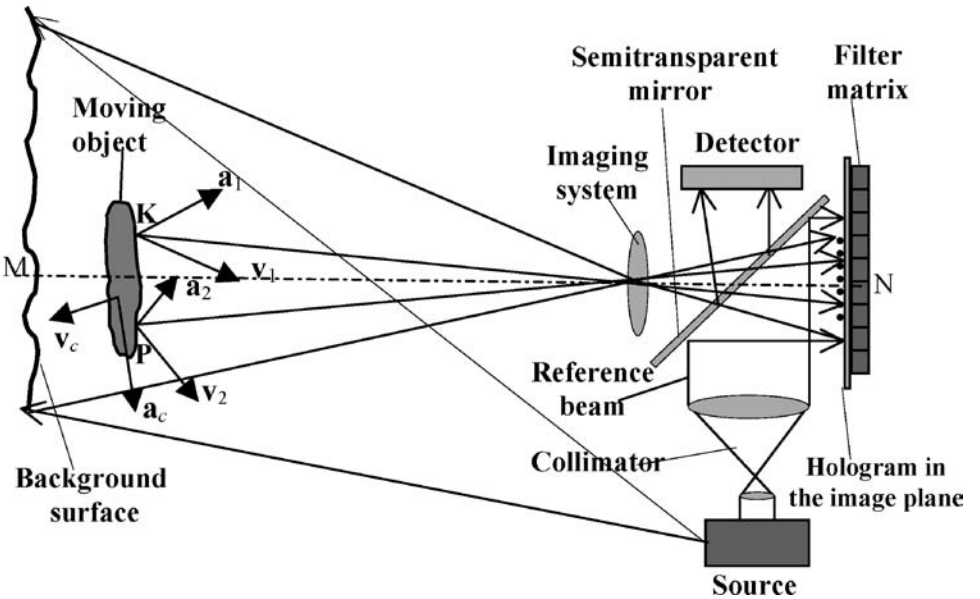

Figure 5.2 The device for processing the scattered field in the case of a high-resolution imaging system. Here, v_1, a_1 and v_2, a_2 are velocities and accelerations of the object with respect to its center of mass. The circular line on the hologram surface is the coherent image of the moving object.

transform, equal to the intensity distribution in the image

$$I_o(\boldsymbol{\delta}, t_0) \sim |E_i|^2 k_i(\mathbf{r} = -\mu\boldsymbol{\delta}, t_0),$$

where $k_i(\mathbf{r} = -\mu\boldsymbol{\delta}, t_0) = (\ell/\sigma)^2 |k(\mathbf{r} = -\mu\boldsymbol{\delta}, t_0)|^2 \exp\{-[(\ell/\sigma)^2(\mathbf{q}^2 - q_N^2)/q_N^2]\}$, $\mu = r_c/z_i$, $q_N = \mathbf{q} \cdot \mathbf{N}$, $\mathbf{q} = \mathbf{r}_c/r_c + (\mathbf{r}_c - \boldsymbol{\rho}_s)/|\mathbf{r}_c - \boldsymbol{\rho}_s|$ is the vector of scattering, σ and ℓ are the standard deviation and the correlation radius of the object surface roughness, $\mathbf{N}$ is the normal to the average surface of the object, $\boldsymbol{\rho}_s$ is the radius vector of the illuminating source, $\mathbf{r}_c$ is the center of mass of the object, and $k(\mathbf{r}, t_0)$ is the reflection coefficient distribution of the object surface at time t_0. Next, one finds the values $\omega_m(\boldsymbol{\delta})$ and $\beta_m(\boldsymbol{\delta})$, which yield the maximum of the Fourier–Fresnel transform modulo.

In addition, one can determine the intensity reflection coefficients for the moving object surface and the background surface, respectively, according to the formulas

$$K_o(\boldsymbol{\delta}, t_0) = \frac{c_i I_o(\boldsymbol{\delta}, t_0)}{|E_i|^2} \text{ and } K_b(\boldsymbol{\delta}, t_0) = \frac{c_i I_b(\boldsymbol{\delta}, t_0)}{|E_i|^2},$$

where c_i is a constant depending on the object's position and the imaging system parameters, and I_o and I_b are intensity distributions in the image of the moving object (the circular line on the hologram surface; see Fig. 5.2) and in the image of the background, respectively. The values $\omega_m(\boldsymbol{\delta}_j)$ and $\beta_m(\boldsymbol{\delta}_j)$, in the jth domain of the object image, where $\boldsymbol{\delta}_j = -\mathbf{r}_j/\mu$ is the radius vector of the jth domain of the object image and $\mathbf{r}_j$ is the radius vector of the jth domain of the object surface that is optically conjugate to the jth domain of the image plane, are related to the dynamic parameters of the object on the jth domain of its surface as follows:

$$\omega_m(\boldsymbol{\delta}_j) = \frac{2\pi(v_{rc} + v_{rj})}{\lambda}, \quad \beta_m(\boldsymbol{\delta}_j) = \frac{2\pi(a_{rc} + a_{rj})}{\lambda},$$

where $v_{rc} = \mathbf{q} \cdot \mathbf{v}_c$, $a_{rc} = \mathbf{q} \cdot \mathbf{a}_c$ are the radial components of the velocity and acceleration vectors $\mathbf{v}_c$ and $\mathbf{a}_c$ of the object's center of mass; $v_{rj} = \mathbf{q} \cdot \mathbf{v}_j(\boldsymbol{\delta}_j)$ and $a_{rj} = \mathbf{q} \cdot \mathbf{a}_j(\boldsymbol{\delta}_j)$ are the radial components of the velocity and acceleration vectors $\mathbf{v}(\boldsymbol{\delta}_j)$ and $\mathbf{a}(\boldsymbol{\delta}_j)$ of the jth domain of the object's surface, which is optically conjugate to the jth domain of the image (Fig. 5.2), with respect to its center of mass. The number of equations is $2N$, where N is the number of domains. At the same time, the number of unknown variables v_{rj}, a_{rj}, v_{rc}, and a_{rc} is $2N + 2$. In this case, the set of equations is sufficient for determining these values; then, the solution of the system has the form

$$\begin{aligned}
\omega_c &= \omega_m(\boldsymbol{\delta}_1) - \omega_m(\boldsymbol{\delta}_2), \\
\beta_c &= \beta_m(\boldsymbol{\delta}_1) - \beta_{\max}(\boldsymbol{\delta}_2), \\
v_{rj} &= \bar{\lambda}[\omega_m(\boldsymbol{\delta}_j) - \omega_c], \\
a_{rj} &= \bar{\lambda}[\beta_m(\boldsymbol{\delta}_j) - \beta_c],
\end{aligned}$$

and

$$v_{rc} = \omega_c, a_{rc} = \bar{\lambda}\beta_c,$$

where $\bar{\lambda} = (\lambda/2\pi)$, and ω_c and β_c are the Doppler frequency and Doppler deviation of the object's center of mass, which are the same for each point of the image since they are determined by the velocity and acceleration of the object's center of mass, and δ_1 and δ_2 are the radius vectors of the first and second domains, respectively.

If the moving object is a nondeformable solid body, then the number of equations can become excessive. This can be seen most explicitly if a nondeformable body rotates around a fixed axis passing through point P orthogonally to the line MN (see Figs. 5.1 and 5.2). In this case, the following three equations are sufficient for determining the angular velocity of rotation Ω and the projections v_{rc} and a_{rc} of the velocity and acceleration of the object's center of mass:

$$\omega_m(\delta_1) = \frac{v_{rc} - (\Delta\Omega/\mu)}{\bar{\lambda}},$$

$$\omega_m(\delta_2) = \frac{v_{rc}}{\bar{\lambda}},$$

and

$$\beta_m(\delta_2) = \frac{a_{rc}}{\bar{\lambda}},$$

where Δ is the distance between the images of the K and P domains of the object's surface (see Fig. 5.2). From these equations, we obtain

$$\Omega = \bar{\lambda}\frac{\omega_m(\delta_1) - \omega_m(\delta_2)}{\mu\Delta},$$

$$v_{rc} = \bar{\lambda}\omega_m(\delta_2),$$

and

$$a_{rc} = \bar{\lambda}\beta_m(\delta_2).$$

The tangential components of the center of mass' velocity and acceleration vectors can be easily found from the displacement of the object image's center of mass, according to the relations $v_{tc} = \mu v_{ic}$ and $a_{tc} = \mu a_{ic}$, where v_{ic} and a_{ic} are the velocity and acceleration of the image's center of mass.

It is interesting to note that in the case of a stable background surface, with the radial components of the velocity and acceleration of its separate domains equal to zero, in its image, $\omega_m(\delta) = \beta_m(\delta) = 0$. (This image is outside the circular line on the hologram surface in Fig. 5.2.) At the same time, in the presence of the object

radial displacements, $\omega_m(\delta) \neq 0$ and $\beta_m(\delta) \neq 0$ in its image (inside the circular line). Then, separating the domain where the last two conditions are satisfied, one can form an image of the moving object even in the case where it does not differ from the background surface; i.e., if the intensity reflection coefficients of the moving object and the background surface are approximately equal, then $K_o \approx K_b$. However, this method of selecting a moving object that is indistinguishable from the background surface cannot be used if the object has tangential displacements. In Sec. 5.4, we consider a method that allows this (see Sec. 5.4).

If the processing time of the scattered field is so small that for the normal components of the object velocities and accelerations, conditions $(V_{pc}T)/\lambda \ll 1$, $(a_{pc}T)/\lambda \ll 1$, $(V_pT)/\lambda \ll 1$, $(a_nT)/\lambda \ll 1$ are satisfied, then one loses first the information about the dynamic parameters of the moving object and, second, the possibility of separating the moving object's image from the background surface's image if the moving object is indistinguishable from the background surface. Consider now the case where $d_\rho \ll (\lambda r_c)/d_o$, in which the imaging system does not resolve the background surface and the moving object. We also suppose that the influence of the noise field can be neglected. It is worth recalling that in time background holography, the object under study is a "sandwich" consisting of the moving object and the background surface.

5.2.2 Time background holography with a low-resolution imaging system

In the case of an imaging system with low resolution, the instantaneous image of the moving object and the background surface consists of a single speckle (the Airy disk),[12] and the generalized image of the object is related to its instantaneous image via the Fourier–Fresnel time transform,[80]

$$E_g(\delta_c, \omega, \beta) = \frac{1}{T} \int_{t_0}^{t_0+T} E_{\mathrm{A}}(\delta_c, t) \exp\left[i\omega t + i\beta t^2\right] dt,$$

where δ_c is the radius vector of the Airy disk's center, and $E_A(\delta_c, t)$ is the instantaneous field in the Airy disk's center on the hologram surface. We see that in this case, the generalized image is a two-dimensional image of the object at coordinates ω, β. In the case of a stable background surface, only a two-dimensional pattern of the moving object is formed. For instance, the two-dimensional image of a rotating ball is an ellipse, with the ratio between the axes being proportional to the angular rotation frequency and the center at point $\omega = \omega_c$, $\beta = \beta_c$.

One can see from the above relations that in the case of a low-resolution imaging system and under the condition that the noise field influence can be neglected, the scattered field is processed as follows (Fig. 5.3). The object is illuminated by a monochromatic source with a coherence length that exceeds twice the distance

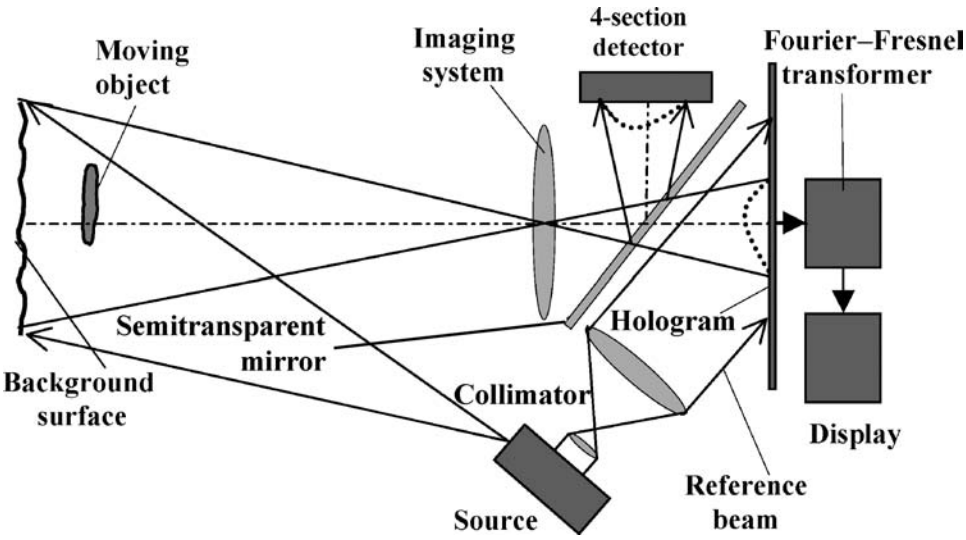

Figure 5.3 A device for time background holography in the case of a low-resolution imaging system. The dash-dot line shows the optical axis of the imaging system. The dotted line shows a single speckle in the coherent image.

between the background surface and the observation plane; the imaging system focuses the field scattered by the object, whose image is formed as a single speckle (the Airy disk). Then, with the help of a semitransparent mirror and a four-section detector, one determines the energy center of this speckle. Further, the imaging system is oriented in such a way that the energy center of the speckle coincides with the optical axis of the imaging system. This allows one to determine the unit vector $\mathbf{n}_c$ directed towards the object, i.e., the angular position of the object.

Simultaneously, using a reference wave created by the illuminating source, one records the dynamic hologram of the focused object image and performs a Fourier–Fresnel time transform of the field E_m in this image within a small domain of the hologram placed at the intersection with the optical axis of the imaging system. As a result of the transformation, a two-dimensional pattern of the object is formed in coordinates ω, β with the center at point $\omega = \omega_c = (2\pi v_r)/\lambda$, $\beta = \beta_c = (2\pi a_{rc})/\lambda$. This image is displayed on the monitor. Processing of the field scattered by the object allows one to determine the object's shape and its dynamic parameters, including the radial components of its velocity and acceleration, v_{rc} and a_{rc}.

Hence, the proposed method of scattered field processing leads, in the case of a low-resolution imaging system, to the building of a two-dimensional image of the moving object even in the presence of a bright background surface with a rather high reflection coefficient K_b. However, for even an almost completely absorbing object moving parallel to the background surface, this procedure yields a two-dimensional image of the moving object formed from the radiation scattered by the background surface.

Thus, for a high-resolution imaging system, time background holography provides imaging of an object moving along the background surface even in the case when the object does not differ from the background surface, i.e., when the intensity reflection coefficients of the object surface and background surface are almost the same, $K_o \approx K_b$. In addition, it allows one to determine the angular rate of the object's rotation, the velocity and acceleration of the object's center of mass, and the distribution of dynamic parameters on the object surface. For a low-resolution imaging system, time background holography provides a two-dimensional pattern of an object moving along a background surface formed from coherent radiation scattered by the object and the background.

We have considered methods of determining the parameters of moving objects by means of time background holography based on a reference beam. However, these methods cannot be used when the illuminating source has a small coherence length. Nevertheless, certain dynamic parameters of moving objects, including the angular rate of rotation, can be determined by means of time background intensity holography without using any reference beam. This type of time background holography, as well as some restrictions and difficulties relating to it, will be considered in Sec. 5.6.

5.3 Using time background holography to detect a moving object

In the foregoing, we discussed detection of a moving object by comparing the functional

$$L_d = \frac{1}{N_n} \int_{t_0}^{t_0+T} |E_{m\Sigma}(\boldsymbol{\rho}, t)|^2 dt d\boldsymbol{\rho},$$

with a given threshold. Here, $E_\Sigma = E + E_n$, where E is the field scattered by the background surface and the object moving parallel to it, and E_n is the noise field, $N_n = I_n S_n \tau_n$, where $I_n = |E_n|^2$ is the noise field spectral density, S_n and τ_n are the correlation area and correlation time of the noise field, respectively. The functional L_d is formed as follows. The studied domain, consisting of the background surface and the moving object, is probed, and the scattered energy is measured. This energy is divided by the spectral density of the noise field. The object is detected if L_d exceeds a given threshold. This method, known historically as the direct detection method,[27] can be used if reflection of the background surface is so weak that the field scattered by it has negligible influence on the detection procedure. In practice, the radiation scattered by the object and the background surface is usually focused on a "pointlike" detector, and the threshold is compared with the value L'_d proportional to L_d,

$$L'_d = \frac{1}{TI_n} \int_{t_0}^{t_0+T} |E_{m\Sigma}(\boldsymbol{\rho}, t)|^2 dt, \tag{5.3}$$

where $E_{m\Sigma} = E_{mo} + E_{mb} + E_{mn}$ is the instantaneous field at the detector input, E_{mo} and E_{mb} are instantaneous fields scattered by the object and the background surface, respectively, and E_{mn} is the instant noise field. However, in the case of a strongly reflecting background surface and a small, weakly reflecting moving object, only the background surface will be detected in practice.

In order to eliminate the influence of a bright background surface on the detection of an object moving along it, one should use detection methods based on pulsed probing of the background surface and the moving object and on time gating the backscattering pulse reflected by the background surface. An important drawback of such methods is the necessity to know *a priori* the distance to the background surface and to the moving object, and the low detection probability for weakly reflecting objects. More practical are methods of moving object detection based on frequency-modulated illumination of the domain under study. Using the frequency analysis based on the fast Fourier transform, one determines the distance to the background surface and to the moving object and estimates variations of these distances, which allows one to detect the presence of the moving object. This method also has low reliability of detection for weakly reflecting objects. In addition, its realization requires complicated processing of the backscattered radiation. All methods mentioned above are based on selecting backscattering from the moving object and suppressing backscattering from the background surface.

There is a well-known simple method of detecting a moving object by observing intensity variations in radiation scattered by the background surface (Fig. 5.4). In this method, the background surface and the moving object are illuminated by a source that can be monochromatic or nonmonochromatic. Then, the intensity of the backscattered radiation is measured by a "pointlike" detector at two different times, which gives $I_d(t_1)$ and $I_d(t_2)$, and the value $\Delta = [I_d(t_1) - I_d(t_2)]/I_n$ is compared with a given threshold. If, for $t_1 - t_2 \gg d_o/-_t$, where d_o is the object size and v_t the tangential component of its velocity, and Δ exceeds the threshold, then the object is considered as detected. This method is realized, for instance, in the Korean company Alpex's infrared sensing switch,[81] which switches on an electrical

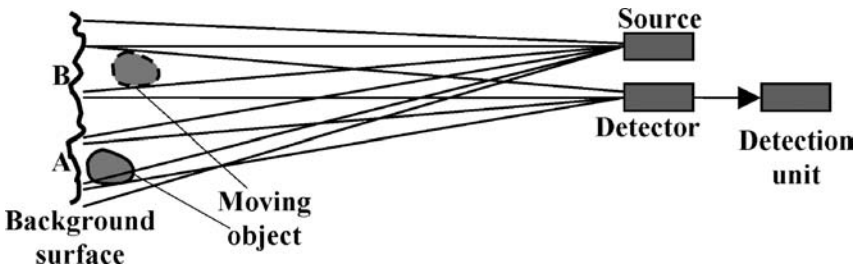

Figure 5.4 Detection of a moving object via variation of the intensity of light scattered by the background surface. A and B are domains of the background surface that are shaded at moments t_1 and t_2 such that $t_2 - t_1 \gg d_o/v_t$, where d_o is the object size, and v_t is the tangential component of its velocity. The dotted curve shows the object position at time t_2.

illumination with different time delays in intervals between 5 seconds to 2 minutes when the moving object falls within view of the device's sensor.

Taking into account relation (5.1), one can show that

$$\Lambda_d \approx \frac{C_b S_g (K_{1b} - K_{2b})}{I_n} + 1, \tag{5.4}$$

where K_{1b} and K_{2b} are intensity reflection coefficients for those domains of the background surface that are shaded at times t_1 and t_2, S_g is the area of the moving object's geometric shadow on the background surface, and the factor C_b is determined by the background surface roughness height parameters and the distance to the background surface. High detection probability is achieved under low-noise conditions, when $\langle \Lambda_d \rangle \gg 1$. However, for a remote background surface and moving object, as a rule, $K_{1b} \cong K_{2b} \cong K_b$ and $\langle \Lambda_d \rangle \cong 1$; hence, the object detection probability is very low. We will now consider a more reliable algorithm for detecting a moving object that is not resolvable by the imaging system.[22] The algorithm is based on forming the image of the background surface, registering, with the help of a reference wave, the field in the image plane at different time moments t and τ, and processing the differences between the fields, $E_{md}(\boldsymbol{\delta}_j, t, \tau) = E_{m\Sigma}(\boldsymbol{\delta}_j, t) - E_{m\Sigma}(\boldsymbol{\delta}_j, \tau)$, in different domains of the image. Here, $E_{m\Sigma}(\boldsymbol{\delta}_j, t) = E_{mo}(\boldsymbol{\delta}_j, t) + E_{mb}(\boldsymbol{\delta}_j, t) + E_{mn}(\boldsymbol{\delta}_j, t)$ is the instant random field in the image plane, which has Gaussian distribution, $E_{mn}(\boldsymbol{\delta}_j, t)$ is the random noise field, which also has Gaussian distribution, and $\boldsymbol{\delta}_j$ is the radius vector of the jth domain of the image. At $t \neq \tau$ and in the absence of noise ($E_n = 0$) and object motion, these differences are equal to zero. If the noise field correlation time is much smaller than the field $E_m(\boldsymbol{\delta}_j, t)$ correlation time, then, as shown in Ref. 22, in order to detect only the moving object, instead of the functional

$$L_d = \frac{1}{N_n} \int_{t_0}^{t_0+T} \int |E_\Sigma(\boldsymbol{\rho}, t)|^2 d\boldsymbol{\rho} dt$$

one should use an analogous non-negative functional

$$L_{dj} = \frac{1}{I_n T^2} \int_{t_0}^{t_0+T} \int_{t_0}^{t_0+T} |E_{md}(\boldsymbol{\delta}_j, t, \tau)|^2 dt = \frac{1}{T I_n} \int_{t_0}^{t_0+T} |E_{m\Sigma}(\boldsymbol{\delta}_j, t)|^2 dt - \frac{1}{I_n} I_t(\boldsymbol{\delta}_j), \tag{5.5}$$

which should be compared with the fixed threshold. Here,

$$I_t(\boldsymbol{\delta}_j) = \left| \frac{1}{T} \int_{t_0}^{t_0+T} E_{m\Sigma}(\boldsymbol{\delta}_j, t) dt \right|^2$$

and a new operation is introduced: determination of the time-averaged intensity of the complex field amplitude $E_{m\Sigma}$ in the jth domain of the image plane. Actually, this is determination of the square modulo of the Fourier–Fresnel spectrum of the field distribution in the image at frequency $\omega = 0$ and deviation $\beta = 0$. The fact that the functional L_d contains this operation justifies using this operation for the study of effects of an object moving along the background surface, including the effect of the average intensity decrease of the complex field amplitude E_{ms}, which we mentioned in Sec. 5.1.

As we will show below, this operation, although it uses a single point $\omega = \beta = 0$, provides much information about the geometric and dynamic properties of moving objects. Taking into account the importance of this operation, we will define it as the principle of coherent field time averaging. Section 5.5 will be devoted to the discussion of this principle. Taking into account relation (5.1) and doing the calculations described in detail in Sec. 5.5, one can show that, for instance, in the case of an almost completely absorbing object, low noise field, and the averaging time $T \gg d_o/v_t$, where v_t is the velocity of the object motion along the background surface (the velocity tangential component),

$$\langle I_t(\boldsymbol{\delta}_j)\rangle = \begin{cases} C_b|k_b(\mathbf{r}_j)|^2\left(\dfrac{\lambda^2 r_c^2}{S_\rho} - 2S_g\right) & \text{for } M_b \gg 1, \\ C_b|k_b(\mathbf{r}_j)|^2(S_b - 2S_g) & \text{for } M_b \ll 1, \end{cases}$$

where C_b is constant, $k_b(\mathbf{r}_j)$ is the reflection coefficient of the jth domain of the background surface, $\mathbf{r}_j$ is its radius vector, and $M_b = (S_b S_g)/(\lambda^2 r_c^2)$; S_b, S_ρ, S_g are the areas of the background surface, the imaging system aperture, and the object geometric shadow on the background surface, respectively. If $T \ll d_o/v_t$ and the object is almost completely absorbing, then

$$\langle I_t(\boldsymbol{\delta}_j)\rangle = \begin{cases} C_b|k_b(\mathbf{r}_j)|^2\left(\dfrac{\lambda^2 r_c^2}{S_\rho} - S_g\right) & \text{for } M_b \gg 1, \\ C_b|k_b(\mathbf{r}_j)|^2(S_b - S_g) & \text{for } M_b \ll 1. \end{cases}$$

From the obtained relations, one can see that at $T \gg d_o/v_t$, the intensity of the time-averaged complex field amplitude decreases by the value $C_b|k_b(\mathbf{r}_j)|^2$. Taking into account the above relations, we obtain that at $T \gg d_o/v_t$ and very low noise,

$$\langle L_{dj}(\boldsymbol{\delta}_j)\rangle \approx L_{dj}(\boldsymbol{\delta}_j) \approx \frac{C_b S_g K_b}{I_n}. \tag{5.6}$$

Figure 5.5 presents a conceptual schematic of detection of an object moving along the background surface in the case of a high-resolution imaging system. The background surface and the object are illuminated by a monochromatic source, and the imaging system forms their images. In the image plane, a matrix detector records the sum fields $E_{m\Sigma}(\boldsymbol{\delta}_j, t) = E_{mo}(\boldsymbol{\delta}_j, t) + E_{mb}(\boldsymbol{\delta}_j, t) + E_{mn}(\boldsymbol{\delta}_j, t)$, where $\boldsymbol{\delta}_j$

is the radius vector of the jth element of the matrix detector, by recording with the help of a reference wave the hologram of an focused image of the object under study.

Furthermore, the signal from each detector element is fed to a corresponding cell of the matrix functional unit. The cells form the functionals $L_{dj}(\boldsymbol{\delta}_j)$ and compare them with the given threshold. In Fig. 5.5, $\boldsymbol{\delta}_j$ is the radius vector of the jth element of the matrix detector and of the jth cell of the matrix functional unit, in which the value of $L_{dj}(\boldsymbol{\delta}_j)$ exceeds the threshold. This means that the moving object's position is in the direction of the jth domain of the background surface, which is optically conjugated to the jth element and given by the radius vector $\mathbf{r}_j$.

If the imaging system does not resolve the background surface along which the object moves, then detection of the field $E_{m\Sigma}$ is performed according to the scheme shown in Fig. 5.6. Here, the image of the background surface and the moving object is a single speckle at the detector input. After field detection, the functional unit forms the value

$$L_c = \frac{1}{I_n}\left(\frac{1}{T}\int_{t_0}^{t_0+T} |E_{m\Sigma}(\boldsymbol{\delta}_c, t)|^2 dt - \frac{1}{T^2}\left|\int_{t_0}^{t_0+T} E_{m\Sigma}(\boldsymbol{\delta}_c, t)dt\right|^2\right), \qquad (5.7)$$

where $\boldsymbol{\delta}_c$ is the radius vector of the detector input center, and compares it with the given threshold. If L_c exceeds the threshold, the object is considered as detected.

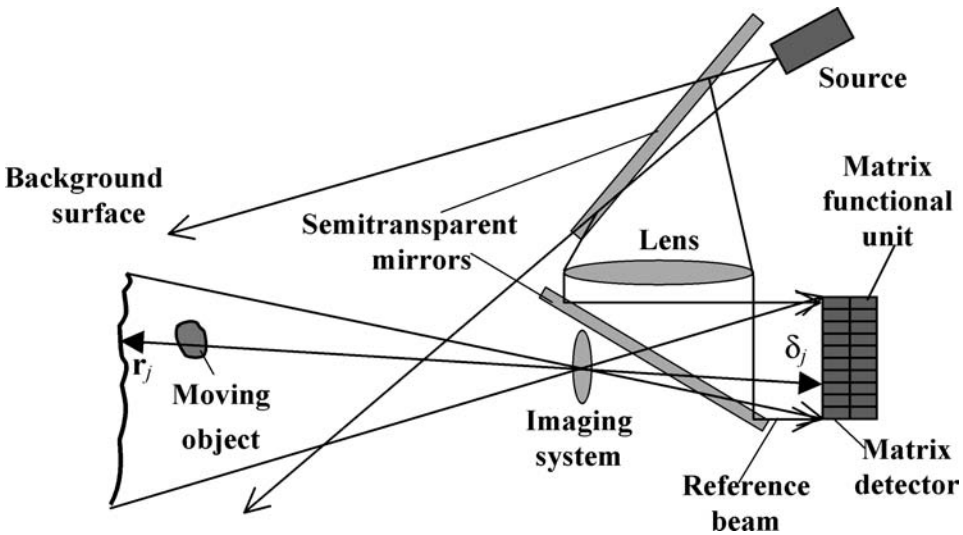

Figure 5.5 Conceptual schematic of moving object detection in the case where the object moves along the background surface and the imaging system has high resolution. Here, $\boldsymbol{\delta}_j$ is the radius vector of the jth element of the matrix detector and the jth cell of the matrix functional unit, and $\mathbf{r}_j$ is the radius vector of the jth domain of the background surface, which is optically conjugate to the jth element.

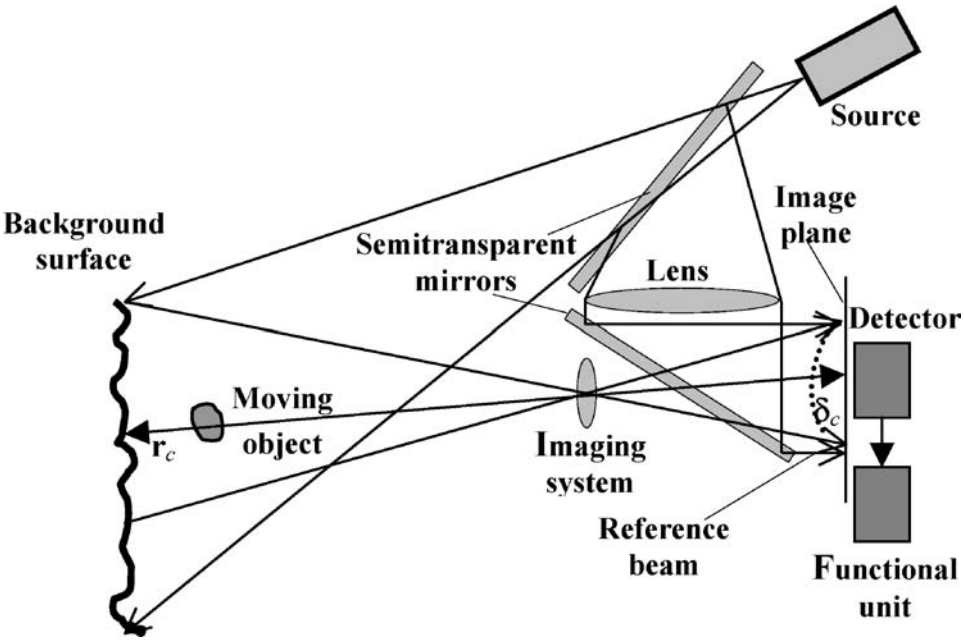

Figure 5.6 Conceptual schematic of moving object detection in the case where the object moves along the background surface and the imaging system has low resolution. Here, $\boldsymbol{\delta}_c$ is the radius vector of the detector input center; $\mathbf{r}_c$ is the radius vector of the background surface's center of mass, which is optically conjugate to the detector input center. The dotted line shows a single speckle in the coherent image of the complex object—a background surface plus the moving object under study.

Let us return to Eq. (5.3). One can show that at $T \gg d_o/v_t$ and under low noise conditions,

$$L_c \approx \langle L_c \rangle = \frac{C_b S_g K_b}{I_n} \sim L'_d. \tag{5.8}$$

This demonstrates that moving object detection is carried out as if we were performing direct detection of the domain on the background surface placed into the geometric shadow of the object. Hence, the probability of detecting the object equals the probability of detecting this part of the background surface. In practice, this probability is very high, which is also confirmed by the experiments described below. Since we consider detection of a moving object that is not resolvable by the imaging system, one can say that L_c performs the spatial filtering of the moving object geometric shadow from the whole background surface. Therefore, by measuring this functional with the help of the device shown in Fig. 5.6, one can draw conclusions about the geometric parameters of the object. In particular, in the case of low additional noise, $\langle |E_{mn}|^2 \rangle \ll \langle |E_{mo}|^2 \rangle$; and under the condition that the parameters C_b, I_n, and K_b are known, and if the object is flat and moves along and close to the background surface, then one can determine the surface area of the

object $S_o = S_g = (L_c I_n)/(C_b K_b)$. It follows that time background holography is a high-resolution method of gaining information about moving objects.[22]

Let us return to relation (5.4) for the case of low noise, where $\Lambda_d \approx C_b S_g (K_{1b} - K_{2b})/I_n$. Using Eqs. (5.5) through (5.8), we obtain that for $K_{1b} \approx K_{2b}$,

$$L_c \approx \frac{C_b S_g K_{1b}}{I_n} \gg \Lambda_d \approx \frac{C_b S_g (K_{1b} - K_{2b})}{I_n}. \tag{5.9}$$

It follows from Eqs. (5.8) and (5.9) that $\Lambda_d \ll L_c$, and hence, for a fixed threshold the probability of detecting an object via the intensity variation of the radiation scattered by the background surface is considerably smaller than the probability of its detection by means of time background holography using the functionals of Eqs. (5.5) and (5.7).

Let us consider an experiment that confirms the possibility of using time background holography to detect a moving object. The corresponding laboratory setup for operating in the microwave range is shown in Fig. 5.7. A solid-state microwave generator based on an avalanche diode generates monochromatic electromagnetic radiation in the 3-cm range.[21] Half of the radiation is sent into a horn-shaped transmitter, which illuminates the background surface and the object moving along it. The second half of the radiation is fed to the phase detector. The same detector registers, through a horn-shaped receiver, the electromagnetic field scattered by the moving object and the background surface.

The signal going to the detection unit from the phase detector is proportional to the intensity of the time-averaged complex amplitude of this field. In the detection unit, the functional L_c [see relation (5.7)] is formed from this signal and is compared with the fixed threshold. If the functional L_c exceeds the threshold, the moving object is considered detected, which is indicated by a mark displayed on the monitor. In the experiment, the moving object's surface had high absorption in the microwave range. The background surface had high reflection in the

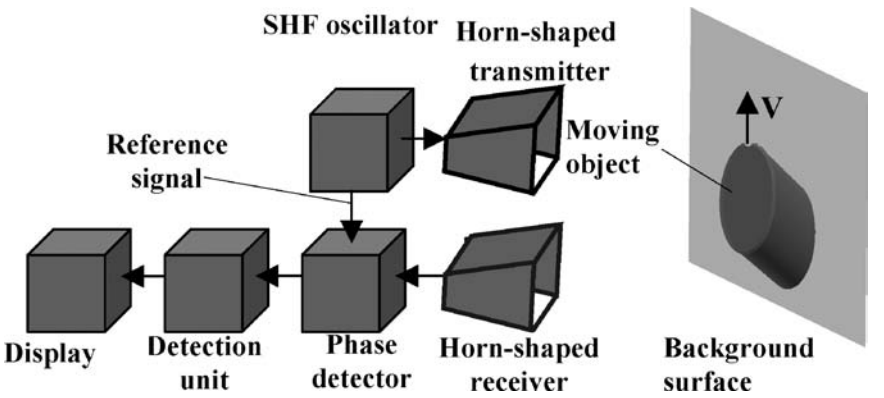

Figure 5.7 The laboratory setup using time background holography for the detection of an object moving along a background surface.

microwave range. The setup demonstrated reliable detection of the object moving along the background surface, even in the case where the object displacement was of the order of its size, $\Delta \approx Tv$, where v is the object's velocity.

Now consider a laboratory setup that uses time background holography in the ultrasonic range[23] to detect objects moving in water (Fig. 5.8). An acoustic generator sends an electrical signal to an ultrasonic transmitter placed into the water and to a phase detector. The ultrasonic transmitter sends monochromatic ultrasonic radiation to both the background surface and the object moving along it. The coherent ultrasonic field scattered by the object and the background surface is registered by an ultrasonic receiver, which is also placed in water. From the receiver, the signal is fed to the phase detector. The signal from the phase detector, which is proportional to the complex amplitude of the scattered field, is sent to the detection unit. Then, quite similarly to the case of microwave time background holography, the detection unit forms the functional L_c from the signal and compares it with the given threshold. If the functional L_c exceeds the given threshold, then the moving object is assumed to be detected, and the corresponding mark is displayed on the monitor.

The objects chosen for this experiment had reflection coefficients only slightly different from the background surface reflection coefficient. The setup demonstrated that objects moving in water can be detected using monochromatic ultrasonic radiation scattered by a randomly inhomogeneous background surface and is

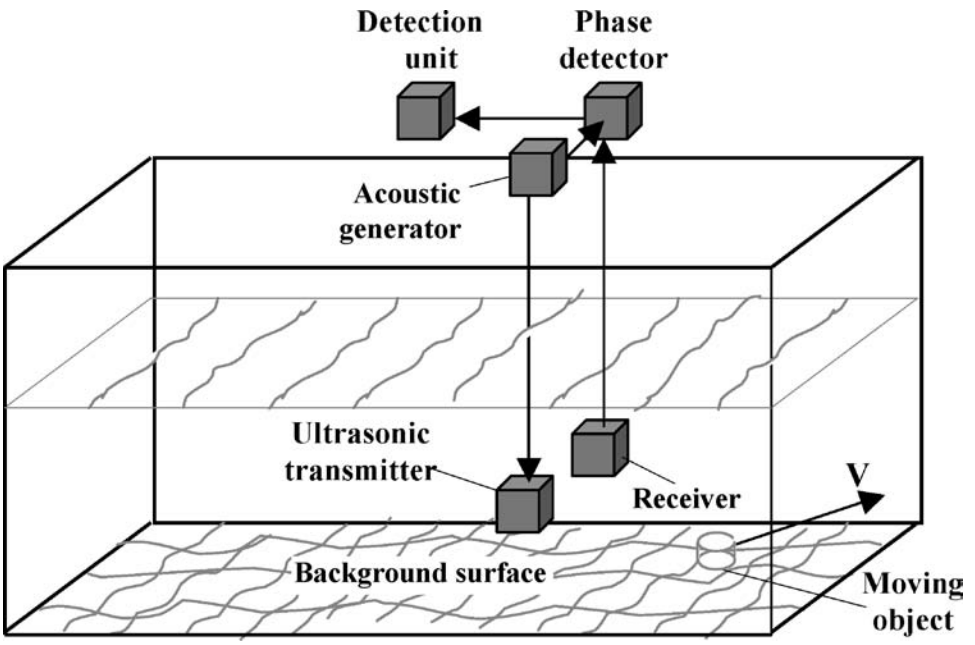

Figure 5.8 The laboratory setup using time background holography for the detection of objects moving in water. The object used in the experiment has reflection properties close to the ones of the background surface.

spatially modulated by these objects on its way to the receiving device. Reliable detection was possible at displacements comparable with the objects' sizes.

In Ref. 22 it is considered whether time background holography can be used for the reliable detection of weakly reflecting atmospheric particle clusters that are not resolvable by the imaging system. In this case, detection is based on probing by coherent laser radiation. In Ref. 22 it is suggested that a device based on the schematic shown in Fig. 5.5 be used in the case of a background surface that is resolvable by the imaging system, and a device based on the schematic in Fig. 5.6 be used in the case of an unresolvable background surface. The same devices can be used for determining the concentration, average size, and average velocity of the polluting particles. Similar devices can be used for detecting moving leukocytes, which are low-contrast particles that are not easily distinguished from the surrounding background, and for finding their concentrations, average size, and average velocity. For probing blood samples, it is also reasonable to use laser radiation.

Thus, time background holography can be efficient for the reliable detection of remote objects moving along a randomly inhomogeneous bright background surface. An object is detected due to coherent fields scattered by the randomly inhomogeneous background surface and spatially modulated by the object on the way to the receiving point. The objects to be detected can be highly reflecting, have the same reflection as the background surface, or be transparent. If they are moving through air, then they should be detected using monochromatic electromagnetic radiation in the optical or radio range. For the detection of objects moving in water, monochromatic acoustic radiation should be used.

Detection of a moving object is performed with time background holography in the same manner as the well-known method of direct detection[27] would be applied to the part of the background surface placed in the geometric shadow of the object. Hence, the probability of detecting the object is equal to the probability of detecting that part of the background surface. In practice, this probability is very high, which is confirmed by the experiments presented here. One can say that the algorithm of moving object detection in the framework of time background holography is based on spatial filtering of the object's geometric shadow from the whole background surface. This algorithm is most efficient in the case of moving objects that are not resolvable by the imaging system. If the imaging system resolves the background surface, then, using a matrix detector, one can not only detect the presence of a moving object but also determine with diffraction accuracy the angular coordinates of the object. If the imaging system does not resolve the background surface, one can only detect the presence of the object. The reliability of detection, as experiments have shown, is high even in the case of object displacements that are comparable with its size.

Thus, time background holography allows us to gain information about moving objects by utilizing coherent fields scattered by the surrounding background and the statistical analysis of the temporal and spatial structure of coherent fields scattered by the background and by moving objects.

5.4 Application of time background holography to the fast detection of moving objects and determination of their parameters

In this section we consider a fast algorithm for detecting arbitrarily reflecting moving objects and a conceptual schematic of a device for detecting and determining coordinates and dynamic and geometric parameters of these objects. First, let us describe the algorithm, which can be carried out by using the detection schematic presented in Fig. 5.5. The functional L_{dj} is calculated in the jth cell of a matrix detection unit [see relation (5.5)]. The object under study and the background surface is probed by radiation that consists of a sequence of pulses with the same width τ_i and time separation τ_d. The pulses scattered back into the matrix detector are registered, and the functional is formed as

$$L_{dj} = \frac{1}{N_0} \sum_{n=1}^{n=N_0} |E'_{ms}(\delta_j, t_n)|^2 - \left| \frac{1}{N_0} \sum_{n=1}^{n=N_0} E'_{ms}(\delta_j, t_n) \right|^2, \tag{5.10}$$

where δ_j is the radius vector of the jth detector cell, $N_0 = T(\tau_i + \tau_d)$ is the number in the sequence of probing pulses within the time T of L_{dj} formation, t_n is the arrival time of the nth returning pulse, $E'_{ms}(\delta_j, t_n) = E_{mb}(\delta_j, t_n) + E_{mn}$ are the pulse fields, which are gated by the jth element of the matrix detector from the radiation scattered by the background surface, including the instant additive noise field E_{mn}. It is supposed that the distance from the background surface is known with a high accuracy *a priori*. As a result of this gating, the fields in the object image, $E_{mo}(\delta_j, t_n)$, collapse. This functional is non-negative for any intensity $I_n = |E_{mn}|^2$ of the additive noise, and turns to zero only if the object is not moving and if the intensity of the additive noise is zero ($I_n = 0$). Therefore, it can be used to detect the moving object and to determine its parameters.[22]

Since L_j are random functionals, one should know their mean values and standard deviations in order to use them for detecting a moving object and determining its coordinates as well as dynamic and geometric parameters. Assuming that the complex amplitude E_{ms} has Gaussian distribution, one can show that the mean value (distribution center) $m_j = \langle L \rangle_j$ and the variation $\sigma_j^2 = \langle L^2 \rangle_j - m_j^2$ of the functionals L_j can be calculated for $Tv_t \gg d_o$, where v_t is the tangential component of the object velocity, d_o is the object size, as

$$m_{1j} \approx \left(\frac{I_j(1 - d_o/v_t T) + I_n}{I_n} \right), \quad \sigma_{1j}^2 \approx \left(\frac{I_j(1 - d_o/v_t T) + I_n}{I_n} \right)^4 \left(\frac{d_o}{v_t T} \right), \tag{5.11}$$

and for $Tv_t \ll d_o$ as

$$m_{2j} \approx 1, \qquad \sigma_{2j}^2 \approx \frac{\tau_n}{T}, \tag{5.11a}$$

where brackets $\langle\rangle$ denote averaging over various realizations of roughness height distribution $\xi(\mathbf{r})$ of the background surface, $\tau_n \ll d_o/v_t$ is the noise field correlation time,

$$I_j = \langle |E_{mb}(\boldsymbol{\delta}_j)|^2 \rangle \sim S_{bj} k_b(\mathbf{r}_j = -\mu\boldsymbol{\delta}_j)|^2 \left(\frac{\sigma_b}{\ell_b}\right)^2 \exp\left[-\left(\frac{\sigma_b q_{\perp j}}{\ell_b q_{Nj}}\right)^2\right] \qquad (5.12)$$

is the mean intensity of the instantaneous image of the jth domain of the background surface shaded by the moving object, S_{bj} and $\mathbf{r}_j$ are the area and the radius vector of the jth shaded domain of the background surface, respectively, σ_b and ℓ_b are the standard deviation and correlation radius of roughness height $\xi_b(\mathbf{r})$ within the shaded domain, $\mathbf{r}$ is the radius vector of the background surface, $k_b(\mathbf{r}_j)$ is the reflection coefficient for the jth shaded domain, and $q_{Nj} \approx (2\mathbf{r}_j \cdot \mathbf{N}_j)/r_j$, $q_{\perp j} \approx (4 - q_{Nj}^2)^{0.5}$, where $\mathbf{N}_j$ is the normal to the mean surface of the jth shaded domain of the background surface. From Eqs. (5.11)–(5.12) we see that the proposed method enables selection of the radiation scattered only by the background surface and spatial filtering of the domain on the background surface shaded by the moving object.

Let us use the mean values and standard deviations calculated from Eqs. (5.11) and (5.11a) to determine the detection threshold and detection probability for objects moving along the background surface (see Fig. 5.9). Recall that the detection threshold is chosen according to the condition that the probabilities of a false alarm of missing the object are small.[27] The probability distribution of the random value L_j is approximated by the gamma distribution

$$W(L_j) = \frac{\beta_j^{\alpha_j}}{\Gamma(\alpha_j)} L_j^{\alpha_j - 1} \exp -\beta_j L_j,$$

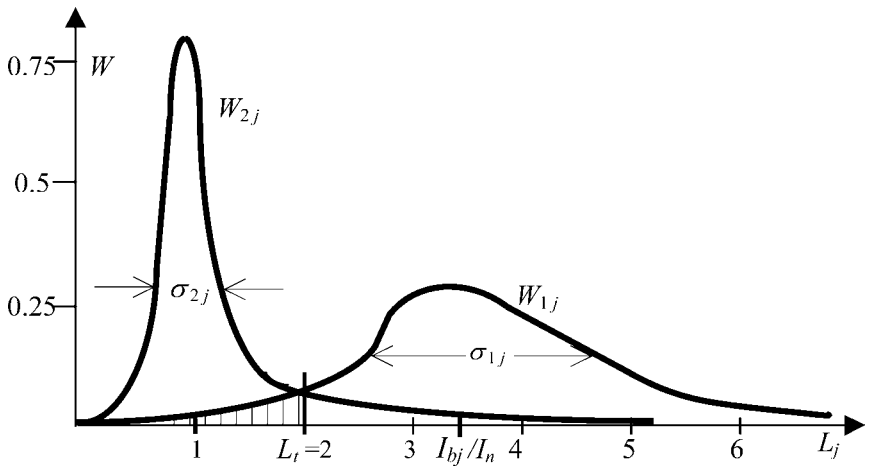

Figure 5.9 The probability density distributions W_{1j} and W_{2j} for the random functional L_j calculated in the jth cell of the matrix detection unit (see Fig. 5.5) in the case of fast object motion ($Tv_t \gg d_o$) and slow object motion ($Tv_t \ll d_o$), respectively.

where $\Gamma(\alpha_j)$ is the gamma function. The distribution W_j is concentrated around the center $m_j = \int_0^\infty L_j W_j(L_j) dL_j = \alpha_j/\beta_j$, with the variation

$$\sigma_j^2 = \int_0^\infty L_j^2 W_j(L_j) dL_j - m_j^2 = \frac{\alpha_j}{\beta_j^2}.$$

From Eqs. (5.11) and (5.11a) we see that if the noise is low ($I_n \ll I_{bj}$) and the object moves sufficiently fast in the horizontal direction ($Tv_t \gg d_o$), the distribution (W_{1j} in Fig. 5.9) is concentrated around the center

$$\frac{\alpha_{1j}}{\beta_{1j}} = m_{1j} \approx \frac{I_{bj}}{I_n}, \tag{5.13}$$

with the variation

$$\frac{\alpha_j}{\beta_{1j}^2} = \sigma_j^2 \approx \left(\frac{I_{bj}}{I_n}\right)^4 \left(\frac{d_o}{Tv_t}\right). \tag{5.13a}$$

From the two preceding equations, one can find the parameters α_{1j} and β_{1j} under the condition $Tv_t \gg d_o$:

$$\alpha_{1j} = \frac{Tv_t}{d_o},$$

and

$$\beta_{1j} = \frac{Tv_t I_n^2}{d_o I_{bj}^2}. \tag{5.14}$$

The probability of missing the object (the area hatched by vertical lines in Fig. 5.9) for the detection threshold $L_t < 0.5 m_{1j}$ is

$$P_{mj} = \int_{L_j=0}^{L_j=L_t} W_{1j}(L_j) dL_j \cong \frac{(\beta_j L_t)^{\alpha_j}}{\Gamma(\alpha_j)(\alpha_j - 1)}.$$

If the horizontal motion of the object is slow, i.e., $Tv_t \ll d_o$, then this distribution is determined only by the noise (W_{2j} in Fig. 5.9). In this case, the distribution is concentrated in a narrow range around the center $\alpha_j/\beta_{2j} = m_{2j} \approx 1 \ll m_{1j} \approx I_{bj}/I_n$ with the variation $\alpha_j/\beta_{2j}^2 = \sigma_{2j}^2 = \tau_n/T$, where $\tau_n \ll d_o/v_t$ and $\alpha_{2j} \approx \beta_{2j} \approx T/\tau_n$. If the signal-to-noise ratio I_{bj}/I_n is sufficiently high, then the center of the probability density distribution W_{1j} of the random value L_j is considerably displaced to the right of center of the probability density distribution W_{2j} (Fig. 5.9). This allows one

to choose a relatively low detection threshold according to the relation $L_t \approx 2m_{2j} \approx 2 \ll m_{1j}$ and still keep almost a zero probability of missing the object. For $\alpha_j \gg 1$, $P_{mj} \approx \{5I_n\sqrt{\alpha_j}/[(\alpha_j - 1)I_{bj}]\}^{\alpha_j}$, and the probability of detecting an object moving along the background surface is $P_{dj} = 1 - P_{mj} \approx 1 - \{5I_n\sqrt{\alpha_j}/[I_{bj}(\alpha_j - 1)]\}^{\alpha_j}$. If $I_{bj}/I_n \gg 1$ and $P_{mj} \ll 1$, then $P_{dj} \approx 1$.

From relations (5.11)–(5.14), we see that the reflection coefficient $k_j(\mathbf{r})$ and the average roughness slope $\gamma_b = \sigma_b/\ell_b$ of the shaded region of the background surface determine the mean intensity I_{bj} of the instantaneous image of the jth domain of the background surface shaded by the moving object and hence, the probability P_{dj} of the object detection. For the case of a smooth surface, $\gamma_b \ll 1$, this can lead to an essential decrease in the detection probability if the background surface and the detection–transmission device are placed according to the condition $q_{tj}/q_{nj} > \gamma_b$.

For accelerating the detection algorithm, the functionals L_{dj} are calculated in the so-called shifting regime. First, the matrix functional unit forms the initial values [Eq. (5.10)] of the function from the received pulses and compares these values with the detection threshold L_t. If these values exceed the threshold, then the object is considered detected, and the functions L_{dj} are fed to the units that determine the coordinates and parameters of the object (Fig. 5.9). The next values of these functions are formed in the same unit during the time interval between the arrivals of a new $(N_0 + 1)$ pulse and the Nth pulse—i.e., the pulse separation τ_d. These values are calculated as follows: the fields $E'_{ms}(\delta_j, t_1)$ of the first pulse are subtracted from the sums $\sum_{n=1}^{n=N_0} E'_{ms}(\delta_j, t_n)$, and then the fields of the $(N_0 + 1)$ pulse $E'_{ms}(\delta_j, t_{N_0+1})$ are added; at the same time, the intensities $|E'_{ms}(\delta_j, t_1)|^2$ are subtracted from the sums $\sum_{n=1}^{n=N_0} |E_{ms}(\delta_j, t_n)|^2$ and the intensities $|E'_{ms}(\delta_j, t_{N_0+1})|^2$ of the $(N_0 + 1)$ pulse are added. As a result, the following functional is formed:

$$L'_{dj} = \frac{1}{N_o} \sum_{n=2}^{n=N_0+1} |E'_{ms}(\delta_j, t_n)|^2 - \left(\left| \frac{1}{N_0} \sum_{n=2}^{n=N_0+1} E'_{ms}(\delta_j, t_n) \right|^2 \right).$$

The formed functionals are compared with the same threshold; if L'_j exceeds this threshold, then the moving object is considered as detected at the moment of registering the $(N_0 + 1)$ pulse, and L'_{dj} is fed to the units to determine the object's coordinates and parameters. Further values of L'_{dj} are formed, compared with the calculated threshold L_t, and similarly processed to determine the object's coordinates and parameters, during the intervals between the arrivals of the $(N_0 + 2)$ and $(N_0 + 3)$ pulses, and so on.

Thus, using the functional L_j to detect the object and, as we will show, to determine its coordinates and parameters, as well as forming the next value of L_{dj}, requires a small number of elementary operations, including multiplication, addition, and comparison with the threshold. A detailed analysis shows that the total number of operations does not exceed 100. This means that for the computing

rate of 10^8 operations per second, the entire procedure takes 1 μsec. Thus, shifting allows one to obtain the information about a moving object in a very short time interval equal to the pulse separation τ_d. The proposed fast algorithm ensures reliable detection of objects moving within view of the imaging system for arbitrarily reflecting objects, including weakly reflecting and transparent objects.

In Fig. 5.10 we present a conceptual schematic of a device that uses the proposed fast algorithm to detect such objects and determine their coordinates and dynamic and geometric parameters. The device can be used to detect and determine the coordinates, velocity, and dimensions of a moving object with arbitrary reflection, including an almost completely absorbing object. The device is a modification of a scheme using the sum-difference method of direction-finding, based on the equal-signal zone principle often used in location techniques,[27] in which two detection–transmission devices probe the moving object. Each device contains sum and difference channels. The sum channels contain imaging systems **IS1** and

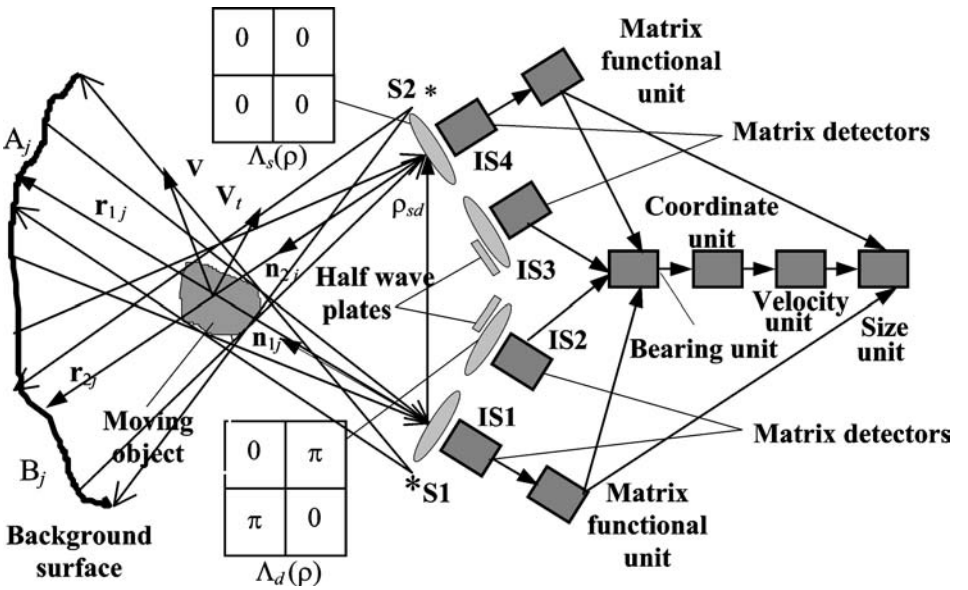

Figure 5.10 Conceptual schematic of a device using the fast algorithm to detect moving objects and determine their coordinates and dynamic and geometric parameters. The four-section square containing two zeros and two π shows the phase distributions of the pupil function $\Lambda_d(\boldsymbol{\rho})$ of the imaging systems **IS2** and **IS3** of the two difference channels. These distributions are formed by using two half-wave plates. The four-section square containing four zeros is the phase distribution of the pupil function $\Lambda_s(\boldsymbol{\rho})$ of the imaging systems **IS1** and **IS4** of the two sum channels. A_j and B_j are shadow domains formed by the moving object on the background surface. **S1** and **S2** are monochromatic sources (transmitters) of the first and second sum-difference channels.

IS4 with the direction diagram

$$D_s(\mathbf{r}) = \frac{1}{S_\rho} \int\limits_{S_\rho} \Lambda_s(\boldsymbol{\rho}) \exp i\left(\frac{2\pi \mathbf{r}\cdot\boldsymbol{\rho}}{r_c\lambda}\right) d\boldsymbol{\rho},$$

where $\boldsymbol{\rho}(u, v)$ is the radius vector of a point in the aperture plane, and u, v are its Cartesian components. The aperture of the imaging system is a square with the pupil function

$$\Lambda_s(\boldsymbol{\rho}) = \begin{cases} 1 & \text{for } |u| \le d_\rho/2,\ |v| \le d_\rho/2, \\ 0 & \text{for } |u| > d_\rho/2,\ |v| > d_\rho/2, \end{cases}$$

where $d_\rho = \sqrt{S_\rho}$ and S_ρ are the size and the area of the aperture, respectively. The difference channel contains an imaging system with the direction diagram

$$D_d(\mathbf{r}) = \frac{1}{S_\rho} \int\limits_{S_\rho} \Lambda_d(\boldsymbol{\rho}) \exp i\left(\frac{2\pi \mathbf{r}\cdot\boldsymbol{\rho}}{r_c\lambda}\right) d\boldsymbol{\rho},$$

where

$$\Lambda_d(\boldsymbol{\rho}) = \begin{cases} 0 & \text{for } |u| > d_\rho/2 \text{ and } |v| > d_\rho/2, \\ 1 & \text{for } d_\rho/2 \ge u \ge 0 \text{ and } d_\rho/2 \ge v \ge 0, \\ & \text{and for } -d_\rho/2 \le u \le 0 \text{ and } -d_\rho/2 \le v \le 0; \\ \exp i\pi & \text{for } d_\rho/2 > u > 0 \text{ and } -d_\rho/2 < v < 0, \\ & \text{and for } -d_\rho/2 < u < 0 \text{ and } d_\rho/2 > v > 0. \end{cases}$$

This diagram is formed by means of transparent half-wave plates placed in the aperture planes of the imaging systems of the difference channels (Fig. 5.10). In the equal-signal directions given by the unit vectors $\mathbf{n}_{1j}$ parallel to the optical axis of the imaging systems **IS1** and **IS2**, and $\mathbf{n}_{2j}$ parallel to the optical axis of the imaging systems **IS3** and **IS4**, $D_d(\mathbf{r}) = 0$, while $D_s(\mathbf{r})$ is maximum in this direction.

Furthermore, the matrix functional units form the functionals L_{1Sj} and L_{2Sj}, respectively. Here, j is the cell number of the matrix detection unit. If the moving object appears in the jth domain of the background surface, optically conjugated to the jth cells of the matrix detection units, and placed in the focal planes of the imaging systems **IS1** and **IS2**; and appears in the Bjth domain of the background surface, optically conjugated to the jth cells of the matrix detection units, and placed in the focal planes of the imaging systems **IS3** and **IS4**, then for $T \gg d_o/v_t$,

$$\langle L_{1Sj}\rangle = \frac{I_{1Sj}(1 - d_o/v_t T) + I_n}{I_n}, \quad \langle L_{2Sj}\rangle = \frac{I_{2Sj}(1 - d_o/v_t T) + I_n}{I_n}, \qquad (5.15)$$

where

$$I_{1Sj} \sim \left(\frac{\ell_b}{\sigma_b}\right)^2 S_{1j}|k_b(\mathbf{n}_{1j})D_s(\mathbf{n}_{1j})D_d(\mathbf{n}_{1j})|^2 \exp\left[-\left(\frac{\ell_b q_{\perp j1}}{\sigma_b q_{j1}}\right)^2\right]$$

and

$$I_{2Sj} \sim \left(\frac{\ell_b}{\sigma_b}\right)^2 S_{2j}|k_b(\mathbf{n}_{2j})D_s(\mathbf{n}_{2j})D_d(\mathbf{n}_{2j})|^2 \exp\left[-\left(\frac{\ell_b q_{\perp j2}}{\sigma_b q_{j2}}\right)^2\right]$$

are the mean intensities of the instantaneous image of the jth domain of the background surface shaded by the moving object in the first and second sum channels, respectively; S_{pj}, where $p = 1, 2$, are their areas; d_j is the domain maximal length; and $\mathbf{r}_{pj}$ are radius vectors connecting the first and the second sum channels with the centers of two domains A_j and B_j on the background surface shaded by the moving object (Fig. 5.10),

$$\begin{aligned} \mathbf{n}_{jp} &= \frac{\mathbf{r}_{jp}}{r_{jp}}, \\ q_{jp} &\approx 2\mathbf{n}_{jp} \cdot \mathbf{N}_j, \\ q_{\perp jp} &= \sqrt{4 - q_{jp}^2}, \quad (p = 1, 2). \end{aligned}$$

Similarly, in two other matrix detector units in the two difference channels, the functionals L_{1dj} and L_{2dj} are formed:

$$\langle L_{1dj}\rangle = \frac{I_{1dj}(1 - d_o/v_t T) + I_n}{I_n}, \quad \langle L_{2dj}\rangle = \frac{I_{2dj}(1 - d_o/v_t T) + I_n}{I_n}, \tag{5.16}$$

where

$$I_{1dj} \sim \left(\frac{\ell_b}{\sigma_b}\right)^2 S_{1j}|k(\mathbf{n}_{1j})D_s(\mathbf{n}_{1j})D_d(\mathbf{n}_{1j})|^2 \exp\left[-\left(\frac{\ell_b q_{\perp j1}}{\sigma_b q_{j1}}\right)^2\right]$$

and

$$I_{2dj} \sim \left(\frac{\ell_b}{\sigma_b}\right)^2 S_{2j}|k(\mathbf{n}_{2j})D_s(\mathbf{n}_{2j})D_d(\mathbf{n}_{2j})|^2 \exp\left[-\left(\frac{\ell_b q_{\perp j2}}{\sigma_b q_{j2}}\right)^2\right]$$

are the mean intensities of the instantaneous image of the jth domain of the background surface shaded by the moving object in the first and second difference channels, respectively.

Furthermore, the functionals L_{1dj}, L_{1Sj}, L_{2dj}, and L_{2Sj} are fed to the matrix detection units and then to the bearing unit (Fig. 5.10) where two bearing parameters are calculated, $\eta_{1j} = L_{1dj}/L_{1Sj}$ and $\eta_{2j} = L_{2dj}/L_{2Sj}$. If the angles φ_j between

the direction towards the object and the axes of the direction diagrams $D_s(\mathbf{r})$ and $D_d(\mathbf{r})$, for the sum and difference channels, and the noise field intensity are small ($I_n \ll I_{1dj}, \underline{I}_{2dj}$), then $\varphi_j \cong \sqrt{\theta_j^2 + \vartheta_j^2}$,

$$\eta_{1j}(\theta_{1j}, \vartheta_{1j}) = \upsilon(\theta_{1j} + \vartheta_{1j}) + \frac{2I_n}{I_{S1j}},$$

and

$$\eta_{2j}(\theta_j, \vartheta_j) = \upsilon(\theta_{2j} + \vartheta_{2j}) + \frac{2I_n}{I_{S2j}},$$

where θ_{1j} and ϑ_{1j} are the angles between the vectors $\mathbf{n}_{1j}$ and the optical axis of the imaging system **IS1**, and θ_{2j} and ϑ_{2j} are the angles between the vectors $\mathbf{n}_{2j}$ and the optical axis of the imaging system **IS4**, and $\upsilon \approx (8\pi d_\rho)/\lambda$ is the steepness of the direction-finding curve. When $\theta_{1j} \to 0$, $\vartheta_{1j} \to 0$, $\theta_{2j} \to 0$, $\vartheta_{2j} \to 0$, then the axes of the imaging system's direction diagrams are simultaneously fixed towards the object at minimum values of the bearing parameters to within an accuracy of $\sigma_\varphi \approx (\upsilon I_n)/I_{bj}$, where $I_{bj} = \min(I_{1Sj}; I_{2Sj})$. At $\sigma_\varphi \ll 0.1$, these axes are directed towards the moving object (Fig. 5.10). Hence, at $\sigma_\varphi \ll 0.1$, the bearing units determine with high accuracy the unit vectors $\mathbf{n}_{1j}$ and $\mathbf{n}_{2j}$ directed from the sum and difference channels, respectively, to the object under study. The vector $\mathbf{n}_{1j}$ determines the object's angular coordinates. The object's trajectory vector is

$$\mathbf{r}_j(t) = \frac{\mathbf{n}_{2j} \times \boldsymbol{\rho}_{sd}}{|\mathbf{n}_{2j}(t) \times \mathbf{n}_{1j}(t)|},$$

where $\boldsymbol{\rho}_{sd}$ is the radius vector connecting the centers of the imaging systems with the sum and difference direction diagrams (Fig. 5.10); the object's distance is $r_j = |\mathbf{r}_j|$, the radial velocity is $v_{rj} = \mathbf{v} \cdot \mathbf{n}_{1j}$, and the tangential velocity is $v_{tj} = |\mathbf{v} - \mathbf{v}_{rj} \cdot \mathbf{n}_{1j}|$.

Finally, using relations (5.15) and (5.16), the value v_t, and the times T_1 and T_2 of forming the functional L_{1Sj} in the size unit (Fig. 5.10), one can calculate the overall size d_o of the object:

$$d_o \sim \frac{v_t T_1 T_2 (\chi_j - 1)}{T_1 T_2},$$

where $\chi_j = L_{1Sj}(T_1)/L_{1Sj}(T_2)$. The proposed device presented in Fig. 5.10 can simultaneously detect several moving objects with arbitrary reflection coefficients, including transparent ones, and measure their coordinates and dynamic and geometric parameters.

5.4.1 Device for monitoring environmental pollution using time background holography

Consider a modification of the device presented in Fig. 5.10 that allows one to monitor environmental pollution. Here, time averaging of coherent fields scattered by pollution particles is performed and random functionals L_{1Sj}, L_{2Sj}, L_{1dj}, and L_{2dj} are formed. In order to detect clusters of moving, weakly reflecting, or transparent pollution particles and determine their coordinates, as well as determine the concentration, average size, and average velocity of the particles in each cluster, one can use the scheme shown in Fig. 5.11. For a reliable detection of these clusters, one should use as a background a metal surface with $\gamma \ll 1$ roughness as suggested in Ref. 22. Such a surface should have a high reflection coefficient and high directivity of scattering.

In this device, angular coordinates for the clusters of pollution particles and their distances are determined in exactly the same manner as these parameters are determined for moving objects by means of the device shown in Fig. 5.10. For determining the concentration, average size, and average velocity of pollution particles in the cluster, an additional unit is introduced: the pollution particles parameters unit.

If we approximate the surface of the kth particle by a sphere with diameter d_k and large-scale roughness ($\gamma_k \sim 1$), one can show that if the cluster shades the jth domain of the background surface, then the jth cell of the matrix detection unit of the first sum channel (the channel including the imaging system **IS1** in Fig. 5.11),

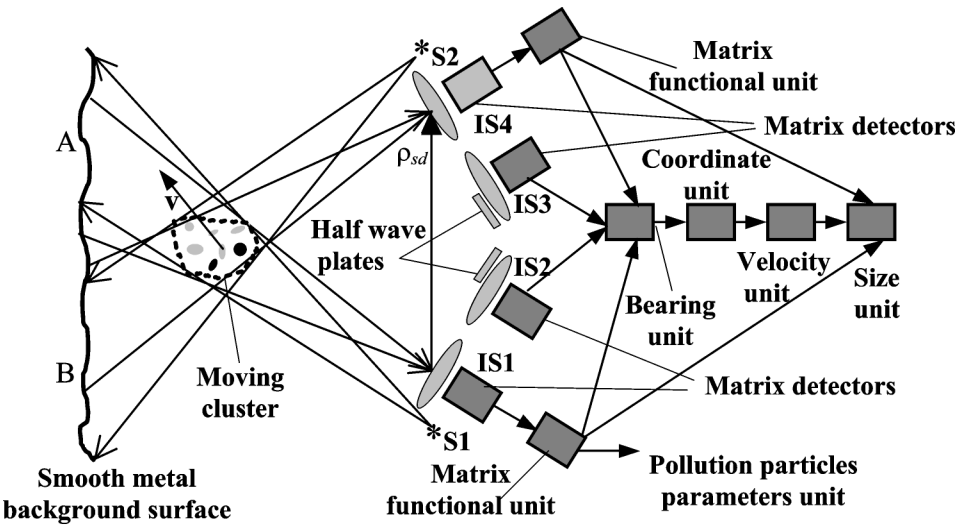

Figure 5.11 Device for monitoring environmental pollution based on time background holography. The small spots in a moving cluster are pollution particles.

which is optically conjugate to the jth domain, forms the functional

$$L_{1Sj} \sim \sum_{k=1}^{k=K_j} d_k^4 \left(1 - \frac{d_k}{v_k T}\right) \cong K_j \langle d^4 \rangle_{dj} - \frac{K_j}{T} \langle d^5 \rangle_{dj} \left\langle \frac{1}{v} \right\rangle_{vj},$$

where K_j is the number of particles in the cluster, i.e., their concentration in the direction towards the background surface; $\langle\rangle_{dj}$ and $\langle\rangle_{vj}$ denote averaging over the particle sizes and velocities, respectively, in the cluster shading the jth background surface domain. If this functional exceeds the threshold L_t, then the moving cluster is detected. After the cluster detection, its direction is found and its coordinates and linear velocities are determined, as shown in Fig. 3.10.

For determining concentration, average size, and velocity of the particles in the cluster for three different times T_p $(p = 1, 2, 3)$, the pollution particles parameters unit forms the dimensionless values

$$\Delta_{jp} = L_{1Sjp} \left[(1/N_p) \sum_{n=1}^{n=N_p} |E'_{ms}(\delta_j, t_n)|^2 \right]^{-1},$$

where $N_p = T_p/(\tau_i + \tau_d)$ $(p = 1, 2)$; the index $1S$ denotes the first sum channel, including the lowest imaging system in Fig. 5.11, and the index j is the number of the jth background surface domain, optically conjugated to the jth cell of the matrix detection unit of the first sum channel. If L_{1Sj1} exceeds the threshold L_t, the conclusion is made that there is a cluster of moving pollution particles in the direction of the jth background surface domain. If contribution of screening pollution particles to the backward scattering of the background surface can be neglected, and if size and velocity dispersion are small, then

$$\Delta_{jp} = \frac{K_j S_\rho \bar{d}_j^4}{\lambda^2 r_c^2} \left(1 - \frac{\bar{d}_j}{\bar{v}_j T_p}\right),$$

where $\bar{d}_j$ and $\bar{v}_j$ are the average size and velocity of the particles. In this case, different times $T_1 < T_2 < T_3$ provide three equations for determining three values $\bar{d}_j$, $\bar{v}_j$, and K_j that characterize environmental pollution in the cluster, located in the direction of the jth background surface domain.

5.5 Time background holography of moving objects placed close to the background surface; the principle of time averaging of coherent wavefields

5.5.1 Introduction

Using time background holography, one can determine the dynamic and geometric parameters of moving objects by performing a rather complicated Fourier–Fresnel

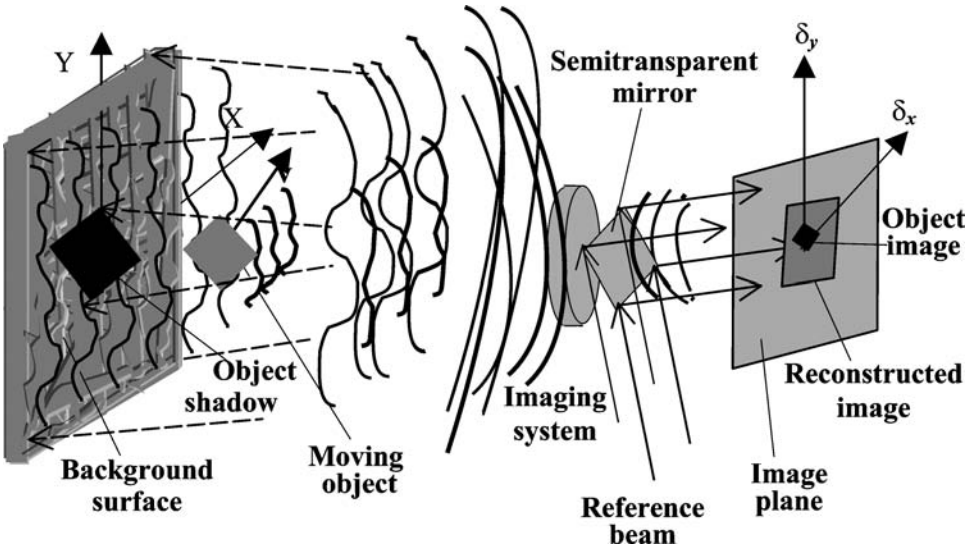

Figure 5.12 Time background holography in the case of time averaging of coherent wavefields by a high-resolution imaging system. The dashed lines denote the illuminating wave; the thick lines denote the waves scattered by the moving object; the thin lines denote the waves scattered by the background surface.

time transform over the fields scattered by the background and by the objects and over the coherent images of the background and the objects (Sec. 5.2). If moving objects are placed close to a randomly inhomogeneous background, this process is significantly simplified by applying the principle of time averaging of scattered coherent fields and fields in coherent images.[79] This principle can be considered as a particular case of time background holography with $\omega = \beta = 0$. In this section, this method is analyzed for the case of arbitrary resolution of the objects by the imaging system and illustrated with experimental data. For simplicity, the principle of time averaging of coherent fields will be demonstrated for the case of a square object moving with a constant velocity against a background that is represented by a fixed, flat, rough surface (Fig. 5.12). Applications of this principle with a system resolution ranging from very high to very low ensure the determination of the geometric and dynamic parameters of any moving object, whether reflecting, transparent, or absorbing. This principle is shown to be very useful in the case of a low-resolution system that observes coherent radiation scattered by a stationary background surface and modulated by a moving absorbing object.

5.5.2 Theory

It can be shown that the setup for realizing the principle of time averaging of coherent fields is based on the idea of focused image holography.[37] According to this

concept, the background surface and the moving object are illuminated by monochromatic, e.g., spherical wave, radiation (Fig. 5.12). The object casts a shadow on the background surface, which moves with the velocity $v_s = (vR)/r_c$, where v is the object's velocity component parallel to the fixed background surface, R is the distance from the object's shadow on the background surface to the receiver, and r_c is the distance from the object to the receiver.

Then, the field scattered by the background surface and modulated by the moving object is focused by an imaging system in the image plane, where, with the help of a reference beam, the dynamic hologram of the moving object and the background surface is recorded. Simultaneously, the instantaneous field in the image, E_i, undergoes a Fourier–Fresnel time transform during a defined time T (Sec. 5.2).

For a defined averaging time T, the reconstructed image contains the moving object image as a black spot on the image of the background surface (see Fig. 5.12) under the condition

$$E_t(\delta_x, \delta_y, \omega, \beta) = \frac{1}{T} \int_{t_0}^{t_0+T} E_i(\delta_x, \delta_y, t) \exp\left(i\omega t + i\beta t^2\right) dt,$$

where t_0 is the initial moment of observing the coherent field, δ_x and δ_y are coordinates in the image plane, and E_i is the instantaneous field in the image. After this, the joint image of the moving object and the background surface is reconstructed. The time-averaged field in the reconstructed image is

$$E(\delta_x, \delta_y) = E_t(\delta_x, \delta_y, \omega = 0, \beta = 0) = \frac{1}{T} \int_{t_0}^{t_0+T} E_i(\delta_x, \delta_y, t) dt. \tag{5.17}$$

The measured intensity in the reconstructed image is $I(\delta_x, \delta_y) = |E(\delta_x, \delta_y)|^2$. If the moving object is placed close to the background surface, edge diffraction effects are inessential, and E_i is represented in the form[12]

$$E_i(\delta_x, \delta_y, t) = E_{ib}(\delta_x, \delta_y, t) + E_{io}(\delta_x, \delta_y, t),$$

where

$$\begin{aligned} E_{ib}(\delta_x, \delta_y, t) &= A_n \int\int k_b(x, y) \exp[i\varphi_b(x, y)] \\ &\quad \times [1 - \Pi(x - v_s t, y)] h(x, y, \delta_x, \delta_y) dx dy, \\ E_{io}(\delta_x, \delta_y, t) &= A_n \exp\left(\frac{i4\pi v_n t}{\lambda}\right) \iint k_o(x, y) \exp[i\varphi_o(x - vt, y)] \\ &\quad \times \Pi(x - v_s t, y) h(x, y, \delta_x, \delta_y) dx dy, \end{aligned} \tag{5.17a}$$

where $A_n \approx (iE_sS_s)/(\lambda R)^2$; E_s and S_s are the field amplitude on the illuminating source and the source aperture area, respectively; λ is the source wavelength; x and y are coordinates on mean surfaces of the background and the moving object; $k_b(x,y)$ is the distribution of the background surface reflection coefficient; $\varphi_b(x,y) = \{4\pi[\xi_b(x,y) + R - z_t]\}/\lambda$, where $\xi_b(x,y)$ is the distribution of the background surface roughness height, R is the distance between the observation plane and the mean background surface, and z_t is the distance between the observation and intermediate planes; $k_o(x,y)$ is the regular component of the light modulation by the object (in the case of an opaque object, it is the distribution of the object surface reflection coefficient);

$$\Pi(x,y) = \begin{cases} 1, |x| < d_s/2, & |y| < d_s/2 \\ 0, |x| \geq d_s/2, & |y| \geq d_s/2 \end{cases}$$

is a function describing the moving shadow of the object, where d_s is the object shadow size; $h(x,y,\delta_x,\delta_y)$ is the imaging system's pulse response, and $\varphi_o(x,y)$ is the random phase modulation introduced by the object into the scattered field. Here, the X axis is directed along the object's velocity component $v = v_{xt}$ (see Fig. 5.1), $v_s = (Rv)/r_c$ is the object shadow's velocity, and v_n is the object's velocity component orthogonal to the fixed background surface.

The mean measured intensity in the reconstructed image of the object's surface is

$$\langle I(\delta_x, \delta_y)\rangle \approx \frac{1}{T^2} \int_{t_0}^{t_0+T} \int_{t_0}^{t_0+T} [B_b(t_1,t_2) + B_o(t_1,t_2)]dt_1 dt_2, \tag{5.18}$$

where the brackets $\langle\rangle$ denote averaging I over the random phase functions $\varphi_o(x,y)$ and $\varphi_b(x,y)$, $B_b(t_1,t_2) = \langle E_{ib}(\delta_x,\delta_y,t_1)E^*_{ib}(\delta_x,\delta_y,t_2)\rangle$, $B_{io}(t_1,t_2) = \langle E_{io}(\delta_x,\delta_y,t_1)E^*_{io}(\delta_x,\delta_y,t_2)\rangle$, and σ_b and ℓ_b are the standard deviation and the correlation radius of the background roughness height, respectively. The resulting relations enable one to determine the mean intensity $\langle I\rangle$ for transparent and opaque moving objects and backgrounds with an arbitrary resolution of the imaging system.

For simplicity, consider now the case of a rough, flat, opaque moving object where $\varphi_o(x,y) = \{4\pi[\xi(x,y) + r_c - z_t]\}/\lambda$; $\xi(x,y)$ is the distribution of the surface roughness height. We will consider the case of a high-resolution imaging system, where $(\lambda r_c)/d_\rho \ll d_o$ (d_o is the object size). Two opposite situations will be discussed: $v \neq 0$, $v_n = 0$, and $v = 0$, $v_n \neq 0$. When $v \neq 0$, $v_n = 0$, or, more precisely, when $\lambda/v_n > T > (10\ell\lambda)/(\sigma v)$, under the assumption that the object displacement $s = vT$ satisfies the condition $(10\lambda\ell)/\sigma < s < d_o$, then, if the distributions of the

functions $\varphi_o(x, y)$ and $\varphi_b(x, y)$ are Gaussian,

$$\langle I(\delta_x, \delta_y)\rangle \sim \begin{cases} |k_b|^2, & \delta_x\mu > vT + d_o \\ \dfrac{\lambda}{vT}\left(1 + \dfrac{d_o - \delta_x\mu}{vT}\right)K_o + \varepsilon\left(\dfrac{\delta_x\mu - d_s}{v_sT}\right)^2 |k_b|^2, & \delta_x\mu < vT + d_o \\ \dfrac{\lambda}{vT}K_o, & vT < \delta_x\mu < d_o \\ \dfrac{\lambda}{vT}\dfrac{\delta_x\mu}{vT}K_o + \varepsilon\left(1 - \dfrac{\delta_x\mu}{v_sT}\right)^2 |k_b|^2, & 0 < \delta_x\mu < vT \\ |k_b|^2, & \delta_x < 0 \end{cases} \tag{5.19}$$

where $\mu = R/z_i \approx r_c/z_i$ is the scaling factor (the imaging system magnification), $K_o = |k(x = -\mu\delta_x, y = -\mu\delta_y)|^2$,

$$\zeta = \frac{\ell}{\sigma}, \quad \varepsilon = 1, \quad \text{with } \frac{\sigma}{\ell} \text{ and } \frac{\sigma_b}{\ell_b} < \frac{d_\rho}{R}, \tag{5.20}$$

if the background surface, object, and random phase functions $\varphi_o(x, y)$ and $\varphi_b(x, y)$ are resolved; or

$$\zeta = \frac{R}{d_\rho}, \quad \varepsilon = \frac{\ell_b}{\sigma_b} \quad \text{with } \frac{\sigma}{\ell} \text{ and } \frac{\sigma_b}{\ell_b} > \frac{d_\rho}{R}, \tag{5.21}$$

if the object and background surface are resolved while the random phase functions $\varphi_o(x, y)$ and $\varphi_b(x, y)$ are not.

From formulas (5.19), it follows that for moving rough objects with any kind of response to the incident radiation, including the cases of transparent objects, objects that are indistinguishable against the background, and highly reflecting opaque objects, we can define averaging times T that ensure formation of their images: if the imaging system resolves random phase functions $\varphi_o(x, y)$ and $\varphi_b(x, y)$, then the averaging time $T > (10\lambda\ell)/(\sigma v)$; if the imaging system does not resolve the random phase functions $\varphi_o(x, y)$ and $\varphi_b(x, y)$, then $T > (10\lambda r_c)/(d_\rho v)$.

The result obtained under condition (5.20) demonstrates that the radiation scattered by every part of a moving object reaches the imaging system aperture, and the Doppler frequency spread is $(\sigma v)/(\lambda\ell)$. As a result, for $T \gg (\lambda\ell)/(\sigma v)$, the phase of the field at each point in the image is changed by more than π during time averaging of this field. Therefore, if one applies the scheme proposed in Fig. 5.12, the measured intensity in the object image is significantly smaller than that in the background image. Hence, in the case of a high-resolution imaging system, the proposed scheme provides the means to distinguish opaque and transparent moving objects from the background. The first to use this approach was Feleppa.[19] He obtained long-exposure holograms of a thin blood sample for determining the mobility of transparent white cells.

Under the condition (5.21), the result implies physically that the radiation from every part of a moving object partly reaches the imaging system aperture, and the

Doppler frequency spread from that part is $(d_\rho v)/(\lambda r_c)$. For $T \gg (\lambda r_c)/(d_\rho v)$, also due to the time averaging of the field scattered by the moving object, the measured intensity in the object's image is significantly smaller than the intensity in the background image. For $vT \gg d_o$, the background is also screened. The radiation intensity value also may be interpreted in two different ways.

The first explanation is similar to the explanation presented in the previous case, where conditions (5.20) are fulfilled. In the course of recording the hologram, fields scattered by the moving object at different small time intervals interfere with the reference beam, and their interference causes different interference fringes within the holographic medium. As a result, if the object displacement $s > (\lambda r_c)/d_\rho$, then the reconstructing rays diffracted by these fringes have opposite phases and form in the reconstructed image of the moving object a field with an intensity that is close to zero. The second explanation is as follows. The reconstructed image (the coherent image of the object[12]) is a speckle pattern with speckle angular width λ/d_ρ; if the object displacement S is larger than $(\lambda r_c)/d_\rho$, which defines the imaging system's resolution, then the reconstructed image moves by more than the speckle size, and the field distribution in the image changes completely. As a result, different field realizations have opposite phases and form in the reconstructed image of the moving object a field with an intensity close to zero.

When $v_n \neq 0$, $v = 0$, or, more precisely, when $\lambda/v_n < T < (10\ell\lambda)/(\sigma v)$, then for an opaque moving object,

$$\langle I(\delta_x, \delta_y)\rangle \sim \begin{cases} |k_b|^2 & \text{for } |\delta_x| \geq d_o/2\mu,\ |\delta_y| \geq d_o/2\mu \\ K_o \mathrm{sinc}\dfrac{2\pi v_n T}{\lambda} & \text{for } |\delta_x| < d_o/2\mu,\ |\delta_y| < d_o/2\mu\,. \end{cases} \tag{5.22}$$

If the object displacement $s = v_n T \gg \lambda$, then the measured intensity $I(\delta_x, \delta_y)$ in the reconstructed image within the region $\delta_x < d_\rho/2\mu$, $\delta_y < d_\rho/2\mu$ is close to zero. It is significantly smaller than the measured intensity in the background surface image.

Thus, from the obtained expressions (5.19) and (5.22), we make the following conclusion: If the moving object is opaque, then the intensity within the region $\delta_x < d_o/2\mu$, $\delta_y < d_o/2\mu$ of the reconstructed image is significantly smaller than the intensity of the background surface image, for a certain small displacement s of the object parallel or perpendicular to the background surface. If the moving object is transparent, then the measured intensity $I(\delta_x, \delta_y)$ within this region is nonzero for any displacement s perpendicular to the background surface.

In the foregoing, we have considered time background holography of opaque moving objects placed close to the background surface. Now consider a transparent moving object for which

$$\varphi_o(x, y) = \frac{4\pi}{\lambda}\left[R - b_n(x, y) + \int_{b_n(x,y)}^{b_f(x,y)} n(x, y, z)dz + z_t - b_f(x, y)\right],$$

where $b_n(x, y)$ and $b_f(x, y)$ are the equations of object boundary surfaces that are close to the background surface, and far from it, respectively; $n(x, y, z)$ is the refractive index inside the object. Furthermore, consider the most interesting case of a transparent moving object whose refractive index varies smoothly along the direction orthogonal to the background surface: $(\lambda\partial \ln n/\partial z) \ll |k_b|$. In this case, backscattering from the background surface is considerably higher than from the moving object, and hence, the object is almost impossible to detect. However, we can rewrite Eqs. (5.19) for the averaged intensity $\langle I\rangle$ by substituting the value $|k_b|^2$ instead of K_o, and the value $\gamma_{bo} = \lambda\sqrt{\langle(\partial\varphi_o/\partial x)^2\rangle + (\sigma/\ell)^2}$ instead of σ/ℓ. From the resulting new Eqs. (5.19), it follows that the motion of a transparent moving object leads to a considerable decrease in intensity in the domain of the background surface image occupied by the object.

5.5.3 Experiments

One can see from relations (5.19) and (5.22) for $I(\delta_x, \delta_y)$ that when measuring the intensity, one can find the average slope of an object's surface roughness $\chi(\delta_x, \delta_y) = [\sigma(\delta_x, \delta_y)]/[\ell(\delta_x, \delta_y)]$ at each point of the object image. To do this we must measure the ratio $\alpha(\delta_x, \delta_y)$ of the image intensities outside and inside the area of the object displacement $s = vT$, for the case $s \ll (10\ell\lambda)/\sigma$, and also the ratio $\beta(\delta_x, \delta_y)$ of the intensities inside and outside of the object image and the object displacement s for the case $(10\ell\lambda)/\sigma < s \ll d_o$. Then, if the condition (5.20) is satisfied, we have the average slope at the point (x, y) of the object surface $\chi(x = -\mu\delta_x, y = -\mu\delta_y) = (\alpha\beta\lambda)/s$, where $\mu = r_c/z_i$.

One of the ways to implement this method of determining the average roughness slope is to record three-dimensional holograms of the moving object and the background surface with two exposure times: one short, $T \ll (10\lambda\ell)/(\sigma v)$, and one long, $d_o/v \gg T > (10\lambda\ell)/(\sigma v)$, and to reconstruct two images of the object from these holograms. In this technique, the object and the background are usually placed close to the hologram, so the condition (5.20) is satisfied; in this case, d_ρ is the hologram size and the scaling factor $\mu = -1$. This technique is implemented by reconstructing images of the object against a stationary diffuse background surface for the cases of short and long exposure times. A rough plate moves by a distance significantly shorter than its size d_o. The hologram is recorded by means of the Denisyuk setup[82] [Fig. 5.13(a)]. In the reconstructed image of the plate, for the case $d_o/v \gg T > (10\lambda\ell)/(\sigma v)$, the area of the moving rough plate was shaded [Fig. 5.13(b)]. The degree of shading depends on the object's displacement $s = vT$ (Fig. 5.14). This fact allows one to use the reconstructed images for determining the average slopes of roughness in various parts of the plate with the help of the formula $\chi = (\alpha\beta\lambda)/s$, by means of measuring parameters α and β in the images reconstructed with holograms recorded with short and long exposure time, respectively.

If $S > (\lambda\ell)/\sigma$, the observer sees the reconstructed image as the background image with black regions for the moving rough object for any kind of response of the

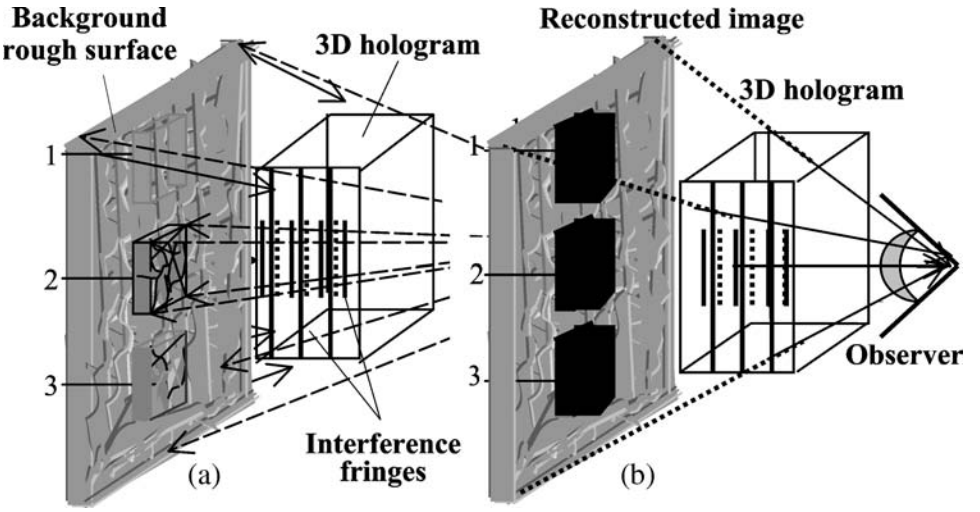

Figure 5.13 The three-dimensional holographic technique for time averaging of coherent wavefields in the case where the moving object and the background are placed close to the hologram. (a) The hologram recording: 1 is a transparent object, 2 is a highly reflecting object, 3 is an object indistinguishable from the background. The dashed lines denote the illuminating wave, the long solid lines are interference fringes relating to the background surface, and the short solid and dashed lines are different interference fringes relating to the moving object. (b) The hologram reconstruction.

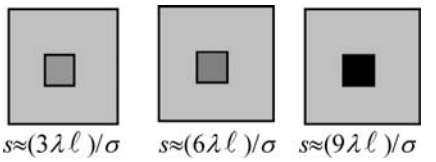

Figure 5.14 Reconstructed images of an opaque moving object indistinguishable from the background surface for various object displacements s.

object to the incident radiation, including the cases of objects that are transparent, indistinguishable against the background, or highly reflecting and opaque. This is due to the fact that at different times of the hologram recording, fields scattered by the moving object interfere with the reference beam and cause different interference fringes within the holographic medium. As a result, if the object displacement $s > (10\lambda\ell)/\sigma$, the reconstructing rays reflected from these fringes have opposite phases and form in the reconstructed image of the moving object a field with an intensity close to zero. As a result, in the regions of the reconstructed object image, the observer sees black shadows [Fig. 5.13(b)]. In Fig. 5.14, reconstructed images of moving objects indistinguishable against the background are demonstrated for various object displacements s.

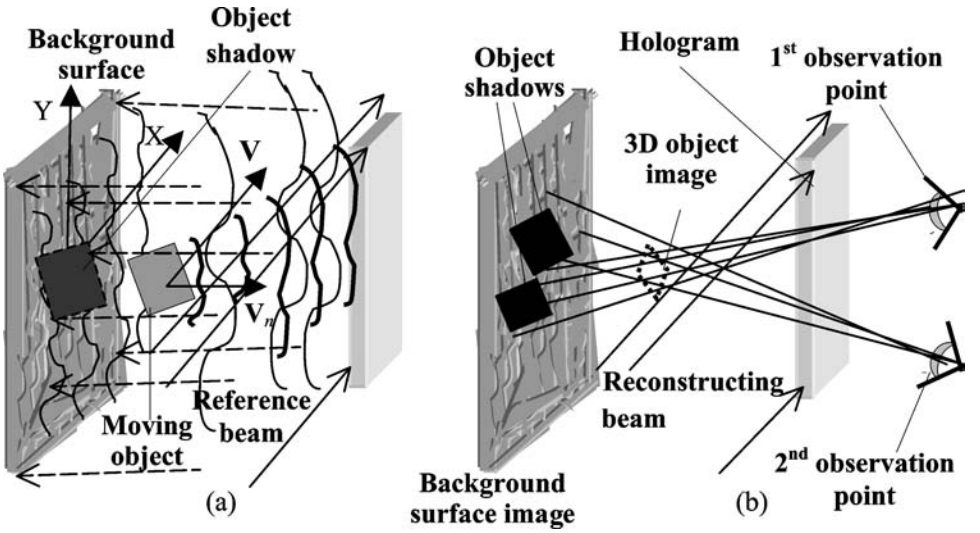

Figure 5.15 The Leith–Upatnieks holographic technique for the case where the object under study is placed far from the background surface and the hologram. (a) The hologram recording; the dashed lines denote the illuminating wave. (b) The hologram reconstruction; the observer watching the three-dimensional reconstructed image of a transparent or opaque moving object from different points will see this image as different black shadows on the reconstructed image of the background surface.

Under the condition (5.21), the moving object is placed far from the background surface and the imaging system. In this case, the Leith–Upatnieks holographic technique[83] of time-averaging of coherent wavefields can be applied (Fig. 5.15). If the recording time T satisfies the condition $d_o/v \gg T \gg (\lambda r_c)/(d_\rho v)$, then different reconstructing rays diffracted by the hologram have opposite phases that cause their cancellation. As a result, an observer looking at the three-dimensional reconstructed image of a transparent or opaque moving object from different vantage points will see this image as different black shadows on the reconstructed image of the background surface.

It is obvious that knowing the size of these black shadows allows one to determine the parameters of opaque and transparent three-dimensional moving objects that are indistinguishable from the background surface. For instance, it is possible to measure the distance between the objects and the background surface, as well as the sizes of the objects, by means of the schematic presented in Fig. 5.16. From the similarity of the triangles in Fig. 5.16 we obtain the following equations for the object size d_o and the distance R_{ob} between the background surface and the moving object:

$$\frac{a}{R_2} = \frac{d_o}{\mu(R_1 - R_{ob})}, \quad \frac{b}{R_2} = \frac{d_o}{\mu(R_2 - R_{ob})},$$

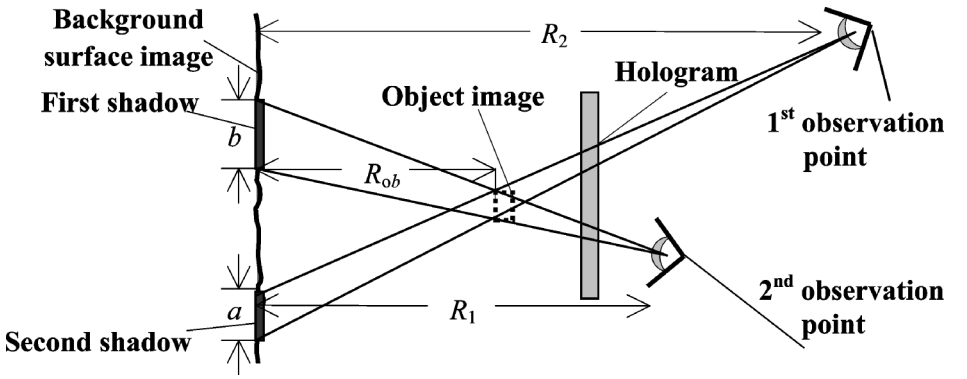

Figure 5.16 Schematic showing the measurement of the object size and the distance between the object and the background surface.

where a and R_1 are the size of the shadow observed from the first point and the distance from the first observation position to the background surface image, respectively; and b and R_2 are the size of the shadow observed from the second point and the distance from the second observation position to the background surface image, respectively (see Fig. 5.15).

If values a, R_1, b, and R_2 are measured by means of the last equations, then we can obtain the object size d_o and the distance R_{ob} for objects with arbitrary electromagnetic properties, including objects indistinguishable from the background surface:

$$R_{ob} = \frac{R_1 R_2 (b - a)}{bR_1 - aR_2},$$
$$d_o = \frac{\mu ab(R_2 - R_1)}{bR_1 - aR_2}.$$

We see that the Leith–Upatnieks holographic technique of time averaging of coherent wavefields allows us to distinguish opaque and transparent three-dimensional moving objects and to determine their parameters if the recording time satisfies the condition

$$\frac{d_o}{v} \gg T \gg \frac{\lambda r_c}{d_\rho v}.$$

In the case of low spatial resolution, $(\lambda r_c)/d_\rho < d_o$, L, then the function $h(x, y, \delta_x, \delta_y)$ in relations (5.17a) is almost constant, and the image of the complex object consisting of the background surface and the moving object in Fig. 5.17 contains a single speckle. In this case, the time-averaging principle can be fulfilled by receiving the intensity of the time-averaged field scattered by the background surface and by the moving object into a speckle (Fig. 5.17). For the case $v \neq 0$,

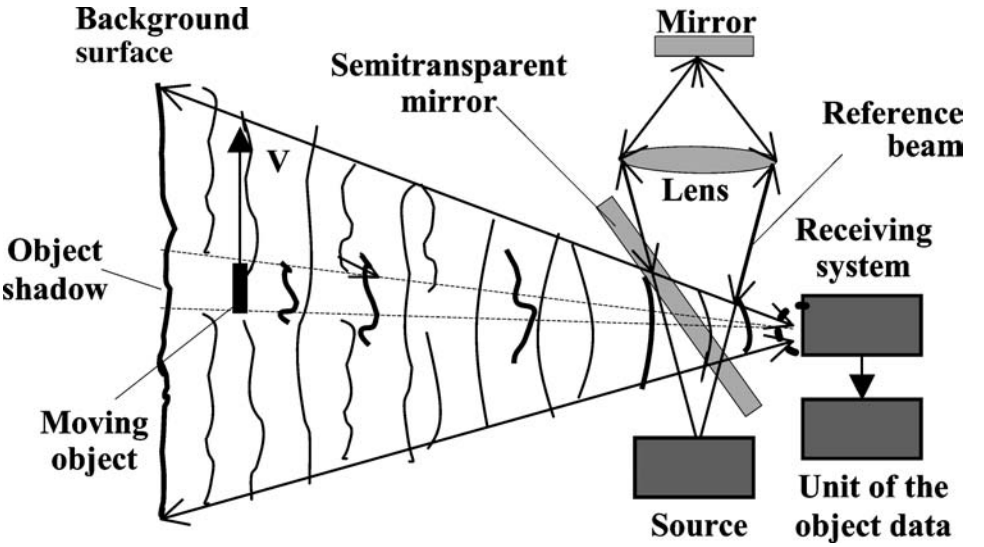

Figure 5.17 Time background holography of a nonresolvable moving object placed close to a nonresolvable background surface. The thick lines denote waves scattered by the moving object. The thin lines denote waves scattered by the background surface. The dotted line denotes a single speckle in the image of the complex object consisting of the background surface and the moving object.

$v_n = 0$, or more precisely, $\lambda/v_n > T > (10\lambda\ell)/(\sigma v)$,

$$B_b(t_1, t_2) \sim |k_b|^2 \left[L^2 - 2\left(\frac{d_o R}{r_c}\right)^2 + \left(\frac{d_o R}{r_c}\right) f_b(t_1 - t_2) \right], \tag{5.23}$$

where

$$f_b(t_1 - t_2) = \begin{cases} \dfrac{d_o R}{r_c} - v_s(t_1 - t_2) & \text{for } t_1 - t_2 \le \dfrac{d_o}{v}, \\ 0 & \text{for } t_1 - t_2 > \dfrac{d_o}{v}; \end{cases}$$

and

$$B_o(t_1, t_2) \sim \left(\frac{\lambda\ell}{\sigma}\right) K_o f_o(t_1 - t_2), \tag{5.23a}$$

where

$$f_o(t_1 - t_2) = d_o^2 \mathrm{sinc}\left[\frac{2\pi d_o v(t_1 - t_2)}{\lambda r_c}\right] \quad \left(\text{with } \frac{\lambda r_c}{d_o} < s \ll d_o\right),$$

d_o is the object size, r_c and $s = vT$ are the distance from the object and its displacement, respectively, and K_o is the intensity coefficient of the object surface reflection.

These results show that in the case of low spatial resolution, the field scattered by the background surface has correlation time $t_b \approx d_o/v$ and the field scattered by the moving object has correlation time $t_o \approx (\lambda r_c)/(d_o v)$, which decreases as the object velocity v increases. Using (5.23) and (5.23a), we can obtain, up to a constant factor, the mean intensity $\langle I \rangle$ of the time-averaged field intensity (measured intensity). Assuming, for simplicity, that the moving object has a flat square form with size d_o, we obtain

$$\langle I \rangle \sim \begin{cases} |k_b|^2 \dfrac{\ell_b}{\sigma_b}(L^2 - d_s^2) + \dfrac{K_o \ell d_o^2}{\sigma} & \text{for } s = vT \ll \dfrac{\lambda r_c}{d_o}, \\ |k_b|^2 (L^2 - d_s^2) & \text{for } \dfrac{\lambda r_c}{d_o} \ll s = vT \ll d_o, \\ |k_b|^2 \dfrac{\ell_b}{\sigma_b}\left(L^2 - \dfrac{4d_s^2}{3}\right) & \text{for } s = vT \approx d_o, \\ |k_b|^2 \dfrac{\ell_b}{\sigma_b}(L^2 - 2d_s^2) & \text{for } s = vT \gg d_o. \end{cases} \tag{5.24}$$

Here, $d_s = (d_o R)/r_c$ is the size of the object's shadow on the background surface, and R and r_c are distances to the background surface and the moving object, respectively.

Physically, these results imply that the scattered rays from the entire moving object reaching the imaging system aperture (Fig. 5.12) have the Doppler frequency spread $\sim (d_o v)/(\lambda r_c)$. Then, for $T \gg (\lambda r_c)/(d_o v)$, the phase of the field scattered by the moving object varies within a range that is significantly larger than 2π. As a result, after time averaging this field, its intensity I is significantly smaller than the signal from the background surface. According to another interpretation of this intensity reduction, the coherent field scattered by the object is speckled (Sec. 1.6), with speckle size being $(\lambda r_c)/(d_o v)$. When the object moves by a distance s, which is larger than the speckle size, the speckle leaves the receiving system aperture and the signal from the object becomes significantly weaker. In the course of the object's motion, it screens different parts of the field scattered by the background surface—so as the object is displaced by its size, the field distribution changes completely.

For this reason, the correlation time of the signal from the background is $t_b \approx d_o/v$, which is in complete agreement with the form of the correlation function $B_b(t_1, t_2)$ from Eq. (5.23). Hence, as the object moves by $s \gg d_o$, the intensity I of the time-averaged field is noticeably reduced compared to its value in the case of a stationary object. This is obvious from the comparison of the relations for I in Eq. (5.24) in the cases of $d_o \gg s \gg (\lambda r_c)/d_o$ and $s \gg d_o$. This reduction takes place even in the presence of a nonresolvable, moving, weakly scattering object.

5.6 Time background intensity holography

5.6.1 Introduction

In Sec. 5.2 we considered time background holography, in which the field in the object image undergoes a Fourier–Fresnel time transform with the kernel $\exp(i\omega t + i\beta t^2)$, where the frequency ω and the deviation β are the transform parameters and t is time. In practice, however, it is not easy to record the field scattered by a remote object and the surrounding background. It is much easier to determine the intensity distribution in the object's image. It is well known that instantaneous distribution provides determination of the object's shape[12] but not its dynamic parameters. In this section, we show that the Fourier–Fresnel time transform of the intensity distribution in a coherent image can be used to determine the parameters of the object motion and the distributions of velocities and accelerations of parts of the object surface if the imaging system resolution is high. In the case of a low-resolution imaging system, this technique can be used to detect the moving object and to generate its two-dimensional speckle pattern, which is the autocorrelation function of its high-quality image.

5.6.2 Theory

The squared modulo of the Fourier–Fresnel transform (the Fourier–Fresnel time filtration) averaged over the object's surface roughness (Fig. 5.18) can be written in the form

$$F(\omega, \beta) = \left\langle \left| \frac{1}{T} \int_{t_0}^{t_0+T} |E_\Sigma(\delta, t)|^2 \exp(i\omega t + i\beta^2)t \right|^2 \right\rangle,$$

where $E_\Sigma(\delta, t) = E(\delta, t) + E_b(\delta, t)$; $E(\delta, t)$ is the field in the coherent image of the moving object, $E_b(\delta, t)$ is the field in the coherent image of the fixed background surface, δ is the radius vector in the image plane, $\langle\rangle$ is the averaging operation, and t_0 and T are the initial time and the observation period, respectively. Assuming that the statistics of this field are Gaussian, which is true when the surface roughness is not resolved by the imaging system, we obtain

$$F = F_0 + F_1, \text{ where } F_0 = \left| \frac{1}{T} \int_{t_0}^{t_0+T} \langle |E_\Sigma(\delta, t)|^2 \rangle \exp(i\omega t + i\beta t) dt \right|^2,$$

and

$$F_1 = \frac{1}{T^2} \int_{t_0}^{t_0+T} \int_{t_0}^{t_o+T} |\langle E_\Sigma(\delta, t_1) E_\Sigma^*(\delta, t_2) \rangle|^2 dt_1 dt_2.$$

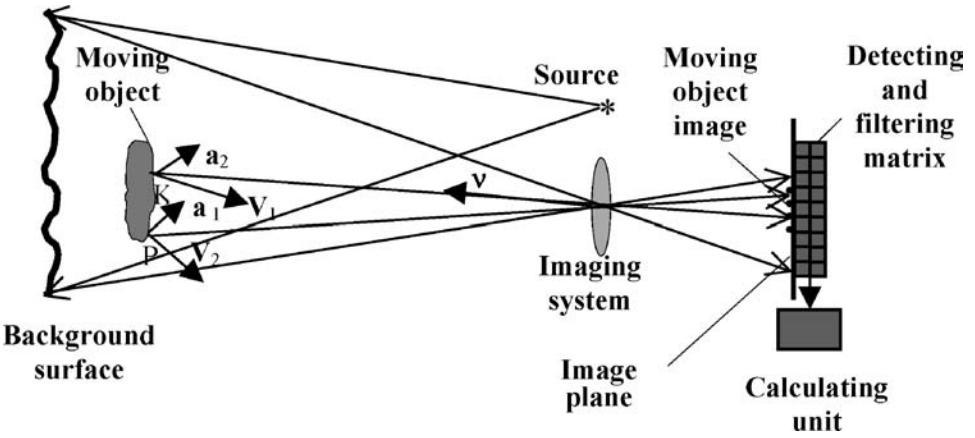

Figure 5.18 Time background intensity holography in the case of a high-resolution imaging system. The detecting and filtering matrix is used for determining, by means of the Fourier–Fresnel transform, the frequency ω and the deviation β, which is necessary for the calculation of the velocity and acceleration of various surface parts. For example, part K of the surface has velocity v_1 and acceleration a_1, and part P has velocity v_2 and acceleration a_2. Here, $\boldsymbol{\nu}$ is the unit vector in the direction of a chosen part of the moving object surface or the background surface.

One can show[84] that

$$\langle E_\Sigma(\delta, t_1)E_\Sigma^*(\delta, t_2)\rangle = \int [k_i(\boldsymbol{\nu}) + k_b(\boldsymbol{\nu})]|h(\boldsymbol{\nu}, \delta)|^2 \times \exp\{i[\hat{\omega}(t_1 - t_2) + i\hat{\beta}(t_1 - t_2)^2]\}d\boldsymbol{\nu}, \quad (5.25)$$

where $\boldsymbol{\nu} = \mathbf{r}_b/R$ on the background surface and $\boldsymbol{\nu} = \mathbf{r}/r_c$ on the surface of the moving object, $\mathbf{r}_b$ is the radius vector of the background surface, R is the distance from the background surface, $\mathbf{r}$ is the radius vector of the moving object surface, $r_c = |\mathbf{r}_c|$, $\mathbf{r}_c$ is the radius vector of the moving object center of mass, $k_i(\boldsymbol{\nu})$ is the function that depends on the moving object surface shape and the distribution of the reflection coefficient on the object surface, $k_b(\boldsymbol{\nu})$ is the distribution of the reflection coefficients on the background surface, $h(\boldsymbol{\nu}, \delta)$ is the pulse response of the imaging system, $\hat{\omega}(\mathbf{r}) = (2\pi/\lambda)\mathbf{q}_c \cdot [\mathbf{v}_c + \mathbf{v}_n(\mathbf{r})]$ and $\hat{\beta}(\mathbf{r}) = (2\pi/\lambda)\mathbf{q}_c \cdot [\mathbf{a}_c + \mathbf{a}_n(\mathbf{r})]$, where $\mathbf{q}_c = 2\mathbf{r}_c/r_c$, $\mathbf{v}_c$ and $\mathbf{a}_c(\mathbf{r})$ are velocity and acceleration of the center of gravity, and $\mathbf{v}_n(\mathbf{r})$ and $\mathbf{a}_n(\mathbf{r})$ are distributions of velocities and accelerations over the object surface. From relation (5.25) we see that the summand F_0 provides no information on the object's motion parameters, so it is independent of time. Therefore, let us concentrate on the summand F_1. For simplicity, let the moving object be opaque. Then, taking into account that the background surface is fixed ($\hat{\omega} = \hat{\beta} = 0$), we have $F_1 = F_i + F_b$, where

$$F_i(\omega, \beta, \delta) = \iint [k_i(\mathbf{r}_1)k_i(\mathbf{r}_2)|h(\mathbf{r}_1, \delta)h^*(\mathbf{r}_2, \delta)|\Theta_i(\mathbf{r}_1, \mathbf{r}_2, \omega, \beta)|^2 d\mathbf{r}_1 d\mathbf{r}_2,$$

$$\Theta_i(\omega, \beta) = \frac{1}{T} \int_{t_0}^{t_0+T} \exp\{i[\hat{\omega}(\mathbf{r}_1) - \hat{\omega}(\mathbf{r}_2) + \omega]t + i[\hat{\beta}(\mathbf{r}_1) - \hat{\beta}(\mathbf{r}_2) + \beta]t^2\},$$

$$F_b(\omega, \beta, \delta) = |\Theta_b(\omega, \beta)|^2 \iint k_i^2(\mathbf{r}_1)|h(\mathbf{r}_1, \delta)|^4 d\mathbf{r}_1 d\mathbf{r}_2,$$

and

$$\Theta_b(\omega, \beta) = \frac{1}{T} \int_{t_0}^{t_0+T} \exp(i\omega t + i\beta t^2) dt.$$

For a sufficiently large T, the function $\Theta_b(\omega, \beta)$ has a sharp maximum at $\omega = \beta = 0$, with unity height. Hence, in this case, the filtered frequency ω and deviation β at each point of the background surface image are equal to zero, and

$$F_b(0, 0, \delta) = \left[\int k_i(\mathbf{r})|h(\mathbf{r}, \delta)|^2 d\mathbf{r}\right]^2;$$

$\Theta_i(\omega, \beta, \mathbf{r}_1, \mathbf{r}_2)$ is maximal if $\mathbf{r}_1$ and $\mathbf{r}_2$ satisfy the relations

$$\hat{\omega}(\mathbf{r}_1) - \hat{\omega}(\mathbf{r}_2) + \omega = 0, \quad \hat{\beta}(\mathbf{r}_1) - \hat{\beta}(\mathbf{r}_2) + \beta = 0. \tag{5.26}$$

For $\hat{\omega}T \gg 1$ and $\hat{\beta}T^2 \gg 1$, the function $\Theta_i(\omega, \beta, \mathbf{r}_1, \mathbf{r}_2)$ becomes acute over $\mathbf{r}_1$ and $\mathbf{r}_2$ as compared with the functions $k_i(\mathbf{r}_1)$, $h(\mathbf{r}_1, \delta)$, $k_i(\mathbf{r}_1)$, and $h(\mathbf{r}_1, \delta)$. In this case,

$$F_i(\omega, \beta, \delta) \sim \int k_i(\mathbf{r}_1)k_i(\mathbf{r}_2(\mathbf{r}_1))|h(\mathbf{r}_1, \delta)h^*(\mathbf{r}_2(\mathbf{r}_1), \delta)d\mathbf{r}_1,$$

where $\mathbf{r}_2$ satisfies Eqs. (5.26), which may be linearized by performing a series expansion of $\hat{\omega}(\mathbf{r}_2)$ and $\hat{\beta}(\mathbf{r}_2)$ in the neighborhood of $\mathbf{r}_1 = \mathbf{r}_2$. As a result, we have a set of linear equations for x_2 and y_2:

$$\vartheta_x(x_2 - x_1) + \vartheta_y(y_2 - y_1) + \omega = 0,$$

and

$$\theta_x(x_2 - x_1) + \theta_y(y_2 - y_1) + \beta = 0, \tag{5.26a}$$

where $\vartheta_x = \partial\hat{\omega}/\partial x$, $\vartheta_y = \partial\hat{\omega}/\partial y$, $\theta_x = \partial\hat{\beta}/\partial x$, and $\theta_y = \partial\hat{\beta}/\partial y$ are partial derivatives at the point $x_1 = x_2$, $y_1 = y_2$. Solving the system (5.26a), we have $x_1 = x_2 + \varepsilon, y_1 = y_2 + \gamma$, where

$$\varepsilon = \frac{\beta\vartheta_y - \omega\theta_y}{D},$$
$$\gamma = \frac{\omega\theta_x - \beta\vartheta_x}{D}, \tag{5.27}$$

and

$$D = \theta_y\vartheta_x - \theta_x\vartheta_y.$$

Taking into account relation (5.27), we obtain

$$F_i(\omega, \beta, \delta) \sim \iint |h(x, y, \delta)h^*(x + \varepsilon, y + \gamma, \delta)|^2 k_i(x, y)k_i(x + \varepsilon, y + \gamma)dxdy.$$

In the case of high resolution (Fig. 5.18), where the number of speckles in the image of the moving object and the number of speckles in the image of the background surface are large, then

$$F_i(\omega, \beta, \delta) \sim k_i^2(\mathbf{r} = -r_c\delta/z_i) \iint |h(x, y, \delta)h^*(x + \varepsilon, y + \gamma, \delta)|^2 dxdy,$$

and

$$F_b(\omega, \beta, \delta) \sim |\Theta_b(\omega, \beta)|^2 k_b^2(\mathbf{r} = -R\delta/z_i) \iint |h(x, y, \delta)|^4 dxdy|\Theta_b(\omega, \beta)|^2,$$

where z_i is the distance from the imaging system aperture to the image plane, and $\Theta_b(0, 0) = 1$. For $\omega > 10/T$ and $\beta > 10/T^2$, $|\Theta_b(\omega, \beta)|^2 \ll 1$. Yet, F_b is proportional to the squared mean intensity distribution $I(\delta)$ in the coherent image of the background surface. Therefore, for frequency $\omega > 10/T$ and the deviation $\beta > 10/T^2$, the intensity $I(\delta)$ is equal to zero at each point of the background image outside of the image of the moving object. At the same time, F_i is proportional to the squared mean intensity distribution in the coherent image of the moving object Θ_i for $\omega > 10/T$, $\beta > 10/T^2$, which is not equal to zero. Hence, within the image of the moving object, the intensity $I(\delta)$ is not equal to zero. For a Gaussian pupil function of the imaging system,[84]

$$F_i(\omega, \beta, \delta) \sim k_i^2\left(\mathbf{r} = -\frac{r_c}{z_i}\right) \exp\left[-\frac{4\pi^2(\varepsilon^2 + \beta^2)d_\rho^2}{(\lambda r_c)^2}\right]. \tag{5.28}$$

Let us see how this result can help determine the parameters of an object. Assume that the object is a solid body rotating with a constant angular velocity $\mathbf{\Omega}$ and $\mathbf{v}_c = \mathbf{a}_c = 0$. In the frame of coordinates (x, y, z) such that the z axis goes along the vector $\mathbf{\Omega}$ and the x axis is normal to the vectors $\mathbf{\Omega}$ and $\mathbf{q}_c$,

$$\hat{\omega} = \frac{2\pi\boldsymbol{\Omega}\sin\alpha}{\lambda},$$
$$\hat{\beta} = \frac{\pi\boldsymbol{\Omega}^2\sin\alpha}{\lambda}, \tag{5.29}$$
$$\varepsilon = \frac{\lambda\omega}{2\pi\boldsymbol{\Omega}\sin\alpha},$$

and

$$\gamma = \frac{\lambda\beta}{\pi\boldsymbol{\Omega}^2\sin\alpha},$$

where α is the angle between the vectors $\boldsymbol{\Omega}$ and $\mathbf{q}_c$. By virtue of relations (5.28) and (5.29),

$$F_i(\omega, \beta, \delta) \sim k_i^2\left(\mathbf{r} = -\frac{r_c}{z_i}\right)\exp\left[-\frac{(\omega^2 + \beta^2/\boldsymbol{\Omega}^2)d_\rho^2}{r_c^2\boldsymbol{\Omega}^2\sin\alpha}\right].$$

At each point of the moving object image, let us find the half-width ω_h of the function F_i over ω for $\beta = 0$, and the half-width β_h of the function F_i over β for $\omega = 0$. Then, we have $\boldsymbol{\Omega} = \beta_h/\omega_h$ and $\alpha = \arcsin[(\omega_h d_\rho)^2/(r_c\beta_h)^2]$. Relations (5.28) are also useful for determining the distributions of velocities and accelerations $\mathbf{v}_n(\mathbf{r})$ and $\mathbf{a}_n(\mathbf{r})$ over the deformed object surface with the help of time background intensity holography (Fig. 5.18). Yet, a drawback of this method is that the value $\varepsilon^2 + \beta^2$ in relation (5.27) is nonlinear in $\mathbf{v}_n(\mathbf{r})$ and $\mathbf{a}_n(\mathbf{r})$; it depends on the filtered frequency ω and deviation β. Application of time background holography to determine their distributions is preferable in this case. In the case of a low-resolution imaging system, for an arbitrary point of the image plane (Fig. 5.19) we

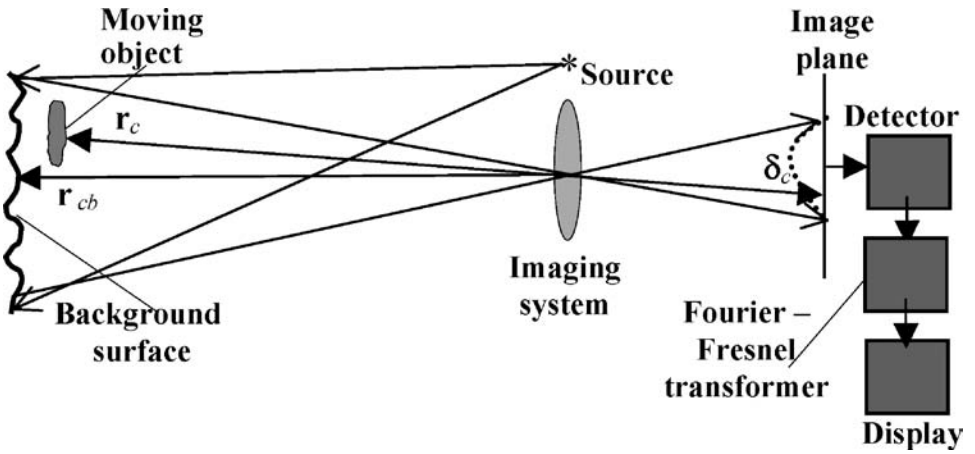

Figure 5.19 Time background intensity holography in the case of a low-resolution imaging system. The dotted line denotes the intensity distribution in the image plane.

have

$$F_i(\omega, \beta, \boldsymbol{\delta}) \sim |h(\mathbf{r} = \mathbf{r}_c, \boldsymbol{\delta})|^4 \iint k_i(x, y) k_i(x + \varepsilon, y + \gamma) dx dy, \quad (5.30)$$

and

$$F_b(\omega, \beta, \boldsymbol{\delta}) \sim |h(\mathbf{r} = \mathbf{r}_c, \boldsymbol{\delta})|^4 \iint k_b^2(x, y) dx dy |\Theta_b(\omega\beta)|^2. \quad (5.31)$$

At the point δ_c optically conjugated to the center of mass of the moving object $\mathbf{r}_c$, $h(\mathbf{r}_c, \boldsymbol{\delta_c}) = 1$ (Fig. 5.19) and

$$F_i(\omega, \beta, \boldsymbol{\delta}) \sim \iint k_i(x, y) k_i(x + \varepsilon, y + \gamma) dx dy, \quad (5.32)$$

and

$$F_b(\omega, \beta, \boldsymbol{\delta}) \sim \iint k_b^2(x, y) dx dy \Theta_b(\omega\beta). \quad (5.33)$$

Finally, as a result of the Fourier–Fresnel time transform of the intensity $|E(\delta_c, t)|^2$ formed by the detector (Fig. 5.19), we see the distribution on the display having average values $F(\omega, \beta) = F_i(\omega, \beta, \delta_c) + F_b(\omega, \beta, \delta_c)$. Here, the function $F_b(\omega, \beta, \delta_c)$ is localized within the area $\omega \approx 1/T$, $\beta \approx 1/T^2$ around the point $\omega = \beta = 0$ and the function $F_i(\omega, \beta, \delta_c)$ is the averaged two-dimensional image of the moving object, which, for a sufficiently large T, occupies a larger area than the function $F_b(\omega, \beta, \delta_c)$. One can show that the realization of this pattern has a speckle structure with speckle area $\sim 1/T^3$ and number of speckles $M \approx \omega_b \beta_b T^2$, where ω_b and β_b are the "effective sizes" of the two-dimensional image in the coordinate plane (ω, β).

It is interesting to note that relation (5.32) gives a two-dimensional image of the moving object, and in the coordinates ε and γ it can be represented as the autocorrelation function of the image, $F_i(\omega, \beta, \boldsymbol{\delta}) \sim \iint k_i(x, y) k_i(x + \varepsilon, y + \gamma) dx dy$. In particular, if the rotating object is a rough sphere with the reflection coefficient constant over the surface, its two-dimensional pattern is

$$F_i(\omega, \beta, \boldsymbol{\delta}) \sim \exp\left[\frac{-(\varepsilon^2 + \gamma^2)}{d_e^2}\right], \quad (5.34)$$

where $d_e = \rho_o \sigma / \ell$ is the effective size of the backscattering area, ρ_o is the sphere radius, and

$$\varepsilon = \frac{\lambda\omega}{2\pi\boldsymbol{\Omega}\sin\alpha}, \quad \gamma = \frac{\lambda\beta}{\pi\boldsymbol{\Omega}^2\sin\alpha}. \quad (5.35)$$

From relation (5.34), we obtain $d_s = (\lambda\omega_h)/(\pi\mathbf{\Omega}^2)$, where, as above, ω_h is the half-width of the function F_i over ω for $\beta = 0$, which is equal to the "effective size" ω_b of the two-dimensional image of the rotating object. Hence, $\omega_b \approx (2\pi\mathbf{\Omega}\sin\alpha)/(\lambda d_s)$. From relations (5.34) and (5.35), we obtain another "effective size," $\beta_b = 2\omega_b\mathbf{\Omega}$. Combining the previous expressions, we can calculate the number of speckles in the two-dimensional image, $M \approx \omega_b\beta_b T^3$, where $\omega_b \approx (2\pi\mathbf{\Omega}\sin\alpha)/(\lambda d_s)$ and $\beta_b = 2\omega_b\mathbf{\Omega}$.

Relations (5.32) and (5.33) can be used for detecting a weakly reflecting moving object in the presence of a bright background surface ($k_b \gg k_i$). One can show that for $\omega \geq 10/T$ and $\beta \geq 10/T^2$, as a rule, $F_b(\omega, \beta, \delta_c) \ll 1$; and if $F_i(\omega, \beta, \delta_c) \approx \iint k_i^2(x, y)dxdy$ exceeds the threshold predetermined by the mean noise level, then the moving object is detected.

Thus, in the case where the object is not resolved in the presence of the background surface, time background intensity holography ensures detection of weakly reflecting and transparent moving objects from the radiation scattered by the bright background surface and forming a two-dimensional speckle pattern given by the autocorrelation function of a high-quality image of the object. It is interesting that the image autocorrelation function also can be obtained via a two-dimensional Fourier space transform of the instantaneous distribution of intensities of the field scattered by the object or, in other terminology, via the Fourier space transform of the object intensity hologram (Sec. 1.3).

In the case of a high-resolution imaging system, time background intensity holography makes it possible to form a high-quality image of a moving deformed object and the background surface along which this object moves, and to determine the velocity and the acceleration of the center of mass and distributions of velocities and accelerations over the object's surface. In addition, this form of holography can be used to select the image of a moving object that is indistinguishable from its background surface.

5.7 Conclusions

1. Time background holography is a prospective new field in remote sensing that provides information about moving objects based on statistical analysis of the temporal and spatial structure of coherent fields scattered by the surrounding background and the objects.
2. In the case of high resolution, time background holography separates the image of an object from the background surface along which it moves, even when the object's surface is similar to the background surface. It also allows one to determine the velocity and acceleration for the object's center of mass and to measure velocity and acceleration distribution on the object's surface. In the case of a low-resolution imaging system , time background holography provides a two-dimensional image of the object.
3. Time background holography ensures reliable detection of moving objects with low reflection or the same reflection as the background surface by using

coherent fields scattered by this surface. This fact is confirmed by experiments with microwaves propagating in air and with ultrasonic waves propagating in water.

4. The method of fast detection of moving objects based on time background holography and on the equal-signal zone principle provides fast measurement of both linear velocities and sizes of objects moving along the background surface and having arbitrary reflection, including the case of weakly reflecting objects. It can be used for reliable detection of clusters of moving, weakly reflecting and transparent pollution particles, for high-accuracy determination of their coordinates, and for measuring concentration, average size, and average velocity of such particles.
5. The method of time averaging of scattered coherent fields as a part of time background holography can be applied effectively for obtaining information about moving objects surrounded by a strongly reflecting background surface; in particular, it can detect moving objects that are indistinguishable from the background surface and determine the standard deviation σ of the moving surface roughness height and its correlation radius ℓ. The method is based on an intensity decrease in the holographic image of a complex object consisting of a moving surface and a stable, randomly inhomogeneous background at places occupied by the moving object. This decrease depends on the time T of recording the hologram and on the ratio σ/ℓ.
6. Time background intensity holography is based on the Fourier–Fresnel time transform of the intensity distribution in the coherent image of the moving object and the surrounding background medium, illuminated by a quasi-monochromatic source with a small coherence length. In the case of a high-resolution imaging system, time background intensity holography enables one to form a high-quality image of a moving deformed object and the background surface along which this object moves, and to determine the velocity and the acceleration of the center of mass and distributions of velocities and accelerations over the object's surface. In addition, this holography method can be used to separate the image of the moving object from the background surface. In the case of a low-resolution imaging system, time background intensity holography provides detection of weakly reflecting and transparent moving objects from the radiation scattered by the bright background surface and the generation of a two-dimensional speckle pattern of the moving object, which is the autocorrelation function of the high-quality image of the object.

Appendix 1

Statistical Characteristics of the Intensity Distribution in a Coherent Image

Consider the statistical characteristics of the intensity distribution in a coherent image $I(\boldsymbol{\delta}) = |E(\boldsymbol{\delta})|^2$, where $E(\boldsymbol{\delta}) = A_i \int k(\mathbf{r}) \exp\{i[\varphi(\mathbf{r}) + 4\pi r/\lambda]\} h(\mathbf{r}, \boldsymbol{\delta}) d\mathbf{r}$ is the complex amplitude of the field in the image plane, $A_i = (E_s S_\rho)/(\lambda r_c z_i)$, E_s is the source field amplitude, S_ρ is the area of the imaging system aperture, r_c is the distance between the object and the imaging system aperture, z_i is the distance between the object's image and the imaging system aperture, $k(\mathbf{r})$ is the distribution of the reflection coefficient on the object's surface, $\varphi(\mathbf{r}) = (2\pi/\lambda) \mathrm{q}_N \xi(\mathbf{r})$ is the phase distribution for the scattered field close to the surface of the object, $\mathrm{q}_N = \mathbf{q} \cdot \mathbf{N}$, $\xi(\mathbf{r})$ is the random distribution of roughness height on the surface of the object, $\mathbf{q} = 2\mathbf{r}/r$, $\mathbf{N}$ is the unit vector normal to the mean surface of the object, $h(\mathbf{r}, \boldsymbol{\delta})$ is the pulse response function of the imaging system, $\mathbf{r}$ is the radius vector on the mean surface of the object, and $\boldsymbol{\delta}$ is the radius vector in the image plane. Let us first analyze the first and second moments of the intensity distribution, $\langle I(\boldsymbol{\delta}) \rangle$ and $\langle I^2(\boldsymbol{\delta}) \rangle$. They can be expressed in terms of the second and the fourth moments of the field $E(\boldsymbol{\delta})$ in the coherent image:

$$\langle I(\boldsymbol{\delta}) \rangle = \left\langle |E(\boldsymbol{\delta})|^2 \right\rangle = \iint |E(\boldsymbol{\delta})|^2 w_2(\xi_1, \xi_2) d\xi_1 d\xi_2,$$

and

$$\left\langle I(\boldsymbol{\delta})^2 \right\rangle = \left\langle |E(\boldsymbol{\delta})|^4 \right\rangle = \iiiint |E(\boldsymbol{\delta})|^4 w_4(\xi_1, \xi_2, \xi_3, \xi_4) d\xi_1 d\xi_2 d\xi_3 d\xi_4,$$

where $w_2(\xi_1, \xi_2)$ and $w_4(\xi_1, \xi_2, \xi_3, \xi_4)$ are, respectively, the two-dimensional and the four-dimensional probability densities of roughness height $\xi(\mathbf{r})$ for the surface (see Sec. 1.2). The brackets $\langle \ldots \rangle$ and the integrals denote averaging $I(\boldsymbol{\delta})$ and $I(\boldsymbol{\delta})^2$ over various realizations of $\xi(\mathbf{r})$.

For simplicity, let the rough object under study be flat and orthogonal to the optical axis of the imaging system. In this case, $\varphi(\mathbf{r}) = [4\pi\xi(\mathbf{r})]/\lambda$. First, note that the function $f_2(\mathbf{r}_1, \mathbf{r}_2) = \exp\{i[\varphi(\mathbf{r}_1) - \varphi(\mathbf{r}_2)]\}$ achieves its maximal value, equal to unity, on the plane $\mathbf{r}_1 = \mathbf{r}_2$; and the function $f_4(\mathbf{r}_1, \mathbf{r}_2, \mathbf{r}_3, \mathbf{r}_4) = \exp\{i[\varphi(\mathbf{r}_1) -$

$\varphi(\mathbf{r}_2) + \varphi(\mathbf{r}_3) - \varphi(\mathbf{r}_4)]\}$ achieves its maximal value, also equal to unity, on two hyperplanes, $(\mathbf{r}_1 = \mathbf{r}_2, \mathbf{r}_3 = \mathbf{r}_4)$ and $(\mathbf{r}_1 = \mathbf{r}_4, \mathbf{r}_2 = \mathbf{r}_3)$. Under the condition that the standard deviation of roughness height is much larger than the wavelength, $\sigma \gg \lambda$, the functions f_2 and f_4 have sharp peaks in the vicinities of these planes. As a result, they can be approximated as follows:

$$f_2 \approx \exp\{i[\varphi'_{x_1}(x_1 - x_2) + \varphi'_{y_1}(y_1 - y_2)]\},$$

and

$$f_4 \approx \exp\{i[\varphi'_{x_1}(x_1 - x_2) + \varphi'_{y_1}(y_1 - y_2) + \varphi'_{x_3}(x_3 - x_4) + \varphi'_{y_3}(y_3 - y_4)]\} + \exp\{i[\varphi'_{x_1}(x_1 - x_4) + \varphi'_{y_1}(y_1 - y_4) + \varphi'_{x_3}(x_2 - x_3) + \varphi'_{y_3}(y_2 - y_3)]\}.$$

Let $\xi(\mathbf{r})$ have Gaussian distribution with zero mean value, $\xi(\mathbf{r})\rangle = 0$. In this case, it follows from Eqs. (1.12) and (1.13) that

$$w_n(\xi_1, \ldots, \xi_n) = \frac{1}{(2\pi)^{n/2}\sqrt{\det(B_{jk})}} \exp\left(-\frac{1}{2}\sum_{j,k=1}^{n} W_{jk}\xi_j\xi_k\right),$$

where $(W_{jk}) = (B_{jk})^{-1}$ is the matrix inverse to the correlation matrix:

$$\sum_{k=1}^{n} W_{jk}B_{km} = \delta_{jm}, \quad B_{jk} = \langle \xi_j\xi_k\rangle.$$

Then, taking into account the Gaussian distribution of $\xi(\mathbf{r})$, it is not difficult to find that

$$\langle f_2(\mathbf{r}_1, \mathbf{r}_2)\rangle \approx \exp\left[-\frac{16\pi^2}{\lambda^2}\langle(\xi'_{x_1})^2\rangle(x_1 - x_2)^2\right]\exp\left[-\frac{16\pi^2}{\lambda^2}\langle(\xi'_{y_1})^2\rangle(y_1 - y_2)^2\right], \tag{A1.1}$$

and

$$\begin{aligned}\langle f_4(\mathbf{r}_1, \mathbf{r}_2, \mathbf{r}_3, \mathbf{r}_4)\rangle \approx{}& \exp\left\{-\frac{16\pi^2}{\lambda^2}\langle(\xi'_{x_1})^2\rangle[(x_1 - x_2)^2 + (x_3 - x_4)^2]\right\} \\ &\times \exp\left\{\frac{32\pi^2}{\lambda^2}\langle(\xi'_{x_1}\xi'_{x_3})\rangle[(x_1 - x_2)(x_3 - x_4)]\right\} \\ &\times \exp\left\{-\frac{16\pi^2}{\lambda^2}\langle(\xi'_{y_1})^2\rangle[(y_1 - y_2)^2 + (y_3 - y_4)^2]\right\} \\ &\times \exp\left\{\frac{32\pi^2}{\lambda^2}\langle(\xi'_{y_1}\xi'_{y_3})\rangle[(y_1 - y_2)(y_3 - y_4)]\right\}\end{aligned}$$

$$+\exp\left\{-\frac{16\pi^2}{\lambda^2}\langle(\xi'_{x_1})^2\rangle[(x_1-x_4)^2+(x_2-x_3)^2]\right\}$$
$$\times\exp\left\{\frac{32\pi^2}{\lambda^2}\langle(\xi'_{x_1}\xi'_{x_3})\rangle[(x_1-x_4)(x_2-x_3)]\right\}$$
$$\times\exp\left\{-\frac{16\pi^2}{\lambda^2}\langle(\xi'_{y_1})^2\rangle[(y_1-y_4)^2+(y_2-y_3)^2]\right\}$$
$$\times\exp\left\{\frac{32\pi^2}{\lambda^2}\langle(\xi'_{y_1}\xi'_{y_3})\rangle[(y_1-y_4)(y_2-y_3)]\right\}. \quad \text{(A1.2)}$$

Furthermore, taking into account Eq. (A1.2), under the assumption that the roughness standard deviation of the object under study $\sigma \gg \lambda$, the surface roughness is isotropic, and hence, the correlation radii of the surface roughness in orthogonal directions satisfy the equation $\ell_x = \ell_y = \ell$, we obtain that

$$\left\langle I^2(\boldsymbol{\delta})\right\rangle = \left\langle |E(\boldsymbol{\delta})|^4\right\rangle = 2A^2\iiiint\exp\left[-\frac{16\pi^2\sigma^2(\mathbf{u}^2+\mathbf{v}^2)}{\lambda^2\ell^2}\right]$$
$$\times\exp\left[-\frac{32\pi^2 B_\gamma(\mathbf{s})}{\lambda^2}\mathbf{uv}\right]h_\omega(\mathbf{r})h_\omega(\mathbf{r}-\mathbf{u}) \quad \text{(A1.3)}$$
$$\times h_\omega(\mathbf{r}-\mathbf{s})h_\omega(\mathbf{r}-\mathbf{s}-\mathbf{v})$$
$$\times k(\mathbf{r})k(\mathbf{r}-\mathbf{u})k(\mathbf{r}-\mathbf{s})k(\mathbf{r}-\mathbf{s}-\mathbf{v})d\mathbf{u}d\mathbf{v}d\mathbf{s}d\mathbf{r},$$

where $\mathbf{s} = (x_1 - x_3, y_1 - y_3)$, $\mathbf{u} = (x_1 - x_2, y_1 - y_2)$, $\mathbf{v} = (x_1 - x_4, y_2 - y_3)$, $B_\gamma(\mathbf{r}_1, \mathbf{r}_3) = \langle\xi'_{x_1}(\mathbf{r}_1)\xi'_{x_3}(\mathbf{r}_3)\rangle = \langle\xi'_{y_1}(\mathbf{r}_1)\xi'_{y_3}(\mathbf{r}_3)\rangle$ is the correlation function of the surface roughness inclination, $\xi'_x = \partial\xi/\partial x$, and $\xi'_y = \partial\xi/\partial y$. Integration in (A1.3) is done within infinite limits since the function $\exp\{-[16\pi^2\sigma^2(\mathbf{u}^2+\mathbf{v}^2)]/(\lambda^2\ell^2)\}$ is sharp at $\sigma \gg \lambda$. Moreover, assuming that the correlation areas of surface roughness and their inclinations are small, expanding the function $\exp[-32\pi^2 B_\gamma(\mathbf{s})\mathbf{uv}/\lambda^2]$ in the exponent under the conditions that $\sigma \gg \lambda$ and $\lambda^2/\ell^2 \ll S_\rho/r_c$, and taking into account Eqs. (A1.1) and (A1.2), we obtain

$$\left\langle I^2\right\rangle = 2\langle I\rangle^2 + 4A^2\int|k(\mathbf{r})h_\omega(\mathbf{r},\boldsymbol{\delta})|^4 d\mathbf{r}\sum_{m=1}^{m=\infty}\frac{1}{\sqrt{m+1}}\int\overline{B}_\gamma^{2m}(\mathbf{s})d\mathbf{s}, \quad \text{(A1.4)}$$

where $\langle I\rangle = A\rho_\varphi^2\int|k(\mathbf{r})h_\omega(\mathbf{r},\boldsymbol{\delta})|^2 d\mathbf{r}$, $\overline{B}_\gamma(\mathbf{s}) = B_\gamma(\mathbf{s})/B_\gamma(0)$, and $\rho_\varphi = (\ell\lambda)/\sigma$ is the correlation radius of the function $\varphi(\mathbf{r})$. Substituting the expression for $\langle I\rangle$ into Eq. (A1.4) and taking into account that

$$\sum_{m=1}^{m=\infty}\frac{1}{\sqrt{m+1}}\int\overline{B}_\gamma^{2m}(\mathbf{s})d\mathbf{s} \approx C_B\ell^2,$$

where the factor $C_B \sim 1$ depends on the form of the correlation function $B_\gamma(\mathbf{s})$, we find that

$$\langle I^2 \rangle = 2\langle I \rangle^2 \left(1 + \frac{1}{N_1}\right), \tag{A1.5}$$

where $N_1 = [C_B \int |k(\mathbf{r})h_\omega(\mathbf{r}, \boldsymbol{\delta})|^4 d\mathbf{r}]/[\int |k(\mathbf{r})h_\omega(\mathbf{r}, \boldsymbol{\delta})|^2 d\mathbf{r}]^2 \approx (S_r/\ell)^2$ is the number of correlation cells within the domain of the object surface resolvable according to the Rayleigh criterion, having the area $S_r = (\lambda^2 r_c^2)/S_\rho$.

The factor C_B depends on the form of the function $B_\gamma(\mathbf{s})$. For instance, if it is represented as a pulse function, which is often used in various simplifying computations, C_B grows infinitely. Therefore, a certain restriction should be imposed on the form of the function. This restriction can be shown to be

$$\int_{-\infty}^{\infty} \overline{B}_\gamma^{2m}(\mathbf{s}) d\mathbf{s} \sim m^{-(1/2+\alpha)},$$

where α is any positive value.[12] These conditions are satisfied in the cases of Gaussian and Lorentzian correlation functions of roughness inclinations ξ'_x and ξ'_y. For the first case, $B_\gamma(\mathbf{s}) = \exp(-|\mathbf{s}|/\ell)$, and for the second one, $B_\gamma(\mathbf{s}) = \exp(-\mathbf{s}^2/\ell^2)$. From Eq. (A1.5), one can obtain the relation for the intensity distribution contrast in a coherent image,

$$C = \frac{\langle I^2 \rangle - \langle I \rangle^2}{\langle I \rangle^2} = 1 + \kappa, \tag{A1.6}$$

where $\kappa \approx C - 1 = 1/N_1$. If the random field $E(\boldsymbol{\delta})$ has Gaussian distribution, then the intensity I satisfies the well-known relation $\langle I^2 \rangle = 2\langle I \rangle^2$.[10] The value κ describes deviations of the random field distribution $E(\boldsymbol{\delta})$ from Gaussian distribution.

From Eq. (A1.6) we see that for a flat rough object, when $N_1 \gg 1$, $\langle I^2 \rangle = 2\langle I \rangle^2$ and $C = 1$. It is interesting to note that similar results can be obtained for an object with arbitrary shape, including a nonflat object, by using the following approximations:

$$\begin{aligned} \langle \exp\{i[\varphi(\mathbf{r}_1) - \varphi(\mathbf{r}_2)]\} \rangle &\approx \rho_\varphi^2 \delta(\mathbf{r}_1 - \mathbf{r}_2), \\ \langle \exp\{i[\varphi(\mathbf{r}_1) - \varphi(\mathbf{r}_2) + \varphi(\mathbf{r}_3) - \varphi(\mathbf{r}_4)]\} \rangle &\approx \rho_\varphi^4 [\delta(\mathbf{r}_1 - \mathbf{r}_2)\delta(\mathbf{r}_3 - \mathbf{r}_4) \\ &\quad + \delta(\mathbf{r}_1 - \mathbf{r}_4)\delta(\mathbf{r}_2 - \mathbf{r}_3)], \end{aligned} \tag{A1.7}$$

where $\delta(\mathbf{r})$ is the delta-function, and $\rho_\varphi = (\ell\lambda)/\sigma$ is the correlation radius of $\varphi(\mathbf{r}_1)$. Taking into account relation (A1.7), let us rewrite the field complex amplitude as $E(\boldsymbol{\delta}) = \int \psi(\mathbf{r}) h(\mathbf{r}, \boldsymbol{\delta}) d\mathbf{r}$, where $\psi(\mathbf{r})$ is a certain random function satisfying the relation

$$\langle \psi(\mathbf{r}_1) \psi * (\mathbf{r}_2) \rangle = A I_i(\mathbf{r}_1) \delta(\mathbf{r}_1 - \mathbf{r}_2),$$

$$\langle \psi(\mathbf{r}_1)\psi*(\mathbf{r}_2)\psi(\mathbf{r}_3)\psi*(\mathbf{r}_4)\rangle = A^2 I(\mathbf{r}_1)I(\mathbf{r}_3)[\delta(\mathbf{r}_1-\mathbf{r}_2)\delta(\mathbf{r}_3-\mathbf{r}_4) + \delta(\mathbf{r}_1-\mathbf{r}_4)\delta(\mathbf{r}_2-\mathbf{r}_3)],$$

where A is a constant value, $\delta(\mathbf{r})$ is a delta-function, and $I_i(\mathbf{r})$ is a function proportional to the average intensity in the high-resolution image $I(\boldsymbol{\delta}) = \langle I(\mathbf{r} = -\mu\boldsymbol{\delta})\rangle$, where $\mu = r_c/z_i$ is the scaling factor. In Sec. 2.3 it is shown that $I_i(\mathbf{r}) \sim k_i(\mathbf{r}) = (\ell^2/\sigma^2)|k(\mathbf{r})|^2 \exp -[\ell^2(\mathrm{q}^2 - \mathrm{q}_N^2)]/(\sigma^2 \mathrm{q}_N^2)$. With the help of the preceding relations, it is easy to obtain the relations $\langle I^2\rangle = 2\langle I\rangle^2$ and $C = 1$. This is a simple phenomenological model. In this model, for instance, we cannot find the dependence of $I(\boldsymbol{\delta})$ on the surface roughness parameter.

Appendix 2

Statistical Characteristics of the Intensity Distribution in a Fourier-Telescopic Image and the Resolution of Fourier Telescopy

Let us refer to relation (4.1), which describes the field scattered by an object, and rewrite it as

$$E(\boldsymbol{\rho}, t) = \exp[i\psi_r(\boldsymbol{\rho})]\frac{E_t S_t}{\lambda^2 r_c^2}\int \Psi(\mathbf{r})u(\mathbf{r}, t)d\mathbf{r}, \tag{A2.1}$$

where

$$u(\mathbf{r}, t) \approx \sum_{n=1}^{n=N} u_n\left(t - \frac{2r}{c}\right)D_n(\mathbf{r})\exp i\left[\omega_n t - 2\frac{\omega_n r}{c} + \frac{\omega_n \mathbf{r}\cdot(\boldsymbol{\rho}_n + \boldsymbol{\rho})}{2r_c c}\right],$$

accounting for the influence of the atmosphere on the direction diagrams of transmitters, $D_n(\mathbf{r}) = (1/S_t)\int A_n(\boldsymbol{\rho}_t)\exp[i\psi_{na}(\boldsymbol{\rho}_t)]\exp[i(2\pi\mathbf{r}\cdot\boldsymbol{\rho}_t)/(\lambda r_c)]d\boldsymbol{\rho}_t$ is the nth transmitter directional diagram, $\boldsymbol{\rho}_t$ is the radius vector of the transmitting apertures, $A_n(\boldsymbol{\rho}_t)$ is the pupil function for the nth transmitter, u_n the pulse shape for the nth transmitter, $\mathbf{r}$ is the radius vector of the mean surface of the object under study, N is the number of transmitters, and $\Psi(\mathbf{r})$ is a function determined by the roughness parameters, reflection characteristics, and the shape of the object surface. The random phase shift distribution on the aperture of the nth transmitter, $\psi_{na}(\boldsymbol{\rho}_t)$, appears due to the radiation propagating from the transmitter to the object, and the random phase shift on the receiving aperture, $\psi_r(\boldsymbol{\rho})$, appears due to the radiation propagating from the object to the receiving aperture. Furthermore, we assume that all pulses have the same shape, $u_n = u_1$, and the phase closure algorithm of the phase errors eliminating $\psi_{na}(\boldsymbol{\rho}_t)$ is performed preliminarily.

Assuming that the pulse width of the illuminating radiation from all transmitters is much longer than the depth of the illuminated surface of the object, under phase compensation conditions, and with an account for relation (A2.1), the correlation function of the intensity distribution in the image is

$$B(\delta_1, \delta_2) = \langle I(\delta_1)I(\delta_2)\rangle - \langle I(\delta_1)\rangle\langle I(\delta_2)\rangle = A^4u^4\left(t - \frac{2r_c}{\mathrm{c}}\right)$$
$$\times \frac{1}{N_p^2}\iiiint \langle \Psi(\mathbf{r}_1)\Psi^*(\mathbf{r}_2)\Psi(\mathbf{r}_3)\Psi^*(\mathbf{r}_4)\rangle$$
$$- \langle \Psi(\mathbf{r}_1)\Psi^*(\mathbf{r}_2)\rangle\langle \Psi(\mathbf{r}_3)\Psi^*(\mathbf{r}_4)\rangle$$
$$\times w(\mathbf{r}_1 - \mathbf{r}_2)w(\mathbf{r}_3 - \mathbf{r}_4)D(\mathbf{r}_1)D^*(\mathbf{r}_2)D(\mathbf{r}_3)D^*(\mathbf{r}_4)$$
$$\times \sum_{m_1,n_1,m_2,n_2} \exp\frac{i\pi}{r_c\lambda}\left(\mathbf{r}_1 \cdot \boldsymbol{\rho}_{m_1} - \mathbf{r}_2 \cdot \boldsymbol{\rho}_{n_1}\right)$$
$$\times \exp i\frac{\pi}{r_c\lambda}\left(\mathbf{r}_3 \cdot \boldsymbol{\rho}_{m_2} - \mathbf{r}_4 \cdot \boldsymbol{\rho}_{n_2}\right)$$
$$\times \exp i\frac{\pi(\delta_1 \cdot \mathbf{p}_1 - \delta_2 \cdot \mathbf{p}_2)}{r_c\lambda} d\mathbf{r}_1 d\mathbf{r}_2 d\mathbf{r}_3 d\mathbf{r}_4, \tag{A2.2}$$

where

$$\mathbf{p}_i = \boldsymbol{\rho}_{m_i} - \boldsymbol{\rho}_{n_i},\ w(\mathbf{r}_1 - \mathbf{r}_2) = \frac{1}{\mathrm{S}_\rho}\int \exp i\frac{\pi\boldsymbol{\rho} \cdot (\mathbf{r}_1 - \mathbf{r}_2)}{r_c\lambda} d\boldsymbol{\rho},\ \boldsymbol{\rho}_m$$

is the radius vector of the mth laser transmitter, N_p is the number of pairs of transmitters,

$$\langle I(\delta)\rangle = \iint I(\delta)w_2(\xi_1, \xi_2)d\xi_1 d\xi_2,$$

and

$$\langle I(\delta_1)I(\delta_2)\rangle = \iiiint I(\delta_1)I(\delta_2)w_4(\xi_1, \xi_2, \xi_3, \xi_4)d\xi_1 d\xi_2 d\xi_3 d\xi_4,$$

where $w_2(\xi_1, \xi_2)$ and $w_4(\xi_1, \xi_2, \xi_3, \xi_4)$ are, respectively, the two-dimensional and the four-dimensional probability densities of roughness height $\xi(\mathbf{r})$ for the surface (see Sec. 1.2).

If the roughness height standard deviation $\sigma \gg \lambda$, then the following relations obtained in Appendix 1 hold for the function $\Psi(\mathbf{r})$:

$$\langle \Psi(\mathbf{r}_1)\Psi^*(\mathbf{r}_2)\rangle \approx AI_i(\mathbf{r}_1)\delta(\mathbf{r}_1 - \mathbf{r}_2),$$
$$\langle \Psi(\mathbf{r}_1)\Psi^*(\mathbf{r}_2)\Psi^*(\mathbf{r}_3)\Psi(\mathbf{r}_4)\rangle \approx A^2I_i(\mathbf{r}_1)I_i(\mathbf{r}_3)[\delta(\mathbf{r}_1 - \mathbf{r}_2)\delta(\mathbf{r}_3 - \mathbf{r}_4)$$
$$+ \delta(\mathbf{r}_1 - \mathbf{r}_4)\delta(\mathbf{r}_3 - \mathbf{r}_2)], \tag{A2.3}$$

where A is a constant value, $I_i(\mathbf{r})$ is a function proportional to the average intensity in the high-resolution image $\langle I(\mathbf{r} = -\mu\delta)\rangle$, $\mu = r_c/z_i$ is the scaling factor (Chapter 2), r_c is the distance from the object's center of mass, and z_i is the distance between the imaging system aperture and the image plane. The case considered here

is a simple phenomenological model; for instance, we cannot find the dependence of $I(\boldsymbol{\delta})$ on the parameters of the surface roughness. In Sec. 2.3 it is shown that $I_i(\mathbf{r}) \sim k_i(\mathbf{r}) \approx (\ell/\sigma)^2 |k(\mathbf{r})|^2 \exp[-(\ell q_\perp/\sigma q_N)^2]$, where σ and ℓ are the roughness height standard deviation and the correlation radius for the object surface, respectively, and

$$q_N = \mathbf{q}\cdot\mathbf{N}, \qquad q_\perp = \sqrt{\mathbf{q}^2 - q_N^2}, \qquad \mathbf{q} = \frac{2\mathbf{r}_c}{r_c}.$$

The intensity distribution in the Fourier-telescopic image is

$$\begin{aligned} I(\boldsymbol{\delta}) = A^2 u^2 \left(t - \frac{2r_c}{c}\right) |D(\mathbf{r}_c)|^2 \iint \psi(\mathbf{r}_1)\psi^*(\mathbf{r}_2) |w(\mathbf{r}_1 - \mathbf{r}_2)|^2 \\ \times \sum_{m,n} \exp\left[i\left(\frac{\pi}{\lambda r_c}\right)(\mathbf{r}_1\cdot\boldsymbol{\rho}_m - \mathbf{r}_2\cdot\boldsymbol{\rho}_n)\right] \\ \times \exp\left(\frac{i\pi\boldsymbol{\delta}\cdot\mathbf{p}}{\lambda r_c}\right) d\mathbf{r}_1 d\mathbf{r}_2, \end{aligned} \tag{A2.4}$$

where $\mathbf{p} = \boldsymbol{\rho}_m - \boldsymbol{\rho}_n$.

After summing over all m and n, taking into account relations (A2.1–A2.4) and the condition $(\lambda r_c)/d_t > d_o$, where d_o is the object size and d_t the transmitter aperture size, and assuming that the radiation scattered by the object occupies a much larger domain than does the receiving aperture, up to inessential factors we obtain

$$B(\boldsymbol{\delta}_1, \boldsymbol{\delta}_2) \sim |D(\mathbf{r}_c)|^4 \iint I_i^2(\mathbf{r}_1) |w(\mathbf{r}_1 - \mathbf{r}_2)|^2 h(\mathbf{r}_1, \boldsymbol{\delta}_1) h(\mathbf{r}_2, \boldsymbol{\delta}_2) d\mathbf{r}_1 d\mathbf{r}_2,$$

where

$$h(\mathbf{r}, \boldsymbol{\delta}) = h_1(\mathbf{r}, \boldsymbol{\delta}) h_2(\mathbf{r}, \boldsymbol{\delta}),$$

$$h_1(\mathbf{r}, \boldsymbol{\delta}) = \sum_m \exp\left\{ \frac{i[\pi\boldsymbol{\rho}_m\cdot(\mathbf{r}/r_c) + (\boldsymbol{\delta}/z_i)]}{\lambda} \right\},$$

and

$$h_2(\mathbf{r}, \boldsymbol{\delta}) = \sum_n \exp\left\{ \frac{i[\pi\boldsymbol{\rho}_n\cdot(\mathbf{r}/r_c) + (\boldsymbol{\delta}/z_i)]}{\lambda} \right\}.$$

If the directional diagram of the transmitter is much larger than the object's angular sizes and the function $h = h_1 h_2^*$ is much narrower than the function $I(\mathbf{r})$, then using

Eqs. (A2.3) and (A2.4) we obtain

$$\langle I(\delta)\rangle \sim k_i(\mathbf{r} = -\mu\delta),$$

where $\mu = r_c/z_i$ is the scaling factor.

From the mean value and the correlation function of the intensity distribution in the Fourier-telescopic image, one can find the correlation area in the image,

$$S_c = \frac{\int B(\delta_1, \delta_2)d\delta_1}{\langle I^2(\delta_2)},$$

the number of speckles,

$$M = \frac{\left[\int \langle I(\delta)\rangle d\delta\right]^2}{\iint B(\delta_1, \delta_2)d\delta_1 d\delta_2},$$

and the contrast of the intensity distribution, $C = B(\delta, \delta)/\langle \mathrm{I}(\delta)\rangle$.

Moreover, assuming, for simplicity, that the receiving aperture has rectangular shape, consider three important cases:

Case 1: Both sizes of the receiving aperture exceed both sizes of the transmitting aperture. Then,

$$B \sim k_i^2(\mathbf{r} = -\mu\delta_1)|D(\mathbf{r}_c)|^4 h(\mu\delta_1 - \mu\delta_2), \tag{A2.5}$$

where

$$h(\mu\delta_1 - \mu\delta_2) \sim \int h[(\mathbf{r}, \delta_1)h^*(\mathbf{r}, \delta_2)d\mathbf{r}].$$

Case 2: Both sizes of the receiving aperture are smaller than the sizes of the transmitting aperture. Then,

$$B \sim I^2(\mathbf{r} = -\mu\delta_1)|D(\mathbf{r} = -\mu\delta_1)|^4 |w(\delta_1 - \delta_2)|^2. \tag{A2.6}$$

Case 3: One of the sizes (say, x) of the receiving aperture is smaller than the corresponding size of the transmitting aperture, while the other size of the receiving aperture is larger than the corresponding size of the transmitting aperture. Then,

$$B \sim I^2(\mathbf{r} = -\mu\delta_1)|D(\mathbf{r} = -\mu\delta_1)|^4 w(\delta_{1x} - \delta_{2x})h_y(\delta_{1y} - \delta_{2y}), \tag{A2.7}$$

where

$$h_y(\delta_{1y} - \delta_{2y}) \sim \int h_1(x, y_1, 0, \delta_{1y}) h_1(x, y_2, 0, \delta_{2y}) h_2^*(x, y_1, 0, \delta_{1y}) \times h_2^*(x, y_2, 0, \delta_{2y}) dx dy_1 dy_2.$$

Let us now consider the statistical characteristics of the intensity distribution in a Fourier-telescopic image for the case where the transmitting system consists of two orthogonal arrays with equidistant identical laser transmitters. This two-section transmitting aperture forms on the object surface a complete set of sinusoidal gratings with various periods and directions, so that one can select the radiation scattered by the object under its illumination by a pair of transmitters from different sections. The index m numbers transmitters from one section, and the index n numbers transmitters from the other section. Consider a particular case of a two-section structure that can be easily analyzed and that allows the phase closure algorithm. This is a structure consisting of two orthogonal arrays of equidistant identical transmitters. The arrays can intersect (the crossed position) or be tangential (the T-position). The transmitters coordinates in this case are

$$x_m = a(m-1), \quad y_m = 0, \quad x_n = 0, \quad y_n = d_t(n-1), \quad d_t = \frac{d_x}{N_x} = \frac{d_y}{N_y},$$

where d_x and d_y are the sizes of the X- and Y-arrays, and N_x and N_y are the numbers of transmitters in the arrays. In this case, up to inessential factors, the average intensity distribution in the restored image can be represented, after summing over m, n, as

$$\langle I(\boldsymbol{\delta}) \rangle \sim |D(\mathbf{r}_c)|^2 \int k_i(\mathbf{r}) h_x(x, \delta_x) h_y^*(y, \delta_y) dx dy. \tag{A2.8}$$

Here,

$$h_y(y, \delta_y) = \frac{\exp i\varphi_x(2d_{2x}, x, \delta_x) - \exp i\varphi_x(2d_{1x}, x, \delta_x)}{N_x \sin[\varphi_x(d_x, x, \delta_x)/N_x]},$$

and

$$h_y(y, \delta_y) = \frac{\exp i\varphi_y(2d_{2y}, y, \delta_y) - \exp i\varphi_y(2d_{1y}, y, \delta_y)}{N_y \sin[\varphi_y(d_y, y, \delta_y)/N_y]},$$

where $\varphi_x(d, x, \delta_x) = (d\pi/\lambda)(x/r_c + \delta_x/z_i)$ and $\varphi_y(d, y, \delta_y) = (d\pi/\lambda)(y/r_c + \delta_y/z_i)$ are the grating factors, d_{2x} and d_{1x} are the coordinates of the X-array edge points, d_{2y} and d_{1y} are the coordinates of the Y-array end points, $d_{2x} = d_{1x} + d_x$, and $d_{2y} = d_{1y} + d_y$. In particular, for the crossed symmetric position of the arrays for which $d_{2x} = -d_{1x}$, $d_x = 2d_{1x}$ and $d_{2y} = -d_{1y}$, $d_y = 2d_{1y}$,

$$I(\boldsymbol{\delta}) \sim |D(\mathbf{r}_c)|^2 \int k_i(\mathbf{r}) h(\mathbf{r}, \boldsymbol{\delta}) d\mathbf{r}, \tag{A2.9}$$

where $h(\mathbf{r}, \boldsymbol{\delta}) = [(2\pi d_x/\lambda)(x/r_c + \delta_x/z_i)]/\{N \sin[(2N\pi d_x/\lambda)(x/r_c + \delta_x/z_i)]\} \times \sin[(2\pi d_y/\lambda)(x/r_c + \delta_y/z_i)]/\{N \sin[(2N\pi d_y/\lambda)(y/r_c + \delta_y/z_i)]\}$.

One can see that because of the periodicity of the grating factors in (A2.9), the average intensity distribution in the reconstructed image is periodically repeated. In the general case, this can lead to overlapping of the reconstructed images. Overlapping can be avoided if the number of transmitters is chosen so that $N_y > M_y = (d_y d_{iy})/(r_c\lambda) \gg 1$, where d_{iy} is the width of the function $k_i(\mathbf{r})$ along the Y axis, and $N_x > M_x = d_x d_{ix}/(r_c\lambda) \gg 1$, where d_{ix} is the width of the object's image [the function $k_i(\mathbf{r} = -\mu\boldsymbol{\delta})$] along the X axis.

Then, the sine function in the denominators of the grating factors in (A2.8) and (A2.9) can be replaced by its argument; as a result, the denominators can be approximated by a product of two functions of the form $\alpha \exp(ivt)\mathrm{sinc}(\alpha t)$. Under the same conditions, taking into account the relation

$$\int_{-\infty}^{\infty} \alpha \exp(ivt)\mathrm{sinc}(\alpha t)dt = \begin{cases} 1 & \text{for } v \le \alpha \\ 0 & \text{for } v > \alpha \end{cases},$$

we obtain that $\langle I(\boldsymbol{\delta})\rangle \sim |D(\mathbf{r}_c)|^2 k_i(\mathbf{r} = \mu\boldsymbol{\delta}_i)$, where $\mu = r_c/z_i$.

The intensity correlation function of the Fourier-telescopic image for the case of orthogonal arrays of equidistant transmitters can be found from the relation

$$\begin{aligned} B(\boldsymbol{\delta}_1, \boldsymbol{\delta}_2) &= \langle I(\boldsymbol{\delta}_1)I(\boldsymbol{\delta}_2)\rangle - \langle I(\boldsymbol{\delta}_1)\rangle\langle I(\boldsymbol{\delta}_2)\rangle \\ &\sim \int k_i(\mathbf{r}_1)k_i(\mathbf{r}_2)|w(\mathbf{r}_1 - \mathbf{r}_2)|^2 h_x(x_1, \delta_{1x})h_y(y_2 + \delta_{1y}) \\ &\quad \times h_x(x_2, \delta_{2x})h_y(y_1, \delta_{2y})d\mathbf{r}_1 d\mathbf{r}_2. \end{aligned} \tag{A2.10}$$

Let us consider the three cases given above in combination with this position of linear arrays. We will suppose that the receiving and transmitting apertures resolve the details of the object's surface.

Case 1: Both sizes of the receiving aperture are larger than both sizes of the transmitting aperture, $d_{rx} > d_x$, $d_{ry} > d_y$. Then,

$$\begin{aligned} B(\boldsymbol{\delta}_1, \boldsymbol{\delta}_2) &\sim |D(\mathbf{r}_c)|^4 \int k_i^2(\mathbf{r})h_x(x, \delta_{1x})h_y(y + \delta_{1y})h_x(x, \delta_{2x})h_y(y, \delta_{2y})d\mathbf{r} \\ &\sim |D(\mathbf{r}_c)|^4 k_i^2(\mathbf{r} = -\mu\boldsymbol{\delta}_1)h_x(\delta_{1x} - \delta_{2x})h_y(\delta_{1y} - \delta_{2y}). \end{aligned} \tag{A2.11}$$

Here, $h_x(\delta_{1x} - \delta_{2x}) = \mathrm{sinc}[\pi\mu d_x(\delta_{1x} - \delta_{2x})/\lambda]$, and $h_y(\delta_{1y} - \delta_{2y}) = \mathrm{sinc}[\pi\mu d_y \times (\delta_{1y} - \delta_{2y})/\lambda]$. For the same case, the number of speckles in the image and the correlation area are $S_c = (z_i\lambda)^2/(d_x d_y) = \rho_x\rho_y$, and $M = M_x M_y$, where $M_x = (d_{rx}d_{ix})/(z_i\lambda)$, and $M_y = (d_{ry}d_{iy})/(z_i\lambda)$. Here, $\rho_x = (z_i\lambda)/d_x$ and $\rho_y = (z_i\lambda)/d_y$ are

correlation radiuses along the X and Y axes, respectively, and the contrast

$$C = C_1 \approx \frac{d_x d_y}{d_{rx} d_{ry}}. \tag{A2.12}$$

It is convenient to rewrite the number of speckles in the Fourier-telescopic image as $M = (d_x d_y d_{ox} d_{oy})/(\lambda r_c)^2$, where d_{ox} and d_{oy} are the sizes of the object's scattering area. In particular, for a flat rectangular object, $d_{ix} = d_{ox}/\mu$ and $d_{iy} = d_{oy}/\mu$; for a spherical object, $d_{ix} = d_{iy} = (\rho_o \sigma)/(\ell \mu)$, where ρ_o is the object's radius.

Case 2: Both sizes of the receiving aperture are smaller than both sizes of the transmitting aperture: $d_{rx} \le d_x$, $d_{ry} \le d_y$. Then,

$$B(\boldsymbol{\delta}_1, \boldsymbol{\delta}_2) \sim |D(\mathbf{r}_c)|^4 k_i^2 (\mathbf{r} = -\mu \boldsymbol{\delta}_1) |w(\boldsymbol{\delta}_1 - \boldsymbol{\delta}_2)|^2, \tag{A2.13}$$

$C = C_2 \approx 1$, $\rho_x = (z_i \lambda)/d_{rx}$, $\rho_y = (z_i \lambda)/d_{ry}$, $S_c = \rho_{rx} \rho_{ry} = (z_i \lambda)^2/(d_{rx} d_{ry})$, and d_{rx} and d_{ry} are the sizes of the receiving aperture along the X and Y axes. In particular, for a flat rectangular object, $d_{ix} = d_{ox}/\mu$ and $d_{iy} = d_{oy}/\mu$; and the number of speckles in the image is $M = (d_{rx} d_{ry} d_{ox} d_{oy})/(r_c^2 \lambda^2)$. For a spherical object, $d_{ix} = d_{iy} = \rho_o/\mu$ and $M = (\sigma^2 d_{rx} d_{ry} \rho_o^2)/(\ell^2 r_c^2 \lambda^2)$.

Case 3: One of the sizes, say, along the Y axis, of the receiving aperture is smaller than the corresponding size of the transmitting aperture, while the other size of the receiving aperture is larger than the corresponding size of the transmitting aperture, $d_{rx} > d_x$, $d_{ry} < d_y$. Then,

$$B(\boldsymbol{\delta}_1, \boldsymbol{\delta}_2) \sim |D(\mathbf{r}_c)|^4 k_i^2 (\mathbf{r} = -\mu \boldsymbol{\delta}_1) h_x(\delta_{1x} - \delta_{2x}) \operatorname{sinc}\left[\frac{\pi \mu d_r (\delta_{1y} - \delta_{2y})}{\lambda} \right], \tag{A2.14}$$

$\rho_x = (z_i \lambda)/d_x$, $\rho_y = (z_i \lambda)/d_{ry}$, $S_c = \rho_x \rho_y = (z_i \lambda)^2/(d_x d_{ry})$, and $C = C_3 \approx d_x/d_{rx}$. For a flat rectangular object, the number of speckles in the image is $M = (d_x d_{ry} d_{ox} d_{oy})/(r_c^2 \lambda^2)$; for a spherical object, $M = (\sigma^2 d_x d_{ry} \rho_o^2)/(\ell^2 r_c^2 \lambda^2)$. More accurate analysis, which is carried out in Appendix 1, with an account for (A1.1) and (A1.2), gives $C = C_j + \varepsilon_j/N_1$. Here, $N_1 = (\lambda^2 r_c^2)/(d_{rx} d_{ry} \ell^2)$ is the number of correlation pixels in the domain of the object surface resolved, according to the Rayleigh criterion, by means of Fourier-telescopic imaging, and ε_j are constants of the first order. In particular, in the second case, $C = 1 + \varepsilon_2/N_1$. The last relation is similar to relation (A1.5).

The X and Y sizes of the resolvable domain on the object's surface in the Fourier telescopy are related to the correlation radiuses in the plane of the restored image as

$$P_{rx} = \mu\rho_x = \frac{r_c\lambda}{d_x}, \quad P_{ry} = \mu\rho_x = \frac{r_c\lambda}{d_y} \text{ for the first case;}$$

$$P_{rx} = \mu\rho_x = \frac{r_c\lambda}{d_{rx}}, \quad P_{ry} = \mu\rho_x = \frac{r_c\lambda}{d_{ry}} \text{ for the second case;}$$

and

$$P_{rx} = \mu\rho_x = \frac{r_c\lambda}{d_x}, \quad P_{ry} = \mu\rho_x = \frac{r_c\lambda}{d_{ry}} \text{ for the third case.}$$

It is interesting to note that in all cases, the number of resolvable domains on the object's surface is equal to the number of speckles in the Fourier-telescopic image.

Appendix 3

Phase Closure Algorithm in Fourier Telescopy

In this book, the analysis of Fourier telescopy and its applications is limited to the case where the influence of an inhomogeneous atmosphere is either neglected or eliminated. Here, we will briefly consider a method of eliminating the influence of inhomogeneous atmosphere based on the phase closure method. In its modern form, this procedure was suggested in Ref. 56 and was further developed in Refs. 66, 69, 70, 72, and 73. Our consideration will be based on Ref. 56.

As a transmitting system, consider a set of T-shaped linear arrays consisting of similar laser transmitters (N_x transmitters in the X-array, and N_y transmitters in the Y-array in Fig. 4.2; for example, in Fig. A3.1, $N_x = 6$ and $N_y = 9$). The nth transmitter of the X-array illuminates the object at different frequencies ω_n. The mth transmitter of the Y-array illuminates the object at different frequencies ω_m. All transmitters simultaneously illuminate the object so that values $\omega_m - \omega_n$ are also different. For simplicity, we also assume that the atmosphere is smoothly inhomogeneous. This allows us to assume that the additional phase accumulated by the radiation, due to atmospheric influence, on the way from the transmitter to the object's surface is the same for any point of the transmitting aperture. In this case, after a corresponding filtering of the scattered field intensity at frequencies $\omega_m - \omega_n$ [see relation (4.4)], the receiving devices form the values

$$\begin{aligned} G_{mn} &= \exp[i(\psi_{mx} - \psi_{ny})]F_{mn}, \\ G_{xm,m-1} &= \exp[i(\psi_{mx} - \psi_{m-1x})]F_{xm,m-1}, \\ G_{yn,n-1} &= \exp[i(\psi_{ny} - \psi_{n-1y})]F_{yn,n-1}, \end{aligned} \tag{A3.1}$$

where

$$F_{mn} \approx \langle F_{mn} \rangle \sim \frac{|D(\mathbf{r}_c)|^2}{S_e} \int k_i(\mathbf{r}) \exp i \frac{2\pi d_t(xm + yn)}{N r_c \lambda} d\mathbf{r}$$

and

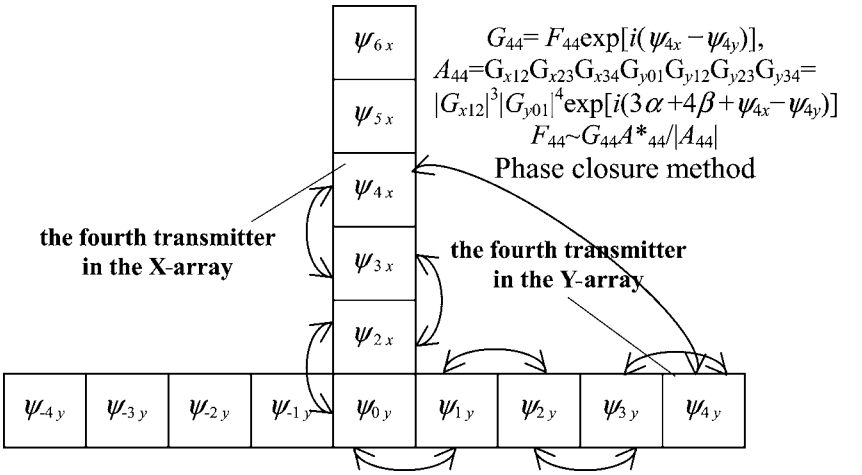

Figure A3.1 An example of reconstructing the Fourier component F_{44} using the phase closure method suggested in Ref. 57. This component is formed by the pair of transmitters shown by a long arc: the fourth transmitter of the first array and the fourth transmitter of the second array. Arcs denote all eight pairs of transmitters participating in the procedure. ψ_{mx} and ψ_{ny} are phase errors accumulated due to radiation propagation in the atmosphere from the transmitters of the X- and Y-arrays to the object. Here, $\psi_{1x} = \psi_{0y}$, $G_{x12} = |G_{x12}| \exp i\alpha$, $G_{y01} = |G_{a01}| \exp i\beta$, and α, β are phases that do not influence the quality of the Fourier-telescopic image.

$$F_{xm,m-1} \sim \frac{|D(\mathbf{r}_c)|^2}{S_e} \int k_i(\mathbf{r}) \exp i\frac{2\pi x}{r_c\lambda} d\mathbf{r},$$

$$F_{yn,n-1} \sim \frac{|D(\mathbf{r}_c)|^2}{S_e} \int k_i(\mathbf{r}) \exp i\frac{2\pi y}{r_c\lambda} d\mathbf{r}$$

are the Fourier components of the object image, d_t is the array size, S_e is the area of the backscattering surface, $\mathbf{r}_c$ is the radius vector of the object's center of mass, $D(\mathbf{r}_c)$ is the value of the transmitter's directional diagram on the object's surface in the absence of the atmospheric influence on the radiation propagation, and

$$k_i(\mathbf{r}) = \frac{l^2}{\sigma^2}|k(\mathbf{r})|^2 \exp\left[-\left(\frac{\ell q_\perp}{\sigma q_N}\right)^2\right] \quad \text{(see Appendix 2).}$$

Here, the indices m and n label transmitters of different linear arrays, and ψ_{mx} and ψ_{ny} are the corresponding phase shifts.

In order to realize the phase closure algorithm, we first filter the value $G_{xm,m-1}$ formed by the beams coming from the mth and the $m-1$st transmitters, then the value $G_{xm-1,m-2}$ formed by the beams coming from the $m-1$st and $m-2$nd transmitters, and so on, to the first and second transmitters of the X-array, then the value formed by the beams coming from the first and the second transmitters of the

Y-array, and so on, up to the value $G_{yn,n-1}$ formed by the beams coming from the nth and the $n-1$st transmitters of the Y-array. Furthermore, we form the value

$$F'_{mn} = \frac{G_{mn}A^*_{mn}}{|A_{mn}|} = F_{mn}\exp[-i(\alpha m + \beta n)],$$

where

$$A_{mn} = \prod_{k=m}^{k=1} G_{xk,k-1} \prod_{j=1}^{j=n} G_{yj+1j} = F^m_{xm,m-1}F^n_{yn,n-1}\exp[i(\psi_{mx} - \psi_{ny})],$$

α and β are phases of the complex functions $F_{xm,m-1}$ and $F_{yn,n-1}$, and the indices k and j relate to transmitters placed on the X- and Y-arrays, respectively.

One can see from the previous relation that reconstruction of the Fourier component F_{mn} of the object image according to the procedure described in Ref. 57 requires $m+n$ pairs of transmitters. For instance (Fig. A3.1), reconstruction of the Fourier component F_{44}, which in the absence of phase shifts ($\psi_{mx} = \psi_{ny} = 0$) would be formed by illuminating the object by the fourth transmitter of the first array and the fourth transmitter of the second array, requires eight pairs of transmitters.

It is interesting to note that the relative fluctuations of a Fourier component are inversely proportional to the number of speckles in the scattered field on the receiving aperture, $M_\rho = (S_\rho)/(\lambda^2 r_c^2)$, where S_ρ is the area of the receiving aperture, r_c is the distance from the object, and S_e is the area of the backscattering surface.[16,73,74] By choosing a sufficiently large number M_ρ, one can make fluctuations of the filtered values G_{mn}, $G_{xm,m+1}$, and $G_{yn,n+1}$ and their products A_{mn} as small as necessary.

Furthermore, by performing an inverse Fourier transform over F'_{mn}, one forms the object's image [see Eq. (4.5)]. One can show that the phases α and β have no noticeable influence on this image. The literature suggests another version of the procedure that allows one to considerably reduce the number of transmitter pairs used to form each Fourier component of the object's image.

Now let us consider in more detail the condition under which the atmosphere can be considered smoothly inhomogeneous. Consider the relative fluctuations η_j of the modulo of the transmitter directional diagram,

$$\eta_n = \frac{\langle |D_n(\mathbf{r}_c)|^2\rangle_\psi - \langle |D_n(\mathbf{r}_c)|^2\rangle^2_\psi}{\langle |D_n(\mathbf{r}_c)|^2\rangle^2_\psi},$$

where $D_n(\mathbf{r}_c)| = (1/S_t)\int A_n(\boldsymbol{\rho}_n)\exp[i\psi_{na}(\boldsymbol{\rho}_n)]\exp[(i2\pi\mathbf{r}_c\cdot\boldsymbol{\rho}_n)/(\lambda r_c)]d\boldsymbol{\rho}_n$ is the nth transmitter directional diagram, $\boldsymbol{\rho}_n$ is the radius vector of the nth transmitter aperture, $A_n(\boldsymbol{\rho}_n)$ is the pupil function for the nth transmitter, $\psi_{na}(\boldsymbol{\rho}_n)$ is the random phase shift distribution on the transmitting aperture of the nth transmitter

accumulated due to radiation propagation in the atmosphere, S_t is the area of the transmitter aperture, and $\mathbf{r}_c$ is the radius vector of the object's center of mass. The brackets $\langle \ldots \rangle_\psi$ denote averaging over various realizations of the random phase shift $\psi_{na}(\boldsymbol{\rho}_n)$ caused by radiation propagating through the atmosphere.

Let $\gamma = (d_t^2 \sigma_\psi^2)/(N^2 \ell_\psi^2) \ll 1$, where σ_ψ and ℓ_ψ are the standard deviation and the correlation radius of the random phase shift $\psi_{na}(\boldsymbol{\rho}_n)$, and hence, the function $\psi_{na}(\boldsymbol{\rho}_n)$ is smooth. Also, let $(\lambda r_c)/d_t \gg d_o$, where d_o is the object's size. Then,

$$D_n(\mathbf{r}_c, \boldsymbol{\nu}) \approx \left(\frac{1}{S_t}\right) \exp i\psi_n \int A_n(\boldsymbol{\rho}_n) \exp\left[i(\boldsymbol{\nu} \cdot \boldsymbol{\rho}_n) + \frac{i(2\pi \mathbf{r}_c \cdot \boldsymbol{\rho}_n)}{\lambda r_c} \right] d\boldsymbol{\rho}_n, \quad \text{(A3.2)}$$

where S_t is the transmitter area, and $\psi_n = \psi_{na}(\boldsymbol{\rho}_n = 0)$ is the total phase shift on the nth transmitter, $\boldsymbol{\nu} = \partial \psi_n(\boldsymbol{\rho}_n)/\partial \boldsymbol{\rho}_n|_{\boldsymbol{\rho}_n = 0}$.

Assuming that $\boldsymbol{\nu}$ has Gaussian distribution with $\langle \boldsymbol{\nu} \rangle_\psi = 0$, and taking into account Eq. (1.14), we have $\langle \boldsymbol{\nu}^2 \rangle_\psi = \sigma_\psi^2/\ell_\psi^2$ and

$$\langle |D_n(\mathbf{r}_c, \boldsymbol{\nu})|^4 \rangle_\psi = \int |D_n(\mathbf{r}_c, \boldsymbol{\nu})|^4 P_\psi(\boldsymbol{\nu}) d\boldsymbol{\nu},$$

$$\langle |D_n(\mathbf{r}_c, \boldsymbol{\nu})|^2 \rangle_\psi = \int |D_n(\mathbf{r}_c, \boldsymbol{\nu})|^2 P_\psi(\boldsymbol{\nu}) d\boldsymbol{\nu},$$

where

$$P(\boldsymbol{\nu}) = \frac{\ell_\psi}{\sqrt{2\pi}\sigma_\psi} \exp\left(-\frac{\boldsymbol{\nu}^2 \ell_\psi^2}{\sigma_\psi^2} \right)$$

is the probability density function of the random value ν. Using Eq. (A3.2) together with the previous relations, approximating the pupil function by a Gaussian dependence, $A_j(\boldsymbol{\rho}) = \exp(-\rho^2/d_t^2)$, and assuming for simplicity that $x_c = y_c = 0$, it is not difficult to obtain that

$$\eta_n = \frac{1 + 2\gamma}{\sqrt{4\gamma + 1}} - 1.$$

Under the condition $\gamma^2 \ll 1$ of a smooth, inhomogeneous atmosphere, $\eta_n \approx \gamma^2$. Hence, under the condition $\gamma^2 \ll 1$, the relative fluctuations η_j of the random variables $|D_n(\mathbf{r}_c)|^2$ are very small. Thus, if σ_ψ and ℓ_ψ satisfy the condition $\gamma^2 = (d_t^4 \sigma_\psi^4)/\ell_\psi^4 \ll 1$—i.e., the atmosphere is smoothly inhomogeneous—then $|D_n(\mathbf{r}_c)|^2 \approx \langle |D_n(\mathbf{r}_c)|^2 \rangle_\psi$. In this case, if all transmitters are similar, $D_n(\mathbf{r}_c) \approx D(\mathbf{r}_c) \exp i\psi_n$, where $D(\mathbf{r}_c)$ is the value of the transmitter's directional diagram on the object's surface in the absence of the atmosphere's influence on the radiation propagation. Then, relations (A3.1) hold.

Appendix 4

The Coherence of Fields Scattered by Sufficiently Large Rough Objects, and the Contrast of the Scattered Field Intensity Distribution

Let us suppose that an object is illuminated by a pointlike radiation source with a narrow spectrum: $\Delta\omega \ll \omega_0$, where $\Delta\omega$ and ω_0 are, respectively, the width and the mean frequency of its spectrum $S_r(\omega)$. In the literature, such sources are usually called quasi-monochromatic.[3] We will consider this notion in more detail. We also assume that the longitudinal size (depth) of the object, L_s, does not exceed 1.5 m, and the testing radiation is practically continuous; more precisely, its pulse width exceeds L_s by at least two orders of magnitude. First, consider a simple example, namely, interference of two spherical waves that appears when radiation is scattered by an object B_1B_2 consisting of two pointlike scatterers.[9] (Fig. A4.1)

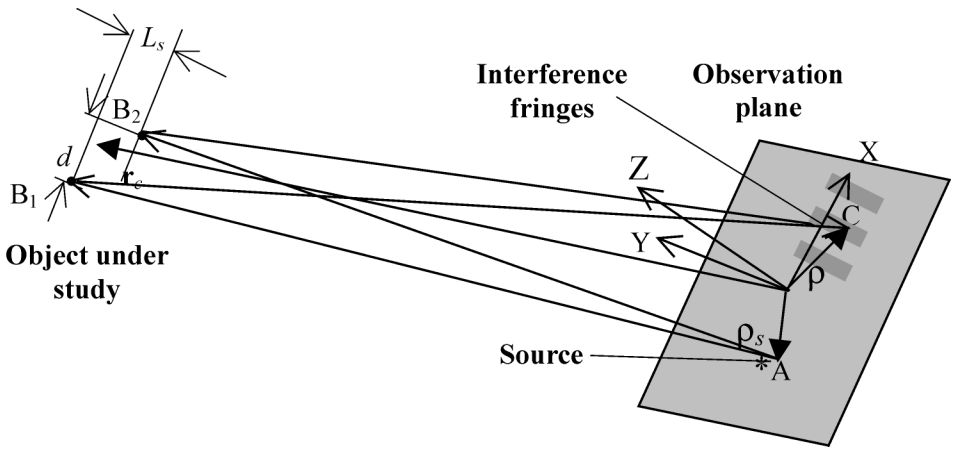

Figure A4.1 Interference of two spherical waves.

The instantaneous intensity distribution for the field $E(\boldsymbol{\rho}, t)$ scattered by the object B_1B_2 can be represented by the form $I(\boldsymbol{\rho}, t) = |E(\boldsymbol{\rho}, t)|^2$, where

$$E(\boldsymbol{\rho}, t) = \sum_{j=1}^{j=N} E_j(\boldsymbol{\rho}, t), \quad N = 2,$$

$$E_j(\boldsymbol{\rho}, t) = \int E_{0j}(\boldsymbol{\rho}, \omega) \exp(-i\omega t) d\omega,$$

$E_{0j}(\boldsymbol{\rho}, \omega) \sim A_j S_r(\omega) H_\omega(\mathbf{r}_j, \boldsymbol{\rho})$, $H_\omega(\mathbf{r}_j, \boldsymbol{\rho}) = \exp\{i[\omega(|\mathbf{r}_j - \boldsymbol{\rho}_s| + |\mathbf{r}_j - \boldsymbol{\rho}|)]/c\}$, A_j is the amplitude of the spherical wave, $\mathbf{r}_j$ is the radius vector of the point B_j, $\boldsymbol{\rho}$ is the radius vector of the observation plane, $\boldsymbol{\rho}_s$ is the source radius vector, and $\mathbf{r}_c$ is the radius vector of the object's center. If the source coherence length $L_c = c/\Delta\omega \ggg L_s$ and $A_1 = A_2$, then $I(\boldsymbol{\rho}, t)$ consists of interference fringes with sinusoidal distribution, the minimum intensity being $I_{\min} = 0$. An important parameter of an interference pattern is the measure of its contrast or, more precisely, the degree to which the intensity distribution differs from constant. This parameter is the *visibility* of interference fringes[9] in the observation plane, $V = (I_{\max} - I_{\min})/(I_{\max} + I_{\min})$, where $I_{\max}$ is the maximum distribution intensity. Since at $L_c \ggg L_s$, $I_{\min} = 0$, then in the case where $A_1 = A_2$, $V = 1$. Let us define the *visibility* of interference fringes under the condition $L_c < 100L_s$, which in reality is most often the case. In practice, one mostly registers the time-averaged intensity distribution

$$\bar{I}(\boldsymbol{\rho}) = \frac{1}{T} \int_{t_0}^{t_0+T} I(\boldsymbol{\rho}, t) dt,$$

where t_0 and T are the initial time and total processing time of the registered signal, respectively.

If $\rho^3/(\lambda^2 r_c) \ll 1$, then, choosing $\boldsymbol{\rho}_s = 0$ and $T \geq 100L_s/c > \Delta\omega^{-1}$, for $L_s =$ 1.5 m, $T \geq 10^{-6}$ sec and for the case where the squared module of the spectrum can be approximated by a Gaussian function,

$$|S_r(\omega)|^2 = \frac{1}{\Delta\omega} \exp\left[-\frac{(\omega - \omega_0)^2}{(\Delta\omega)^2}\right],$$

we obtain

$$\bar{I}(\boldsymbol{\rho}) \sim 1 + \cos\left(\varphi + \frac{2\pi dx}{\lambda r_c}\right) \exp\left[-\left(\frac{L^2}{L_c^2}\right)\right], \tag{A4.1}$$

where $L \approx 2L_s + dx/r_c$ is the path difference for the rays, $L = AB_1 + B_1C - AB + BC$, φ is a phase constant, and x is the coordinate in the observation plane in

the direction orthogonal to the interference fringes (Fig. A4.1). The period of the interference pattern is $\sim \lambda r_c/d$, where d is the transverse size of the object, and λ is the mean wavelength of the source. One can see from Eq. (A4.1) that $V = \exp[-(L^2/L_c^2)]$. Close to the source, where $dx/r_c \ll 2L_s$, $V = \exp[-(4L_s^2/L_c^2)]$. If the coherence length of the source is much larger than twice the depth of the object BB_1, $L_c > 10L_s$, then $V = 1$ with high accuracy, like in the case of a very large coherence length source ($L_c = c/\Delta\omega \ggg L_s$). In this case, we will call the field scattered by the object BB_1 a coherent field. In the opposite case, where $L_c \ll 2L_s$, $V = 0$.

If the object consists of three or more pointlike scatterers ($N \geq 3$), then the interference pattern in the scattered field is much more complicated. In such a pattern, maxima can differ considerably from each other. Therefore, instead of visibility, it is reasonable to introduce integral characteristics describing deviation of the time-averaged intensity distribution $\bar{I}(\boldsymbol{\rho})$ in the interference pattern from a constant value. One of the simplest characteristics of this kind is the contrast of the intensity distribution $\bar{I}(\boldsymbol{\rho})$, which is equal to the difference between the mean square of this distribution and the square of the mean intensity in the distribution normalized to the square of the mean intensity:

$$C_s = \frac{\dfrac{1}{S_\rho}\int \bar{I}^2(\boldsymbol{\rho})d\boldsymbol{\rho} - \left[\dfrac{1}{S_\rho}\int \bar{I}(\boldsymbol{\rho})d\boldsymbol{\rho}\right]^2}{\left[\dfrac{1}{S_\rho}\int \bar{I}(\boldsymbol{\rho})d\boldsymbol{\rho}\right]^2}. \tag{A4.2}$$

For a constant intensity distribution, $C_s = 0$. In the case of the object B_1B_2 considered above, $C_s = \exp[-2(L^2/L_c^2)]/2 = V^2/2$. The same relation can be used for calculating the contrast of instantaneous intensity distributions.

For the field $E(\boldsymbol{\rho}, t)$ scattered by a rough object, the intensity distribution $I(\boldsymbol{\rho}, t)$ is even more complicated. This pattern is very difficult to analyze without a statistical description (see Sec. 1.2). The same relates to the instantaneous and time-averaged intensity distributions,

$$I(\boldsymbol{\rho}, t) \text{ and } \bar{I}(\boldsymbol{\rho}) = \frac{1}{T}\int_{t_0}^{t_0+T} I(\boldsymbol{\rho}, t)dt.$$

For this reason, these distributions are treated as realizations of random processes generated by a fixed distribution $\xi(\boldsymbol{r})$ of the surface roughness height of the object under study. This representation enables one to obtain analytical relations for the contrast C_s, which can characterize deviation of the intensity distribution from constant in the case of complicated distributions. As before, we assume that the object is illuminated by a pointlike narrow-band source (Fig. A4.2). Then, in the

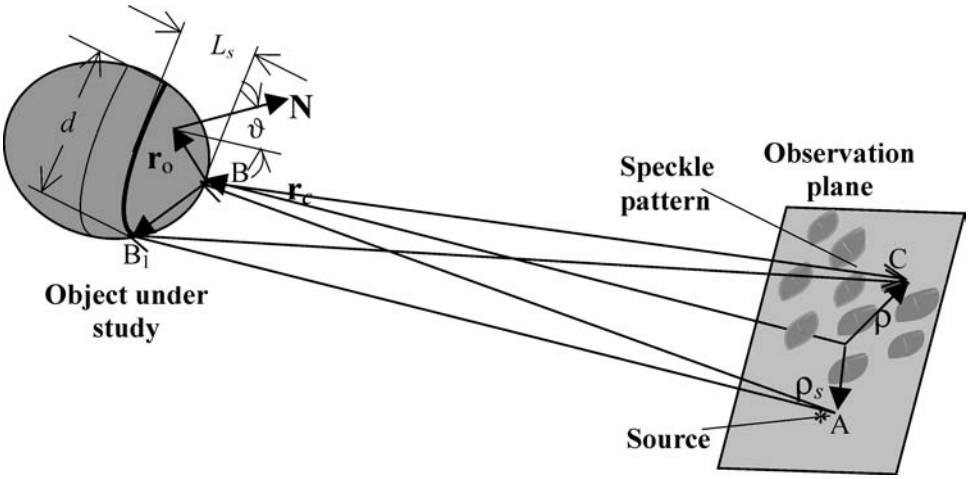

Figure A4.2 Formation of the scattered field in the case where the rough object is illuminated by a narrow-band source. The thick arc on the object surface denotes the boundary of the backscattering surface domain.

case of a rough object,

$$\bar{I}(\boldsymbol{\rho}) = \frac{1}{T}\int_{t_0}^{t_0+T} |E(\boldsymbol{\rho}, t)|^2 dt,$$

where $E(\boldsymbol{\rho}, t) = \int E_0(\boldsymbol{\rho}, \omega)\exp(-i\omega t)d\omega$ is the field scattered by the object at one of the frequencies [see relation (1.32)], K is a constant, $\mathbf{N}$ is the normal to the object's mean surface, $\mathbf{q} = -\boldsymbol{\nu}_i + \boldsymbol{\nu}_o$, $\boldsymbol{\nu}_i = (\mathbf{r}_c - \boldsymbol{\rho}_s)/|\mathbf{r}_c - \boldsymbol{\rho}_s|$, $\boldsymbol{\nu}_o = -\mathbf{r}_c/r_c$, $H_\omega(\mathbf{r}, \boldsymbol{\rho}) = \exp\{i[\omega(|\mathbf{r} - \boldsymbol{\rho}_s| + |\mathbf{r} - \boldsymbol{\rho}|)]/c\}$, and $\mathbf{r}$ is the radius-vector of the object's mean surface. Here, $\mathbf{r}_c$ is the radius vector of the point B, which is the top of the maximum backscattering domain, and for which the vectors $\mathbf{N}$ and $\mathbf{q}$ are parallel.

Let us first define the correlation function of a field scattered by a rough object, using the same analysis as we used in the case of monochromatic illumination of the source [see relation (1.36)]. Assuming that the standard deviation of the rough surface $\sigma \gg \lambda = (2\pi c)/\omega_0$ and that $\sigma/\ell \gg d/r_c$, where ℓ is the correlation radius of the rough surface, and d is the size of the backscattering domain, which will be defined below, we obtain the correlation function of the scattered field in the form

$$\begin{aligned}\langle E(\boldsymbol{\rho}_1, t_1)E^*(\boldsymbol{\rho}_2, t_2)\rangle = |K|^2 \iiint k_i(\mathbf{r})H_{\omega 1}(\mathbf{r}, \boldsymbol{\rho}_1)H^*_{\omega 2}(\mathbf{r}, \boldsymbol{\rho}_2) \\ \times \exp\left[\frac{-q_N^2\sigma^2(\omega_1 - \omega_2)^2}{c^2}\right] S_r(\omega_1)S_r^*(\omega_2) \\ \times \exp[i(\omega_1 t_1 - \omega_2 t_2)]d\mathbf{r}d\omega_1 d\omega_2, \qquad \text{(A4.3)}\end{aligned}$$

where

$$k_i(\mathbf{r}) \approx |k(\mathbf{r})|^2 \exp -\left[\frac{\tan\vartheta(\mathbf{r})\ell}{\sigma}\right]^2, \quad \vartheta(\mathbf{r}) = \arctan\left(\frac{\sqrt{\mathrm{q}^2 - q_N^2}}{q_N}\right),$$

$q_N(\mathbf{r}) = \mathbf{q}\cdot\mathbf{N}(\mathbf{r})$, and the symbol $\langle\rangle$ denotes averaging over various realizations $\xi(\mathbf{r})$ of the surface roughness height.

The main contribution to the integral (A4.3) is given by the domain of the scattering surface bounded by the factor $\exp\{-[\tan\vartheta(\mathbf{r})\ell/\sigma]\}^2$. This domain, corresponding to the range $0 \le \mathbf{r}_o \le \mathbf{r}_{om}$, where $\mathbf{r}_o = \mathbf{r} - \mathbf{r}_c$ and $\mathbf{r}_{om}$ satisfies the equation $\vartheta(\mathbf{r}_{om}) = 2\sigma/\ell$, is the domain of backscattering, for which all scattered waves come to the observation point $\boldsymbol{\rho}$; in Fig. A4.2 it is shown by a thick arc on the surface of the object. One can see from the figure that the maximum path difference for rays coming from the source $\boldsymbol{\rho}_s$ to the point $\mathbf{r}$ on the mean surface of the object and from point $\mathbf{r}$ to the observation point $\boldsymbol{\rho}$ is $L_m = \mathrm{AB}_1 + \mathrm{B}_1\mathrm{C} - \mathrm{AB} + \mathrm{BC} = |\mathbf{r}_c + \mathbf{r}_{om} - \boldsymbol{\rho}_s| + |\mathbf{r}_c + \mathbf{r}_{om} - \boldsymbol{\rho}| - r_c - |\mathbf{r}_c - \boldsymbol{\rho}|$. At r_o, $\rho \ll r_c$ and for the observation plane orthogonal to the radius vector $\mathbf{r}_c$, $L_m \approx 2L_s$, where $L_s = \mathbf{q}\cdot\mathbf{r}_{om}$. One can show that $L_s \sim (\sigma/\ell)^2\rho_o$, where ρ_o is the curvature radius of the mean surface. The parameter L_s is equal to the depth of the backscattering domain or, equivalently, to the distance between the two points of the surface that are, respectively, closest to the observation plane and furthest from it. Within the selected domain, the path difference for rays coming from the source point $\boldsymbol{\rho}_s$ to the point $\mathbf{r}$ and from the point $\mathbf{r}$ to the observation plane $\boldsymbol{\rho}$ does not exceed $2L_s$. One can also see from the figure that at $2L_s \ll L_c$, all rays coming from the backscattering domain interfere with each other. Below we will show that in this case, the interference pattern is a speckle pattern with contrast close to unity; whereas under the opposite condition, $2L_s \gg L_c$, a speckle pattern is also formed, but the contrast in this case is much smaller than unity.

If the number of elements of the object's surface scattering radiation to the observation point is very large, which is satisfied under the condition $\ell^2 \ll S_e$, where ℓ is the correlation radius of the rough surface and S_e is the area of the backscattering domain, then the scattered field has a Gaussian distribution. In this case, the relation

$$\langle I(\boldsymbol{\rho}_1, t_1)I(\boldsymbol{\rho}_2, t_2)\rangle - \langle I(\boldsymbol{\rho}_1, t_1)\rangle\langle I(\boldsymbol{\rho}_2, t_2)\rangle = |\langle E(\boldsymbol{\rho}_1, t_1)E^*(\boldsymbol{\rho}_2, t_2)\rangle|^2$$

is valid, which is analogous to relation (1.36). Taking this into account, one can represent the correlation function of the time-averaged intensity distribution in the scattered field in the form

$$\begin{aligned} B_a(\boldsymbol{\rho}_1, \boldsymbol{\rho}_2) &= \langle \bar{I}(\boldsymbol{\rho}_1)\bar{I}(\boldsymbol{\rho}_2)\rangle - \langle \bar{I}(\boldsymbol{\rho}_1)\rangle\langle \bar{I}(\boldsymbol{\rho}_2)\rangle \\ &= \frac{1}{T^2}\int_{t_0}^{t_0+T}\int_{t_0}^{t_0+T} |\langle E(\boldsymbol{\rho}_1, t_1)E^*(\boldsymbol{\rho}_2, t_2)\rangle|^2 dt_1 dt_2. \end{aligned}$$

The results obtained above can be used for determining the contrast of the time-averaged intensity distribution (A1.2). One can show that under the condition $\ell^2 \ll S_e$, C_s is approximately equal to the relative fluctuations of $\bar{I}$:

$$C_s \approx C = \frac{\langle \bar{I}^2 \rangle - \langle \bar{I} \rangle^2}{\langle \bar{I} \rangle^2} = B_a(\boldsymbol{\rho}, \boldsymbol{\rho}) \langle \bar{I}(\boldsymbol{\rho}) \rangle^{-2}. \tag{A4.4}$$

In the literature, the parameter C is referred to as the contrast[10] or blinking index.[29] In this book, we usually call it the contrast. Suppose that $\rho^3/\lambda^2 r_c \ll 1$ and the data-processing time satisfies the condition $T > 100L_s/c > 1/\Delta\omega$. If $L_s \gg (\rho d)/r_c$ and $100L_s > L_c > q_N \sigma$, which is usually the case in practice, we obtain, taking into account relation (A4.3), that

$$\langle \bar{I}(\boldsymbol{\rho}) \rangle \approx K \int k_i(\mathbf{r}_1) d\mathbf{r}, B_a(\boldsymbol{\rho}, \boldsymbol{\rho}) \approx K^2 \iint k_i(\mathbf{r}_1) |R(\mathbf{r}_1, \mathbf{r}_2)|^2 k_i(\mathbf{r}_2) d\mathbf{r}_1 d\mathbf{r}_2,$$

where $R(\mathbf{r}_1, \mathbf{r}_2) = \int |S_r(\omega)|^2 \exp\{-i\omega[(|\mathbf{r}_1 - \boldsymbol{\rho}_s| + r_1 - |\mathbf{r}_2 - \boldsymbol{\rho}_s| - r_2)/c]\} d\omega$.

For the Gaussian spectrum

$$|S_r(\omega)|^2 = \frac{1}{\Delta\omega} \exp\left[-\frac{(\omega - \omega_0)^2}{(\Delta\omega)^2} \right],$$

omitting inessential factors, we find the correlation function in the form $R(\mathbf{r}_1, \mathbf{r}_2) = \exp\{-[(|\mathbf{r}_1 - \boldsymbol{\rho}_s| + r_1 - |\mathbf{r}_2 - \boldsymbol{\rho}_s| - r_2)^2/L_c^2]\}$.

At $L_c > 10L_s$, $R(\mathbf{r}_1, \mathbf{r}_2) \approx 1$. In this case, $C \approx 1$. The same result is obtained [see Eq. (1.43)] for $\ell^2/S_e \ll 1$ in the case of illuminating the object by monochromatic light. One can show that at $L_c > 10L_s$, the correlation radii for speckle patterns in the time-averaged intensity distribution $\bar{I}(\boldsymbol{\rho})$ and in the instantaneous intensity distribution $I(\boldsymbol{\rho}, t)$ in the case of monochromatic illumination coincide and are equal to $\rho_c \sim \lambda r_c/d$. Hence, at $L_c > 10L_s$ the scattered field forms a speckle pattern with almost unity contrast, as in the case of monochromatic illumination. In this case, the scattered field at each observation point is formed as a superposition of the amplitudes of all waves scattered by the object's surface and reaching the observation point $\boldsymbol{\rho}$. Such a field is defined as a *coherent field*. Thus, if $L_c > 10L_s$, which means that the coherence length of the source is much larger than twice the depth of the backscattering surface domain for the rough object (the distance between the object's most distant point and its closest point to the observation plane), then the field scattered by the object is a coherent field. For the same parameters r_c, L_s, and d, both the visibility of interference fringes for a two-point object (Fig. A4.2) and the contrast of the speckle pattern for a rough object (Fig. A4.2) are close to unity; and the correlation radius of the speckle pattern in the case of a rough object is equal to the period of interference fringes in the case of a two-point object. Therefore, in practice, it is reasonable to consider the scattered field as coherent when its speckle pattern has a contrast close to unity.

If the coherence length of the source satisfies the condition $L_c \ll 2L_s$, then the contrast can be calculated analytically for relatively simple shapes of the backscattering surface domains, such as a frustum of a cone. Approximating the backscattering surface by a frustum of a cone, with its large base coinciding with the boundary of the backscattering surface (the thick line in Fig. A4.2) and with its small base placed at the distance L_c from the top of the surface (point B in Fig. A4.2), one can show that $C \approx L_c/2L_s \ll 1$. Under the condition $L_c \gg 2L_s$ we will define the field scattered by the rough object as a *partially coherent field*. In practice, it is reasonable to consider the field as partially coherent if the contrast of the speckle pattern in Fig. A4.2 becomes less than unity. This occurs for $L_c \leq 10L_s$. If the coherence length of the source is much smaller than twice the depth of the backscattering surface of the rough object, $L_c \ll 2L_s$, then the contrast of the speckle pattern in the scattered field is considerably less than unity. Taking all of this into account, it is possible to distinguish between a coherent and a partially coherent field: for $L_c > 10L_s$, the scattered field is coherent; for $10\lambda \leq L_c \leq 10L_s$, it is partially coherent; and for $L_c \leq 10\lambda$ ($\Delta\omega \geq 0.1\omega_0$), it is incoherent.

These results have a simple physical interpretation. Let the object be illuminated by continuous radiation with coherence length L_c. If $L_c \ll 2L_s$, then the backscattering surface (shown in Fig. A4.3 by a thick arc) consists of $N_c = 2L_s/L_c$ ring-shaped domains. Inside of each domain, various parts of the surface scatter waves that can interfere with each other. As a result, these waves form in the observation plane speckle patterns with unity contrast. At the same time, if parts of the surface are placed in different, even neighboring ring domains, waves scattered by them do not interfere. Therefore, in the observation domain, N_c statistically independent speckle patterns are summed. Each of these patterns has a unique distribution of speckles. When these speckle patterns are summed, fluctuations in the resulting scattered field interference pattern are reduced N_c times. Hence, the intensity distribution contrast in the resulting speckle pattern is $C_s \approx 1/N_c$.

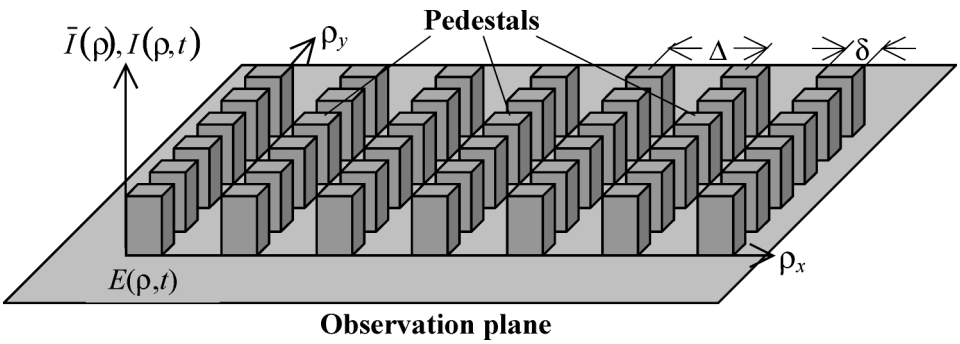

Figure A4.3 Intensity distribution of the scattered field consisting of equidistant pedestals with square bases $\delta \times \delta$ and the distances Δ between the centers. Here, ρ_x and ρ_y are components of the radius vector $\boldsymbol{\rho}$ in the plane where the scattered field $E(\boldsymbol{\rho}, t)$ is observed.

Inequalities $L_c > 10L_s$, $10\lambda \le L_c \le 10L_s$, and $L_c \le 10\lambda$ can also be used for defining the achromaticity of the source illuminating an object with known parameters of shape and roughness, since $L_s \sim (\sigma/\ell)^2\rho_o$, where ρ_o is the curvature radius of the mean surface. If $L_c > 10L_s$, i.e., the spectral bandwidth of the illuminating source $\Delta\omega < c/10L_s$, then the source is practically monochromatic. The scattered field in this case is a coherent field. If $L_c \le 10L_s$, i.e., if the spectral bandwidth of the illuminating source satisfies the condition $\Delta\omega \ge c/10L_s$, we call the source quasi-monochromatic. In the case of such illumination, the scattered field is partially coherent. If $L_c \le 10\lambda$, i.e., $\Delta\omega \ge 0.1\omega_0$, then the source is polychromatic and the scattered field is incoherent. It is interesting to note that if a rough object is illuminated by a quasi-monochromatic source with coherence length $L_c \ll 2L_s$, then the contrast of the speckle pattern in the scattered field is much smaller than unity. In this case, the intensity distribution in the scattered field is practically the same as for the case of white-light illumination.

Finally, let us use relation (A4.2) for the contrast C_s and give a qualitative explanation for various values of the contrast in the speckle patterns of scattered fields and images that were considered in Chapters 1 and 2 and this appendix. To do this, suppose that in relation (A4.2), the instantaneous intensity distribution $I(\boldsymbol{\rho}, t)$ or the time-averaged intensity distribution $\bar{I}(\boldsymbol{\rho})$ consists of equidistant pedestals with square bases of size $\delta \times \delta$, the distance between the centers of neighboring pedestals being Δ (Fig. A4.3). It is easy to show that in this case, $C_s = (\Delta/\delta)^2 - 1$. In particular, if $\Delta \to \delta$, $C_s \to 0$ and $I(\boldsymbol{\rho}, t)$ (or $\bar{I}(\boldsymbol{\rho})$) is constant. This case illustrates the situation that occurs for a very small coherence length illuminating source: for an incoherent scattered field and for an incoherent image, the intensity distribution has practically zero contrast (see Sec. 2.5). At $\Delta = \sqrt{2}\delta$, when the distance between the neighboring pedestals is approximately equal to the base size, $C_s = 1$. This is a model for the speckle pattern in the Fresnel zone of the scattered coherent field (see Sec. 1.3) and in a coherent image formed under the condition that separate elements of the rough surface are not resolved by the imaging system (see Sec. 2.2.1). Then, the contrast of the speckle pattern is close to unity and the distance between neighboring speckles is approximately equal to the speckle size. At $\Delta \gg \delta$, when the distance between the neighboring pedestals by far exceeds the base size, $C_s \approx (\Delta/\delta)^2 \gg 1$. This is a model of speckle pattern formation in the scattered coherent field at a small distance from the scattering surface ($r_c < \ell^2/\lambda$; Sec. 1.3) and in a coherent image formed under the condition that separate elements of the rough surface are resolved by the imaging system (see Sec. 2.2.2). Then, the contrast of the speckle pattern can be much larger than unity, and the distances between the neighboring speckles can considerably exceed their sizes.

Conclusions

1. Coherence of fields scattered by rough objects depends strongly on the coherence length L_c of the illuminating radiation and on the geometric parameters of the scattering object. A scattered field is called *coherent* if at each point of

the observation domain it is formed by means of amplitude summation (interference) of all scattered waves coming to that point. Such a field is formed if $L_c \geq 10L_s$, where L_s is the depth of the backscattering surface of the object. A scattered field is called *partially coherent* if at each point of its observation it is formed by means of amplitude summation (interference) of waves scattered by separate parts of the object's surface. Such a field is formed under the condition $10L_s \geq L_c \geq 10\lambda$. If $L_c \leq 10\lambda$, i.e., $\Delta\omega \geq 0.1\omega_0$, then the source is polychromatic and the scattered field is *incoherent*.

2. If the number of scattering surface elements is large, then the intensity distribution in the scattered field forms a speckle pattern, which in the case of a coherent scattered field has almost unity contrast, and in the case of a partially coherent and an incoherent field, has a contrast much less than unity.
3. From conclusion 1 it follows that radiation sources used in remote sensing to illuminate objects can be categorized according to their achromaticity. If $L_c \geq 10L_s$, then the source is practically monochromatic and the scattered field is coherent. In the literature, such a source is often called a coherent source. If $10L_s \geq L_c \geq 10\lambda$, then the source is quasi-monochromatic and the scattered field is partially coherent. In the literature, such a source is usually called low-coherent. If $L_c \leq 10\lambda$, i.e., $\Delta\omega \geq 0.1\omega_0$, where $\Delta\omega$ and ω_0 are, respectively, the width and the mean frequency of the source spectrum, then the source is polychromatic.

Appendix 5

Physics of Speckle Pattern Formation in the Images of Rough Objects

Let us describe the formation of the coherent image of a rough surface illuminated by a plane monochromatic wave with the wavelength λ.[39] Consider a somewhat idealized case where the rough surface is flat and the roughness height standard deviation is large compared to the wavelength, $\sigma \gg \lambda$. The surface will be considered as a strongly deformed mirror (see Figs. A5.1–A5.3). In this case, it can be viewed as a set of separate elements, which can be approximated by convex or concave parabolic mirrors smoothly joined together. Their diameters are random and, on average, equal to the correlation radius of the surface roughness height ℓ. Their focal lengths are also random and, on the average, are equal to $\ell^2/2\sigma$. In this representation, the rough surface is a source of secondary spherical waves coming from separate elements and focusing at points placed on different sides of the flat mean surface. In Figs. A5.1–A5.3, these are random points A, B, C, D, F, K, which we will call points of random focusing. Their optical conjugates are points placed on different sides of the image plane. The image plane itself is optically conjugate to the flat mean surface. Each point of the coherent image of the rough surface is formed due to the superposition of waves focused by the imaging system to this point of the image plane.

Further, let us analyze how the coherent image of the rough surface is formed for different sizes d_ρ of the imaging system aperture. Here, one can distinguish between three typical cases.

Case 1: $0 < d_\rho < (\lambda r_c)/\ell$. Here, r_c is the distance from the imaging system aperture to the flat mean surface (Fig. A5.1). From these inequalities, it follows that the size $(\lambda r_c)/d_\rho$ of the minimum resolvable domain of the rough surface, according to the Rayleigh criterion, exceeds the roughness height correlation radius ℓ. In the figure, this is the domain between points A and K. Under this condition, the field at each point of the image plane is a superposition of a large number of waves scattered by that domain. All the waves are focused into the area shown in Fig. A5.1 by an oval. According to the central limit theorem, the resulting field distribution is close to Gaussian, and its intensity contrast C or, in other words, the contrast of the speckle pattern in the coherent image, is close to unity ($C \approx 1$).

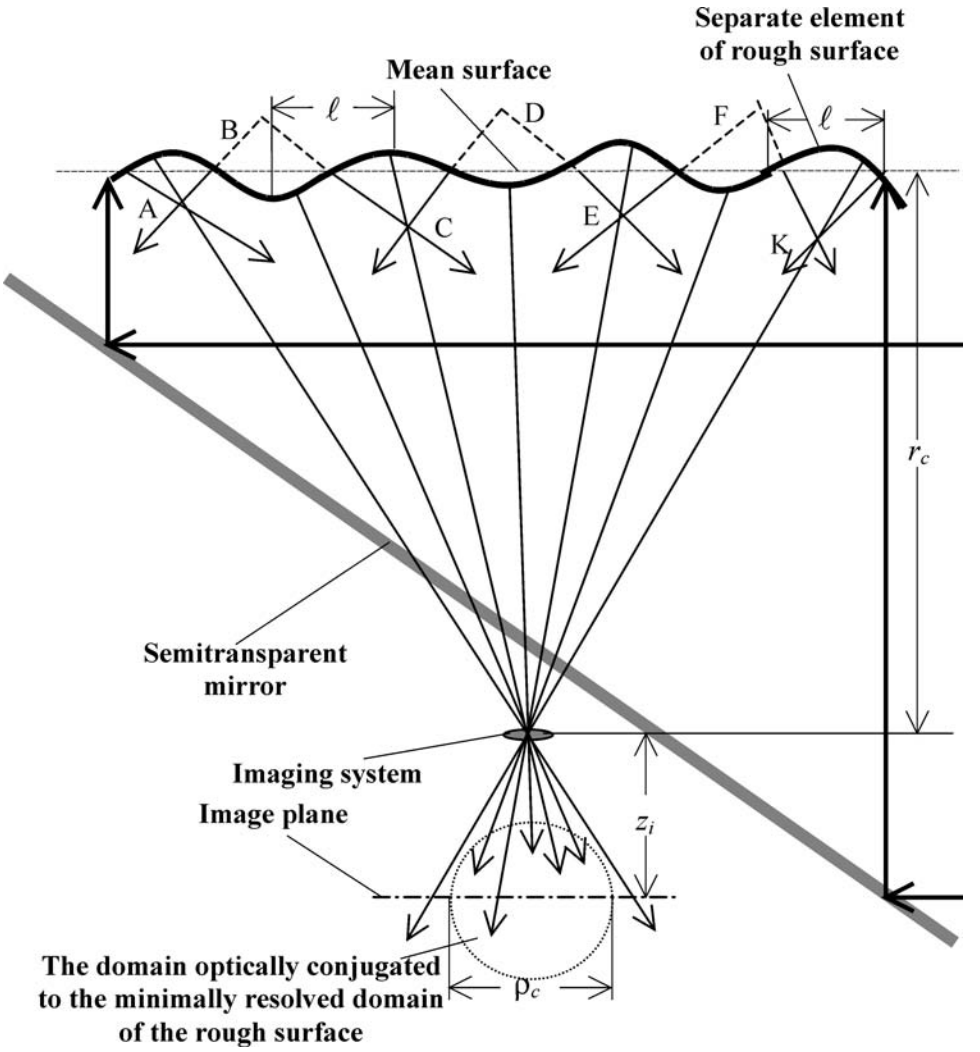

Figure A5.1 Formation of the coherent image of a rough surface (thick curve) for the case of a small-aperture imaging system, $d_\rho < (\lambda r_c)/\ell$. Here, ℓ is the correlation radius of the object surface roughness height. The thick arrows denote rays propagating from the monochromatic source. The thin arrows denote secondary spherical waves propagating from the rough surface. The contrast of the speckle pattern is $C \approx 1$. The correlation radius of the speckle pattern is $\rho_c \approx (\lambda z_i)/d_\rho$.

The contrast can be used to estimate the ratio between the sizes of bright spots in the speckle pattern and the dark intervals between them. For this purpose, let us approximate the speckle pattern by equidistant rectangular pedestals with square bases $\rho_c \times \rho_c$ and equal sizes (see Fig. A4.2 in Appendix 4). In this case, the pedestals imitate bright spots in the speckle pattern and their size ρ_c imitates the correlation radius. Then, $C \approx (\Delta/\rho_c)^2 - 1$, where Δ is the distance between the

centers of neighboring bright spots (speckles). If the contrast $C \approx 1$, then the size of the dark spaces is of the same order as the spot size ρ_c. If $0 < d_\rho < (\lambda r_c)/\ell$, then the bright spot size can be estimated from the condition that in this case, the speckle pattern is formed mainly by diffraction by the imaging system aperture. As a result, random points A, B, C, D, F, and K are transformed in the image plane into an Airy disk (a speckle). The average size of the domain where the brightness of this spot is almost constant, i.e., the correlation radius of the speckle pattern, is

$$\rho_c \approx \frac{\lambda z_i}{d_\rho}, \tag{A5.1}$$

where z_i is the distance between the image plane and the imaging system's aperture. As one can see from Fig. A5.1, the longitudinal size of the oval area is equal to the correlation radius of the speckle pattern, ρ_c.

Hence, under the condition $0 < d_\rho < (\lambda r_c)/\ell$, a coherent image is a speckle pattern consisting of bright Airy disks (speckles) separated by dark spaces, which are approximately the same size as an average speckle. Experiments confirm that a speckle pattern consists of speckles, which are the Airy disks. In particular, for a circular imaging system aperture, the pattern consists of a set of Airy disks deformed by each other so that each disk is a concentric ring with a bright spot at the center. The contrast of the speckle pattern is $C \approx 1$ and its correlation radius is $\rho_c \approx (\lambda z_i)/d_\rho$. Let us further increase the size d_ρ of the imaging system aperture. Then, the correlation radius ρ_c will be reduced to a certain minimum, which can be estimated for the second interval of d_ρ variation.

Case 2: $(\lambda r_c)/\ell < d_\rho < (\sigma r_c)/\ell$ (Fig. A5.2). In this case, the speckle pattern of a coherent image is formed mainly geometrically. Every second spherical wave coming from a single element of a rough surface is focused at some distance from the image plane. In Fig. A5.2, we show for simplicity a wave that comes from the edge element and is focused at the point K′ optically conjugate to the point of random focusing, K. Then, in the image plane, there appears a bright defocused spot, i.e., a speckle. Its size is determined by the correlation radius of the speckle pattern, ρ_c. A simple geometric analysis shows that at $r_c \gg \ell^2/2\sigma$,

$$\rho_c = \frac{d_\rho z_i \ell^2}{\sigma r_c^2}, \tag{A5.2}$$

and that under the condition $(\lambda r_c)/\ell < d_\rho < \sigma/\ell$, the distance between the neighboring speckles is

$$\Delta \approx \frac{z_i \ell}{r_c} \gg \rho_c. \tag{A5.3}$$

One can see from this relation that under the condition $(\lambda r_c)/\ell < d_\rho < \sigma/\ell$, the field in the image plane is formed by spatially separated contributions of secondary

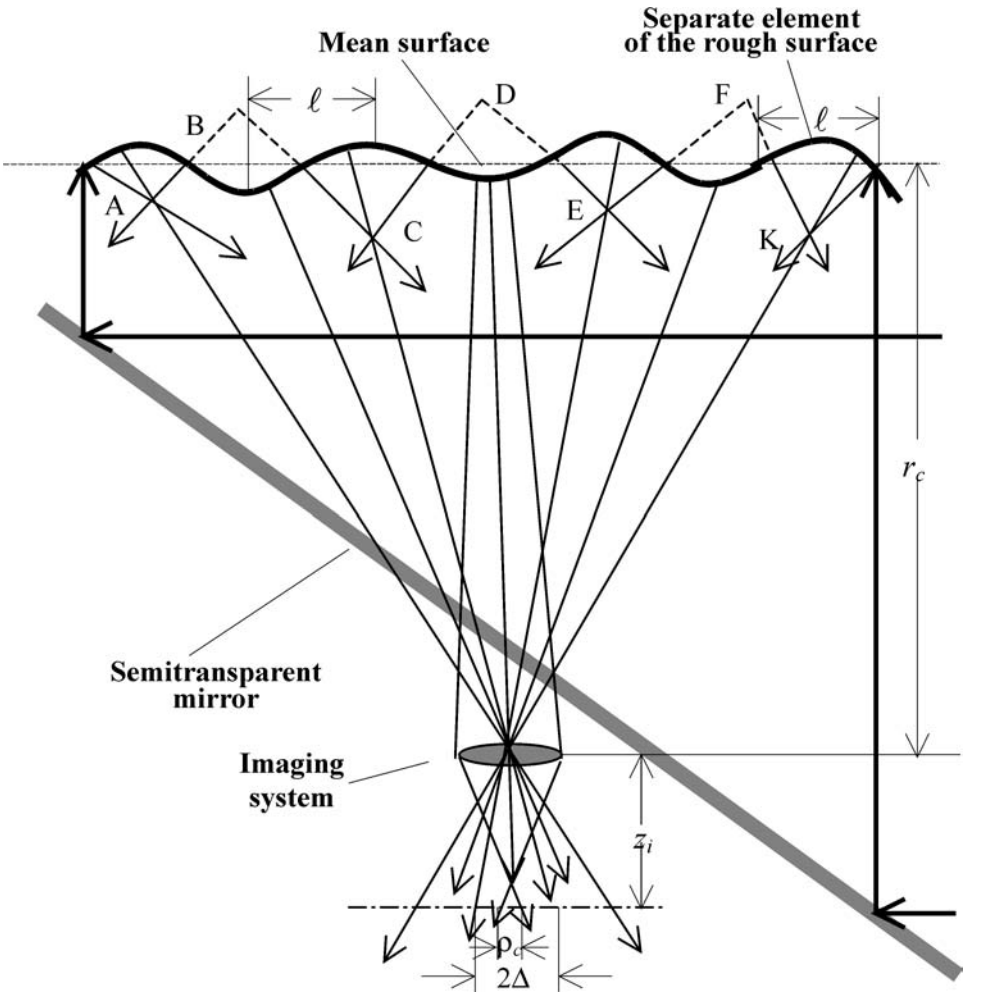

Figure A5.2 Formation of the coherent image of a rough object for an intermediate-aperture imaging system, $(\lambda r_c)/\ell < d_\rho < (r_c\sigma)/\ell$. Here, σ is the standard deviation of the object surface roughness height. The maximum contrast of the speckle pattern is $C \approx \sigma/\lambda$. The minimum correlation radius of the speckle pattern is $\rho_{cm} = (z_i\sqrt{\lambda\sigma})/(\ell r_c)$, with the imaging system aperture $d_\rho \approx (r_c\sqrt{\lambda\sigma})/\ell$.

spherical waves coming from separate elements. Therefore, the field statistics in the coherent image is essentially non-Gaussian and the contrast of the speckle pattern is

$$C \approx \left(\frac{\Delta}{\rho_c}\right)^2 \gg 1. \tag{A5.4}$$

From relation (A5.2), it is clear that when starting from a certain size d_ρ of the imaging system aperture, the speckle pattern correlation radius ρ_c increases

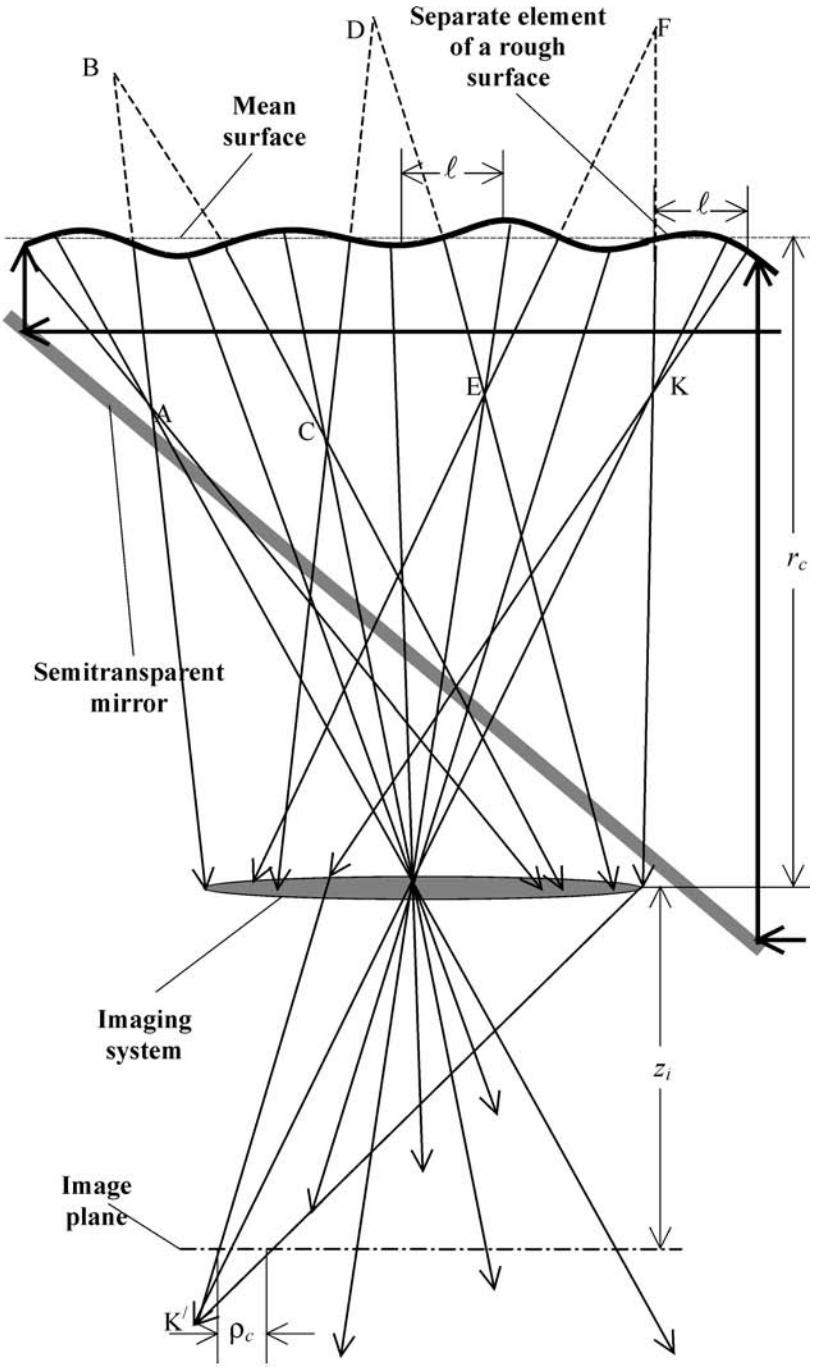

Figure A5.3 Formation of the coherent image of a rough object for a large-aperture imaging system, $d_\rho > (r_c\sigma)/\ell$. Here, the case of a smooth surface is presented. The contrast of the speckle pattern is $C \ll 1$; the correlation radius of the speckle pattern is $\rho_c \approx \ell/\mu$, where $\mu = r_c/z_i$ is the scaling factor.

with d_ρ. This critical size can be estimated by setting an equality between relations (A5.1) and (A5.2):

$$\frac{\lambda z_i}{d_\rho} = \frac{d_\rho z_i \ell^2}{\sigma r_c^2}. \tag{A5.5}$$

From Eq. (A5.5) we obtain $d_\rho = (r_c\sqrt{\lambda\sigma})/\ell$. Substituting this relation in (A5.2), we obtain the following estimate for the maximal correlation radius of the speckle pattern:

$$\rho_{cm} \approx \frac{z_i\sqrt{\lambda/\sigma}}{\ell r_c}. \tag{A5.6}$$

At $d_\rho = (r_c\sqrt{\lambda\sigma})/\ell$, the contrast of the speckle pattern achieves its maximum value, which can be estimated, with an account for (A5.3), (A5.4), and (A5.6), as $C_m \approx \sigma/\lambda$. Since $\sigma \gg \lambda$, $C_m \gg 1$.

Thus, at a certain size of imaging system aperture $d_\rho \approx (r_c\sqrt{\lambda\sigma})/\ell$, the contrast of the speckle pattern in a coherent image considerably exceeds unity, which indicates that the field statistics in the image are essentially non-Gaussian. In this case, the speckle pattern consists of single, isolated speckles with large distances between the neighboring speckles.

Case 3: $d_\rho > (\sigma r_c)/\ell$. Now, all secondary spherical waves coming from separate elements of the rough surface and passing through the points of random focusing (Fig. A5.3) enter the imaging system aperture. For instance, the secondary wave passing through point K enters the imaging system aperture and is then focused into the optically conjugate point K′. In Fig. A5.3, an example is given of a surface with more smooth inhomogeneities than are shown in Figs. A5.1 and A5.2. The mean size of the defocusing spots (speckles) in the image plane is in this case $\rho_c \approx \ell/\mu$, where $\mu = z_i/r_c$ is the scaling factor. This means that at $d_\rho > \sigma/\ell$, the correlation radius of the speckle pattern tends to ℓ/μ with an increase of d_ρ, and the speckles overlap. Therefore, the contrast of the speckle pattern in a coherent image is much less than unity, $C \ll 1$. At very large d_ρ and a constant reflection coefficient at different points of the object surface, the imaging system forms an almost exact copy of the field distribution $E_i(\mathbf{r})$ in the plane monochromatic wave illuminating the surface. Here, E_i is the amplitude of the illuminating wave. In this case the intensity at each point of the coherent image $I(\boldsymbol{\delta}) \sim |E_i(\mathbf{r})|^2$, and if, for example, $|E_i(\mathbf{r})|^2$ is constant, then the intensity $I(\boldsymbol{\delta})$ is constant as well. Such an image has zero contrast, $C = 0$. The same situation takes place in an aberration-free image of a flat mirrorlike surface, which can be formed by an imaging system with an aperture of arbitrary size.

References

1. M. Von Laue, *Geschichte der Physik*, Athenaum-Verlag, Bonn (1950).
2. L. Mandel and E. Wolf, Eds., *Optical Coherence and Quantum Optics*, Cambridge University Press, New York (1995).
3. M. Born and E. Wolf, *Principles of Optics*, Pergamon Press, New York (1964).
4. J.D. Rigden and E.F. Gordon, "Granularity of scattered maser light," *Proc. IRE*, **50**, pp. 2367–2370 (1962).
5. V.V. Anisimov, S.M. Kosel, and G.R. Lokshin, "About space-time statistical features of coherent radiation scattered by moving diffuse reflector," *Optika i Spektroscopia*, **27**(3), pp. 483–489 (1969) (in Russian).
6. J.C. Dainty, *Laser Speckle and Related Phenomena (Topics in Applied Physics)*, Springer-Verlag, Berlin (1975).
7. M. May, "Information inferred from observation of speckles," *J. Physics E*, **10**, pp. 849–859 (1977).
8. M. Mandrosov and V. Moyseev, "Informative features of speckle coherent images: overview," *Zarubeznaya Electronica*, **2**, pp. 3–41 (1982) (in Russian).
9. R. Jones and C. Wykes, *Holographic and Speckle Interferometry*, Cambridge University Press, New York (1983).
10. J. Goodman, *Statistical Optics*, John Wiley and Sons, Inc., New York (1985).
11. I.N. Troitsky and N.D. Ustinov, *Statistical Theory of Holography*, Radio i Svias, Moscow (1981) (in Russian).
12. P.A. Bakut, M.I. Mandrosov, I.N. Matveev, and N.D. Ustinov, *Theory of Coherent Images*, Radio i Svias, Moscow (1987) (in Russian).
13. T. Okamato and T. Asakura, "The statistics of dynamic speckles," in *Progress in Optics*, Vol. XXXIV, E. Wolf, Ed., pp. 183–248, North-Holland, Amsterdam (1995).
14. D.G. Voelz, S. O'Keefe, J.D. Gonglewski, D.B. Rider, and K.J. Schulze, "High-resolution imagery of a space object using an unconventional laser-illumination imaging technique," in *Optics in Atmospheric Propagation and Random Phenomena*, A. Kohnle and A.D. Devir, Eds., SPIE Proc. **2312**, pp. 202–211 (1994).
15. S.D. Ford, D.G. Voelz, V.L. Gamiz, S.L. Storm, S.R. Czyzak, J. Oldenettel, and A. Hunter, "Geo Light Imaging National Testbed (GLINT): past, present, future," in *Digital Image Recovery and Synthesis IV*, T.J. Schulz and P.S. Idell, Eds., SPIE Proc. **3815**, pp. 2–10 (1999).

16. P.A. Bakut and V.I. Mandrosov, "Properties of Fourier telescopic images of remote rough objects," in *Digital Image Recovery and Synthesis IV*, T.J. Schulz and P.S. Idell, Eds., SPIE Proc. **3815**, pp. 49–59 (1999).
17. V.I. Mandrosov, P.A. Bakut, and V.L. Gamiz, "Compensation of strongly heterogeneous atmospheric distortions in Fourier telescopy of remote rough objects," in *Atmospheric Propagation, Adaptive Systems, and Laser Radar Technology for Remote Sensing*, J.D. Gonglewski, et al., Eds., SPIE Proc. **4167**, pp. 192–197 (2001).
18. V.I. Mandrosov, "Panoramic microscope with interfering illuminating beams," in *Optical Biopsies and Microscopic Techniques III*, I.J. Bigio, et al., Eds., SPIE Proc. **3568**, pp. 167–177 (1999).
19. E.P. Feleppa, "Holographic motion-induced contrast images," *J. Cell. Biol.*, **40**, pp. 838–847 (1969).
20. R. Jain, "Dynamic scene analysis," in *Progress in Pattern Recognition*, **2**, L.N. Kanal and A. Rosenfeld, Eds., North-Holland, Amsterdam, pp. 125–132 (1985).
21. A.N. Anuashvili, I.V. Prangishvili, V.I. Mandrosov, and L.I. Weiss, "Time background holography of moving objects," in *Coherent Measuring and Data Processing Methods and Devices*, V.I. Mandrosov, Ed., SPIE Proc. **1978**, pp. 201–208 (1993).
22. I.V. Prangishvili, E.I. Akopov, A.N. Anuashvili, and V.I. Mandrosov, "Analysis of environment polluted by moving particles with the help of a spatially inhomogeneous laser beam," in *CIS Selected Papers: Optical Monitoring of the Environment*, N.N. Belov and E.I. Akopov, Eds., SPIE Proc. **2107**, pp. 437–448 (1993).
23. A.N. Anuashvili and Ye. A. Kharlamov, "Moving object detector operating by time averaging of coherent acoustic fields," in *Coherent Measuring and Data Processing Methods and Devices*, V.I. Mandrosov, Ed., SPIE Proc., **1978**, pp. 209–212 (1993).
24. H. Gramer, *Mathematical Methods of Statistics*, University of Stockholm, Stockholm (1946).
25. A.P. Husu, Yu.P. Vittenberg, and V.A. Palmaov, *Roughness of Surfaces: Theoretical Probability Approach*, Nauka, Moscow (1975) (in Russian).
26. Ia.S. Schifrin, *Issues of Statistical Theory of Antennas*, Radio i Svias, Moscow (1970) (in Russian).
27. P.A. Bakut, et al., *Issues of Statistical Radiolocation*, Radio i Svias, **1**, Moscow (1962), **2**, Moscow (1964) (in Russian).
28. P. Beckmann and A. Spizzichino, *Scattering of Electromagnetic Waves from a Rough Surface*, Pergamon Press, Oxford (1963).
29. S.M. Ritov, Yu.A. Kravtsov, and V.I. Tatarsky, *Introduction to Statistical Radiophysics*, **2**, Nauka, Moscow (1978) (in Russian).
30. F.G. Bass and I.M. Fuks, *Scattering from a Statistically Uneven Surface*, Radio i Svias, Moscow (1978) (in Russian).

31. E. Jakeman and P. Pussey, "Non-Gaussian fluctuation in electromagnetic radiation by random phase screen," *J. Physics A.*, **8**, pp. 369–378 (1979).
32. S.I. Belousov and I.G. Yakushkin, "Correlation of an intensity fluctuation of a collimated beam, scattered by the rough surface," *Proc. of Symposium of Waves Diffraction and Propagation*, **42**, pp. 137–142, Moscow (1981) (in Russian).
33. P.A. Bakut, F.V. Bunkin, D.F. Vlasov, and V.I. Mandrosov, "Effect of double passing of laser beam through ocean surface waves and top layers on echo-signal in laser air probing process," *Proceedings of All-Union Conf. on Coherent and Non-linear Optics*, Part 2, pp. 562–564, Moscow (1985) (in Russian).
34. P.A. Bakut, V.I. Mandrosov, et al., "Analysis of laser images quality of diffusive objects," *Kvantovaja Elektronika*, **5**(6), pp. 1257–1262 (1978) (in Russian).
35. J. Goodman, "Dependence of image speckle contrast on surface roughness," *Opt. Commun.*, **14**, pp. 849–858 (1975).
36. E. Jakeman, "Speckle statistics with a small number of scatterers," *Optical Engineering*, **23**(4), pp. 453–459 (1984).
37. I.S. Klimenko, *Holography of Focused Images and Speckle Interferometry*, Mir, Moscow (1986) (in Russian).
38. V.I. Mandrosov, "Statistical characteristics of optic images of rough surface," *Izvestia Vuzov* (*Radiophysics series*), **29**(10), pp. 1273–1279 (1986) (in Russian).
39. V.I. Mandrosov, "On using speckle structures of coherent images of rough objects for determining their parameters," *Optical Engineering Bulletin of SPIE/Russian Department*, (2), pp. 27–34, Moscow (1994).
40. J. Ohtsubo, "Non-Gaussian speckle: a computer simulation," *Applied Optics*, **21**(22), pp. 4167–4175 (1982).
41. V.I. Mandrosov, "Statistical characteristics of coherent images of non-plane surfaces," *Zhurnal Nauchnoy i Prikladnoy Fotografii i Kinematografii*, **30**(3), pp. 161–165 (1985) (in Russian).
42. P.A. Bakut, A.I. Deriugina, and V.I. Mandrosov, "A posteriori increase of resolution in optical system generating averaged monochromatic images," *Radiotechnika i Electronika*, **29**(8), pp. 1589–1596 (1984) (in Russian).
43. H. Pederson, "On contrast of polychromatic speckle pattern and its dependence on surface roughness," *Optica Acta*, **22**, pp. 15–22 (1975).
44. V.I. Mandrosov, "Statistical models of coherent fields scattered by moving objects and their use for object parameter determination," in *Coherent Measuring and Data Processing Methods and Devices*, V.I. Mandrosov, Ed., SPIE Proc. **1978**, pp. 2–11 (1993).
45. F.P. Chiang and C.C. Kin, "Strain determination on curved surfaces using far-field objective laser speckles," *Optical Engineering*, **21**(3), pp. 441–446 (1982).
46. K. Ebeling, "Measurement of in-plane mechanical vibration in the sub-angstrom range by use of speckle imaging," *Opt. Commun.*, **24**, pp. 125–131 (1978).

47. J.C. Marron and K.S. Schroeder, "Speckle from rotating objects," *Applied Optics*, **27**(20), pp. 4279–4287 (1988).
48. I.A. Popov and L.M. Veselov, "Tangential velocity measurement of diffuse object by using modulated dynamic speckle," in *Second International Conference on Vibration Measurements by Laser Techniques: Advances and Applications*, E.P. Tomasini, Ed., SPIE Proc. **2868**, pp. 550–558 (1996).
49. Yu.M. Bogdanov, *Mechanical Devices*, Machinostroenie, Moscow (1960) (in Russian).
50. Yu.H. Dubnistchev, "Measuring linear velocity of the solid body movement by Doppler spectrum scheme," *Optika i Spectroskopia*, **34**(3), pp. 587–593 (1973) (in Russian).
51. V.V. Barinov and V.I. Mandrosov, "Doppler method of measuring angular velocities of objects," in *Holographic Measuring Systems*, Proceedings of Novosibirsk's Electrotechnical Institute, **17**, pp. 31–37, Novosibirsk (1978) (in Russian).
52. V.V. Barinov and K.B. Tatarintsev, "Correlation characteristics of coherent images of diffusely scattering objects," in *Holographic Measuring Systems*, Proceedings of Novosibirsk's Electrotechnical Institute, **17**, pp. 38–46, Novosibirsk (1981) (in Russian).
53. A.S. Bogomolov, N.G. Vlasov, and A.E. Chtanko, "Investigating diffusely reflecting objects by speckle interferometry methods with the open aperture," *Journal of Tech. Phys*., (8), pp. 1896–1903 (1978) (in Russian).
54. P.A. Bakut, et al., "Methods of noncoherent holography and active Michelson interferometry for processing light fields," *Optika i Spectroscopia*, **59**, pp. 701–712 (1985) (in Russian).
55. Yu.V. Zhulina, "Phase error compensation in discrete aperture for observing moving objects," *Radioengineering and Electronics*, **10**, pp. 2061–2070 (1986) (in Russian).
56. N.D. Ustinov, et al., "Active aperture synthesis method for observation through perturbing media," *Kvantovoia Electronica*, **14**(1), pp. 108–110 (1987) (in Russian).
57. L.X. Sica, "Method for calibrating heterodyne receiver arrays," *Applied Optics*, **30**(15), pp. 1886–1888 (1991).
58. A. Volpov, et al., "Statistical modeling of the signal in small object imaging using active interferometry," *Optika of Atmosferi i Okeana*, **3**(12), pp. 1249–1257 (1990) (in Russian).
59. D.G. Voelz, et al., "Image synthesis from nonimaged laser-speckle patterns: comparison of theory, computer simulation, and laboratory results," *Applied Optics*, **30**(23), pp. 3333–3344 (1991).
60. L. Sica, "Estimator and signal-to-noise ratio for an integrative synthetic aperture imaging technique," *Applied Optics*, **30**(2), pp. 206–213 (1991).
61. L. Sica, "Effects of nonredundance on a synthetic-aperture imaging system," *J. Opt. Soc. Am. A.*, **10**(4), pp. 567–572 (1993).

62. L. Sica, "Image speckle contrast reduction resulting from integrative synthetic aperture imaging," *Applied Optics*, **31**(1), pp. 120–125 (1992).
63. R.A. Hutchin, "Sheared coherent interferometric photography: a technique for lensless imaging," in *Digital Image Recovery and Synthesis II*, P.S. Idell, Ed., SPIE Proc. **2029**, pp. 161–168 (1993).
64. D.B. Rider, D.G. Voelz, D. Stone, K.J. Schulze, D.R. Dean, and K.A. Bush, "Statistical and radiometric measurements of coherently illuminated, nonaugmented, low-earth-orbit satellites," in *Optics in Atmospheric Propagation and Random Phenomena*, A. Kohnle and A.D. Devir, Eds., SPIE Proc. **2312**, pp. 193–201 (1994).
65. B.F. Campbell, L. Rubin, and R.B. Holmes, "Synthetic-aperture imaging through an aberrating medium: experimental demonstration," *Applied Optics*, **34**(26), pp. 5932–5937 (1995).
66. R.B. Holmes, et al., "Analysis and simulation of a synthetic-aperture technique for imaging through a turbulent medium," *J. Opt. Soc. Am. A.*, **13**(2), pp. 351–364 (1996).
67. R.B. Holmes, S.S. Ma, A. Bhowmik, and C. Greninger, "Aperture-synthesis techniques that use very low power illumination," in *Advanced Imaging Technologies and Commercial Applications*, N.C. Clark and J.D. Gonglewski, Eds., SPIE Proc. **2566**, pp. 177–185 (1995).
68. K.R. MacDonald, et al., "Experimental demonstration of Fourier telescopy," in *Digital Image Recovery and Synthesis IV*, T.J. Schulz and P.S. Idell, Eds., SPIE Proc. **3815**, pp. 23–29 (1999).
69. T.J. Brinkley and D.G. Sandler, "Effects of atmospheric turbulence and jitter on Fourier telescopy imaging systems," in *Digital Image Recovery and Synthesis IV*, T.J. Schulz and P.S. Idell, Eds., SPIE Proc. **3815**, pp. 42–48 (1999).
70. R.B. Holmes and T.J. Brinkley, "Reconstruction of images of deep-space objects using Fourier telescopy," in *Digital Image Recovery and Synthesis IV*, T.J. Schulz and P.S. Idell, Eds., SPIE Proc. **3815**, pp. 11–22 (1999).
71. R. Hutching, "Microscope for Producing High Resolution Images without Precision Optics," U.S. Patent No. 4,584,484 (April 22, 1986).
72. M.S. Belen'kii, "Coherence degradation of a speckle field and turbulence effects on Fourier telescopy imaging system," in *Free-Space Laser Communication and Laser Imaging*, D.G. Voelz and J.C. Ricklin, Eds., SPIE Proc. **4489**, pp. 48–59 (2002).
73. M.S. Belen'kii, K. Hughes, T.J. Brinkley, and J.R. Oldenettel, "Effect of turbulence on downlink and horizontal path on high-order coherence moments in Fourier telescopy system," in *Free-Space Laser Communication and Laser Imaging II*, J.C. Ricklin and D.G. Voelz, Eds., SPIE Proc. **4821**, pp. 62–73 (2002).
74. Ye.I. Kachanov, *Methods and Tools of Hydro-acoustical Holography*, Sudostroenie, Leningrad (1989) (in Russian).

75. A. Peters, "Sonar System with Area Moving Object Indicator," U.S. Patent, IIC CI, G o1 S 15 /66/ (August 29, 1989).
76. C.C. Aleksoff, "Time-average holography extended," *Appl. Phys. Lett.*, **14**(1), pp. 23–24 (1969).
77. V.M. Ginsburg, et al., *Optical Holography: Practical Applications*, Radio i Svias, Moscow (1978) (in Russian).
78. A.N. Anuashvili, "New principle of moving object image reception," in *Coherent Measuring and Data Processing Methods and Devices*, V.I. Mandrosov, Ed., SPIE Proc. **1978**, pp. 147–155 (1993).
79. A.N. Anuashvili, V.I. Mandrosov, and Ya. Tsveraidze, "Principle of time averaging of coherent wave fields and its application to determining the parameters of moving objects," in *Coherent Measuring and Data Processing Methods and Devices*, V.I. Mandrosov, Ed., SPIE Proc. **1978**, pp. 156–162 (1993).
80. V.I. Mandrosov, A.I. Nekrasov, and V.V. Ratushnyi, "Information capacity of random coherent fields scattered by moving rough objects," in *Coherent Measuring and Data Processing Methods and Devices*, V.I. Mandrosov, Ed., SPIE Proc. **1978**, pp. 77–87 (1993).
81. Infrared Sensing Switch. ALPEX Wiring Device, made in Korea (1998).
82. E. Leith and J. Upatnieks, "Reconstructed wavefront and communication theory," *J. Opt. Soc. Am.*, **52**, pp. 1123–1130 (1962).
83. Yu.N. Denisyuk, "On representing optical properties of an object in the field of radiation scattered by it," *Optika i Spectroskopia*, **144**, pp. 1275–1285 (1963).
84. V.I. Mandrosov and A.I. Nekrasov, "Determining geometric and dynamic parameters of objects from intensity distribution of their coherent images," in *Coherent Measuring and Data Processing Methods and Devices*, V.I. Mandrosov, Ed., SPIE Proc. **1978**, pp. 133–140 (1993).

Index

Born in 1940, Valery I. Mandrosov received his Ph.D. in physics and mathematics in 1974 with a concentration in the field of radiophysics, including quantum radiophysics. He received a Doctor of Technical Sciences in 1989 in the field of optical location and ranging, optical communication, and optical data processing. He is a member of SPIE and the editor of the 1993 SPIE Proceedings Vol. 1978, *Coherent Measuring and Data Processing Methods and Devices*. He has authored more than 100 publications, including the 1987 Russian book *Theory of Coherent Images*, and has 25 inventions in the field: object detection, recognition and parameters determination, laser location and ranging, statistical models of coherent radiation scattered by moving rough objects, holography, and Fourier telescopy. Currently he is lecturing at the Moscow Institute of Physics and Technology.